UNIVERSITY OF MODENA AND REGGIO EMILIA

"ENZO FERRARI" DEPARTMENT OF ENGINEERING

PhD "Enzo Ferrari"

in Industrial and Environmental Engineering

XXXV Cycle

Academic Year 2021/2022

Technologies and Applications of Microfluidics for Scientific Research

Tutor

Prof. Massimo Borghi

Co-Tutor

Prof. Barbara Zardin

PhD Course Coordinator

Prof. Alberto Muscio

Candidate

Claudio Ongaro

"*We set sail on this new sea because there is new knowledge to be gained, and new rights to be won, and they must be won and used for the progress of all people...*
We choose to go ... and do the other things, not because they are easy, but because they are hard; because that goal will serve to organize and measure the best of our energies and skills, because that challenge is one that we are willing to accept, one we are unwilling to postpone, and one we intend to win, and the others, too."

September 12, 1962, Kennedy John F.
Rice University, Houston TX

Thanks

Here I wish to thank all the academics who guided, helped, and collaborated with me.

I hope I have not forgotten anyone because everyone's support has been indispensable for my PhD research.

University of Modena and Reggio Emilia

"Enzo Ferrari" Department of Engineering

Academic Discipline: "Fluid Machines"

- Prof. Massimo Borghi
- Prof. Barbara Zardin
- Prof. Alessandro d'Adamo
- Alice Betti MSc
- Giuseppe Corda MSc
- Giuseppe Capuzzimati BSc

Academic Discipline: "Electronics"

- Prof. Luca Selmi
- Denis Brandalise MSc
- Daniele Goldoni MSc

Academic Discipline: "Electrical and Electronic Measurements"

- Prof. Luigi Rovati
- Alberto Ferrari PhD

Academic Discipline: "Science and Technology of Materials"

- Prof. Marcello Romagnoli
- Prof. Luca Lusvarghi

Department of Engineering Sciences and Methods

Academic Discipline: "Technologies and Processing Systems"

- Prof. Diego Angeli
- Elisabetta Salerno PhD
- Luca Grassi MSc
- Alessandro Spila BSc
- Francesco Formentini BSc

Academic Discipline: "Technologies and Processing Systems"

- Prof. Leonardo Orazi
- Vincenzina Siciliani MSc

Department of Physics, Computer Science and Mathematics

Academic Discipline: “Applied Physics”

- Prof. Andrea Alessandrini
- Beatrice Bighi MSc

Department of Life Sciences

Academic Discipline: “General and Inorganic Chemistry”

- Prof. Fabio Biscarini

Academic Discipline: “Chemistry-Physics”

- Prof. Glauco Ponterini

Department of Surgical, Medical, Dental and Morphological Sciences

Academic Discipline: “Human Anatomy”

- Prof. Jessika Bertacchini
- Giulia Orlandi PhD

Department of Biomedical, Metabolic and Neurosciences

Academic Discipline: “Medical Genetics”

- Prof. Rossella Tupler
- Valentina Salsi PhD
- Floriana Napoli PhD
- Antonio Vallarola PhD
- Sara Pini MSc

Interdepartmental Center for Large Instruments

- Massimo Tonelli MSc
- Mauro Zapparoli MSc
- Jonathan Vinet PhD
- Cinzia Restani MSc

Politecnico di Milano

Dipartimento di Elettronica, Informazione e Bioingegneria

Academic Discipline: “Industrial Bioengineering”

- Prof. Marco Rasponi

CNR - NANO Institute of Nanoscience - Modena

Research line: “Lithographic Nanotechnology”

- Prof. Alessandro Di Bona

CNR - ISTEC Institute of Science and Technology for Ceramics – Faenza (RA)

Research line: "Bioceramics and Bio-Hybrid Composites"

- Andrea Ruffini PhD

CNR - IFN Istituto di Fotonica e Nanotecnologie - Milano

Research line: "Femtosecond Laser Micromachining"

- Prof. Roberto Osellame
- Prof. Francesca Bragheri

I also wish to add special thanks to the company GreenBone Ortho S.p.A., Faenza – Italy, for the technical support received and the free supply of numerous samples of its b.Bone™ product, essential for my research.

Riassunto

La microfluidica è il settore scientifico che si occupa dei fluidi che scorrono in circuiti con sezioni micrometriche e con velocità talmente basse, e di conseguenza numeri di Reynolds, tali da assicurare sempre un flusso laminare. Queste caratteristiche rendono i circuiti microfluidici ideali per gestire piccole quantità di fluidi in sensori e dispositivi, specialmente nel settore biomedicale. Si hanno così i micro-analizzatori o i micro-dispositivi di processo (*lab-on-chip*), i simulatori di organi (*organ-on-chip*), fino ai simulatori di più funzioni umane (*human-on-chip*). L'obiettivo di questa ricerca è di realizzare una base della conoscenza per la progettazione, produzione e sperimentazione di dispositivi microfluidici per la ricerca biomedica e industriale. Nel settore della ricerca, la tecnologia più utilizzata per realizzare circuiti microfluidici è la fotolitografia che permette di realizzare stampi in negativo con elementi di dimensioni micrometriche. Versando negli stampi (*replica molding*) del PDMS, una resina siliconica, e facendolo polimerizzare a caldo si realizzano circuiti microfluidici complessi con dimensioni compatte. I circuiti vengono poi sigillati con vetrini incollati tramite attivazione al plasma (*plasma bonding*). Lo scopo di questa ricerca è stato duplice, da un lato progettare e realizzare un dispositivo microfluidico per analizzare l'influenza (*shear-stress*) che ha il flusso di liquido di cultura sulla proliferazione cellulare ossea, dall'altro progettare e applicare una tecnologia *general purpose* per realizzare circuiti microfluidici più rapidamente e a costi più bassi rispetto alla tecnologia tradizionale. Da diversi anni sono utilizzati dei circuiti microfluidici per l'analisi delle cellule ossee, ma tali circuiti erano normalmente costituiti da un canale di proliferazione a sezione costante con solo l'altezza di dimensioni micrometriche, rappresentazione 2D di quello che avviene nelle ossa, risultando dei semplici esperimenti *in vitro* dove veniva fatto circolare il liquido di coltura. Questa ricerca è invece partita utilizzando come supporto cellulare (*scaffold*) una matrice di idrossiapatite, il componente minerale delle ossa, ricavato da strutture biologiche naturali e creando così un ambiente simile a quello *in vivo*. La struttura complessa e varia dei canali del supporto, il vero circuito 3D microfluidico, ha insita la difficoltà di caratterizzare i vari campioni, naturalmente uno diverso dall'altro, risolta con modellizzazioni della geometria dei canali partendo da scansioni ottiche, con prove sperimentali e con medie statistiche su gruppi di campioni omogenei. I risultati degli esperimenti, eseguiti su un ampio spettro di flussi, sono stati congruenti con i risultati delle ricerche precedenti, validando così la tecnica di modellizzazione per la caratterizzazione dei campioni. Successivamente la ricerca fu ampliata esaminando l'influenza dei bassi livelli di *shear stress* utilizzando un dispositivo progettato e realizzato tramite *replica molding* con PDMS.

La seconda parte della ricerca è partita dalla considerazione che la realizzazione di circuiti microfluidici tramite stampi fotolitografici e PDMS comporta molti passaggi, tempi lunghi di realizzazione e costi elevati dei materiali impiegati. Questa ricerca è invece partita dalla consolidata tecnologia di ablazione tramite impulsi laser concentrati in picosecondi per realizzare circuiti microfluidici su provini in vetro. I circuiti vengono poi sigillati con uno strato di silicone incollato tramite attivazione al plasma. Sono stati creati dei campioni standard in vetro e la qualità della geometria dei canali è stata validata mediante microscopio confocale. È stato validato l'utilizzo di siliconi commerciali, già disponibili in fogli e con costi estremamente ridotti, creando una metodologia di prova in pressione e utilizzandola su un largo numero di campioni incollati al plasma con parametri di attivazione differenti per determinare la loro migliore combinazione. È stata così validata una differente ma altrettanto efficace tecnologia realizzativa per dispositivi microfluidici. In Appendice un progetto precedente, sempre all'interno del corso di dottorato, che ha utilizzato il laser a picosecondi per tagliare una guarnizione di PDMS per uno spettroscopio. L'esperienza di questo progetto fu utile per sviluppare la ricerca esposta precedentemente. Tutte le ricerche si sono concluse con pubblicazioni scientifiche sia come articoli di giornale che atti di convegni.

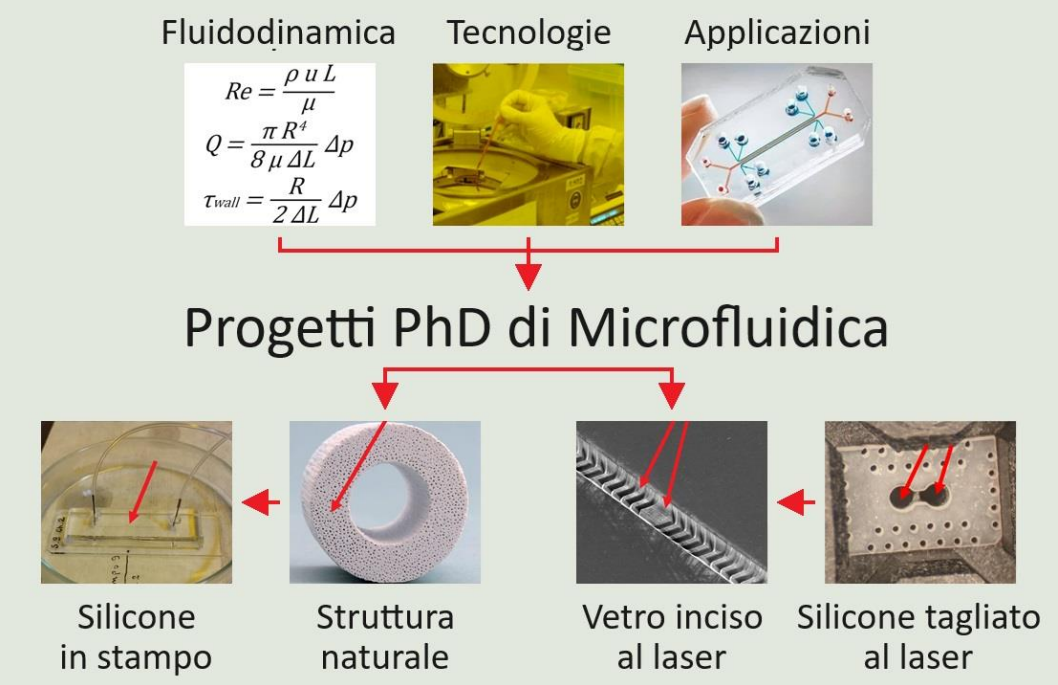

Fig. A. *Riassunto grafico dei progetti PhD.*

Abstract

Microfluidics is the scientific sector that deals with fluids that flow in circuits with micrometric sections and with such low speeds, and consequently Reynolds numbers, as to always ensure a laminar flow. These characteristics make microfluidic circuits ideal for managing small quantities of fluids in sensors and devices, especially in the biomedical sector. Thus, we have micro-analyzers or micro-process devices (lab-on-chip), organ simulators (organ-on-chip), up to simulators of multiple human functions (human-on-chip). The objective of this research is to create a knowledge base for the design, production and testing of microfluidic devices for biomedical and industrial research. In the research sector, the most used technology to create microfluidic circuits is photolithography which allows the creation of negative molds with elements of micrometric dimensions. By pouring PDMS, a silicone resin, into the molds (replica molding) and hot curing it, complex microfluidic circuits with compact dimensions are created. The circuits are sealed by plasma bonding of a layer of glass. The aim of this research was twofold, on the one hand to design and implement a microfluidic device to analyze the shear-stress influence of the culture fluid flow on bone cell proliferation, on the other hand to design and apply a general-purpose technology to make microfluidic circuits more quickly and at lower costs than traditional technology. For several years, microfluidic circuits have been used for the analysis of bone cells, but these circuits were normally made up of a constant section proliferation channel with only the height of micrometric dimensions, a 2D representation of what happens in the bones, resulting in simple *in vitro* experiments where the culture fluid was circulated. Instead, this research started using a cellular scaffold of hydroxyapatite, the mineral component of bone, derived from natural biological structures, thus creating an environment like that *in vivo*. The complex and varied structure of the scaffold channels, the true microfluidic 3D circuit, has inherent the difficulty of characterizing the various samples, naturally one different from the other, solved with modeling of the geometry of the channels starting from optical scans, with experimental tests and with statistical averages on groups of homogeneous samples. The results of the experiments, performed on a broad spectrum of flows, were congruent with the results of previous research, thus validating the modeling technique for the characterization of the samples. Subsequently the research was expanded by examining the influence of low levels of shear stress using a device designed and manufactured by replica molding with PDMS. The second part of the research started from the consideration that the realization of microfluidic circuits using photolithographic molds and PDMS involves many steps, long production times and expensive materials.

Instead, this research started from the consolidated technology of ablation by laser pulses concentrated in picoseconds to create microfluidic circuits on a layer of glass.The circuits are sealed by plasma bonding of a layer of silicone. Standard glass samples were created, and the quality of the channel geometry was validated by confocal microscope scanning. The use of commercial silicones, already available in sheets and with extremely low costs, has been validated by creating a pressure test methodology and using it on many samples with different plasma bonding parameters to determine their best combination. A different but equally effective manufacturing technology for microfluidic devices was thus validated. In the Appendix is a previous project, always within the doctoral course, which used the picosecond laser to cut a PDMS gasket for a spectroscope. The experience of this project was useful for developing the research outlined above. All this research resulted in scientific publications both as articles and conference papers.

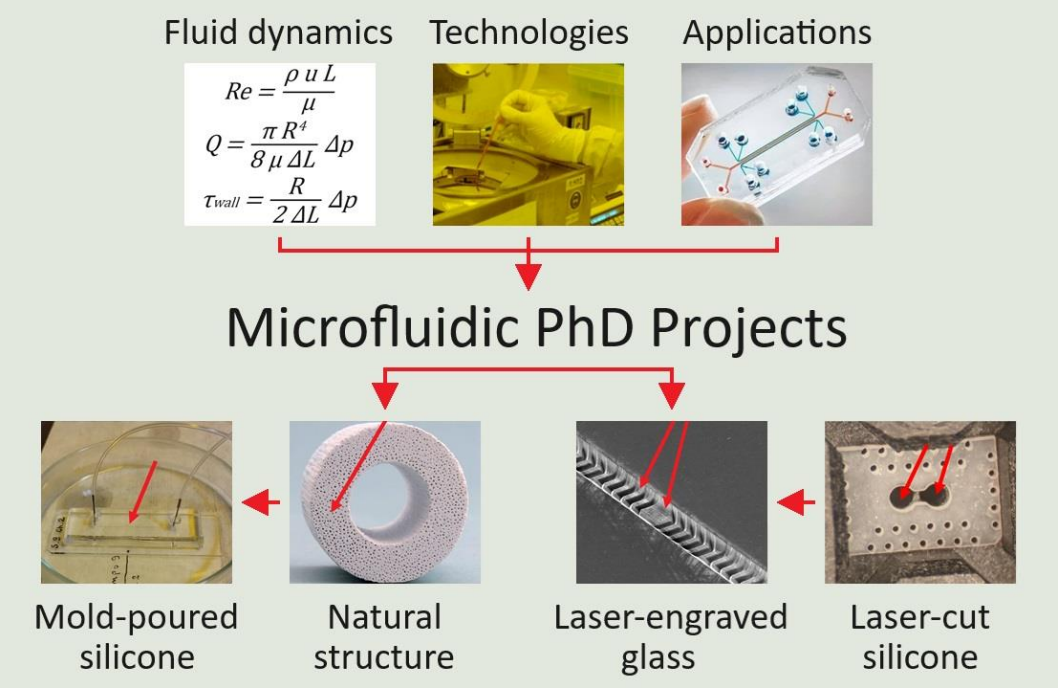

Fig. B. *Graphical abstract of the PhD projects.*

Table of Contents

Introduction

The aim of my PhD course was to be preparatory to the establishment of a new academic discipline, Microfluidics, within the "Enzo Ferrari" Engineering Department of the University of Modena and Reggio Emilia. The Department, and in particular the academic discipline "Fluid Machines", was contacted several times by other Departments to collaborate on research concerning Microfluidics, but without being able to follow up on the requests due to the lack of specific know-how.

The first fundamental step was to get to know the state of the art through visits to centers of excellence in Microfluidics, such as the Department of Electronics, Information and Bioengineering of Polytechnics of Milan, or National Research Council centers, and extensive bibliographic research.

The second step was to adapt your knowledge in Fluid Machines, to solve specific problems in Microfluidics, thanks to our new skills as well as numerous experimental tests which gave us the necessary confidence for microfluidic research.

The topic of the first research was the relationship between shear stress and bone cell proliferation. For this purpose, a bioreactor with a new biomimetic material as microfluidic cell scaffold was used. Subsequently, a PDMS microfluidic chip was designed and manufactured in place of the bioreactor to analyze the low levels of shear stress.

PDMS technology requires many processing steps and is therefore not very suitable for scientific research that requires quick and inexpensive experiments.

The topic of the second research was therefore a new technology more suitable for microfluidic research. For this purpose, previous experience with picosecond laser, which allows processing in the micron range, was useful. Thus microfluidic chips were then built and validated.

List of Symbols

Greek symbols

α	angle
$\delta_{i,j}$	Kronecker delta
θ	angle, angular coordinate
λ	coefficient of bulk viscosity or Lamé's constant
μ	dynamic viscosity
ρ	mass density
σ_{ME}	mixing efficiency deviation
τ	shear stress
$\tau_{i,j}$	stress tensor
τ_{wall}	wall shear stress
χ	variable

Latin symbols

A	area
A_{SC}	scaffold base area
c, C	concentration
D	diameter, mass diffusivity or diffusion coefficient
D_{PO}	scaffold pore diameter
D_{SC}	scaffold diameter
g	gravity acceleration
h, H	height
H_0	null hypothesis
H_a	alternative hypothesis
H_{SC}	scaffold height
i, j	row and column coordinates of a matrix
J	diffusive flux
l	length
L	characteristic length
L_{PO}	scaffold pore length
m, M	mass
ME	mixing efficiency

N_{PO}	number of channel-like pores in the scaffold
p, P	pressure
PD	density of the channel-like pores in the scaffold
Pe	Péclet number
pH	potential of hydrogen
Q	flow rate
Q_{TOT}	total rate of the flow through the scaffold
r	radial coordinate
r, R	radius
Re	Reynolds number
Rf	fluid dynamic resistance
Rf_{SC}	total fluid dynamic resistance of the scaffold
R_{PO}	scaffold pore radius
R_{SC}	scaffold radius
t	time
u, v, w	cartesian velocity components
u_{MAX}	maximum velocity
u_{mean}	mean velocity
V	volume
w, W	width
x, y, z	cartesian coordinates

Acronyms

2D	Bidimensional
3D	Tridimensional
ALPL	Alkaline Phosphatase
AMEM	Minimum Essential Medium Eagle - alpha modification
B-HA	type B Hydroxyapatite scaffold
BPA	Bradford Protein Assay
BSA	Bovine Serum Albumin
CAD	Computer-Aided Design
CAGR	Compound Annual Growth Rate
CAM	Computer-Aided Manufacturing
CDF	Cumulative Density Function

CFD	Computational Fluid Dynamics
CMOS	Complementary Metal-Oxide Semiconductor
CNC	Computer Numerical Control
COVID	Coronavirus Disease
Ct	Comparative threshold method
CT	Computed Tomography scan
CTR	Control sample
DMEM	Dulbecco's Modified Eagle's Medium
DSL	Debye Screening Length
EDL	Electrical Double Layer
EIS	Electrical Impedance Spectroscopy
ETD	Everhart–Thornley Detector
FBS	Fetal Bovine Serum
FDA	Food and Drug Administration
FEG	Field Emission Gun
FLICE	Femtosecond Laser Irradiation and Chemical Etching
FSS	Fluid Shear Stress
GAPDH	Glyceraldehyde 3-Phosphate Dehydrogenase
HA	Hydroxyapatite
HDM	Herringbone Mixer Device
HFIS	High-Frequency Impedance Spectroscopy
HoC	Human-on-Chip
IPA	Isopropyl Alcohol
LASER	Light Amplification by Stimulated Emission of Radiation
LCS	Lacunar-Canalicular System
LoC	Lab-on-Chip
μSLA	Micro Stereolithography
μTAS	Micro Total Analysis Systems
MEM	Eagle's Minimum Essential Medium
mRNA	messenger Ribonucleic Acid
NBS	Newborn Bovine Serum
NEA	(CMOS) Nano-Electrode Array
OoC	Organ-on-Chip
PBS	Sodium Perborate

PCB	Printed Circuit Board
PCR	Polymerase Chain Reaction
PDMS	Polydimethylsiloxane
PE	Polyethylene
PDF	Probability Density Function
PMMA	Poly(methyl methacrylate)
PoC	Point-of-Care
PP	Polypropylene
PPF	Polypropylene Fiber
PPFC	Parallel-Plate Flow Chamber
PTN	Pleiotrophin, or osteoblast stimulating factor 1
RF	Radio Frequency
RUNX2	Runt-related transcription factor 2
SARS	Severe Acute Respiratory Syndrome
SEM	Scanning Electron Microscope
SFDR	Scaled fluid dynamic resistance
TIG	Tungsten Inert Gas welding
TMJ	Temporomandibular Joint
UV	Ultraviolet light

1. Microfluidics: Features and Development

1.1. Introduction

The manipulation of small quantities of fluids (gasses and/or liquids) to perform analyzes or investigations in the medical, biological, physical, or material fields is of great interest both for scientific research and for industrial application. The term microfluidics refers to the science and technology that manipulates small quantities of fluid within structures or channels that have dimensions in the micrometer scale or smaller. The main technological application is the creation of entire laboratories inside chips, the so-called “Lab-on-chip" (LoC). There are many advantages that this technology has compared to traditional tests. The most important is that working with such small samples allows you to use smaller quantities of chemicals and reagents and to have greater control over the motion of fluids and their interaction. This translates into both lower costs but also greater safety, as it allows greater containment and control of any toxic substances involved in the tests and greater reliability of the results. Furthermore, as for microelectronics, there is a constant growth of integration in a single chip of multiple functions that can work in parallel, extremely useful in genomic research, but also the possibility of reconfiguring the circuits granting great flexibility in the execution of the test.

The great advantage of using small-sized chips with low energy consumption allows them to be used directly to monitor and help human functions (point of care), but also in industry and security by providing a vast and timely network of information in real time. Modern wireless and high-speed connections with digital networks via common electronic devices allow for the sharing of vast amounts of data all over the world, for example a patient can be followed in real time by his doctor thousands of kilometers away or the quality air and water can be monitored by thousands of micro stations, non-invasive for the environment.

The main engineering challenge in this field, and of this research, is to develop ever faster and cheaper methods to produce these chips and to allow this technology to be used more in mass production, making some tests still complex, faster, and accessible. There are no frontiers to the applications of microfluidics and many fields are still to be explored. Its capabilities make it possible to find new synergies with already consolidated technologies, allowing technological leaps that were previously unthinkable.

1.2. Definition and Physical Characteristics

In classical engineering, when we speak of liter fluidics, we usually think of the great works of man. In fluid machines we come to have a total displacement of 2.56×10^4 L in the WÄRTSILÄ RT-FLEX96C 14-cylinder diesel engine [1], the largest piston engine in the world, and a total flow rate of 4×10^7 L/s in the 32 Francis turbines installed in the Three Gorges Dam [2], the largest power plant in the world.

For microfluidics we are at the opposite extreme, we refer to it as a technology based on geometrically constrained minute volume transport through channels in a glass or plastic chip. The prefix "micro" in microfluidics refers to small volumes (nL, pL, fL), Table 1.2.1, small size, low energy consumption, or physical effects of the micro domain [3].

Table 1.2.1. *Multiples and submultiples of liter* [4]

10^{-15} L	femtoliter	fL	μm^3	cubic micrometer
10^{-12} L	picoliter	pL	$10^3\ \mu m^3$	thousand cubic micrometers
10^{-9} L	nanoliter	nL	$10^6\ \mu m^3$	million cubic micrometers
10^{-6} L	microliter	µL	mm^3	cubic millimeter
10^{-3} L	milliliter	mL	cm^3	cubic centimeter
10^0 L	liter	L	dm^3	cubic decimeter
10^3 L	kiloliter	kL	m^3	cubic meter

To get an idea, a circuit is defined as microfluidic when the section of its channels is less than 100x100 µm [5], with a flow rate usually less than 0.1 µL/s (1×10^{-7} L/s) which implies Reynolds numbers less than 1 (with water at 20°C).

As seen above, in the field of microfluidics the Reynolds number is very low, the flows are completely laminar, and viscous forces are much more important than inertial forces.

There are other physical phenomena which may be predominant in microfluidics, for example capillary effects on free surfaces, super hydrophobicity, viscoelasticity in polymer solutions and electrokinetic effects.

There are other physical phenomena which are limited in microfluidics, such as mixing which, in the absence of a turbulent flow, can only occur by diffusion which, being less efficient, takes very long times compared to those with turbulence [6].

1.3. History and Trends

The first microfluidic application for research is believed to be the gas chromatographic air analyzer made by Stanford University in 1979, its manufacturing technology derived directly from the integrated circuit industry [7]. The microfluidic circuit was etched by photolithography on a 50 mm diameter silicon wafer [8], Figure 1.3.1.

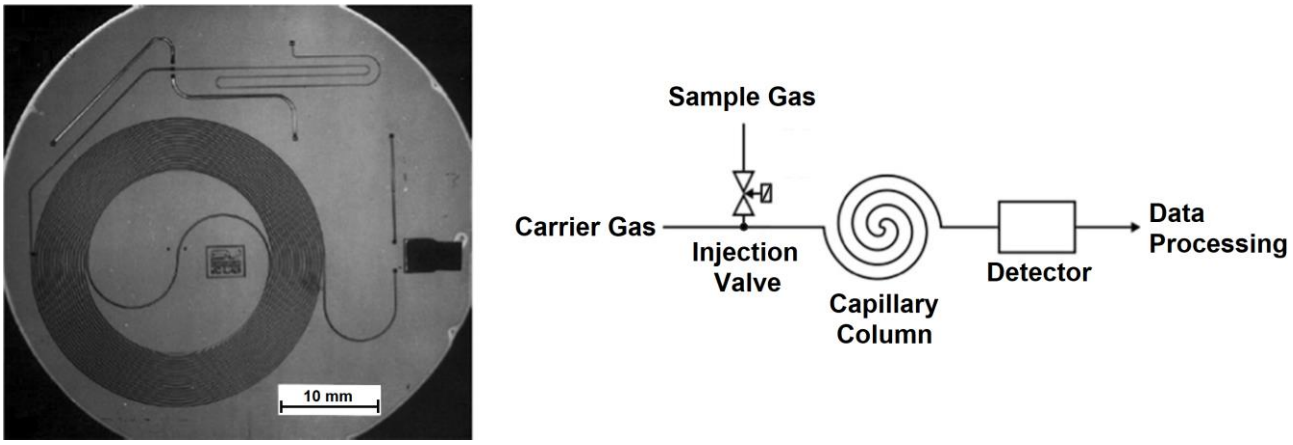

Fig. 1.3.1. *The Stanford Gas Chromatography System (redraw from* [5]*).*

This first step started the construction of increasingly complex circuits up to the "miniaturized Total Analysis System" (μTAS), where the collection and transport of the sample to be analyzed, all preparation phases including the chemical reactions and separations, as well as the required analyses, are performed in a single chip.

In the 1980s, the explosion of research in both cellular and molecular biology, particularly genomics, highlighted the limitations of silicon for the microfluidic chips. Its opacity, impermeability to gasses, stiffness made it difficult for optical observation, cell life and the creation of moving parts such as miniature valves.

Research therefore began to use glass which has the same limitations as silicon but high transparency, and then polymers, in particular polydimethylsiloxane (PDMS) which has established itself for its transparency, gas permeability and flexibility [9].

For these reasons, currently most of the research microfluidic circuits are made in PDMS [10], the global market value of microfluidic chips by material type follows the same trend [11], Figure 1.3.2.

The silicon technology is used to create a negative mold into which liquid PDMS is poured and polymerized, the mold allows many chips to be made (soft photolithography).

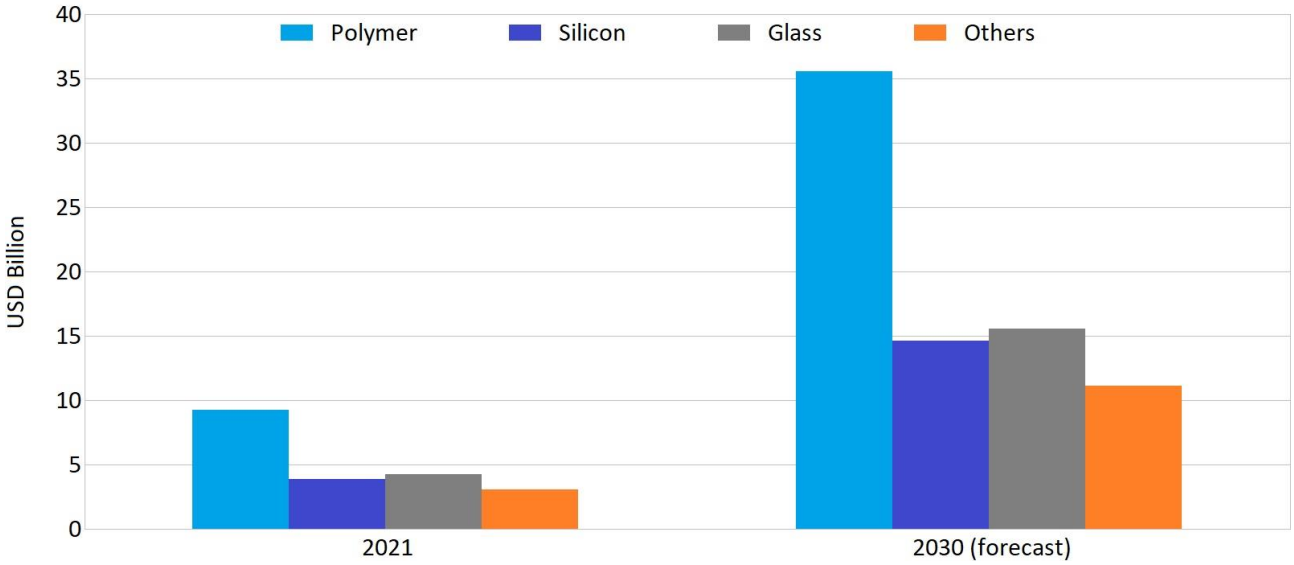

Fig. 1.3.2. *Microfluidics Industry Share: Market Forecast 2021-2030 for material type dynamics (redraw from* [11]*). The global microfluidics market revenue is expected to register a Compound Annual Growth Rate (CAGR) of 16.1% during the forecast period.*

PDMS has made possible the easy fabrication of microfluidic circuits on multiple layers and with integrated active components, achieving an extreme variety of transport and process functions, and allowing to perform multiple experiments in parallel on the same chip [12] [13], Figure 1.3.3.

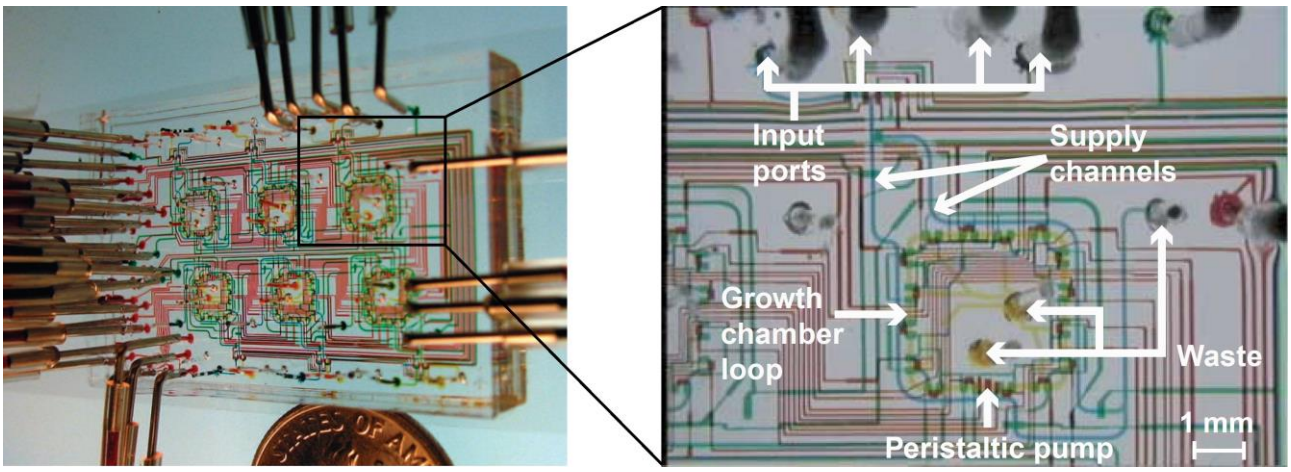

Fig. 1.3.3. *A multiprocess microfluidic chip for bacteria culture (redraw from* [12] [13]*).*

The availability of better materials, more performing and economical technologies, a greater proficiency in the possible applications of microfluidics has allowed an exponential increase in its use in scientific research, in parallel increasingly scientific documents based on microfluidics have been published [14], Figure 1.3.4.

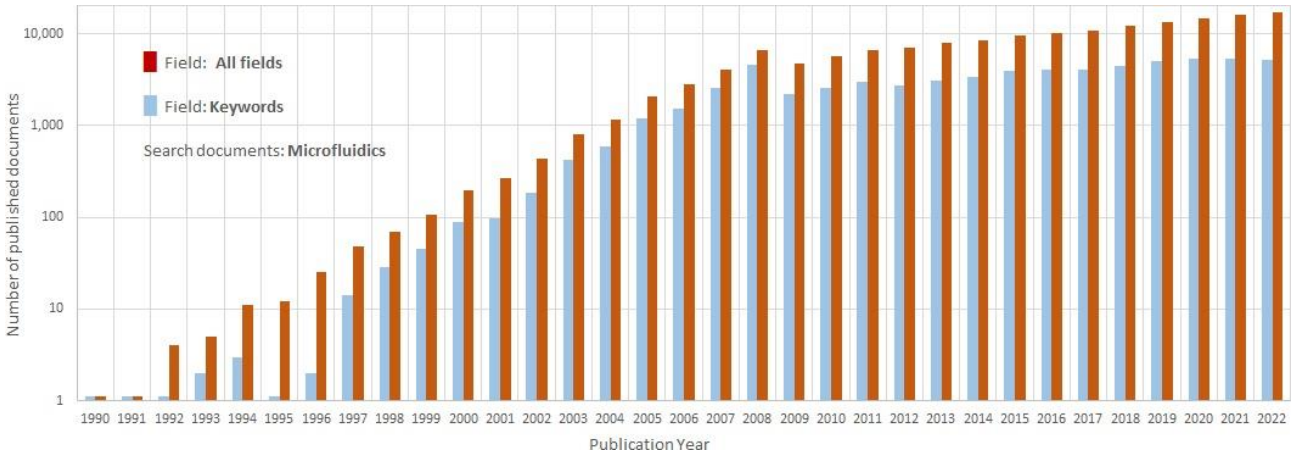

Fig. 1.3.4. *Number of published documents about microfluidics (redraw from* [15]*).*

From the first biological analyzes on liquids or cells using μTAS chips, now called lab(oratories)-on-chip (LoC), research evolved by replicating parts of the human body (skin, lungs, heart, liver, bone marrow, etc.) creating the organs-on-chip (OoC) to mimic their biological functions under different types of stimulation (physical, chemical, pharmacological, biological, etc.) and analyze their response.

Considering that the functioning of a single organ also depends on the other organs, for specific problems research has evolved by assembling multiple organs-on-chips, creating the human-on-chips (HoC) [16], Figure 1.3.5.

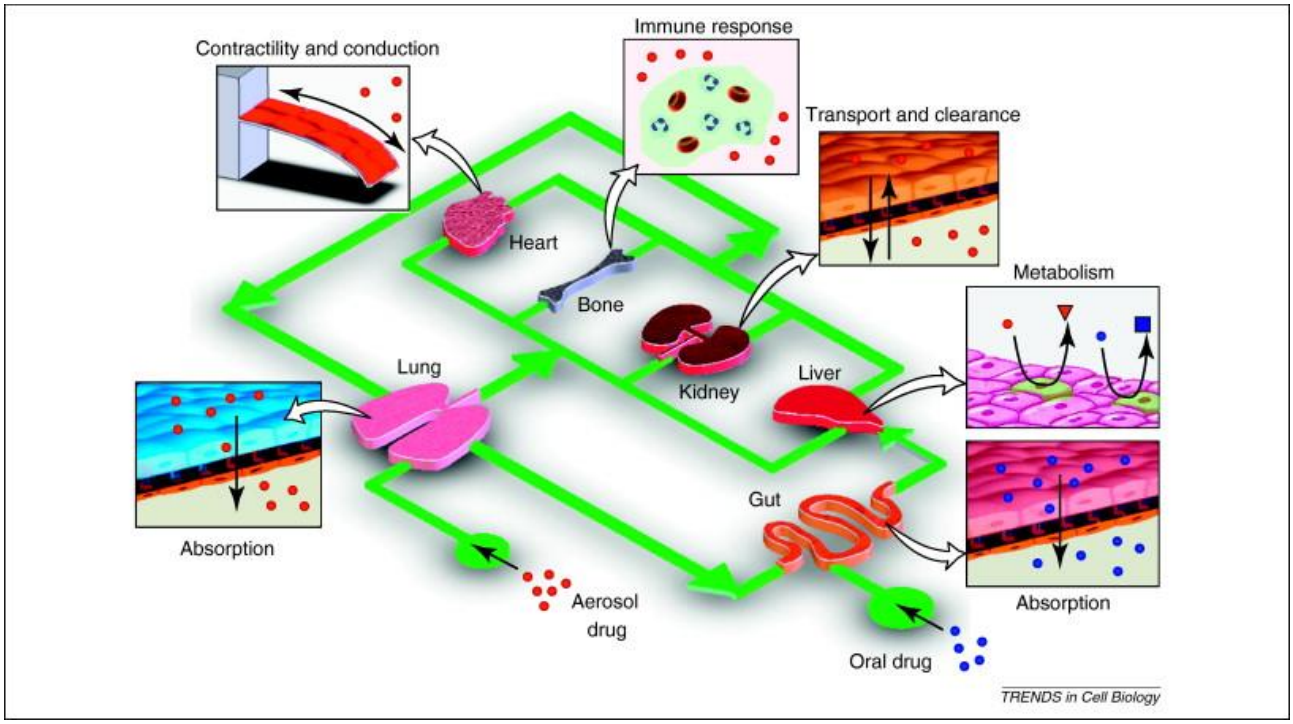

Fig. 1.3.5. *A human-on-chip concept to mimic drug absorption* [16].

The small size of lab-on-chips, their low energy requirements, the possibility of connecting with portable electronic devices such as smartphones, has given common people the possibility to constantly monitor some critical functions of their body and share them in real time with their doctor wherever and in whatever activity they are, without any limitation on their lifestyle [17]. Figure 1.3.6.

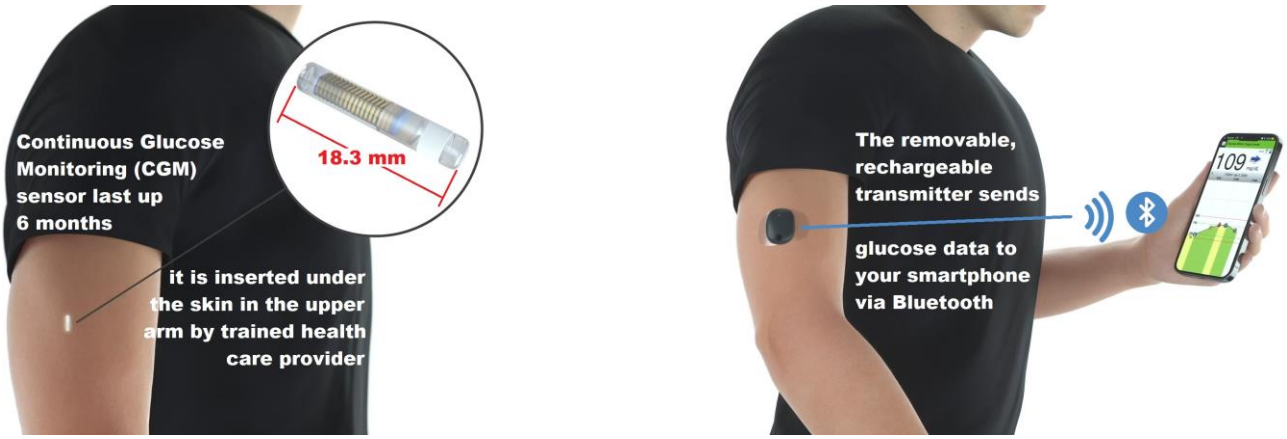

Fig. 1.3.6. *A wearable Continuous Glucose Monitoring (CGM) system (redraw from* [18]*).*

If life sciences are the scientific fields that have benefited the most from microfluidics applications, Figure 1.3.7, there are also other fields such as optics (e.g., adjustable micro-lenses [19], Figure 1.3.8, optical sensors [20], lasers [21]), engineering (e.g., inkjet printing [22], industrial diagnostics [23] [24], Figure 1.3.9, new materials [25]), electronics (e.g., flexible components for high frequency [26], Figure 1.3.10), and food processing [27].

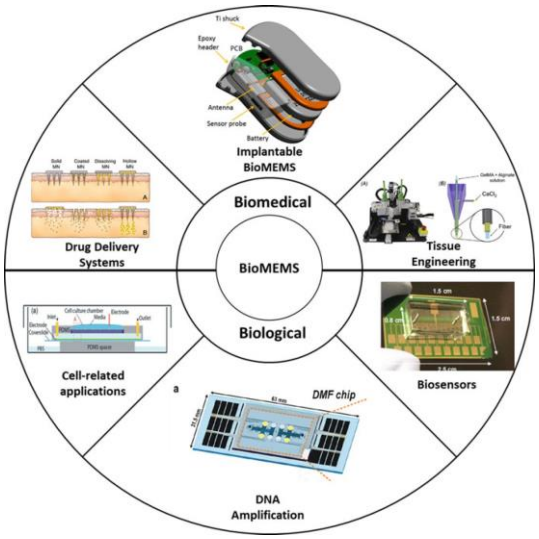

Fig. 1.3.7. *Different areas of application of life sciences* [28].

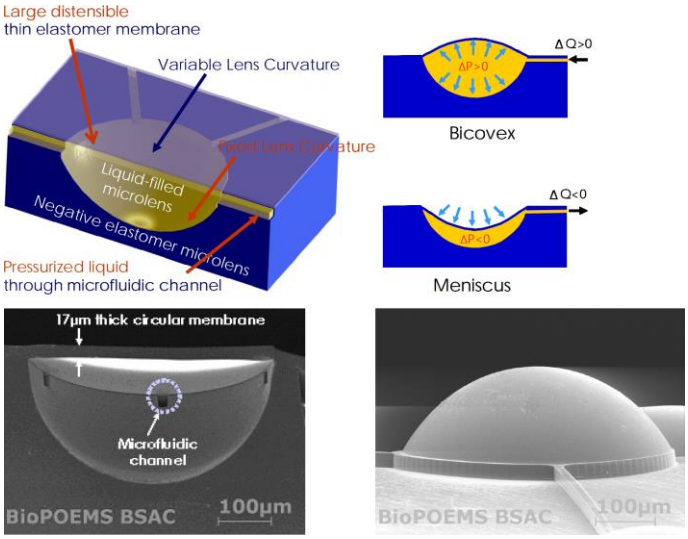

Fig. 1.3.8. *Tunable microdoublet lens* [19].

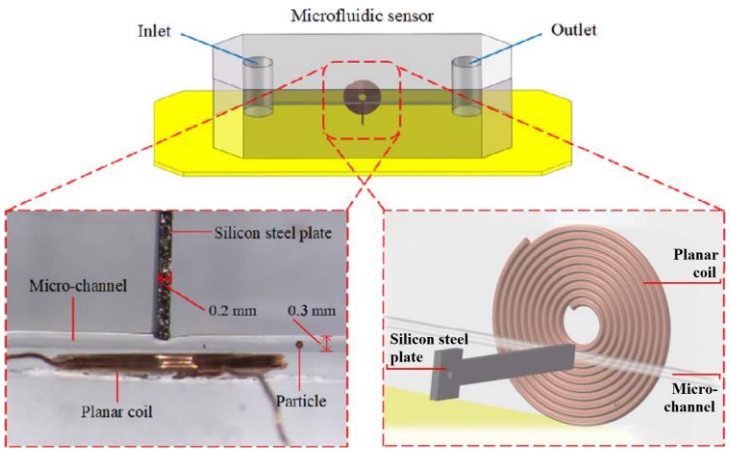

Fig. 1.3.9. *Microfluidic sensor to detect contaminants in hydraulic oil (redraw from* [23]*).*

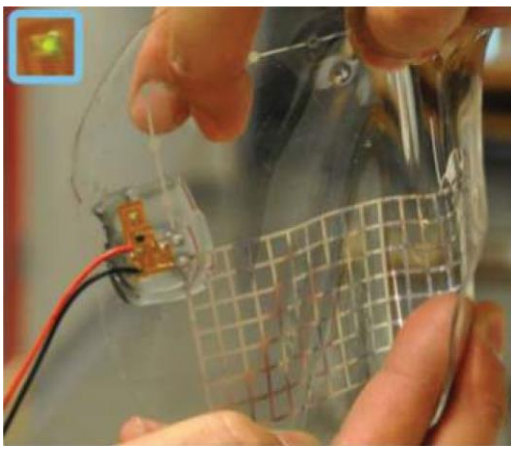

Fig. 1.3.10. *Microfluidic 900 MHz RF sensor with a 15% strain* [26].

Microfluidics has one of major trends and evolutions in the industry markets, applications, and business models [29]. The microfluidic market benefited from mass production of low-cost tests for COVID infections, the so-called point-of-care (PoC) for rapid diagnosis outside of reference laboratories.

But, despite this, the microfluidic market is growing much faster in value than in volume, indicating that higher value products are acquiring a large market area, and new application fields are emerging [30], Figure 1.3.11.

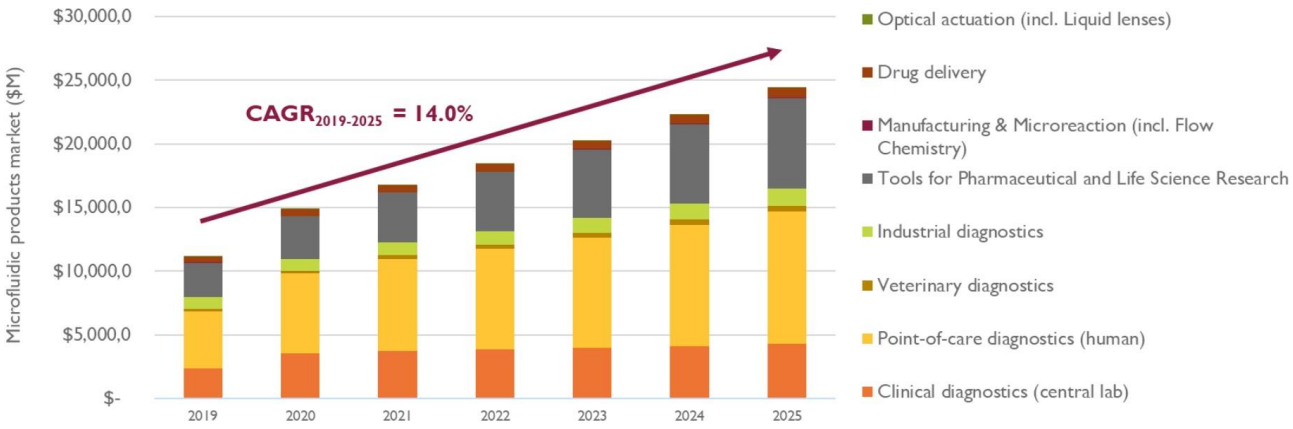

Fig. 1.3.11. *Trend of the microfluidic product market* [30].

Note: *CAGR is the compounded annual growth rate in a period.*

It is evident that microfluidics is revolutionizing entire fields of application and is discovering new ones, allowing functions hitherto forbidden to current technology.

2. Microfluidic Physics

2.1. Introduction

Microfluidics, as an applied science, has its roots in Physics. The laws and equations that regulate the behavior of fluids are also valid in this field and are normally used.

The peculiarity of microfluidics lies in the fluids used, typically liquids which in most cases are water-based, in the small dimensions of the channels that contain them, and in the slow flows to which they are subject. This leads to simplifications in the laws and equations, which are valid in general, allowing their more immediate application on many specific cases used in microfluidics. Furthermore, dimensionless numbers, such as the Reynolds number and the Péclet number which are the result of simple ratios between a few physical quantities, allow us to know roughly, but quickly, the behavior of microfluidic flows.

Currently the design of microfluidic circuits is performed using Computational Fluid Dynamics, the researcher is entrusted only with the modeling of the circuit and the definition of the parameters while it is the powerful computational calculation that solves the complexity and the number of equations that regulate the flow in the circuit.

But the time required for modeling and the computational cost are not low, knowing the basics of the physical laws and equations used in microfluidics, in which contexts to use them, and what the fundamental parameters are allows the researcher to set up the problem and obtain more quickly solutions with CFD, with fewer unsuccessful attempts.

The purpose of this chapter is to provide the researcher, who begins his learning path in microfluidics, with the simple basics that will help him to have an aware approach to the subject, to be able to correctly frame the different problems, and quickly choose the most suitable solutions.

2.2. Scaling Laws

To investigate the behavior of fluids at the micrometric level, it is important to understand how dimensions affect the forces involved and the mass transport. For this aim, the scaling laws are helpful, they govern the variation of the physical quantities (e.g., force, speed) with the size of the object or system under examination, keeping the other quantities (e.g., time, pressure, temperature) constant.

As an example, we can consider volume forces, such as gravity and inertia, and surface forces, such as surface tension and viscosity. The basic scaling law for the ratio of these two classes of forces can be expressed as follows:

$$\frac{surface\ forces}{volume\ forces} \propto \frac{l^2}{l^3} = l^{-1} \tag{2.2.1}$$

This implies that when we reduce lengths down to the microscale of lab-on-chip systems the volume forces, which are predominant in our daily lives, become unimportant; instead, surface forces become prominent. Hence weight, volume force, normally predominates and an object falls under the effect of gravity. But when an object of the same mass density, ρ, is very small, the weight becomes insignificant compared to the frictional force of the air, surface force. Thus, a small updraft can sustain the object. To demonstrate this, we consider the balance between the viscous friction force and the force of gravity:

$$\mu u L \sim mg \tag{2.2.2}$$

where μ is the dynamic viscosity of the air, u is the fall velocity of the object, m is its mass, and L is its characteristic length.

The velocity u is expressed by Equation (2.2.2) as follows:

$$u \sim \frac{mg}{\mu L} \propto \frac{\rho L^3 g}{\mu L} \propto \frac{L^3}{L} = L^2 \tag{2.2.3}$$

As can be seen from Equation (2.2.3), when the size of the object is small, an updraft with very low velocity is sufficient to sustain it [31].

The same happens for the inertia force, volume force, which in the macro scale is predominant in the change of direction of the flow of a fluid, while in the micro scale the viscous friction force is predominant.

In fluid flow, the inertia force causes turbulence while the viscous frictional force maintains the laminar flow, this means that in the micro scale the flow is laminar.

The Reynolds number *Re* is a dimensionless physical quantity which compares the relative quantities of inertial forces and viscous forces of a fluid and allows to determine its type of flow.

$$Re = \frac{\rho u L}{\mu} = \frac{\rho u^2 L^2}{\mu u L} \propto \frac{inertial\ forces}{viscous\ forces} \tag{2.2.4}$$

where ρ is the density of the fluid and L is the characteristic length of the flow type.
The flow of a fluid is certainly laminar for Reynolds numbers lower than 1500 [32], for higher numbers there is a transition phase which leads to a turbulent flow, and which depends on the roughness of the channel. Since microfluidic circuits have a Reynolds number lower than one, the fluid flowing in them always has a laminar flow.

This behavior of the flow in microfluidic circuits allows on the one hand to facilitate many applications, being free from turbulence, on the other hand, leads to difficulties related for example to the mixing between two fluids. Indeed, since their flows are highly laminar, the flow lines do not interfere with each other, resulting in little or no mixing, Figure 2.2.1.

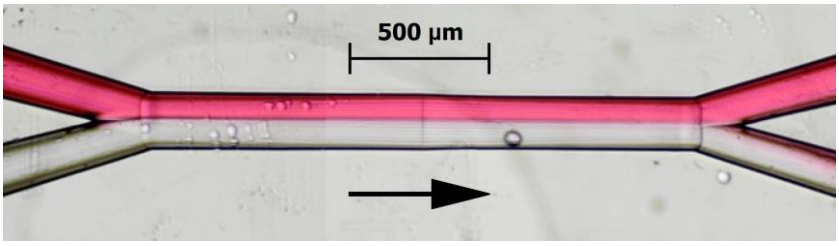

Fig. 2.2.1. *Effect of a low Reynolds number in a microfluidic circuit leading to poor mixing between the two fluids* [33].

When this feature is an obstacle, for example in a microfluidic chip where there are multiple culture cells that we want to feed with different mixes between nutrients and drugs, then it is necessary to create vortices that mix the flow lines of the two fluids. There are many geometric solutions of which the most effective are abrupt changes in the direction of the flow or the introduction of many close section variations in the channel [33].

2.3. Microfluidic Advection

The basic equations of the bulk motion of a fluid, or advection, are applicable to microfluidics and include three conservation principles, which are the conservation of mass, energy and momentum, and their respective equations: continuity equation, dynamic energy equation (Bernoulli equation) and momentum equation (Navier-Stokes equation) respectively.

In this paragraph the basic concepts and equations that will allow the study and understanding of the functioning of microfluidic devices and the behavior of the fluids inside them will be reported. We will focus on the transport mechanisms as they are the basis of the design of microfluidic circuits, i.e., the fundamental aim of this research.

2.3.1. Equation of continuity: conservation of mass

An approach to describe a fluid in motion is to examine what happens at a microscopic level where the stochastic motions of individual particles can be distinguished. However, this multi-body problem of molecular dynamics is very complex for a liquid given the very large number of molecules that compose it.

The standard way of solving this kind of problem is the continuity approximation; according to this hypothesis the fluid is infinitely divisible without variations of nature. The continuity approximation is also applicable to the microscale, in fact the measurement scale in microfluidics is micrometer, which is much larger than the average diameter of a water molecule, equal to 0.27 nanometers [34], the main component of the fluids used in microfluidics. Therefore, the single-phase fluid mass in the micrometric scale must obey the continuity equation and it is thanks to this assumption that the equations of classical fluid mechanics can be applied to microfluidics. In this way the flow is considered constant, and fluid properties such as density, pressure and velocity remain constant at each point, the change in these physical quantities due to molecular motion is assumed to be negligible [32].

To simplify the procedure, we consider a fluid element, Figure 2.3.1, of m mass with $\Delta x\Delta y\Delta z$ volume, fluid velocities u, v, and w along x, y, and z respectively, density ρ of the fluid under examination, and time t. For the system considered, the conservation of mass is:

$$\frac{\partial m}{\partial t} = \frac{\partial(\rho \Delta x \Delta y \Delta z)}{\partial t} = \rho u \Delta y \Delta z + \rho v \Delta x \Delta z + \rho w \Delta x \Delta y + \\ - \left[\rho u + \frac{\partial(\rho u)}{\partial x}\Delta x\right]\Delta y \Delta z - \left[\rho v + \frac{\partial(\rho v)}{\partial y}\Delta y\right]\Delta x \Delta z - \left[\rho v + \frac{\partial(\rho w)}{\partial z}\Delta z\right]\Delta x \Delta y \qquad (2.3.1)$$

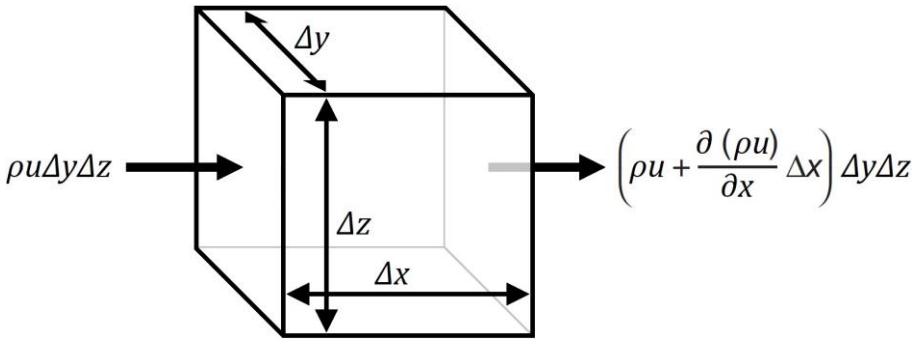

Fig. 2.3.1. *Variation of mass flow along the x-axis for a volume element ΔxΔyΔz (redraw from* [32]*).*

Simplifying and dividing Equation (2.3.1) by *ΔxΔyΔz*, we obtain:

$$\frac{\partial \rho}{\partial t} + \frac{u\partial \rho}{\partial x} + \frac{v\partial \rho}{\partial y} + \frac{w\partial \rho}{\partial z} + \rho\left[\frac{\partial u}{\partial x} + \frac{\partial v}{\partial y} + \frac{\partial w}{\partial z}\right] = 0 \tag{2.3.2}$$

Defining the operator D/Dt, substantial derivative of a tensor field dependent only on position and time coordinates, as:

$$\frac{D}{Dt} = \frac{\partial}{\partial t} + u\frac{\partial}{\partial x} + v\frac{\partial}{\partial y} + w\frac{\partial}{\partial z} \tag{2.3.3}$$

we can write Equation (2.3.2) as follow:

$$\frac{D\rho}{Dt} + \rho\left[\frac{\partial u}{\partial x} + \frac{\partial v}{\partial y} + \frac{\partial w}{\partial z}\right] = 0 \tag{2.3.4}$$

Defining the operator ∇ applied to a vector field, in this case the velocity, divergence of $\bar{V}$ as:

$$\nabla \cdot \bar{u} = \sum_{i=x,y,z} \frac{\partial u_i}{\partial x_i} \tag{2.3.5}$$

where $\bar{u}$ is the velocity vector (u, v, w), we can write Equation (2.3.4) in the vector form as follow:

$$\frac{D\rho}{Dt} + \rho\nabla \cdot \bar{u} = 0 \tag{2.3.6}$$

If we consider a fluid with density ρ constant, as in the microfluidic applications, $D\rho/Dt = 0$ and we can reduce the Equation (2.3.4) and (2.3.6) as follows:

$$\frac{\partial u}{\partial x} + \frac{\partial v}{\partial y} + \frac{\partial w}{\partial z} = 0 \tag{2.3.7}$$

$$\nabla \cdot \bar{u} = 0 \tag{2.3.8}$$

2.3.2. Bernoulli equation: conservation of energy

Bernoulli's principle states that, for inviscid steady fluid flow, an increase of the fluid velocity occurs simultaneously with a decrease in fluid pressure or a decrease in the fluid potential energy, Figure 2.3.2.

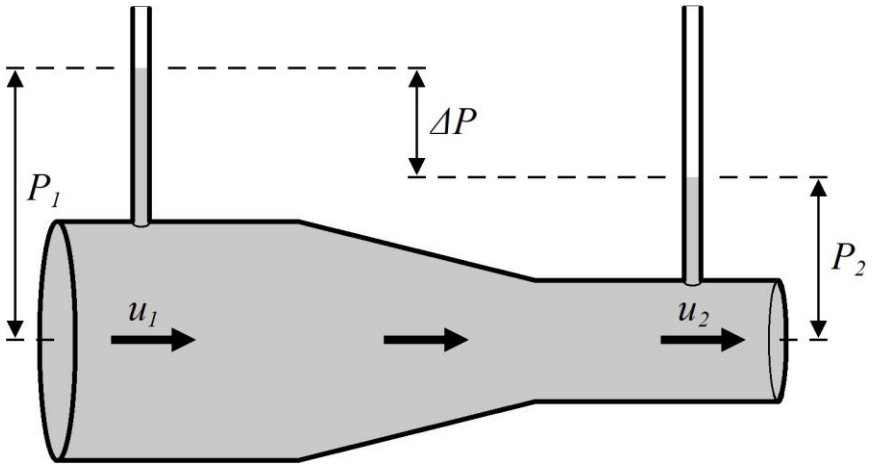

Fig. 2.3.2. *Fluid flowing through a constriction (redraw from* [35]*).*
By mass conservation $v_2 > v_1$, therefore by Bernoulli's principle $P_2 < P$.

Thanks to the work of Leonhard Euler, Bernoulli's equation was derived from the relations of Bernoulli's principle. The equation, in different forms, can be applied to diverse types of fluid flows to describe their energy balance.

The simplest form of Bernoulli's equation is obtained when it is applied to an incompressible fluid, such as a liquid or gas with a Mach number much lower than one. The density of the fluid can be considered constant, independent of the variation of the pressure in the line flow.

If there are no losses due to viscous friction, we can apply the law of conservation of energy to the fluid and write Bernoulli's equation as the sum of its kinetic energy due to its motion and its potential energy, due to its position in the Earth's gravitational field and its static pressure. The sum of all these forms of energy of the fluid must remain constant in the line flow [32]:

$$P + \rho g h + \frac{1}{2}\rho u^2 = constant \tag{2.3.9}$$

where P is the static pressure, h the height above some reference level, u the velocity, ρ the density, and g the gravity acceleration for any chosen elemental volume in the fluid flow line. The term ($1/2\rho u^2$) is known as the dynamic pressure, and the total pressure is the sum of the static pressure P and this dynamic pressure. Dividing Equation (2.3.9) by (ρg), we obtain:

$$\frac{P}{\rho g} + h + \frac{1}{2}\frac{u^2}{g} = constant \tag{2.3.10}$$

The sum of the elevation h and the static pressure head (P/ρg) is known as the hydraulic head.

2.3.3. Navier-Stokes equation: conservation of momentum

Momentum is a vector, the product of the mass and velocity of an object. The conservation of momentum implies that it can only change by the action of forces, as imposed by Newton's second law of motion. Considering a unitary volume of fluid, it becomes:

$$\frac{D\rho\overline{u}}{Dt} = \rho\overline{g} + \nabla \cdot \tau_{ij} \quad i,j = 1,2,3 \tag{2.3.11}$$

where $\overline{u}$ is the velocity vector of the flow, t is the time, ρ is the density of the fluid, $\overline{g}$ is the vector of gravity acceleration, ∇ is the divergence of the stress tensor τ_{ij}. The term ($D\rho\overline{u}/Dt$) represents the change in momentum over time, ($\rho\overline{g}$) the body force, and ($\nabla \cdot \tau_{ij}$) the surface forces applied to the fluid of unitary volume.

According to the general deformation law of Newtonian viscous fluid given by Stokes, the stress tensor τ_{ij}, is expressed as [36]:

$$\tau_{ij} = -p\delta_{ij} + \mu\left(\frac{\partial u_i}{\partial x_j} + \frac{\partial u_j}{\partial x_i}\right) + \delta_{ij}\lambda\nabla\cdot\overline{u} \tag{2.3.12}$$

where p is the static pressure, δ_{ij} is the Kronecker delta, μ is the dynamic viscosity, and λ is the coefficient of bulk viscosity or Lamé's constant. Substituting Equation (2.3.12) into Equation (2.3.11), we obtain the Navier-Stokes equation, in vector form, of Newtonian viscous fluids:

$$\frac{D\rho\overline{u}}{Dt} = \rho\overline{g} + \nabla\cdot p + \frac{\partial}{\partial x_i}\left[\mu\left(\frac{\partial u_i}{\partial x_j} + \frac{\partial u_j}{\partial x_i}\right) + \delta_{ij}\lambda\nabla\cdot\overline{u}\right] \tag{2.3.13}$$

where the term $(\nabla\cdot p)$ represents the pressure force, and $(\partial[\,]/\partial x_i)$ the viscous forces.

If we consider a fluid with constant density and dynamic viscosity, applying the conservation of mass, for Equation (2.3.8) $\nabla\cdot\overline{u} = 0$, we obtain:

$$\rho\frac{D\overline{u}}{Dt} = \rho\overline{g} + \nabla\cdot p + \mu\frac{\partial}{\partial x_i}\left(\frac{\partial u_i}{\partial x_j} + \frac{\partial u_j}{\partial x_i}\right) \tag{2.3.14}$$

or, in its compact form:

$$\rho\frac{D\overline{u}}{Dt} = \rho\overline{g} + \nabla\mathrm{p} + \mu\nabla^2\overline{u} \tag{2.3.15}$$

In scalar form, we have the three Navier-Stokes equations for incompressible and constant-viscosity fluids according to the velocity vector $\bar{u}$ components *(u, v, w)* [35]:

$$\rho\left(\frac{\partial u}{\partial t} + u\frac{\partial u}{\partial x} + v\frac{\partial u}{\partial y} + w\frac{\partial u}{\partial z}\right) = \rho g_x - \frac{\partial p}{\partial x} + \mu\left(\frac{\partial^2 u}{\partial x^2} + \frac{\partial^2 u}{\partial y^2} + \frac{\partial^2 u}{\partial z^2}\right) \tag{2.3.16}$$

$$\rho\left(\frac{\partial v}{\partial t}+u\frac{\partial v}{\partial x}+v\frac{\partial v}{\partial y}+w\frac{\partial v}{\partial z}\right)=\rho g_y-\frac{\partial p}{\partial y}+\mu\left(\frac{\partial^2 v}{\partial x^2}+\frac{\partial^2 v}{\partial y^2}+\frac{\partial^2 v}{\partial z^2}\right) \quad (2.3.17)$$

$$\rho\left(\frac{\partial z}{\partial t}+u\frac{\partial z}{\partial x}+v\frac{\partial z}{\partial y}+w\frac{\partial z}{\partial z}\right)=\rho g_z-\frac{\partial p}{\partial z}+\mu\left(\frac{\partial^2 z}{\partial x^2}+\frac{\partial^2 z}{\partial y^2}+\frac{\partial^2 z}{\partial z^2}\right) \quad (2.3.18)$$

The Navier-Stokes equations are widely used to describe the behavior of fluids in terms of continuous functions of space and time. The laws on which they depend are considered in terms of flux rather than variations of their instantaneous values. In mathematical terms this is represented as partial derivatives of the dependent fluid variables and being non-linear they almost never admit an analytical solution, but an approximate solution obtained with a numerical method. The solution of the equations provides the field of fluid speeds, from which it will then be possible to derive all the other quantities that characterize the flow.

2.3.4. Hagen-Poiseuille equation: conservation of momentum for laminar flow

In the calculation of flow, the Navier-Stokes equation is difficult to solve due to its non-linearity. Despite this, a considerable number of exact but specific solutions have been found which satisfy the complete equations for some special geometry [31] [37]. One of these solutions is the Hagen-Poiseuille equation, which describes the relationship between the pressure drop in a fluid flowing through a long, narrow channel of constant, axisymmetric cross section, and the flow rate of the fluid.

To derive the Hagen-Poiseuille equation, we need to make several assumptions. First, we assume that the fluid is incompressible, i.e., that its density remains constant. Second, we assume that the flow is steady, meaning that the velocity vector is constant at any given point in time and the pressure is constant in every cross–section. Third, we assume that the flow is fully developed, meaning that the velocity profile is fully developed and does not change along the length of the channel. Fourth, we assume that the influence of the gravitational field is negligible. Finally, we assume that the flow is laminar, meaning that the fluid moves in layers that do not mix with each other.

As we can see, all these assumptions are respected in common microfluidic circuits, with special regard to laminar flow. Thus, the Hagen-Poiseuille equation is used to determine their flows, allowing a simple and rapid calculation of the main quantities that characterize them. The Hagen-Poiseuille equation is developed here, in two different forms, for cylindrical channel and for rectangular channel.

2.3.4.1. Hagen-Poiseuille equation for cylindrical channel

We consider a cylindrical channel of radius R, of indefinite length with horizontal *x*-axis, and radial coordinate *r* measured outwards from the *x*-axis. The flow velocity components in the radial and tangential directions are zero, and the velocity component *u* in the axial direction is only dependent on *r*. With the previous assumptions, the Navier-Stokes Equation (2.3.16) in cylindrical coordinates reduces to [37]:

$$\mu \left(\frac{\partial^2 u}{\partial r^2} + \frac{1}{r}\frac{\partial u}{\partial r}\right) = \mu \frac{1}{r} \frac{\partial}{\partial r} \left(r \frac{\partial u}{\partial r}\right) = - \frac{\partial p}{\partial x} \tag{2.3.19}$$

If we assume that the pressure gradient is constant along the channel, then we can write it as:

$$\frac{\partial p}{\partial x} = \frac{\Delta p}{\Delta L} \tag{2.3.20}$$

where Δp is the pressure drop between the ends of a section of channel of length ΔL, and Equation (2.3.19) becomes:

$$\mu \frac{1}{r} \frac{\partial}{\partial r} \left(r \frac{\partial u}{\partial r}\right) = - \frac{\Delta p}{\Delta L} \tag{2.3.21}$$

This partial differential Equation (2.3.21) is solvable with a double integration over *r* as [31]:

$$u = - \frac{\Delta p}{\Delta L} \frac{r^2}{4\mu} + A\, ln|r| + B \tag{2.3.22}$$

Since the velocity *u* cannot be infinite when $r = 0$, on physical grounds, we set the first constant $A = 0$. Furthermore, the no-slip boundary condition sets $u = 0$ when $r = R$, and by applying these two conditions in the Equation (2.3.22), we obtain the second constant *B*:

$$B = \frac{\Delta p}{\Delta L} \frac{R^2}{4\mu} \tag{2.3.23}$$

Substituting the two constants, *A* and *B*, into Equation (2.3.22), we obtain the flow velocity profile along the *r*-axis:

$$u = \frac{\Delta p}{\Delta L}\,\frac{R^2 - r^2}{4\mu} \tag{2.3.24}$$

Equation (2.3.24) shows, Figure 2.3.3, that along the *r*-axis the flow velocity profile has a parabolic profile, with the following maximum for $r = 0$:

$$u_{MAX} = \frac{\Delta p}{\Delta L}\,\frac{R^2}{4\mu} \tag{2.3.25}$$

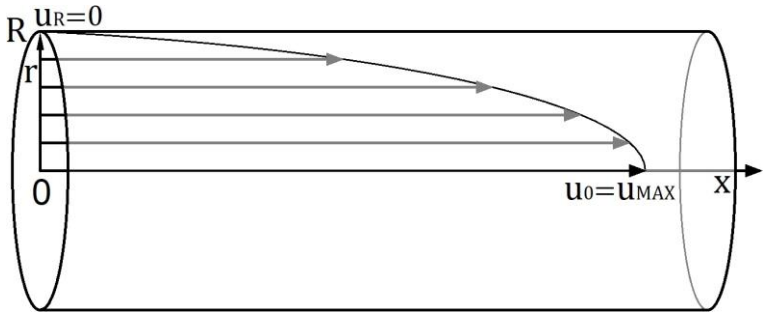

Fig. 2.3.3. *A fluid laminar flow in a cylindrical channel has a parabolic velocity profile. Velocity is zero at r=R and reaches a maximum at r=0.*

Integrating the flow velocity of Equation (2.3.24) on the area of the channel cross section, we obtain the volumetric flow rate *Q*, known as the classical Hagen-Poiseuille equation:

$$Q = \int_0^R u\, 2\pi r dr = \frac{\pi}{2\mu}\frac{\Delta p}{\Delta L}\int_0^R (R^2 - r^2) r dr = \frac{\pi R^4}{8\mu}\,\frac{\Delta p}{\Delta L} \tag{2.3.26}$$

Now we define the fluid dynamic resistance *Rf* for cylindrical channels as:

$$Rf = \frac{8\mu}{\pi R^4}\Delta L \tag{2.3.27}$$

which depends only on the physical characteristics of the fluid and the cylindrical channel.

Substituting the Equation (2.3.27) into Equation (2.3.26), we obtain the generalized Poiseuille equation:

$$Q = \frac{\Delta p}{Rf} \tag{2.3.28}$$

By dividing the volumetric flow rate *Q* of Equation (2.3.26) by the area of the channel cross section, we obtain the mean velocity u_{mean}:

$$u_{mean} = \frac{\pi R^4}{8\mu}\frac{\Delta p}{\Delta L}\frac{1}{\pi R^2} = \frac{R^2}{8\mu}\frac{\Delta p}{\Delta L} \tag{2.3.29}$$

2.3.4.2. Hagen-Poiseuille equation for rectangular channel

We consider a channel of indefinite length with a rectangular cross section, of height *h* and width *w*, centered with horizontal *x*-axis. The height *h* is parallel to the vertical *y*-axis and the width *w* is parallel to the *z*-axis. We assume a high aspect ratio, *w* >> *h*, such that we can consider the velocity profile constant along the width of the channel and dependent only on *y*. With the previous assumptions, the Navier-Stokes Equation (2.3.16) in cartesian coordinates, reduces to:

$$\mu\left(\frac{\partial^2 u}{\partial y^2}\right) = -\frac{\partial p}{\partial x} \tag{2.3.30}$$

If we assume that the pressure gradient is constant along the channel, we can substitute Equation (2.3.20) in Equation (2.3.30), and obtain:

$$\mu\frac{\partial^2 u}{\partial y^2} = -\frac{\Delta p}{\Delta L} \tag{2.3.31}$$

where Δp is the pressure drop between the ends of a section of channel of length ΔL.

We integrate Equation (2.3.31), and obtain:

$$\mu \frac{\partial u}{\partial y} = -\frac{\Delta p}{\Delta L} y + A \tag{2.3.32}$$

By analogy with the cylindrical channel, we assume that for $y = 0$ the velocity u is maximum, and the derivative of the velocity (∂u/∂y) in this point is equal to zero. This condition is satisfied with the constant A equals to zero. Imposing this condition, and integrating Equation (2.3.32), we obtain:

$$u = -\frac{\Delta p}{\Delta L} \frac{y^2}{2\mu} + B \tag{2.3.33}$$

The no-slip boundary condition sets $u = 0$ when $y = h/2$, and by applying this condition in the Equation (2.3.33), we obtain the constant B:

$$B = \frac{\Delta p}{\Delta L} \frac{\left(\frac{h}{2}\right)^2}{2\mu} \tag{2.3.34}$$

Substituting the constant B into Equation (2.3.33), we obtain the flow velocity profile along the y-axis:

$$u = \frac{\Delta p}{\Delta L} \frac{h^2 - 4y^2}{8\mu} \tag{2.3.35}$$

Equation (2.3.35) shows, Figure 2.3.4, that along the y-axis the flow velocity profile has a parabolic profile, with the following maximum for $y = 0$:

$$u_{MAX} = \frac{\Delta p}{\Delta L} \frac{h^2}{8\mu} \tag{2.3.36}$$

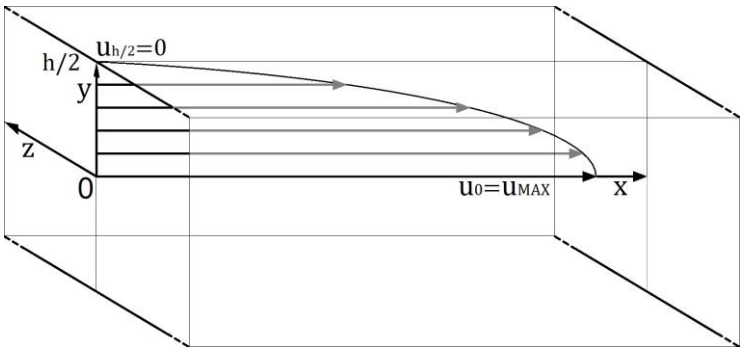

Fig. 2.3.4. *A fluid laminar flow in a rectangular channel has a parabolic velocity profile. Velocity is zero at y=h/2 and reaches a maximum at y=0.*

Integrating the flow velocity of Equation (2.3.35) on the area of the channel cross section, we obtain the volumetric flow rate *Q*:

$$Q = \int_{-h/2}^{h/2} u\, w dy = \frac{w}{8\mu}\frac{\Delta p}{\Delta L}\int_{-h/2}^{h/2}(h^2 - 4y^2)dy = \frac{w\, h^3}{12\mu}\,\frac{\Delta p}{\Delta L} \tag{2.3.37}$$

By dividing the volumetric flow rate *Q* of Equation (2.3.37) by the area of the channel cross section, we obtain the mean velocity u_{mean}:

$$u_{mean} = \frac{w\, h^3}{12\mu}\,\frac{\Delta p}{\Delta L}\,\frac{1}{h\, w} = \frac{h^2}{12\mu}\,\frac{\Delta p}{\Delta L} \tag{2.3.38}$$

Microfluidic channels of rectangular cross section are more used than those of cylindrical cross section, but the assumption *w* >> *h* is seldom satisfied. For rectangular channels, with any ratio of width to height, no finite analytical solution is known.

An analytical solution can be derived via Fourier series expansion of Boussinesq equations [36]. To avoid the computational cost in solving Fourier series expansions, however, is normally used an approximate version in algebraic form [38], truncating the series:

$$Q \approx \frac{w\, h^3}{12\mu}\,\frac{\Delta p}{\Delta L}\left(1 - 0.63\frac{h}{w}\right) \tag{2.3.39}$$

The approximation is fair. For the worst case, the square *h* = *w*, the error is just 13% [31].

2.3.5. Fluid shear stress

The dynamic viscosity μ is defined as the proportionality constant between the shear stress τ applied to the fluid and the resulting rate of shear strain. The shear strain is defined as the ratio $\partial x/\partial y$ of the lateral deformation ∂x to the thickness ∂y of the layer being displaced, and the rate of shear strain is simply $(\partial x/\partial y)/\partial t=\partial u/\partial y$, namely, the induced velocity gradient.

For a Newtonian fluid we therefore have the following relationship between stress, rate of shear strain, and the dynamic viscosity [35]:

$$\tau = \mu \frac{\partial u}{\partial y} \tag{2.3.40}$$

The fluid shear stress (FSS) by laminar flow is developed here, in two different forms, for cylindrical channel and for rectangular channel.

2.3.5.1. Shear stress by laminar flow for cylindrical channel

We consider the same cylindrical channel of Section 2.3.4.1, with the same assumptions, and Equation (2.3.40) in cylindrical coordinates:

$$\tau = \mu \frac{\partial u}{\partial r} \tag{2.3.41}$$

By differentiating Equation (2.3.24) with respect to ∂r, we obtain:

$$\frac{\partial u}{\partial r} = \frac{\partial}{\partial r}\left(\frac{\Delta p}{\Delta L}\frac{R^2 - r^2}{4\mu}\right) = -\frac{\Delta p}{\Delta L}\frac{r}{2\mu} \tag{2.3.42}$$

By substituting Equations (2.3.42) into Equation (2.3.41), we obtain:

$$\tau = -\mu\frac{\Delta p}{\Delta L}\frac{r}{2\mu} = -\frac{r\Delta p}{2\Delta L} \tag{2.3.43}$$

This equation expresses the shear stress value at a point distant r from the channel axis, a positive shear stress vector τ is in the direction of a negative pressure gradient Δp.

By substituting the radius R of the channel into the variable r of Equation (2.3.43), we obtain the wall shear stress for a cylindrical channel:

$$\tau_{wall} = -\frac{R\Delta p}{2\Delta L} \tag{2.3.44}$$

We can get another expression of the shear stress inverting Equation (2.3.29):

$$\frac{\Delta p}{\Delta L} = \frac{8\mu\, u_{mean}}{R^2} \tag{2.3.45}$$

where u_{mean} is the mean constant fluid velocity in any section of the cylindrical channel.

By substituting Equations (2.3.45) into Equation (2.3.44), we obtain:

$$\tau_{wall} = -\frac{R}{2}\frac{8\mu\, u_{mean}}{R^2} = -\mu\frac{4\, u_{mean}}{R} \tag{2.3.46}$$

where the minus sign indicates that the shear stress vector τ has the opposite sign to the velocity vector u_{mean}.

Remembering that $u_{mean} = Q/\pi R^2$, where Q is volumetric flow rate, and substituting it into Equation (2.3.46), we also obtain:

$$\tau_{wall} = -\mu\frac{4Q}{\pi R^3} \tag{2.3.47}$$

2.3.5.2. Shear stress by laminar flow for rectangular channel

We consider the same rectangular channel with high aspect ratio *w/h* of Section 2.3.4.2, and with the same assumptions. By differentiating Equation (2.3.35) with respect to *∂y*, we obtain:

$$\frac{\partial u}{\partial y} = \frac{\partial}{\partial y}\left(\frac{\Delta p}{\Delta L}\,\frac{h^2 - 4y^2}{8\mu}\right) = -\frac{\Delta p}{\Delta L}\,\frac{y}{\mu} \tag{2.3.48}$$

By substituting Equations (2.3.48) into Equation (2.3.40), we obtain:

$$\tau = -\mu\frac{\Delta p}{\Delta L}\,\frac{y}{\mu} = -\frac{y\Delta p}{\Delta L} \tag{2.3.49}$$

This equation expresses the shear stress value at a point distant *y* from the channel axis along its height, a positive shear stress *τ* is in the direction of a negative pressure gradient *Δp*.

Substituting the half height *h/2* of the channel into the variable *y* of Equation (2.3.49), we obtain the wall shear stress along the width *w* of a rectangular channel with high aspect ratio:

$$\tau_{wall} = -\frac{h\Delta p}{2\Delta L} \tag{2.3.50}$$

We can get another expression of the shear stress inverting Equation (2.3.38):

$$\frac{\Delta p}{\Delta L} = \frac{12\mu\, u_{mean}}{h^2} \tag{2.3.51}$$

where u_{mean} is the mean constant fluid velocity in any section of the rectangular channel.

By substituting Equations (2.3.51) into Equation (2.3.50), we obtain:

$$\tau_{wall} = -\frac{h}{2}\frac{12\mu\, u_{mean}}{h^2} = -\mu\frac{6\, u_{mean}}{h} \tag{2.3.52}$$

where the minus sign indicates that the shear stress vector τ has the opposite sign to the velocity vector u_{mean}.

Remembering that $u_{mean} = Q/wh$, where Q is volumetric flow rate, and substituting it into Equation (2.3.52), we also obtain:

$$\tau_{wall} = \tau_{wall} = -\mu \frac{6\,Q}{w\,h^2} \tag{2.3.53}$$

2.3.6. Darcy's law

Darcy's law applies to the flow of a fluid through a porous medium and relates the flow rate of the fluid to the pressure drop across the porous medium. If the flow is fully developed and the gravitational force is negligible, Darcy's law is expressed in the simplified form [39]:

$$Q = \frac{k\,A\,\Delta p}{\mu\,l} \tag{2.3.54}$$

where Q is the flow rate of the fluid, k is the permeability of the porous medium, A is the cross section of the porous medium, Δp is the pressure drop between the ends of the length l of the porous medium, and μ is the dynamic viscosity of the fluid.

In analogy with Section 2.3.4.1, we define the fluid dynamic resistance Rf for a porous medium as:

$$Rf = \frac{\mu\,l}{k\,A} \tag{2.3.55}$$

which depends only on the physical characteristics of the fluid and the porous medium.

Substituting the Equation (2.3.55) into Equation (2.3.55), we obtain:

$$Q = \frac{\Delta p}{Rf} \tag{2.3.56}$$

formally identical to the Equation (2.3.28), the generalized Poiseuille equation.

2.4. Microfluidic Diffusion

We have previously seen the bulk motion of a fluid generated by the field of forces acting on it and regulated by its viscosity. But it is not the only possible mechanism of mass transport, in fact we will now analyze the fluid movement due to molecular exchange.

This process, called diffusion, occurs constantly in a fluid due to random molecular motion. A volume of fluid is continually losing some molecules and gaining others, so that the specific content of a given volume is always changing. Diffusion is related to the transport of molecules of the same nature from regions of high concentration to regions of low concentration, to reach a final equilibrium state of uniform concentration [31].

For example, this is the case of different gas molecules in a volume with a stable total pressure, but with locally varying partial pressures, or of molecules of a solute in a solvent, with locally varying concentrations.

2.4.1. Fick's first law of diffusion

To define a mathematical model that regulates diffusion, we consider a channel with a constant cross-section of area *A* and its axis coinciding with the x-axis, Figure 2.4.1.

The molecules contained in the channel move randomly, with component along the x axis of the mean displacement equal to ∂x in time ∂t, half of the molecules will move in one direction and half in the other.

Now we consider two symmetrical cross-sections, with respect to the one at point $x=0$ and distant from it by ∂x. We have thus defined two equal volumes, $V=A\partial x$, to the left and to the right of the cross-section at point $x=0$ of the x-axis.

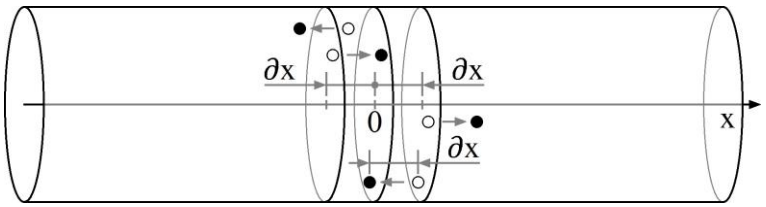

Fig. 2.4.1. *Molecular diffusion model.*

By defining with *c* the concentration, in quantity of mass per unit of volume, of the molecules in the volume on the right and with $c+\partial c$ the concentration in the one on the left, indicating with M_r and M_l the quantity of mass of the molecules in the two volumes, we obtain:

$$M_r = cA\partial x \qquad M_l = (c + \partial c)A\partial x \tag{2.4.1}$$

So, in time ∂t, a mass $M_r/2$ moves ∂x to the left, i.e., beyond the cross-section at point $x=0$, and a mass $M_l/2$ to the right. Thus, we can express the component J_X, net flux along the x-axis of the mass of the molecules through the cross-section at point $x=0$, of the diffusive flux vector $\boldsymbol{J}$, as:

$$J_x = \frac{\frac{M_r}{2} - \frac{M_l}{2}}{A\partial t} = \frac{c_0 A\partial x - (c_0 + \partial c)A\partial x}{2A\partial t} = -\frac{\partial c \partial x}{2\partial t} \tag{2.4.2}$$

Now we define the diffusion coefficient D, or mass diffusivity, as:

$$D = \frac{(\partial x)^2}{2\partial t} \tag{2.4.3}$$

Substituting Equation (2.4.3) into Equation (2.4.2), we obtain:

$$J_x = -D\frac{\partial c}{\partial x} \tag{2.4.4}$$

Generalizing to three dimensions, we can write in compact form the diffusive flux vector $\boldsymbol{J}$, at an arbitrary point, as:

$$\boldsymbol{J} = -D\nabla c \tag{2.4.5}$$

This equation is called the Fick's first law of diffusion, and states that the diffusive flux vector is proportional to the diffusion coefficient and the concentration gradient of the molecules, the negative sign indicates that the molecules diffuse oppositely to the concentration gradient.

2.4.2. Fick's second law of diffusion

Although Fick's first law gives us an expression for the mass flux due to the diffusion process, we still need an equation describing the change in concentration of the diffusing mass with time at an arbitrary point. To achieve this, we consider the mass conservation along the x-axis, we obtain:

$$A\partial x\frac{\partial c}{\partial t} + A\partial J_x = 0 \quad \rightarrow \quad \frac{\partial c}{\partial t} + \frac{\partial J_x}{\partial x} = 0 \tag{2.4.6}$$

Substituting Equation (2.4.4) into Equation (2.4.6), we obtain:

$$\frac{\partial c}{\partial t} + \frac{\partial}{\partial x}\left(-D\frac{\partial c}{\partial x}\right) = 0 \tag{2.4.7}$$

If we assume that the diffusion coefficient *D* is constant, we obtain:

$$\frac{\partial c}{\partial t} = D\frac{\partial^2 c}{\partial x^2} \tag{2.4.8}$$

Generalizing to three dimensions, we write in compact form the Equation (2.4.8) as:

$$\frac{\partial c}{\partial t} = D\nabla^2 c \tag{2.4.9}$$

This equation is called the Fick's second law of diffusion and is a partial differential equation that predicts how the diffusion causes the concentration to change with respect to time.

2.4.2.1. Solution of point source diffusion

We consider an infinite channel with a constant cross-section A and its axis coinciding with the x-axis. A mass *M* of dye is injected at the point *x=0* and at time *t=0* [31], Figure 2.4.2.

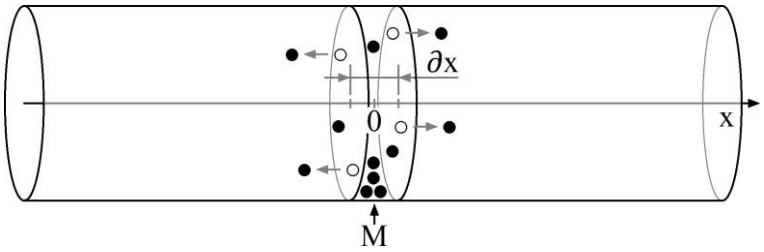

Fig. 2.4.2. *Point source diffusion model.*

In one dimension, the solution for Equation (2.4.8) requires two boundary conditions and an initial condition. As boundary conditions, we impose that at x =±∞ the concentration *c* remains zero:

$$c(\pm\infty, t) = 0 \tag{2.4.10}$$

The initial condition is that the dye tracer is injected instantaneously and uniformly in the volume delimited by two symmetrical cross-sections, with respect to the point *x=0*, and distant from each other by the infinitesimal distance *∂x*:

$$c(x,0) = \frac{M}{A\partial x} \tag{2.4.11}$$

where *∂x* is zero everywhere except at *x=0*, where it is infinite, but the integral of the delta function from –∞ to +∞ is 1.

The fundamental solution of this problem is:

$$c = \frac{M}{A\sqrt{4\pi Dt}}\, exp\left(-\frac{x^2}{4Dt}\right) \tag{2.4.12}$$

The solutions are Gaussian curves, Figure 2.4.3. Their width increases as the square root of the time, a characteristic of diffusive phenomena. At the same time, the amplitude decreases as $1/\sqrt{t}$ to keep the area constant, given that the area corresponds to the initial mass.

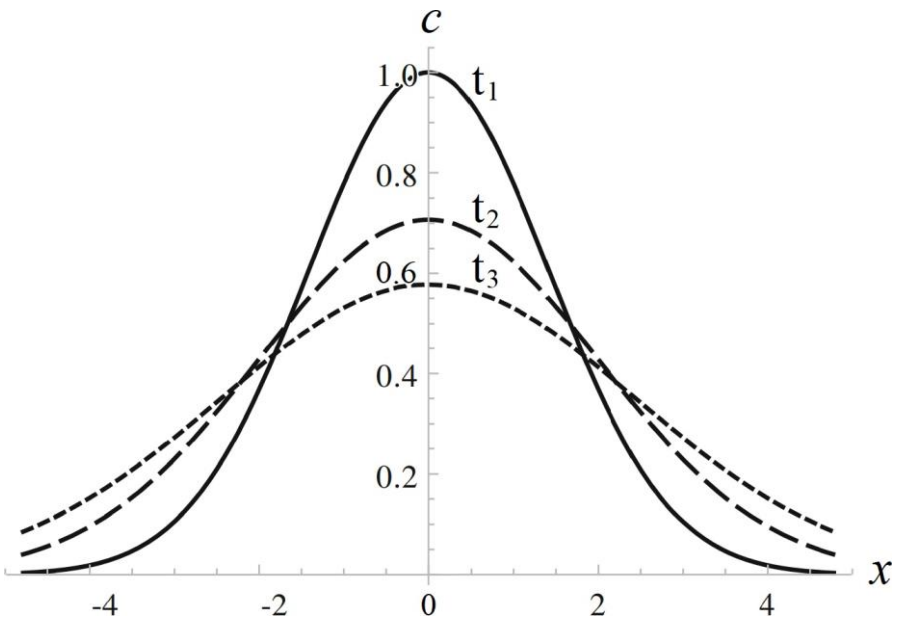

Fig. 2.4.3. *Solution of the diffusion equation in one dimension for three different times ($t_1 < t_2 < t_3$) after the injection (redraw from* [31]*).*

2.4.3. Advective-Diffusive Transport

The advection-diffusion equation is based on the superposition principle: the effects of advection and diffusion can be added if the two phenomena are independent. In advection, each molecule will move $u\partial t$ in the direction of flow due the velocity field. In diffusion, each molecule will move left or right by one step, $\pm\partial x$, during a time ∂t, due to the random molecular motion. These processes are clearly additive and independent: the net motion of the molecule is $u\partial t \pm \partial x$.

We define the mean component u_X, along the x-axis, of a laminar velocity field $\boldsymbol{u}$. Thus, we can express the component J_X, along the x-axis, of the total flux vector $\boldsymbol{J}$ for an advective-diffusive transport, from Equation (2.4.4) adding the contribution of the product of the concentration of the molecules c and the mean component u_X of the velocity field, as:

$$J_x = u_x c - D\frac{\partial c}{\partial x} \tag{2.4.13}$$

Now, substituting the Equation (2.4.13) in the mass conservation Equation (2.4.6), we obtain:

$$\frac{\partial c}{\partial t} + \frac{\partial}{\partial x}\left(u_x c - D\frac{\partial c}{\partial x}\right) = 0 \tag{2.4.14}$$

If we assume that the diffusion coefficient D and the component u_X of the velocity field are constant, we obtain:

$$\frac{\partial c}{\partial t} + u_x\frac{\partial c}{\partial x} = D\frac{\partial^2 c}{\partial x^2} \tag{2.4.15}$$

Generalizing to three dimensions, we write in compact form the Equation (2.4.15) as:

$$\frac{\partial c}{\partial t} + \boldsymbol{u}\cdot\nabla c = D\nabla^2 c \tag{2.4.16}$$

This is a partial differential equation that describes how the diffusion and the velocity field affect the change in concentration with respect to time.

2.4.3.1. Solution of point source diffusion and advection

This problem derives from the point source problem, by superimposing the advection, a flow with uniform velocity *u* parallel to the x-axis, on the diffusion, Figure 2.4.4.

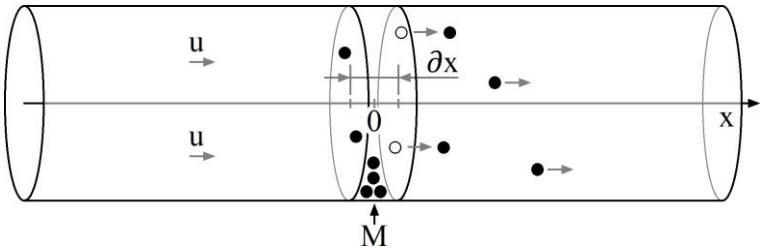

Fig. 2.4.4. *Point source with flow diffusion model.*

The solution to this problem is simplified if, instead of calculating the aggregate of the two phenomena using Equation (2.4.16), we simply add their effects, calculated separately.

Over time, the flow shifts the distribution of concentrations by a distance $x = ut$, so we define the variable χ as:

$$\chi = x - ut \tag{2.4.17}$$

We change the variable x with the variable χ in Equation (2.4.8), and we obtain:

$$\frac{\partial c}{\partial t} = D\frac{\partial^2 c}{\partial \chi^2} \tag{2.4.18}$$

Changing the variable x with the variable χ means replacing the fixed reference system with a mobile one, centered on the distribution of concentrations. With the same initial and boundary conditions, the fundamental solution of Equation (2.4.18) is identical to that of Equation (2.4.8):

$$c = \frac{M}{A\sqrt{4\pi Dt}}\ exp\left(-\frac{\chi^2}{4Dt}\right) \tag{2.4.19}$$

Now, substituting Equation (2.4.17) in Equation (2.4.19), we obtain the solution in the absolute system:

$$c = \frac{M}{A\sqrt{4\pi Dt}}\ exp\left[-\frac{(x-ut)^2}{4Dt}\right] \tag{2.4.20}$$

Figure 2.4.5 shows the solution of point source diffusion and advection in the absolute system, the concentration curves have the same shape as those in the Figure 2.4.3 but are translated along the x- axis because of the advective transport.

This example is interesting since it highlights the importance of both diffusive and advective transport. If the flow were stronger, the diffusion cloud would have less time to spread out and concentration curves would be narrower at the time steps. Conversely, if the diffusion were faster, i.e., larger *D* or larger initial concentration, the diffusion cloud would spread out more and the concentration curves would be less narrow in the time steps and would overlap more.

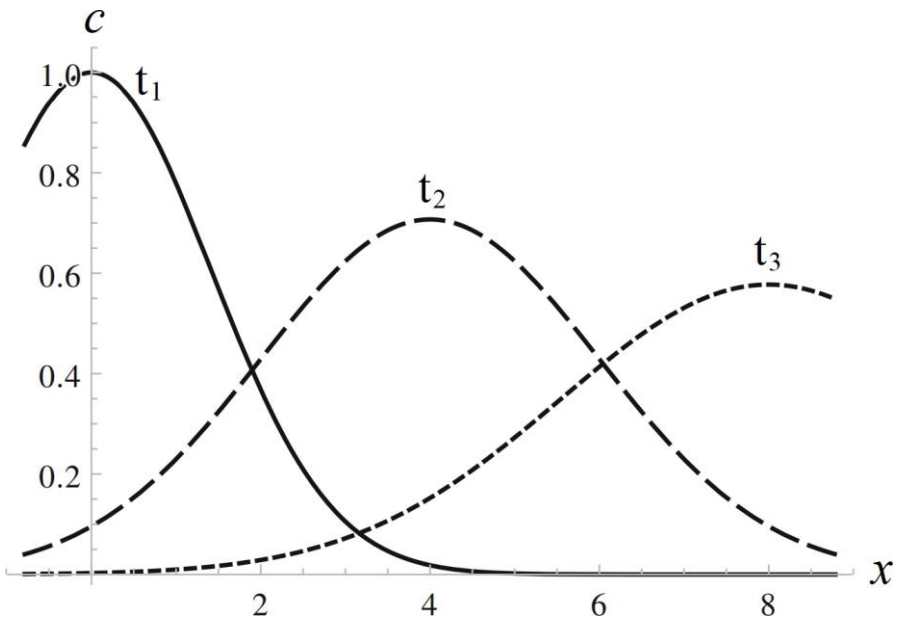

Fig. 2.4.5. *Solution of the advective-diffusive equation in one dimension for three different times ($t_1 < t_2 < t_3$) after the injection (redraw from* [31]*).*

2.4.3.2. Advection-diffusion problem in microfluidic mixer

As seen in figure 2.2.1, in microfluidics two different fluids mix with difficulty due to the high laminar flow, as indicated by very low Reynolds numbers.

Now, we analyze the advection-diffusion problem of a microfluidic mixer. The geometry used is a channel with a Y-junction where a solute flow of uniform concentration c_0 meets a solvent flow at the junction. Due to the laminarity of the flow, mixing occurs in the central channel only by diffusion and there is an equivalence between time and length, i.e., in the steady state regime, measuring the concentration profile at a given length is equivalent of measuring the concentration at a given time [31].

Figure 2.4.6-A shows the distribution of concentrations in the mixer using a numerical simulation. Dilution occurs at the junction and spreads along the rectangular central channel wide *W*, with flow direction from top to bottom. Figure 2.4.6-B shows the concentration profile in the cross-section of the channel at different times.

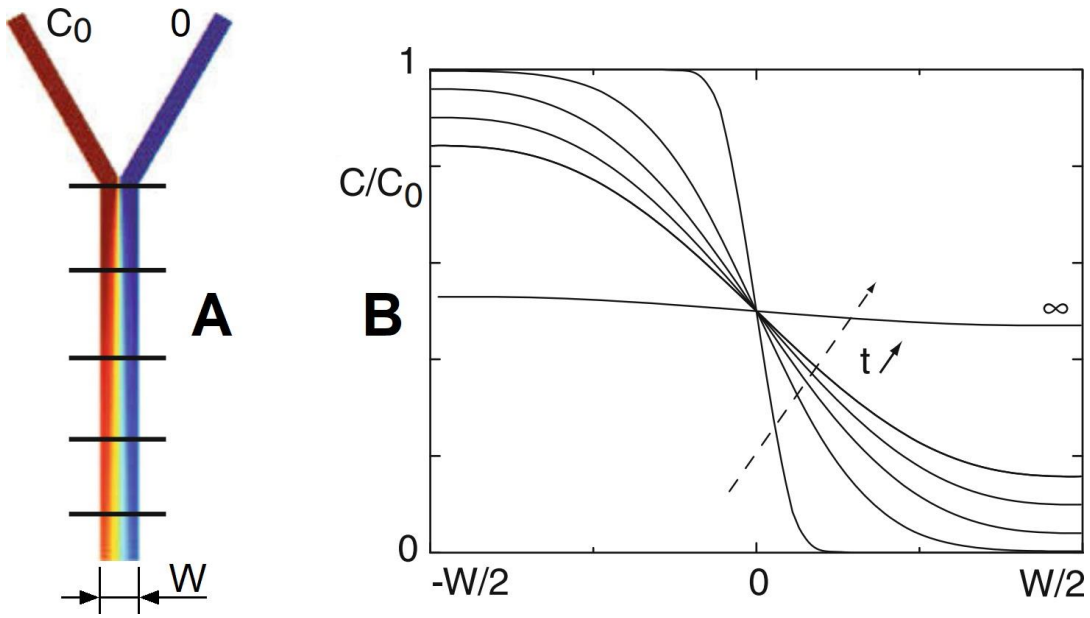

Fig. 2.4.6. *Distribution and evolution of the concentration in the microfluidic mixer* [31].

It is easy to understand that for very long times, tending towards infinity, due to a long central channel or to a slow advection, the concentration carried by the flow tends to be uniformly distributed across the width W of the central channel with value $c_0/2$, Figure 2.4.6.

2.4.3.3. Péclet number: advection-diffusion ratio

Figure 2.4.7 shows the different cases examined of combined advection-diffusion transport.

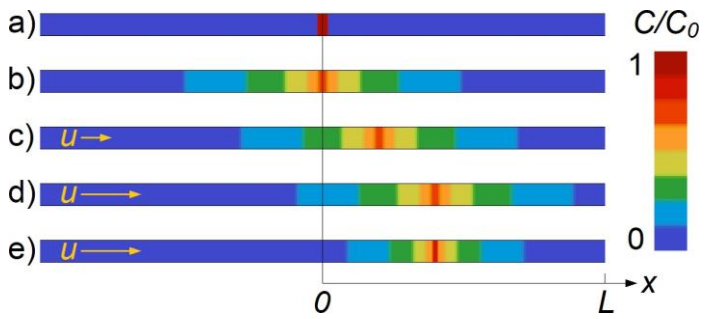

Fig. 2.4.7. *(a) Point source diffusion at t=0, (b) at t=t_1. (c) Point source diffusion with advection at t=t_1, (d) with higher advection, (e) with higher advection and less diffusion.*

As can be seen, with the same elapsed time $t=t_1$, the higher the advection, the more the diffusion cloud is transported downstream but does not change its distribution. The concentration distribution can change, for example if the diffusion coefficient D is reduced, then the diffusion is reduced and its peak concentration is increased, or the opposite if the coefficient is increased. Therefore, by changing the parameters, the trend of diffusion, i.e., the value of the concentration in time and space, can change considerably.

Fluid flows in ordinary life, due to their high Reynolds numbers, are continually agitated by the chaotic eddies generated by turbulence. As a result, mixing gradients are high and mixing times are short. Fluid flows in microfluidics, due to their low Reynolds numbers, are laminar and mixing occurs only by diffusion, which can lead to long mixing times [6].

In microfluidics, knowing quickly and simply how diffusion behaves and its relationship with advection would be important in the study and design of microfluidic circuits that require the mixing of two or more fluids. With Fick's second law, Equation (2.4.9), we have seen how concentration varies in time and space in the case of simple diffusion. Then adding the $\boldsymbol{u}\cdot\nabla c$ term to the first member of the equation, we obtained Equation (2.4.16) for advective-diffusive transport. This apparently simple addition complicates the mathematical solution tremendously, admitting exact solutions only in rare circumstances. The difficulty is that these systems often contain some regions where diffusion dominates, and others where advection dominates. Mathematically speaking, any approximation scheme that works in one region is bound to fail in the other [40].

A simple method to determine whether the diffusive or advective aspect is predominant in a mixing is to consider a channel and compare the time it takes for a molecule to diffuse across the width of the channel with the time it takes for the molecule to travel the same distance dragged by the flow along the channel. We define W the width of the channel, D the diffusion coefficient, and u the mean velocity of the flow, as a first approximation W^2/D [41] is the diffusion time for crossing the channel width W, and W/u is the time that the flow travels through a space equal to W, so we obtain:

$$\frac{diffusion\ time}{advection\ time} \approx \frac{\frac{W^2}{D}}{\frac{W}{u}} = \frac{Wu}{D} = Pe_W \tag{2.4.21}$$

The dimensionless number on the right is known as the Péclet number (Pe_L), here with subscript W to specify the channel width as the characteristic length scale. When Pe_L is less than 1000, molecular diffusion becomes an important mechanism for mixing [35].

2.4.3.4. The Péclet number in an advection-diffusion problem

We consider a water flow rate Q of 0.04 µL/s in a mixer microfluidic channel with a width W of 0.4 mm and a height H of 0.1 mm. We inject in the channel a dilute electrolyte, NaCl, which has a diffusion coefficient D at 293 K of 1.74×10^{-9} m^2/s [35].

First, given the aspect ratio of the dimensions of the rectangular channel, $W/H=4$, we calculate its hydraulic diameter D_H to use it as the characteristic length scale of the channel:

$$D_H = \frac{2WH}{W+H} = \frac{2\times0.4\times10^{-3}m\times0.1\times10^{-3}m}{0.4\times10^{-3}m+0.1\times10^{-3}m} = 1.6\times10^{-4}m \quad (2.4.22)$$

Then, since $A=WxH$ is the area of the channel, we can calculate the mean velocity u of the water flow Q:

$$u = \frac{Q}{A} = \frac{Q}{W\times H} = \frac{0.04\times10^{-9}m^3/s}{0.4\times10^{-3}m\times0.1\times10^{-3}m} = 1.0\times10^{-3}m/s \quad (2.4.23)$$

Now, the water density ρ at 293 K is 1.0×10^3 kg/m^3 and its dynamic viscosity μ is 1.0×10^{-3} Pa·s, and, from Equation 2.2.4, we can calculate the Reynolds number of the water flow in the channel:

$$Re = \frac{\rho u D_H}{\mu} = \frac{1\times10^3kg/m^3\times1\times10^{-3}m/s\times1.6\times10^{-4}m}{1\times10^{-3}Pa\cdot s} = 0.16 \quad (2.4.24)$$

This Reynolds number is much lower than the critical number of turbulent transition Re_{cr}=2000÷3000, therefore the flow is certainly laminar, as we could logically expect from a microfluidic circuit.

Now, we calculate the Péclet number:

$$Pe_{DH} = \frac{uD_H}{D} = \frac{1\times10^{-3}m/s\times1.6\times10^{-4}m}{1.74\times10^{-9}m^2/s} = 92.0 \quad (2.4.25)$$

Given the low Reynolds number and the relatively high diffusion coefficient, i.e. under the same conditions, serum albumin BSA has a much lower $D=5.9\times10^{-11}m^2/s$ [35], this Péclet number is much lower than the critical Péclet number, Pe_{cr}=1000, and therefore diffusion is predominant over advection for mixing in this case.

If in a first approximation, as for Equation (2.4.21), $t_d = W^2/D$ is the diffusion time for crossing the channel width W, we obtain:

$$t_d \approx \frac{W^2}{D} = \frac{(0.4 \times 10^{-3} m)^2}{1.74 \times 10^{-9} m^2/s} = 92.0\ s \tag{2.4.26}$$

At the same time, the water flow and the diffusion front have traveled the distance l_d:

$$l_d = u \cdot t_d \approx 1 \times 10^{-3} m/s \times 92.0\ s = 92.0\ \times 10^{-3} m \tag{2.4.27}$$

i.e., 230 times the channel width W.

This result indicates that the time required for mixing by diffusion alone, as occurs in simple microfluidic channels, is too long. Furthermore, a straight channel of this length is not compatible with the dimensions of a microfluidic chip, whose length normally does not exceed a few tens of millimeters. A first solution is to give the channel the shape of a serpentine to reduce its overall dimensions but, as we will see later, the best solution is to create variations in the section of the channel to have a locally turbulent flow, improve mixing and reduce time and length.

3. Microfluidic Technology

3.1. Introduction

Normally in engineering, processing technologies follow the discovery of new materials, i.e. to use materials with innovative characteristics, existing technologies had to be adapted or new ones created. Think of aluminum whose rapid welding with valid mechanical characteristics was only possible with the introduction of pulsed TIG or of glass fiber, then carbon, which was usable only with suitable impregnation techniques with plastic matrices.

The same is true for microfluidics, when attempts to create the first microfluidic circuits began in the 1950s, the materials were already available. They are still the same now, silicon, glass, plastic materials, but there simply were not technologies capable of processing them on a micrometric scale. The classic mechanical processes for chip removal, such as milling, still have difficulty creating channels with a width of less than 200 μm and with considerable operational limitations [42], [43].

Only with the availability of the technology for the realization of integrated electronic circuits, it was possible to obtain microfluidic circuits from silicon wafers, then also from glass layers, through photolithography, followed by wet (chemical) or dry (plasma) etching [44]. With this technology it is possible to create planar incisions, even on several levels with different heights.

This step is important because from it derived the soft lithography, which is universally used in research, where a negative mold is created through photolithography, then an elastomeric polymer, polydimethylsiloxane or PDMS, is poured into it. The poured PDMS, after its polymerization, is extracted from the mold and sealed, obtaining the microfluidic circuit [45].

The purpose of this chapter is to extensively expose this fundamental technology for microfluidics research, to evaluate its strengths and weaknesses in comparison with other technologies, scientifically interesting but less widespread than PDMS technology.

The mass production of microfluidic circuits, which require very different technologies such as hot embossing or paper-based microfluidic technologies, is not examined here. All common people have experience of these devices having used them, such as pregnancy tests, implantable or portable blood glucose monitors, tests for SARS-CoV-2, manufactured in billions of pieces. But it is important to note that the microfluidic process of these technologies was mainly developed by research, using PDMS technology [46], [47], [48]. Furthermore, known, and consolidated technologies such as (wet or dry) chemical etching or electron beam engraving will not be examined.

3.2. PDMS Technology

Polydimethylsiloxane (PDMS) is a silicone polymer, it has viscoelastic characteristics but at room temperature it behaves like an elastic solid, such as rubber, with excellent elongation under load. It is characterized by a remarkable resistance to temperature, to chemical attacks, to oxidation, it is an excellent electrical insulator and resistant to aging; moreover it has high transparency, it is biocompatible, gas permeable, chemically inert, it is neither toxic nor flammable. Furthermore, this polymer does not bind to glass, metal, or plastic during polymerization. In uncured form, for pour-into-mold applications, it is very flowable allowing it to copy the mold perfectly, filling sub-micrometer scale engravings.

All these characteristics make it the ideal material for the fabrication of microfluidic circuits.

3.2.1. Photomask Realization

The photomask is a chrome-coated glass lithographic template designed to optically transfer the drawing of the microfluidic circuit on a 1:1 scale to wafers or other substrates to fabricate a mold. Briefly, the drawing is transferred to a lithography machine, laser writer or e-beam writer, then printed in a layer of photoresist coated onto the photomask plate. The imaged pattern is next developed to form a template over the opaque chrome and then the chrome is etched away where there is no photoresist. After the etch process is complete, the remaining photoresist is removed, the plate cleaned, and ready to create the mold [49].

For low-cost but lower quality applications, transparent plastic masks are used on which the drawing is reproduced using a high-resolution ink-jet printer.

The process of making a photomask, especially if in glass, is complex and requires a lot of precision, any slightest error will be reproduced on the mold. Normally the creation of a photomask is entrusted to specialized companies that produce them from a CAD drawing provided by the customer [50]. The design, and therefore the photomask, can include more than one microfluidic circuit, allowing to obtain multiple molds, equal or different.

3.2.2. Master Mold Fabrication

The basis of the mold is a monocrystalline silicon wafer, with a diameter of 100 mm (4") and a thickness of 500 µm for typical microfluidic applications [51]. Before conducting any operation, it must be carefully cleaned with suitable solvents and the subsequent operations must be performed in a cleanroom. Given the micrometric dimensions of the channels of the microfluidic circuit, any speck of dust or contamination can irreparably damage the circuit.

The wafer is coated on top by a layer of resist, a UV photosensitive emulsion which normally is a negative type, i.e. the development eliminates the part non-exposed to UV light. The mold must show the geometry of the microfluidic circuit in negative, therefore the resist parts that will remain will correspond to the voids of the circuit, e.g. the channels. To eliminate unwanted resist exposures to UV, the cleanroom must have yellow lighting, Figure 3.2.1. The thickness of the layer determines the height of the channels of the microfluidic circuit, resists with different viscosities are available for different thickness. To evenly distribute the resist after the coating, the wafer is placed in a spin coater and spun according to a programmed cycle in which speed determines the final thickness of the layer, expelling the excess resist.

Fig. 3.2.1. *Manual application of photoresist to a blank mask before using the spin coater inside a cleanroom with yellow lighting* [49].

To properly dry the resist, the wafer is placed on a hot plate, with the resist up, and soft-baked in multiple heat-up and cool-down cycles to avoid wrinkles on the resist surface, with controlled temperature and time depending on the thickness of the resist layer.

The resist is now ready to be exposed to UV light, for the maximum precision in the reproduction of the photomask design, it is necessary that the design must be placed into close contact with the resist layer. To achieve vertical sidewalls in the layer, it is recommended to use a long pass filter to eliminate shorter wavelength UV radiation, which has a higher refractive index and therefore more bent optical path.

The optimal duration of exposure depends on the light energy per unit area of the UV light that illuminates the resist through the transparent areas of the photomask, and the thickness of the resist layer. After exposure, the wafer is placed on the hotplate for a post-exposure bake, with controlled temperature and time depending on the thickness of the resist layer, to cross-link the UV-exposed resist.

The resist can now be developed by immersion in solvent-based developer, to dissolve the non-exposed parts. Strong agitation, e.g. by an ultrasonic bath, is recommended to develop thick resist layers. The development time depends on the thickness of the resist layer and the level of agitation. After the development, the wafer is rinsed with fresh developer and dried with a blow of filtered air. To obtain the best mechanical characteristics of the cross-linked resist, a final hard bake is required with time and temperature depending on its use [52].

If it is necessary to create a microfluidic circuit with different designs on several layers, Figure 3.2.2, even with different thicknesses but always with open geometries, it is sufficient to create several photomasks, one for each layer, and repeat the coating, exposure, and development process for each layer.

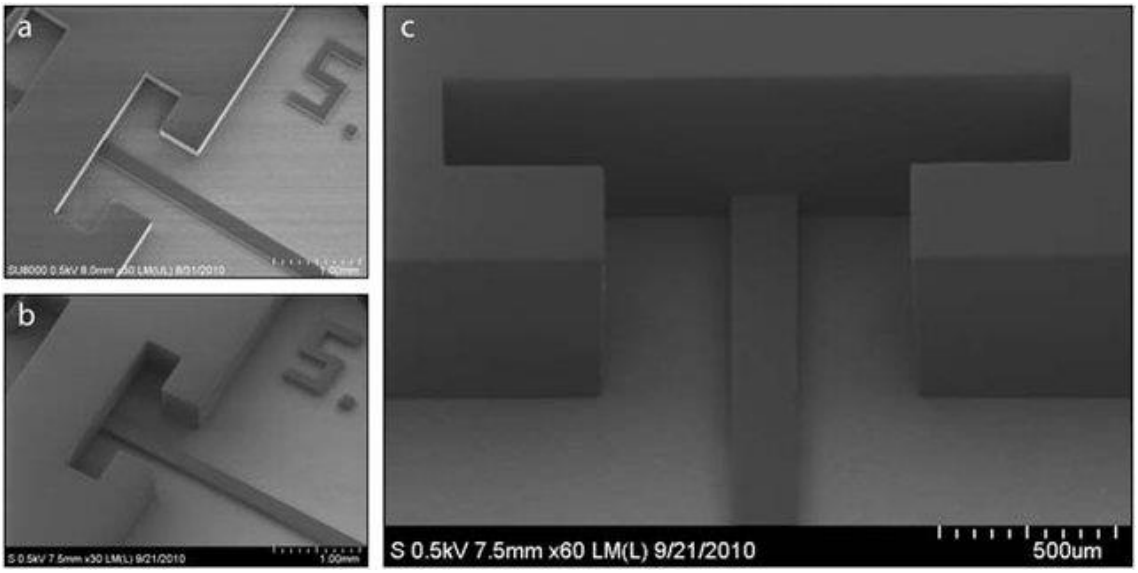

Fig. 3.2.2. *SEM images of resist molds* [53]. *(a) Mold with 250 µm thick walls and 80×200 µm microfluidic channel. (b) Mold with 500 µm thick walls and 80×200 µm microfluidic channel. (c) Image of (b) mold illustrating the negative pitch or sidewall irregularity.*

The construction of the mold is finished by adding a frame around its perimeter, to contain the PDMS to be cured, and if necessary with some accessories, such as inlet-outlet wells.

The finished mold must be subjected to a silanization process, chemical modification of the surface through the creation of a monolayer of silane, by immersion in vapor of dichloromethylsilane, or another silicon-based volatile inorganic compound, which prevents the PDMS from adhering to the mold surface with consequent possible damage to its reliefs [54].

3.2.3. PDMS Casting

For any general applications including microfluidics, PDMS is used in the two-part form, the base polymer, and the curing agent. The curing agent concentration directly impacts the modulus and hardness properties to a great extent and is the major variable parameter in many applications [55]. When liquid components are thoroughly mixed, the cure reaction of the mixture begins with the mixing process. Initially, cure is evidenced by a gradual increase in viscosity, followed by gelation and conversion to a solid but flexible elastomer. PDMS cures without exotherm at a constant rate regardless of sectional thickness or degree of confinement [56].

After thoroughly mixing the components, and respecting the required dosage, the mixture must be placed in a vacuum desiccator and degassing cycles must be made to eliminate all air bubbles. The mixed and degassed PDMS can be poured directly into the mold in which it is to be cured. Care must be taken to minimize air entrapment. Whenever possible, pouring should be done in a vacuum chamber, particularly if the mold has many small voids. If this technique cannot be used, the PDMS must be degassed after it has been poured.

The pot life is defined as the time required for viscosity to double after base and curing agent are mixed and is highly temperature dependent, at room temperature the pot life is more than one hour [55] and allows all previous operations to be conducted without appreciably altering the excellent flowable characteristics of the PDMS.

After degassing, The PDMS is cured in a thermostatic chamber for a few hours, depending on the temperature setting [56], then it can be manually extracted from the mold.

3.2.4. Finishing and Sealing

The microfluidic circuit must be finished by cutting off its excess PDMS parts, separating it from any other circuits made simultaneously in the same mold, and piercing it with a hole puncher at the inlet and outlet points.

Now the microfluidic circuit can be sealed by bonding, on the side that was previously in contact with the mold, a solid or flexible substrate, e.g. glass, silicon, or various polymers, forming the microfluidic device. The use of adhesives to bond microfluidic devices has long since been almost completely abandoned, both due to their possible non-compatibility with the liquids flowing inside the circuits, and due to the risk that their small excesses may block channels. Silicon-based materials, e.g. glass, silicone plastics, or PDMS itself, can be relatively easily bonded to PDMS via simple surface activation, and thus this is the most widespread way of sealing the channels. Plasma treatment is by far the most used method for contaminant removing and surface activation. A large variety of gasses can be used, oxygen or common clean air are the most used, from medium vacuum to atmospheric pressure [57]. The correct treatment parameters, power, and time, depend on the materials to be treated, the type of gas used and its absolute pressure in the chamber.

Thus, in the plasma bonding technique, the microfluidic circuit and the substrate are cleaned with a solvent, for example ethanol, then placed together in a plasma machine for the activation of their surfaces and bonded at the end of the activation treatment by simple contact between them. Positioning errors are no longer recoverable because the bonding is immediate.

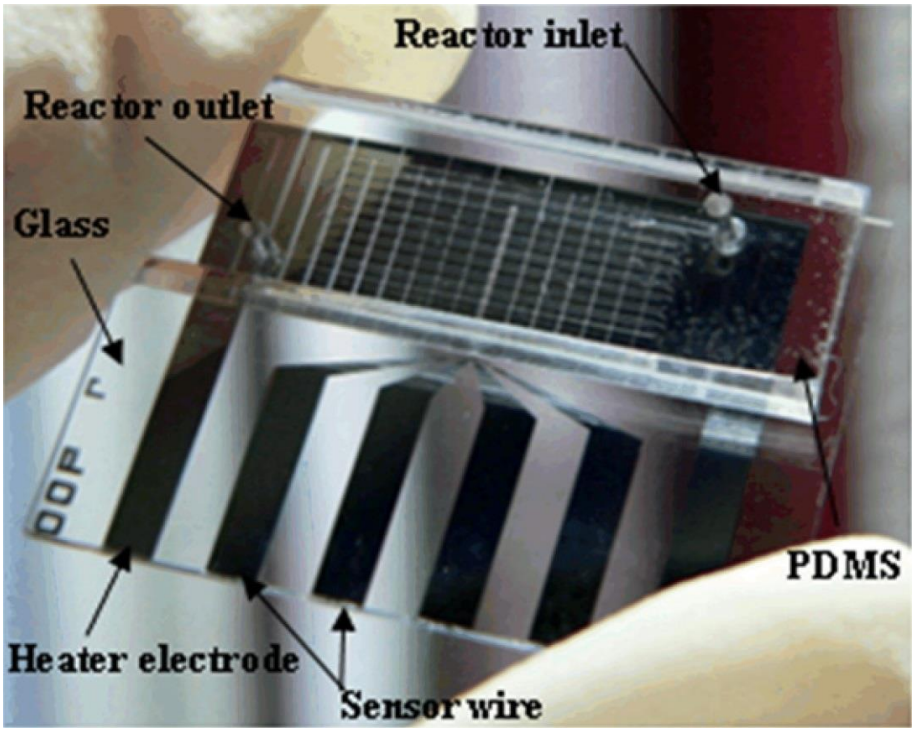

Fig. 3.2.3. *PDMS–glass serpentine microchannel chip for time domain PCR* [58].

3.2.5. PDMS Characteristics

PDMS is the most widely used material in scientific research for the construction of microfluidic circuits [9]. Below are listed the main characteristics that have decreed its success but also those that limit its application.

3.2.5.1. Physical Characteristics

PDMS, density 1.03 kg/dm³, is a highly transparent material with a refractive index of approximately 1.4 for a light wavelength from 589 to 1554 nm [56], this allows for easy inspections of the processes taking place within the microfluidic circuits.

It has good gas permeability, Table 3.2.1, this allows it to maintain the correct gas mix that guarantees life in biological experiments. Obviously, this characteristic is a limitation when gas exchanges between the microfluidic circuit and the external environment are not desired.

Table 3.2.1. *Permeability, Solubility, and Diffusivity Parameters in PDMS at 35 °C* [59].

Penetrant	P_o[a] [Barrer]	$m \times 10^3$ [1/atm]	S^∞ [cm³(STP)/ cm³ · atm]	$n \times 10^3$ [1/atm]	$D_o \times 10^6$ [cm²/s]	$q \times 10^3$ [1/atm]
H_2	890 ± 30	−3.8 ± 3.5	0.05 ± 0.008	5 ± 10	140 ± 5	−8.2 ± 3.4
O_2	800 ± 20	−3.4 ± 2.7	0.18 ± 0.01	4.9 ± 2.9	34 ± 1	−7.6 ± 2.6
N_2	400 ± 10	−3.5 ± 3.4	0.09 ± 0.008	2.6 ± 5.5	34 ± 1	−5.6 ± 1.0
CO_2	3800 ± 70	4.0 ± 2.0	1.29 ± 0.01	5.9 ± 0.7	22 ± 1	−1.6 ± 2.9
CH_4	1200 ± 40	−0.2 ± 3.4	0.42 ± 0.01	1.0 ± 1.4	22 ± 1	−1.2 ± 3.4
C_2H_6	3300 ± 100	28 ± 4	2.2 ± 0.02	5.5 ± 0.7	11.3 ± 0.3	20 ± 4
C_3H_8	4100 ± 300	410 ± 60	5.0 ± 0.07	150 ± 7	5.1 ± 0.3	200 ± 40
CF_4	200 ± 10	−6.5 ± 3.2	0.19 ± 0.01	0.3 ± 3.9	8.0 ± 0.2	−6.7 ± 3.2
C_2F_6	190 ± 10	−0.2 ± 3.0	0.33 ± 0.01	1.7 ± 1.4	4.4 ± 0.1	−1.9 ± 2.9
C_3F_8	280 ± 10	24 ± 10	0.85 ± 0.02	2.7 ± 4.4	2.5 ± 0.1	20 ± 10

[a] 1 Barrer = 10^{-10} cm³(STP) · cm/cm² · s · cm Hg.

3.2.5.2. Chemical Characteristics

PDMS is chemical inert and does not swell in contact with water, on the contrary it swells in contact with nonpolar solvents (e.g., hydrocarbons, toluene, and dichloromethane) and is not useful for manipulations requiring these solvents [60]. However, some organic solvents cause only small deformations, such as alcohol solvents, and are normally used with PDMS.

The nature of PDMS is usually hydrophobic, it can be transformed to hydrophilic by oxygen or air plasma exposure that introduces polar functional groups (SiOH) on the surface [61], but this transformation is temporary and after a while PDMS becomes hydrophobic again. This is a serious issue in biological assays as it modifies protein absorption [55].

3.2.5.3. Mechanical and Technological Characteristics

PDMS is a soft material, hardness from 43.8 to 54.0 Shore A, Young's modulus from 1.32 to 2.97 MPa, ultimate tensile strength from 5.13 to 3.51 MPa, all depending on the curing temperature from 25 to 200 °C [62]. This softness makes PDMS a material that is easy to extract from the mold without marring it and adaptable to sealing surfaces during bonding without glue, it also allows easy technological processing such as cutting and piercing when cured. Conversely, this property can cause relief deformation of microfluidic circuits when the aspect ratio is high [45].

When calculating the dimensions of the mold, it must also be considered that the PDMS shrinks by about 1% upon curing [45], this is not a problem in the extraction of the PDMS from the mold, because the shrinkage pressure on the mold reliefs is low due to its softness.

3.2.5.4. Costs

The cost per kilogram of medical PDMS used for the fabrication of biological microfluidic circuits is about two orders of magnitude higher than that of common technical plastics, e.g. PE (polyethylene) or PMMA (polymethyl methacrylate) but given that on average a chip has a mass of only a few grams, the cost of the material is a fraction of the cost to fabricate it.

The cost of fabrication is essentially the cost of the photomask and the master mold, the steps involving PDMS are relatively inexpensive using mainly laboratory machines and personnel, resources typical of academic research, this makes it a very useful material for giving students practical experience.

Obviously, if many mold changes or many identical chips are required, PDMS chips are no longer cost-effective and other technologies must be used.

3.3. PMMA Technology

Polymethyl methacrylate (PMMA) is a thermoplastic polymer, one of the most used materials, after PDMS, for microfluidic chips with the features of low price, excellent optic transparency, and excellent electric and mechanical properties. It has a density of 1.19 kg/dm^3, Young's modulus of 3.3 GPa, ultimate tensile strength of 70 MPa [63], hardness of M68-105 Rockwell, mold (linear) shrinkage of 0.1-0.4% [64].

Because it can decompose into methyl methacrylate (MMA) at high temperature and can be reused, PMMA is an ideal material for preparing "green microchips". It has been reported as the least hydrophobic polymer among the commonly used plastic materials [65].

PMMA is biocompatible but can be partially swelled in water [66], it swells and dissolves in alcohol and in many organic solvents [67].

While PDMS is used in medical applications, so its quality control during production is rigorous and its properties do not vary much from batch to batch, with the other polymers that mainly derive from the industrial sector, such as PMMA, there is much more variability in terms of polymer properties and achieving chip-to-chip reproducibility is more difficult [10].

PMMA is mainly used in the production of large quantities of microfluidic chips using technologies such as hot embossing or injection molding [65], which require very expensive machinery and equipment that are amortized only with high productions.

PMMA, for small productions, cannot directly use casting in a mold obtained by photolithography, because due to its high rigidity it cannot be extracted from the mold without damaging it. To use this technology it is necessary to invert the process, i.e. create a positive main mold by photolithography, from this obtain a negative secondary mold in PDMS, and in this secondary mold cast the PMMA to obtain the microfluidic chips, safe extraction is allowed by the softness of the PDMS, this variant of technology is called replica molding. The sealing of the PMMA chip cannot be done by plasma bonding because PMMA does not contain silicon to be activated, so other technologies are used such as thermo-bonding of a PMMA secondary blank layer. Obviously, this technology to produce a few PMMA chips is more complex than that with PDMS, but it may be necessary when, e.g., better mechanical characteristics are required.

3.4. Laser Technology

As can be seen from the previous examples, photolithography technology consists of many steps and therefore relatively long lead times. The researchers immediately thought of a simpler alternative by using a laser source, initially CO_2 [68], to engrave the microfluidic circuit directly on the bulk material of the chip, using the thermal energy of the light beam to melt and vaporize the material to be removed. The chip thus obtained must be finished and sealed with known technologies.

As might be expected, each material behaves differently to laser machining, often with negative results. Due to the high temperatures of the beam, hard materials, such as glass, tend to crack under thermal stress and soft materials, such as plastics, to burn in the exposed area.

A marked improvement has been obtained with pulsed lasers in which the energy of the light beam is concentrated in pulses of a few nanoseconds [69]. This high concentration of energy allows to directly ablate the atoms of the material to be worked with reduced heating of the surrounding areas [51], and is possible to use almost any material.

The main limitations of all laser technologies are the need to seal the microfluidic chip and the process time. The time is competitive for the creation of few chips, but it lengthens proportionally to the number of chips to be produced because all the processing steps must be repeated for each chip, it is not possible to reduce the steps using a mold as for PDMS.

3.5. FLICE Technology

An interesting variant of laser machining is the femtosecond laser irradiation followed by chemical etching (FLICE) inside a compact glass chip. This technique consists of two steps, first a permanent glass modification following nonlinear absorption of focused femtosecond laser pulses in the whole 3D volume of the microfluidic circuit using a CAD/CAM system, second etching of the laser modified glass by a hydrofluoric acid (HF) solution in water. Femtosecond laser irradiation enhances the etching rate by up to two orders of magnitude, enabling the manufacturing of channels with high length/cross-section ratio [70].

There are many advantages attributed to this microfabrication method in comparison with traditional technologies, including the ability to quickly realize 3D monolithic structures completely buried in the glass without the requirement of masks or a clean room. With FLICE, there is no need to create complex 2.5D multi-layer chips to be subsequently bonded as with traditional technologies, a process which often leads to sealing problems [33].

Important problems are the danger of chemical etching using HF, and the limitation of the lengths of the microfluidic channels with small cross-section, due to the conical shaping.

This effect is due to the action of the chemical etching which, from the external areas, advances into the channels irradiated by the laser. This progress also takes place slowly in the non-irradiated areas, therefore the areas etched first have a larger section than those engraved last, Figure 3.5.1. This effect can be compensated for by a counter-taper of the laser irradiation but is limited by the minimum irradiable cross-section.

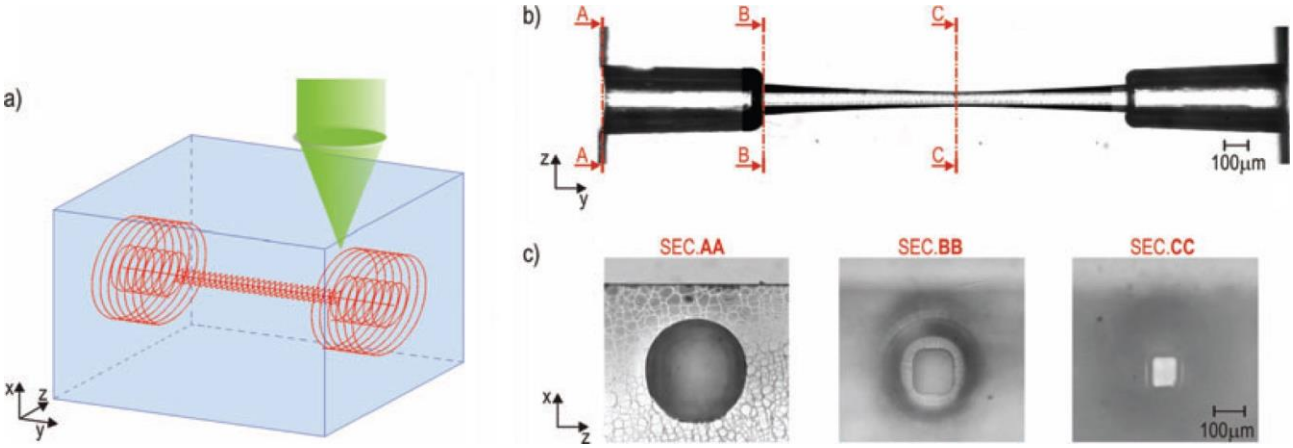

Fig. 3.5.1. *FLICE Technology* [70]. *(a)Irradiation path for channel formation (red lines) and the focused laser beam (green). (b)Microchannel axial section after chemical etching showing the conical shaping. (c)Microchannel cross-sections along the channel axis.*

3.6. Conclusions

As we have seen, the possible technologies and materials are numerous and given the large variety of microfluidic circuits and their applications, there is no perfect solution for everything, each solution has its drawbacks [10].

The choice of the material can be suggested by the environment in which the microfluidic chip must operate. If we are in the biological field, PDMS, with its biocompatibility, transparency, and gas permeability, is certainly the best candidate. If, on the other hand, we are in the field of industrial sensors, where good mechanical characteristics are required, then technical plastics have a good chance. Or, if we want high resistance to chemical attack, glass is a great solution.

The choice of technology can be suggested by the number of chips that need to be made, if few pieces are needed, laser technologies are certainly advantageous. If we want more chips, up to a hundred pieces, the use of a mold becomes competitive with acceptable unitary costs. This choice can also be determined by the time available to make the chips, by the equipment and experience of the personnel available, by the simplicity of execution. Here the various technologies must be chosen on a case-by-case basis.

4. Microfluidics-Based 3D Cell Culture Models for Bone Regeneration

4.1. Introduction

The activity of this research was to design and create a bioreactor with a 3D scaffold for the study of bone cell proliferation, with the aim of deepening existing research through a better understanding of the bone remodeling process. The development of a 3D scaffold for bone cell culture would have been a fundamental step towards a realistic study in a human-like environment, providing unprecedented insight into cell-matrix interaction and paving the way for innovative applications in other areas of life sciences. Although several scaffolds for bone proliferation had already been studied, both artificial and derived from human bone, there had not yet been extensive studies on human-like scaffolds of natural origin.

4.2. Bone Anatomy and Physiology

The bones of the skeleton provide structural support for the rest of the body, movements of its parts through muscles and joints, and protection. They provide its biochemical balance, hormonal reserve, and environment for bone marrow function.

Bone is composed of about 30% of flexible organic matrix, collagen fibrils, which provides for elasticity and flexibility, and 70% of calcium phosphate, hydroxyapatite (HA), which provides mechanical rigidity and load bearing.

The bone structure is composed of dense and solid cortical bone surrounding the cancellous or spongy bone, a honeycomb-like network of trabecular plates and rods interspersed in the bone marrow compartment. Cortical bone and spongy bone are normally formed in a lamellar pattern, in which collagen fibrils are laid down in alternating orientations, like plywood, giving a significant strength to the structure, Figure 4.2.1. Periosteum is a fibrous connective tissue sheath that surrounds the outer cortical surface of bone.

The cortical bone is composed of osteons or Haversian systems which form a branched network within it, their walls are formed by concentric lamellae which give the osteons their typical cylindrical shape [71].

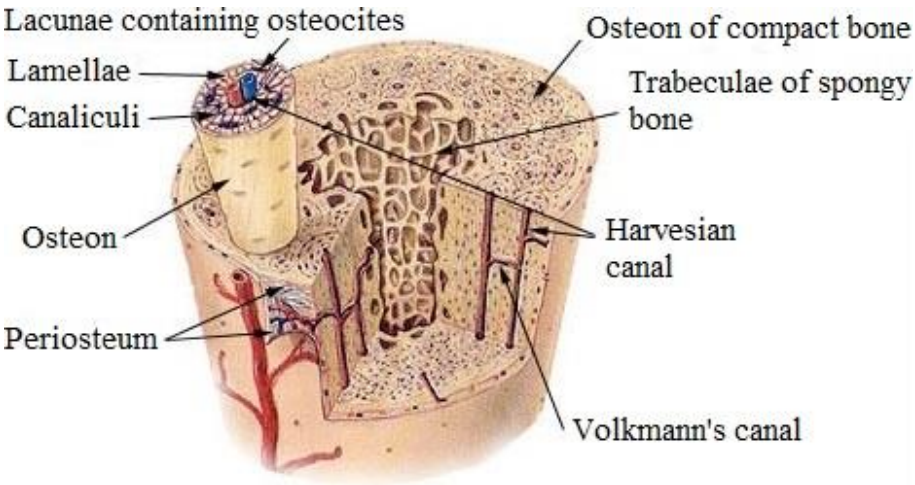

Fig. 4.2.1. *Section of a typical long bone showing both compact (cortical) and cancellous (spongy) bone* [72].

4.2.1. Blood and Interstitial Flow

There are two main types of fluid in bone tissue, blood and interstitial fluid, Figure 4.2.2. The chemical composition of these fluids varies with time and location in bone. Blood arrives through the arterial system containing oxygen and other nutrients and the blood components depart via the venous system containing less oxygen and reduced nutrition.

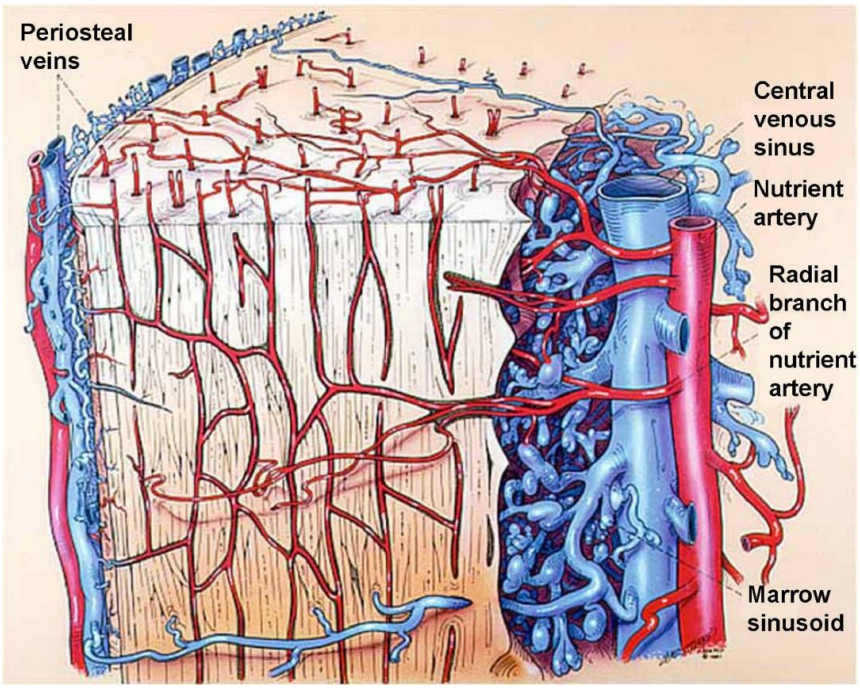

Fig. 4.2.2. *The capillary network within the cortical bone* [72]. *The major arterial supply to the diaphysis is from the nutrient artery. There is an abundant capillary bed throughout the bone tissue that drains outwards to the periosteal veins.*

Within the bone, as within other tissues, substances pass from the blood through the arterial walls into the interstitial fluid of the extracellular matrix (ECM). Outside the bone structure, the ECM consists of the spaces that exist between cells that cover the structure, such as osteoclasts, osteoblasts, and the bone lining cells. Within the bone structure, the ECM consists of its canaliculi and lacunae which also contain other cells, the osteocytes. The movement of the interstitial fluid carries these substances to the cells of the bone and, at the same time, carries off the waste materials from the cells. Bone tissue would not live without these fluid movements [72].

4.2.2. Bone Remodeling

Bone remodeling is an essential biological process to ensure proper bone strength and mineral homeostasis. Remodeling allows the repair of old and damaged bone and adjustment of the bone's architecture to changes in external loading, both positive and negative. There is usually an increase in chest bone structure in swimmers or a loss of bone mass in astronauts and seniors. Where the old bone structure is no longer needed, specialized cells, called osteoclasts, remove the organic and mineral matrix, while where the structure needs to be increased, other cells, called osteoblasts, deposit new matrix. These cells work together during this ongoing process [73].

The remodeling cycle, Figure 4.2.3, is composed of four consecutive phases [71]:

- Activation: it starts with the recruitment and activation of mononuclear monocyte-macrophage osteoclast precursors from the circulation, lifting of the endosteum that contains the lining cells off the bone surface, and fusion of multiple mononuclear cells to form multinucleated preosteoclasts.
- Resorption: osteoclast precursors bind to the bone matrix to form annular sealing zones of multinucleated osteoclasts over the bone resorption compartments. The resorption phase is completed by mononuclear cells after the multinucleated osteoclasts undergo apoptosis. Osteoclast formation, activation, and resorption are regulated by the status of the osteoclast surface receptor RANK. Its activation depends on the ratio between RANKL ligand and its decoy receptor OPG, both produced by osteoclast precursors and mature osteoclasts, which regulate this ratio according to physiological influences or mechanical stress [74].
- Reversal: the resorbed surface is smoothed by mononuclear macrophage-like cells and prepared for matrix deposition.

- Formation: osteoblasts lay down new bone by secreting a collagen matrix and controlling its mineralization. Throughout this process, some osteoblasts become buried within the matrix and differentiate to osteocytes which reside in the fully mineralized lacunar-canalicular system (LCS) [75]. At the end of this phase, the osteoblasts transform into bone-lining cells or undergo apoptosis.

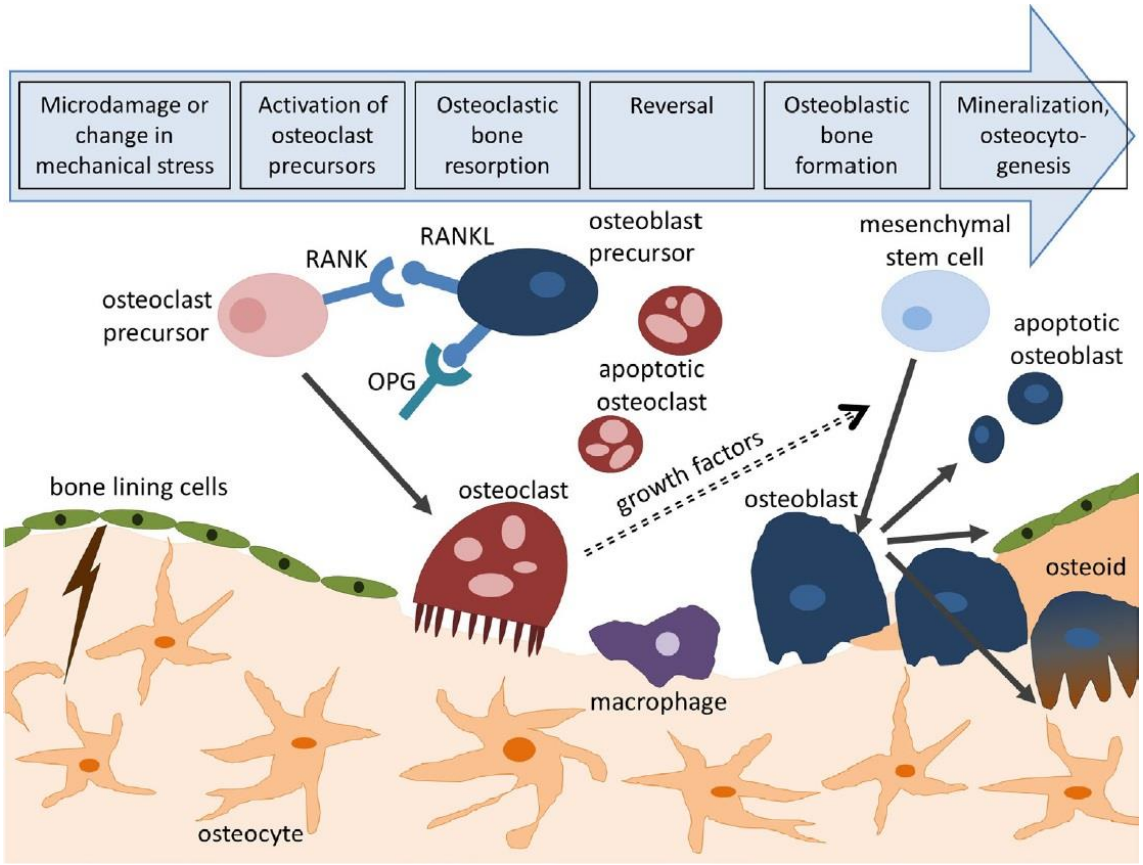

Fig. 4.2.3. *The four consecutive steps of bone remodeling cycle: activation of osteoclasts, bone resorption, reversal bone smoothing, and formation of new bone by osteoblasts* [73].

4.3. Role of Fluid Shear Stress in Bone Remodeling

As seen previously, the bone modeling mechanism is complex, the three main types of bone cells involved, osteoclasts for bone resorption, osteoblasts, and osteocytes for bone formation, work simultaneously regulating each other through biochemical signals according to the external signals they receive.

Many studies were performed on the influence of external signals on bone formation, such as the influence of fluid shear stress (FSS) of nutrients on osteoblasts. This is because FSS is greatly influenced by the pathological state of the organism and by external mechanical stresses, and because the osteoblasts, being all outside the bone surface, are exposed to a higher FSS than osteocytes that are within the bone structure [73].

Recent studies investigated the effect of newborn bovine serum (NBS) on the intracellular calcium (Ca^{2+}) response of cultured osteoblastic cell stimulated by 2D fluid flow in a parallel-plate flow chamber, which allows a constant shear stress along the rectangular cross section of the chamber perpendicular to the flow, see Section 2.3.4.2, finding a significant increase in the calcium response for a shear stress of 3.5 Pa [76], Figure 4.3.1. The importance of calcium in bone remodeling arises from its use as a component in the mineralization of protein matrix by osteoblasts to form new bone with a hydroxyapatite structure, which consists mainly of calcium [71], and as a regulatory signal proliferation, differentiation, apoptosis, and metabolism of bone cells such as osteoblasts [77], [78].

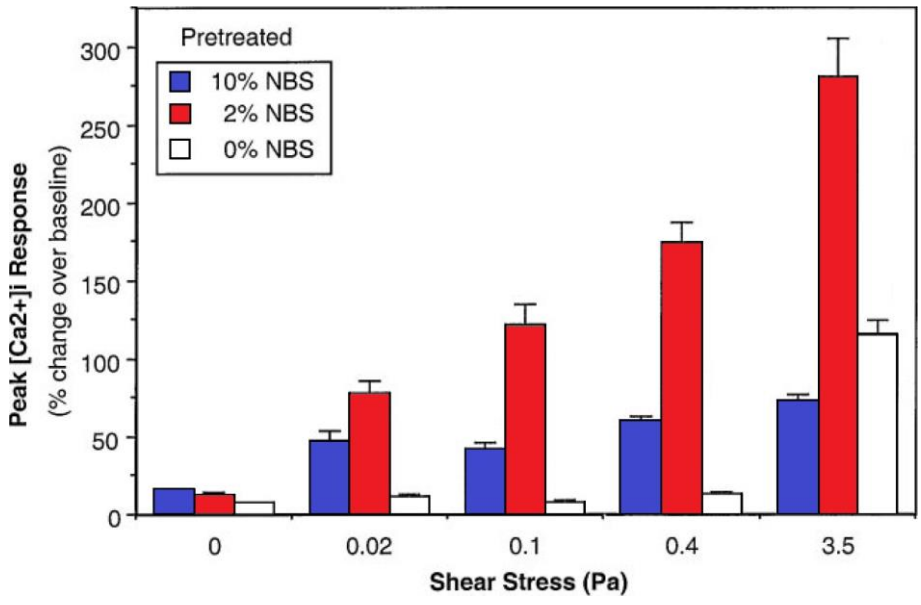

Fig. 4.3.1. *The peak calcium increase (mean + std. error)* [76]. *Applied shear stresses from 0 to 3.5 Pa. Cells preconditioned and then perfused in media with 0%, 2% or 10% serum.*

Other studies focused on the effect of low levels of shear stress, from 1 µPa to 0.4 Pa [73], on osteoblasts cultured in 2D microfluidic chambers obtained in PDMS chips [79], [38], miming slow interstitial flow by using microfluidic resistors, Figure 4.3.2. The results always expressed an increase in osteoblast activity, expressed both in terms of increased intracellular calcium and proliferation index.

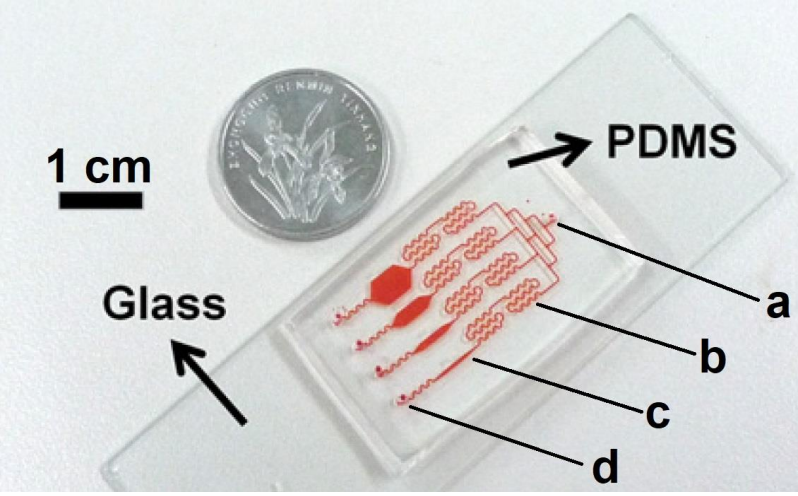

Fig. 4.3.2. *Microfluidic device for bone cell proliferation with different shear stresses* [79]. *(a) Nutrient flow inlet. (b) Microfluidic resistor. (c) Cell chamber. (d) Flow outlet.*

All these studies provided important insights into understanding the role of shear stress in bone remodeling, but their limitation was the artificial environment in which bone cells were cultured. Even using culture substrates, the environment was certainly distant from the real bone matrix, both from a biochemical and morphological point of view.

To overcome this limitation, several studies used part of human decellularized bone as scaffold for bone cell culture under the stimulus of different levels of shear stress, the scaffold was the real microfluidic circuit and was inserted into a bioreactor which fed it with the flow of nutrients [80], [81], Figure 4.3.3.

The use of 3D natural-origin scaffold for bone cell culture was a significant improvement in mimicking *in vitro* the influence of shear stress on *in vivo* bone formation. The only limitation of this method was the reduced availability of samples with similar characteristics to perform extensive tests that gave comparable results. To overcome deontological and permission problems, non-human bone parts had been used as scaffolds and thus having more availability of samples, but the problem of having bone parts without a standard morphological structure would still have remained, this leads to the indeterminacy of the shear stress to which the cells were subjected.

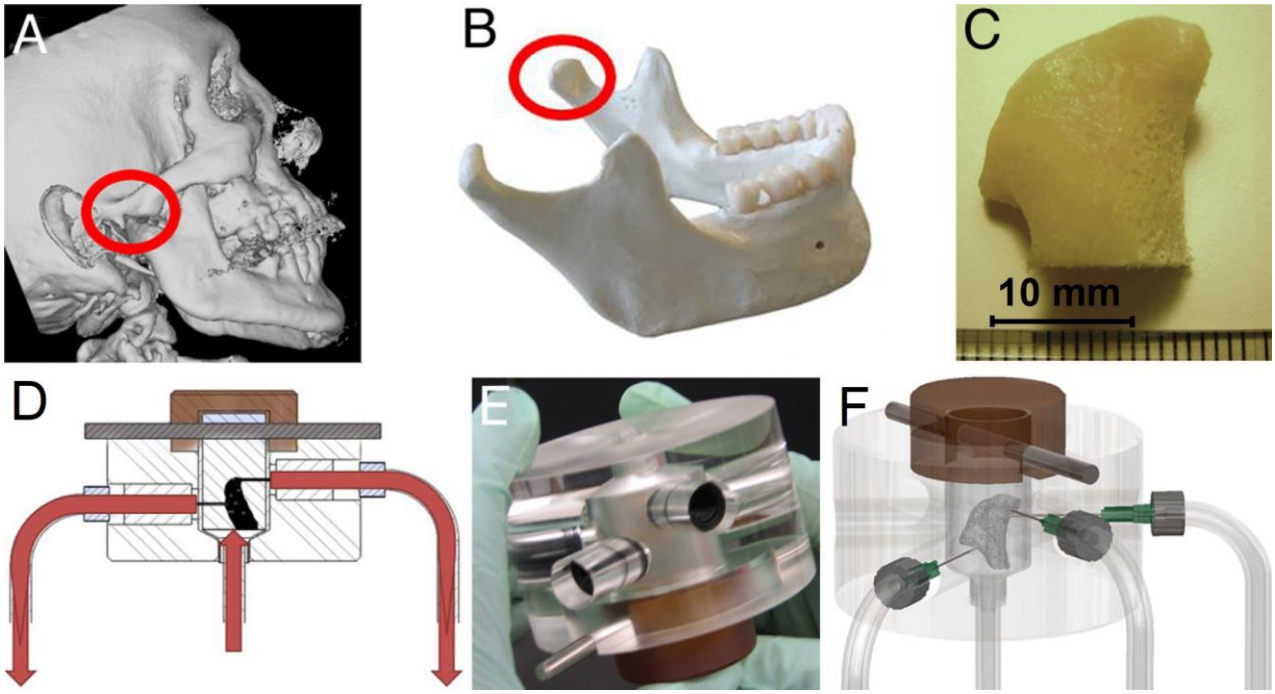

Fig. 4.3.3. *Scaffold from human decellularized bone for bone cell culture* [80]. *(A-B) CT images of human TMJ condyles. (C) Machined TMJ-shaped scaffold from decellularized trabecular bone. (D) Nutrient flow circuit of the scaffold inside the bioreactor. (E) The bioreactor body. (F) 3D CAD image of the bioreactor with the scaffold flow connections.*

As an alternative to using decellularized bone, collagen hydrogel scaffolds were created, using a 3D printer or other systems, in which the bone cells would be implanted [82], Figure 4.3.4. Subsequently the scaffolds were inserted into a microfluidic chip or in a bioreactor to study cell proliferation with different flows of nutrient liquid [83], [84].

These sponge-like scaffolds, effective under static liquid conditions in a cell-culture disc, from the point of view of biological effects in a dynamic environment, are different from a decellularized bone matrix because are unlikely to reproduce its complex geometry and consequently the flows of nutrients.

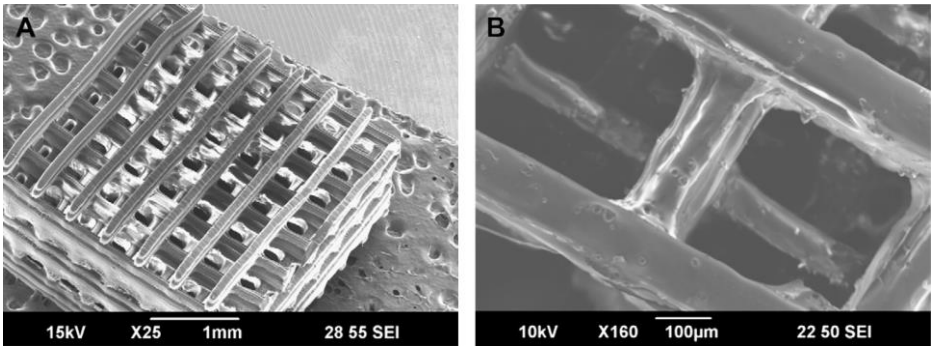

Fig. 4.3.4. *3D scaffold obtained by microstereolithography (µSLA) of PPF* [82].

4.4. 3D scaffold obtained by transformation of natural structures

Innovative 3D scaffolds have recently been developed, obtained from natural structures as plants, which overcome the problems and limitations of the previous scaffolds, an example is the b.Bone™ (GreenBone Ortho S.p.A., Faenza, Italy) [85].

The b.Bone™ is composed of hydroxyapatite [$Ca_5(PO_4)_3(OH)$] in a porous and highly interconnected 3D structure which mimics the hierarchical architecture and morphology of natural human bone [86], Figure 4.4.1.

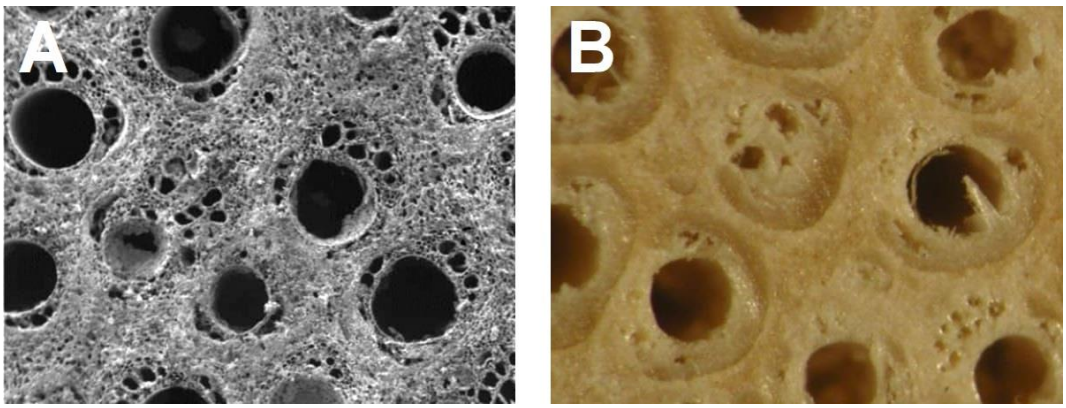

Fig. 4.4.1. *(A) b.Bone™ structure. (B) Typical human bone structure* [85].

GreenBone technology transforms a native structure, rattan wood, into inorganic biomaterial by a multi-step process, maintaining the original morphology and hierarchical architecture with pore structures on a micrometer scale [87]. Rattan, Figure 4.4.2, is a naturally renewable palm that grows in the tropical regions of Africa and Asia, and it has multiple uses, such as for furniture, handicrafts and building material.

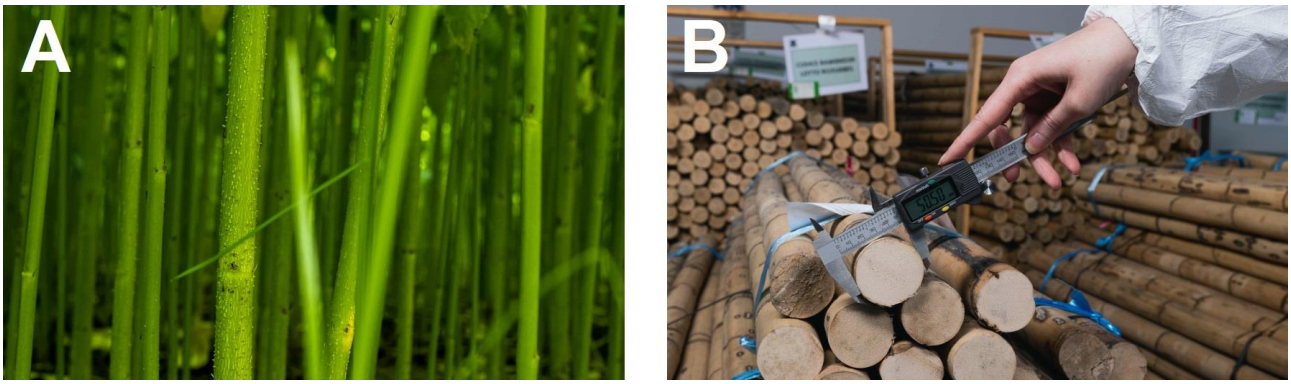

Fig. 4.4.2. *(A) Native rattan. (B) Semi-finished rattan* [85].

Rattan wood was selected as a bone model for its outstanding similarity with the structure of osteons, which constitute a main functional unit of the bone hierarchical architecture [86].

The main steps of the transformation process, from rattan to hydroxyapatite, Figure 4.4.3, are [88], [89]:

- Pyrolysis: the wood is transformed into a carbon matrix by heating in an inert atmosphere at 600-1000°C to allow the decomposition and elimination of all organic substances.
- Carburization: the carbon is transformed into calcium carbide (CaC) by infiltration of calcium vapor at 900-1200°C.
- Oxidation: the calcium carbide is transformed into calcium oxide (CaO) by heating in air at 1000-1200°C.
- Carbonation: the calcium oxide is transformed into calcium carbonate ($CaCO_3$) by heating at 750-850 °C in an CO_2 atmosphere at 4-20 MPa.
- Phosphating: the calcium carbonate is transformed into hydroxyapatite by immersion in phosphate salts at 25-300°C.

This multi-step process allows for fine chemical control of the final product and thus for enhancing and modulating the bioactivity of the final inorganic structure.

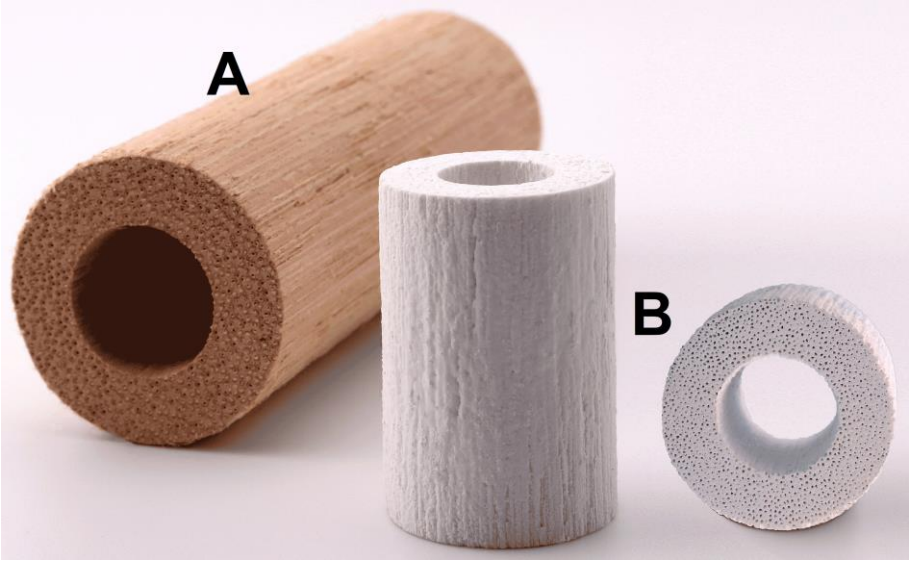

Fig. 4.4.3. *(A) Unprocessed rattan wood. (B) Post-process hydroxyapatite samples* [85].

The b.Bone™ was studied, produced, and patented as a bone graft for the treatment of voids, lacunae or defects in the bone resulting from surgical removal or traumatic injuries, particularly in the pelvis or limbs, Figure 4.4.4. It acts as a bridge for the bone defect, promoting bone remodeling and its bio-resorption. Its biocompatibility and multi-level organized structure ensure vascular remodeling, proliferation, and organization of bone cells.

It allows appropriate fluid imbibition, including bone marrow aspirate, due to its interconnected micro- and macro- porosity [90].

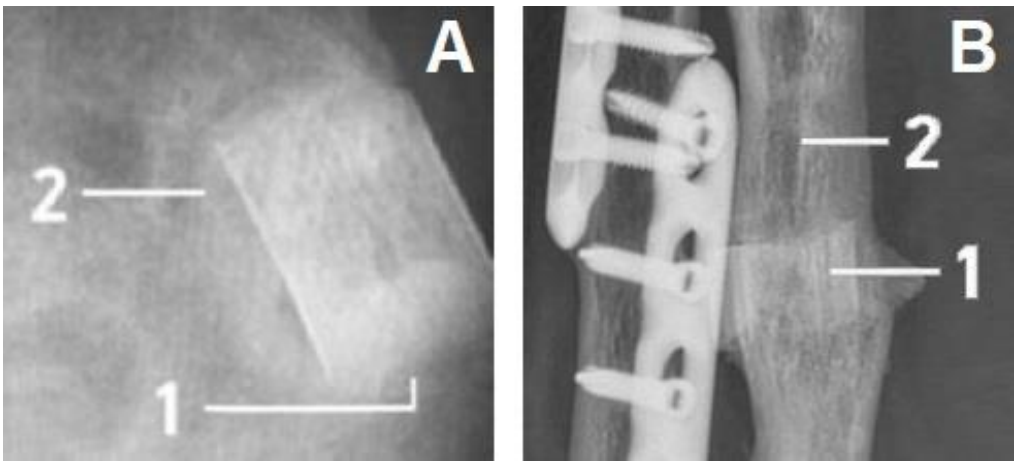

Fig. 4.4.4. *[A] Magnification at 6-month follow-up shows integration of b.Bone™ (1), with mineralization like the pelvic bone texture (2). [B] Magnification at 19-month follow-up shows integration of b.Bone™ (1) in radius reconstruction (2)* [85].

4.4.1. Scaffold morphology

Figure 4.4.5 shows the distribution of internal pore volume of the biomorphic hydroxyapatite of b.Bone™ compared with the average of internal pore volume of the hierarchically structured hydroxyapatites obtained artificially with other technologies known in the art.

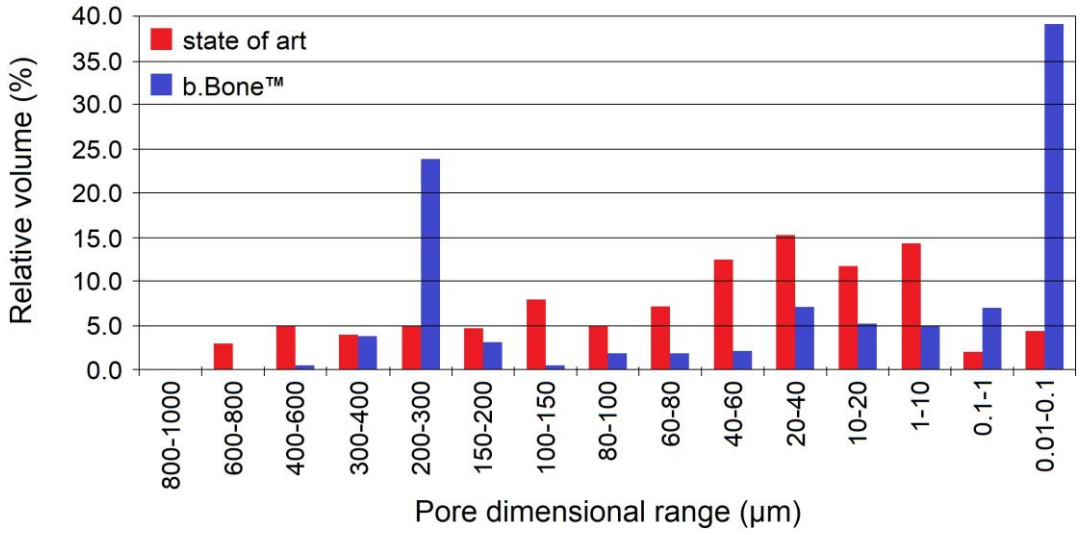

Fig. 4.4.5. *Distribution of internal pore volume of b.Bone™ compared with state of art* [89].

The distribution of pores in the b.Bone™ is concentrated in two zones, the first with diameters between 200 and 300μm, with a mean diameter D_{PO} of 250μm, the second with diameters less than 0.01 and 0.1 μm.

The pores of the first zone, mainly channel-like pores in the longitudinal direction which mimic the Haversian systems, Figure 4.4.6, permit cell colonization and proliferation and the formation of an appropriate vascularization tree. They are the object of the research.

The micro-pores of the second zone, that partially interconnect the channel-like pores, permit exchange of nutrient fluids and discharge of the waste products of cell metabolism [89].

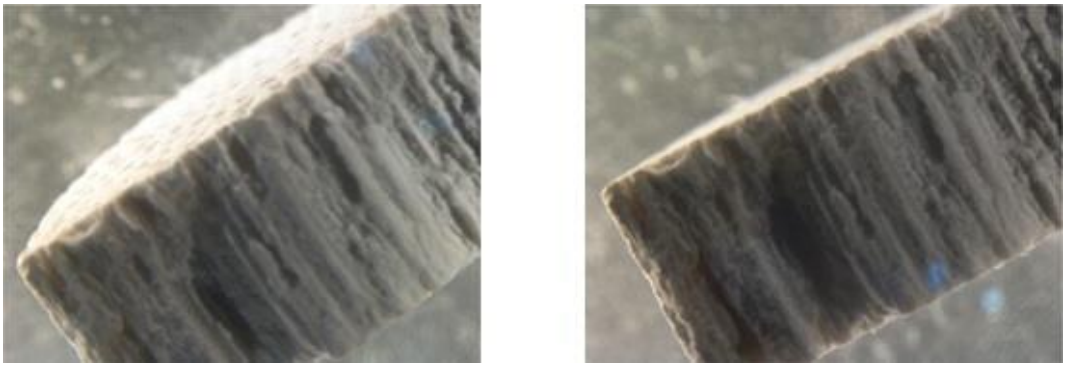

Fig. 4.4.6. *Axial sections of cylindrical b.Bone™ samples showing the longitudinal direction of the channel-like pores* [89].

Figure 4.4.7 shows the SEM image of calcium carbide structure of b.Bone™ after pyrolysis, the red square with a side of 1 mm shows the density of the channel-like pores *PD* which, with a graphic calculation of areas, gives an approximate value of 3.5 pores/mm².

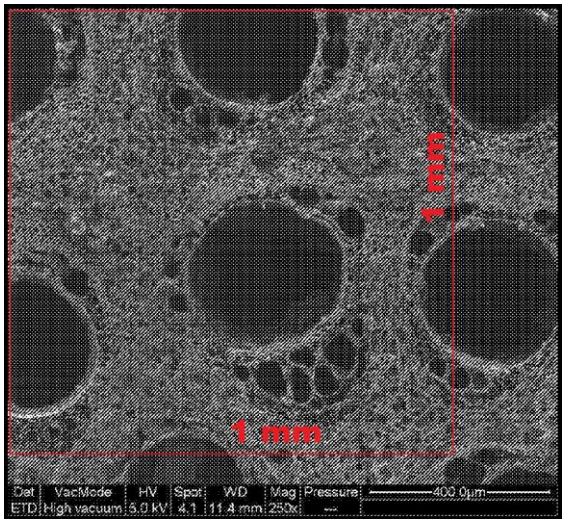

Fig. 4.4.7. *Channel-like pore density of b.Bone™ (redraw from* [89]*)*

4.5. Theoretical characterization of the scaffold

In the scientific literature there are many studies on bone cell proliferation induced by the shear stress of the flow of biological fluids, in most of them the experiments were performed in devices made up of two parallel plates between which the cells are inserted and then flowed.

Greater cell proliferation was found with high levels of shear stress, an example of research that used these levels is reported in Table 4.5.1.

Table 4.5.1. *Osteoblastic responses to medium and high fluid shear stress* [73].

Shear stress (Pa)	**Flow type**	**Flow time**	**References**
0.6	s	12 h	Johnson et al. (1996)
0.1-2.4	s, p	30 min	Reich and Frangos (1991)
0.7	p	1 h	Klein-Nulend et al. (1997)
0.4-1.2	p	15 min	Bakker et al. (2001)
2	o	2 h	You et al. (2001a)
1.2	s	1 h	Pavalko et al. (1998)
1.2	s	5 min	Genetos et al. (2004)
1	p	12 h	Myers et al. (2007)

Note: *Fluid shear stress (s, steady; p, pulsatile; o, oscillatory) is applied to monolayer cell cultures in a parallel-plate flow chamber (PPFC).*

For this reason, the present research used shear stress levels in the range of Table 4.5.1 for the theoretical characterization of a virtual sample useful for initial fluid dynamic indications.

Even at low levels of shear stress some research has found an increase in cell proliferation, in Table 4.5.2 an example from scientific literature.

Table 4.5.2. *Osteoblastic responses to low fluid shear stress* [73].

Shear stress (Pa)	**Flow type**	**Flow time**	**References**
$1\text{-}63 \cdot 10^{-6}$	o	10-96 h	Liegibel et al. (2004)
0.03-0.3	s	2 min	Kou et al. (2011)
0.5	s	24 h	Xing et al. (2014)
$1.5\text{-}412 \cdot 10^{-6}$	s	24 h	Yu et al. (2014)

Note: *Fluid shear stress (s, steady; p, pulsatile; o, oscillatory) is applied to monolayer cell cultures in a parallel-plate flow chamber (PPFC).*

4.5.1. Dimensions of the scaffold

The GreenBone company made available for this research scaffold samples in the form of a full cylinder with a diameter D_{SC} of 10 mm and a height H_{SC} of 4 mm, the fluid dynamic calculations were based on these nominal dimensions.

4.5.2. Test fluids

Water at 20°C, at 37°C, and Dulbecco's Modified Eagle's Medium (DMEM) + 10% Fetal Bovine Serum (FBS) at 37°C, a widely used cell culture medium with known physical characteristics [91], were chosen for the characterization tests. All fluids are considered Newtonian, in Table 4.5.1 their physical characteristics.

Table 4.5.1. *Physical characteristics of the test fluids* [91].

	Density ρ	Dynamic viscosity μ
	kg/m^3	10^{-3} Pa·s
Water at 20°C	998.2	1.003
Water at 37°C	993.3	0.691
DMEM + 10% FBS at 37°C	1009.3	0.930

4.5.3. Formulas for the theoretical characterization

The aim of the characterization of the scaffold is to obtain, in function of different fluid shear stress, the mean velocity in the channel-like pores, the total rate of the flow passing through the scaffold via the pores, the pressure drop between the two faces of the scaffold, and the total fluid dynamic resistance of the scaffold.

To have a simplified calculation, it was assumed that the channel-like pores were cylindrical, i.e., with constant circular section and longitudinal axe from one face of the scaffold to the other, and that all the flow passed through them, neglecting the interconnecting micro-pores due to their small diameter, as reported in the Section 4.4.1.

Furthermore, it was assumed that the channel-like pores had a density *PD* of 3.5 pores/ mm^2, as in Figure 4.4.7, and were all of the same diameter D_{PO} equal to 250µm, average of the largest group of pores highlighted in Figure 4.4.5.

Thus, rearranging Equation (2.3.46), we obtain the mean constant fluid velocity u_{mean} in a channel-like pore:

$$u_{mean} = -\frac{R_{PO} \cdot \tau_{wall}}{4\mu} \tag{4.5.1}$$

where $R_{PO} = D_{PO}/2$ is the pore radius, τ_{wall} is the fluid shear stress *FSS* on the cylindrical wall of the pore, and μ is the dynamic viscosity of the fluid under test.

We obtain the Reynolds number *Re* of the flow in a channel-like pore from Equation (2.2.4):

$$Re = \frac{\rho u L}{\mu} = \frac{\rho\, u_{mean}\, D_{PO}}{\mu} \tag{4.5.2}$$

The number of channel-like pores N_{PO} in the scaffold is:

$$N_{PO} = \pi\, {R_{SC}}^2 PD = \frac{\pi}{4}\, {D_{SC}}^2 PD \tag{4.5.3}$$

where R_{SC} is the scaffold radius, and *PD* is the density of the pores.

The total rate Q_{TOT} of the flow passing through the scaffold via the pores is:

$$Q_{TOT} = \pi\, {R_{PO}}^2 \cdot N_{PO} \cdot u_{mean} \tag{4.5.4}$$

Rearranging Equation (2.3.29), we obtain the pressure drop Δp between the ends of a channel-like pore:

$$\Delta p = \frac{8\mu\, L_{PO}}{{R_{PO}}^2}\ u_{mean} \tag{4.5.5}$$

where $L_{PO} = H_{SC} = \Delta L$ is the length of the pore.

Substituting Equation (4.5.1) in Equation (4.5.5), we obtain:

$$\Delta p = -\frac{8\mu\, L_{PO}}{{R_{PO}}^2}\,\frac{R_{PO}\cdot\tau_{wall}}{4\mu} = -\frac{2L_{PO}\cdot\tau_{wall}}{R_{PO}} \tag{4.5.6}$$

Considering the assumptions of the Section 2.3.6 and assuming the scaffold as a porous medium, we can obtain the fluid dynamic resistance of the scaffold Rf_{SC} rearranging the Darcy's law, Equation (2.3.56):

$$Rf_{SC} = \frac{\Delta p}{Q_{TOT}} \tag{4.5.7}$$

Substituting Equation (4.5.5) and Equation (4.5.4) in Equation (4.5.7), finally we obtain:

$$Rf_{SC} = \frac{8\mu\, L_{PO}}{{R_{PO}}^2}\;u_{mean}\;\frac{1}{\pi\,{R_{PO}}^2\cdot N_{PO}\cdot u_{mean}} = \frac{8\mu\, L_{PO}}{\pi\,{R_{PO}}^4\cdot N_{PO}} \tag{4.5.8}$$

4.5.4. Theoretical characterization calculations

By substituting the data from Section 4.5.1 and Section 4.5.2 into the formulas of Section 4.5.3, we obtain the scaffold characterization for different values of shear stress and fluid type, using a spreadsheet, Figure 4.5.4 for water at 20°C, Figure 4.5.5 for water at 37°C, and Figure 4.5.6 for DMEM + 10% FBS.

Density of water @ 20°C	ρ	**998.2**	kg/m³		
Dynamic viscosity of water @ 20°C	μ	**1.0E-03**	Pa*s		
Scaffold diameter	D_{SC}	**10**	mm		
Scaffold base area	A_{SC}	79	mm²		
Scaffold heigth	H_{SC}	**4**	mm		
Channel-like pore length	L_{PO}	4.0E-03	m		
Channel-like pore diameter	D_{PO}	**250**	μm		
Channel-like pore radius	R_{PO}	1.25E-04	m		
Channel-like pore density	PD	**3.5**	1/mm²		
Number of pores	N_{PO}	275			
Fluid Shear Stress	u_{mean}	Re	Q_{TOT}	Δp	Rf_{SC}
Pa	m/s		m³/s	Pa	Pa*s/m³
0.5	1.6E-02	3.9	2.1E-07	32	1.5E+08
1.0	3.1E-02	7.8	4.2E-07	64	1.5E+08
1.5	4.7E-02	11.6	6.3E-07	96	1.5E+08
2.0	6.2E-02	15.5	8.4E-07	128	1.5E+08
2.5	7.8E-02	19.4	1.1E-06	160	1.5E+08
3.0	9.3E-02	23.3	1.3E-06	192	1.5E+08
3.5	1.1E-01	27.1	1.5E-06	224	1.5E+08
4.0	1.2E-01	31.0	1.7E-06	256	1.5E+08

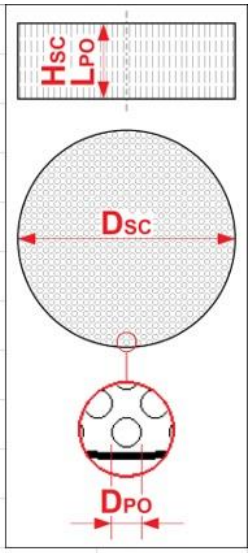

Fig. 4.5.1. *Fluid dynamic characterization of the scaffold with water @20°C.*

Note: *Red numbers are entered data, black numbers are calculated values.*

As we can see in Figure 4.5.1, the Reynolds numbers *Re* are very low, much lower than the critical number of turbulent transition Re_{cr}=2000÷3000, therefore the flow of the fluid in the scaffold channel-like pores is certainly always laminar.

The pressure drops *Δp* required to obtain the various levels of shear stress *FSS* are also very low, hydrostatic heads of a few millimeters are sufficient to generate them.

The fluid dynamic resistance of the scaffold Rf_{SC} is the same for all the levels of shear stress *FSS*. Obviously, because Rf_{SC} does not depend on the velocity of the flow passing via the channel-like pores, Equation (4.5.8).

Density of water @ 37°C	ρ	**993.3**	kg/m³	
Dynamic viscosity of water @ 37°C	μ	**6.9E-04**	Pa*s	
Scaffold diameter	DSC	**10**	mm	
Scaffold base area	ASC	79	mm²	
Scaffold heigth	HSC	**4**	mm	
Channel-like pore length	LPO	4.0E-03	m	
Channel-like pore diameter	DPO	**250**	μm	
Channel-like pore radius	RPO	1.25E-04	m	
Channel-like pore density	PD	**3.5**	1/mm²	
Number of pores	NPO	275		

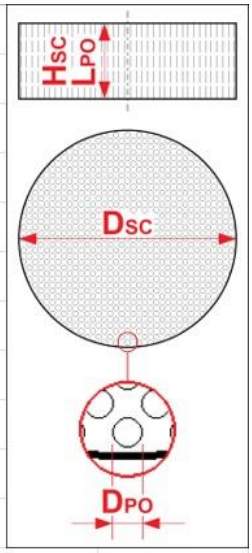

Fluid Shear Stress	umean	Re	QTOT	Δp	RfSC
Pa	m/s		m³/s	Pa	Pa*s/m³
0.5	2.3E-02	8.1	3.0E-07	32	1.0E+08
1.0	4.5E-02	16.2	6.1E-07	64	1.0E+08
1.5	6.8E-02	24.4	9.1E-07	96	1.0E+08
2.0	9.0E-02	32.5	1.2E-06	128	1.0E+08
2.5	1.1E-01	40.6	1.5E-06	160	1.0E+08
3.0	1.4E-01	48.7	1.8E-06	192	1.0E+08
3.5	1.6E-01	56.8	2.1E-06	224	1.0E+08
4.0	1.8E-01	65.0	2.4E-06	256	1.0E+08

Fig. 4.5.2. *Fluid dynamic characterization of the scaffold with water @37°C.*
Note: *Red numbers are entered data, black numbers are calculated values.*

All the considerations made for Figure 4.5.1 also apply to Figure 4.5.2 even if the physical characteristics of the fluid have changed. The density ρ of the two fluids is approximately the same, while the dynamic viscosity μ is appreciably reduced by the increase in temperature. This resulted in an increase in mean velocities u_{mean}, Reynolds numbers *Re*, total flow rate Q_{TOT}, and a decrease in the total fluid dynamic resistance of the scaffold Rf_{SC}.
The pressure drops Δp have not changed because they do not depend on dynamic viscosity μ, but only on the physical dimensions of the channel-like pore and the shear stress *FSS*, Equation (4.5.6).

Density of DMEM @ 37°C	ρ	1009.3	kg/m³	
Dynamic viscosity of DMEM @ 37°C	μ	9.3E-04	Pa*s	
Scaffold diameter	D_{SC}	10	mm	
Scaffold base area	A_{SC}	79	mm²	
Scaffold heigth	H_{SC}	4	mm	
Channel-like pore length	L_{PO}	4.0E-03	m	
Channel-like pore diameter	D_{PO}	250	μm	
Channel-like pore radius	R_{PO}	1.25E-04	m	
Channel-like pore density	PD	3.5	1/mm²	
Number of pores	N_{PO}	275		

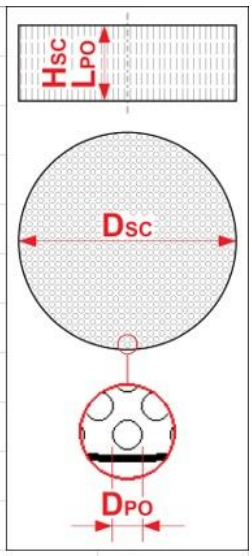

Fluid Shear Stress	u_{mean}	Re	Q_{TOT}	Δp	Rf_{SC}
Pa	m/s		m³/s	Pa	Pa*s/m³
0.5	1.7E-02	4.6	2.3E-07	32	1.4E+08
1.0	3.4E-02	9.1	4.5E-07	64	1.4E+08
1.5	5.0E-02	13.7	6.8E-07	96	1.4E+08
2.0	6.7E-02	18.2	9.1E-07	128	1.4E+08
2.5	8.4E-02	22.8	1.1E-06	160	1.4E+08
3.0	1.0E-01	27.4	1.4E-06	192	1.4E+08
3.5	1.2E-01	31.9	1.6E-06	224	1.4E+08
4.0	1.3E-01	36.5	1.8E-06	256	1.4E+08

Fig. 4.5.3. *Fluid dynamic characterization of the scaffold with DMEM + 10% FBS @37°C.*
Note: *Red numbers are entered data, black numbers are calculated values.*

All the considerations made for Figure 4.5.2 also apply to Figure 4.5.3. The density ρ of the two fluids is approximately the same, while the dynamic viscosity μ of DMEM is greater than that of water, even if the test temperatures are the same.
This resulted in a decrease in mean velocities u_{mean}, Reynolds numbers Re, total flow rate Q_{TOT}, and an increase in the total fluid dynamic resistance of the scaffold Rf_{SC}.

4.6. Device for experimental characterization tests

The results of the theoretical characterization of the virtual scaffold gave the first indications on the possible fluid dynamic characteristics of the real scaffolds. A series of tests for the experimental characterization of real scaffolds was undertaken to confirm the theoretical data.

4.6.1. Design of the characterization device

The tests had to measure the quantities of fluid flowing through the scaffold over given periods of time, or to measure the time it took for a given amount of fluid to flow through the scaffold, under a measured hydrostatic head. This allowed the flow and the pressure drop between the two flat faces of the scaffold to be determined, allowing the fluid dynamic resistance of the scaffold to be calculated.

The simplest device to achieve this goal was to design an upper reservoir which, through the scaffold, made its fluid flow into a lower reservoir. The upper reservoir had a vertical ruler through which the fluid level above the scaffold could be read. Choosing a constant step on the ruler, the time the fluid level reached at each step was to be measured. Each step made it possible to simultaneously know the quantity of fluid flowing and the hydrostatic head.

The features, that the device had to have, were:

- Upper reservoir completely open at the top.
- Housing of the scaffold on the bottom of the upper reservoir by means of a gasket.
- Capacity of the upper reservoir of sufficient fluid to perform the tests.
- Capacity of the lower reservoir greater than the upper reservoir.
- Lower reservoir equipped with air vent.

A 3D CAD drawing of the device was made, according to the required features, Figure 4.6.1.

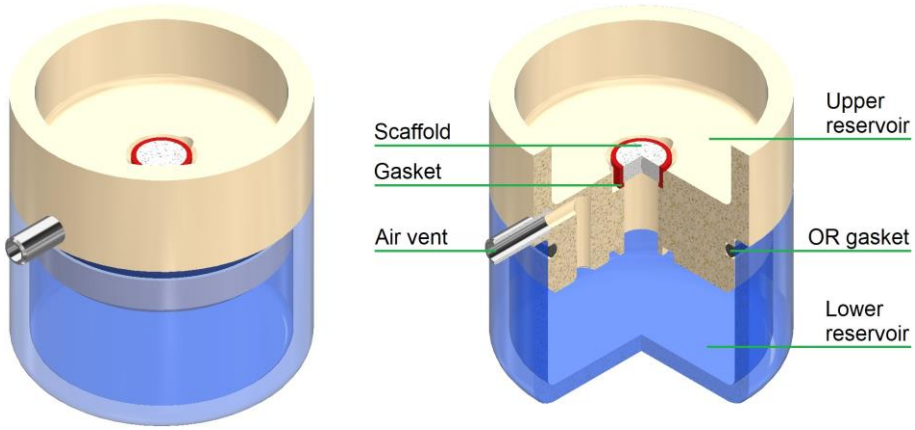

Fig. 4.6.1. *3D CAD drawing of the device for experimental characterization tests.*

4.6.2. Realization of the characterization device

The main problem in realizing the characterization device was that, while a commercial glass cup could have been used for the lower reservoir, the upper reservoir had to be made by mechanical machining of a suitable material, with the consequent costs and time needed to realize the prototype.

The characterization device of the drawing in Figure 4.6.1, was similar to a biological filter device, the 500 mL Vacuum Filter/Storage Bottle System (Corning® Inc., AZ-USA) Figure 4.6.2-A, which with a few modifications, e.g., removing the filter and adding a ruler, the filter device could be made compatible with the required features of the characterization device, Figure 4.6.2-B.

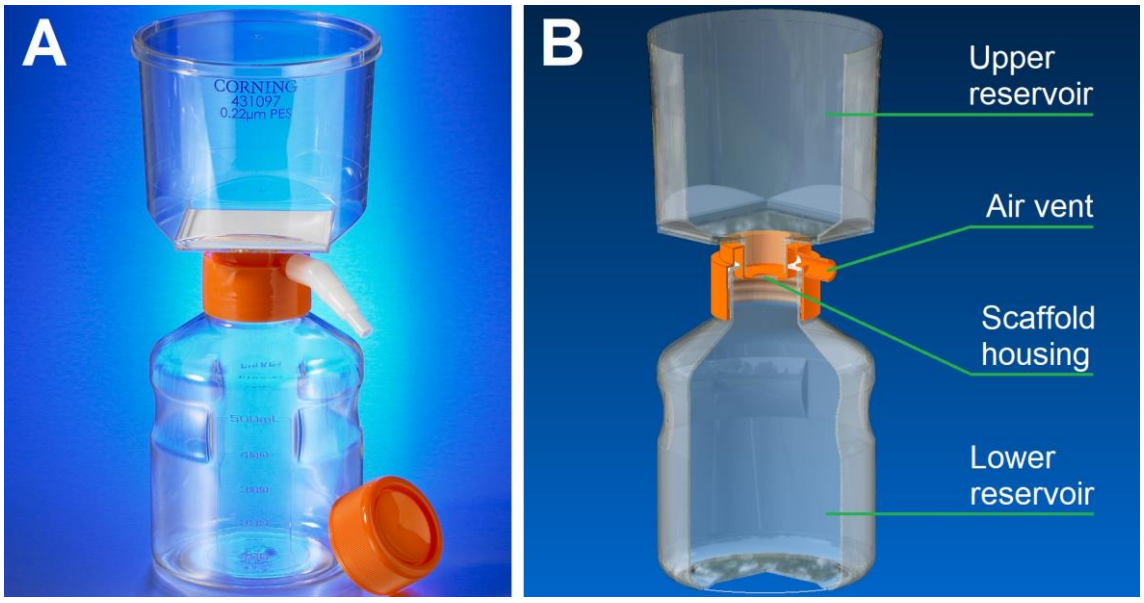

Fig. 4.6.2. *(A) Corning® 500 mL Vacuum Filter/Storage Bottle System* [92]. *(B) 3D CAD drawing of the device after filter removal.*

The upper reservoir is an inverted truncated cone with an internal top diameter D_1=100.13 mm, which decreases downwards by a coefficient α=0.1014, the ratio between the reduction in diameter and depth.

The lower face of the scaffold is positioned at a depth h_0=106.8 mm from the upper surface of the reservoir, at the level of the narrowing of the scaffold housing. At this depth, the upper reservoir has an inner theoretical diameter D_0=89.30 mm (beyond h_M=73 mm in depth the upper reservoir is no longer a truncated cone), Figure 4.6.3.

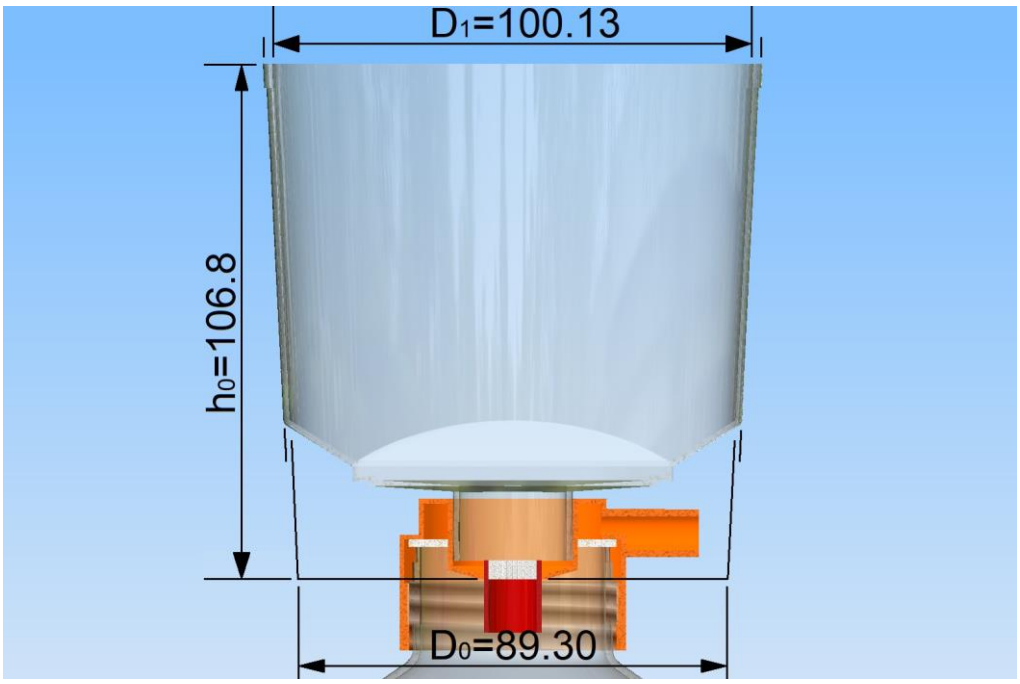

Fig. 4.6.3. *Characteristic dimensions [mm] of the upper reservoir.*

Figure 4.6.4 shows the scaffold and gasket before and after assembly in their housing.

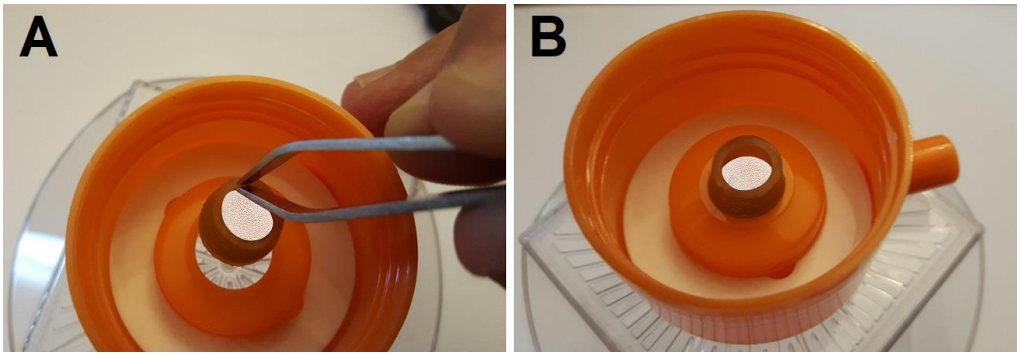

Fig. 4.6.4. *(A)The scaffold and gasket before assembly in their housing.*
(B) The scaffold and gasket assembled in their housing.

The scaffold gasket was made by cutting a 15 mm length of Do 12 mm/Di 10 mm silicone hose (Incofar S.r.l., Modena, Italy).

4.7. Experimental characterization of the scaffold

After the realization of the characterization device, it was possible to undertake experimental characterization tests on a large batch of scaffolds to have statistical significance, given their intrinsic morphological differences, with the different fluid of Table 4.5.1.

4.7.1. Formulas for the calculation of the experimental tests

During the scaffold characterization test, the upper reservoir empties into the lower reservoir through the scaffold, the fluid level in the upper reservoir, the hydrostatic head on the scaffold, and fluid flow rate decrease.

Since the flow inside the channel-like pores is perfectly laminar, as a first approximation we consider the flow fully developed inside the pores of the scaffold, neglecting the small entry region of the pores. With this assumption, considering the scaffold as a porous medium, we can use the Darcy's law [39], Equation (2.3.56), and rearranging it we obtain:

$$\Delta p = Rf_{SC} * Q_{TOT} = Rf_{SC} \frac{\partial V}{\partial t} \tag{4.7.1}$$

where ∂V is the infinitesimal volume of fluid passing through the scaffold in the infinitesimal time ∂t. We can write the pressure drop Δp as hydrostatic head on the scaffold:

$$\Delta p = \rho g h \tag{4.7.2}$$

where h is a generic height of the fluid level with respect to the lower face of the scaffold. All the potential energy of the column of fluid of height h is dissipated by the fluid dynamic resistance of the scaffold, as we can see from Equation (2.3.10), considering above and below the column the relative pressure and the velocity of the fluid equal to zero.

Considering that the upper reservoir is an inverted truncated cone, its internal diameter D_h at height h is equal to:

$$D_h = D_0 + \alpha h \tag{4.7.3}$$

with the meaning of D_0 and α given in Section 4.6.2.

Thus, we can write the infinitesimal volume of fluid ∂V as:

$$\partial V = -\frac{\pi}{4} {D_h}^2 \partial h = -\frac{\pi}{4} (D_0 + \alpha h)^2 \partial h \tag{4.7.4}$$

where ∂h is the infinitesimal drop of the fluid level in the infinitesimal time ∂t, i.e., the infinitesimal height of cylinder of volume ∂V and diameter D_h. The minus sign in the second term of the equation because for a negative ∂h, decrease in height h of the fluid level, a positive volume ∂V of fluid leaving the upper reservoir must correspond.

Substituting Equation (4.7.2) and Equation (4.7.4) in Equation (4.7.1), and rearranging, finally we obtain:

$$-Rf_{SC} \frac{\pi}{4\rho g} (D_0 + \alpha h)^2 \frac{\partial h}{h} = \partial t \tag{4.7.5}$$

By integrating the Equation (4.7.5) between the generic heights h_1 and h_2 of the fluid level, with h_1 greater than h_2, which are reached in the generic instants t_1 and t_2, with t_1 preceding t_2, we obtain:

$$-Rf_{SC} \frac{\pi}{4\rho g} \int_{h_1}^{h_2} \frac{(D_0 + \alpha h)^2}{h} \partial h = \int_{t_1}^{t_2} \partial t \tag{4.7.6}$$

Solving the integrals of the Equation (4.7.6), and rearranging, finally we obtain the fluid dynamic resistance of the scaffold Rf_{SC} as function of the generic heights h_1 and h_2 of the fluid level, and the corresponding generic instants t_1 and t_2:

$$Rf_{SC} = \frac{4\rho g}{\pi} \frac{t_2 - t_1}{\left[\frac{\alpha^2}{2}\left({h_1}^2 - {h_2}^2\right) + 2\alpha D_0 (h_1 - h_2) + {D_0}^2 \ln\left(\frac{h_1}{h_2}\right)\right]} \tag{4.7.7}$$

4.7.2. Test scaffolds

The tests were performed on cylinder-like scaffolds of hydroxyapatite, named B-HA and numbered from 1 to 17. In Table 4.7.1 the diameter D_{SC} and the height H_{SC} of the scaffolds.

Table 4.7.1. *Summary of the dimensions of test scaffolds (by E. Salerno).*

B-HA	D_{SC} mm	H_{SC} mm
1	10.5	3.9
2	10.9	4.1
3	10.8	4.8
4	10.4	4.3
5	10.6	3.9
6	10.7	3.8
7	10.5	3.8
8	10.6	3.7
9	10.7	3.8

B-HA	D_{SC} mm	H_{SC} mm
10	10.8	4.6
11	10.4	4.5
12	10.6	4.6
13	10.7	4.1
14	10.4	4.5
15	10.8	4.1
16	10.4	4.3
17	10.5	4.2

We noticed that the dimensions of the scaffolds were all different, their shape was not exactly a cylinder, and there were irregularities in both flat and cylindrical surfaces.

But the biggest differences are found in the structure, size, and density of the pores, even in the scaffold itself. The Figure 4.7.1 shows the SMZ800 stereo microscope (Nikon Instruments Inc., NY- USA) images of the flat faces, front and rear, of three scaffolds taken as an example.

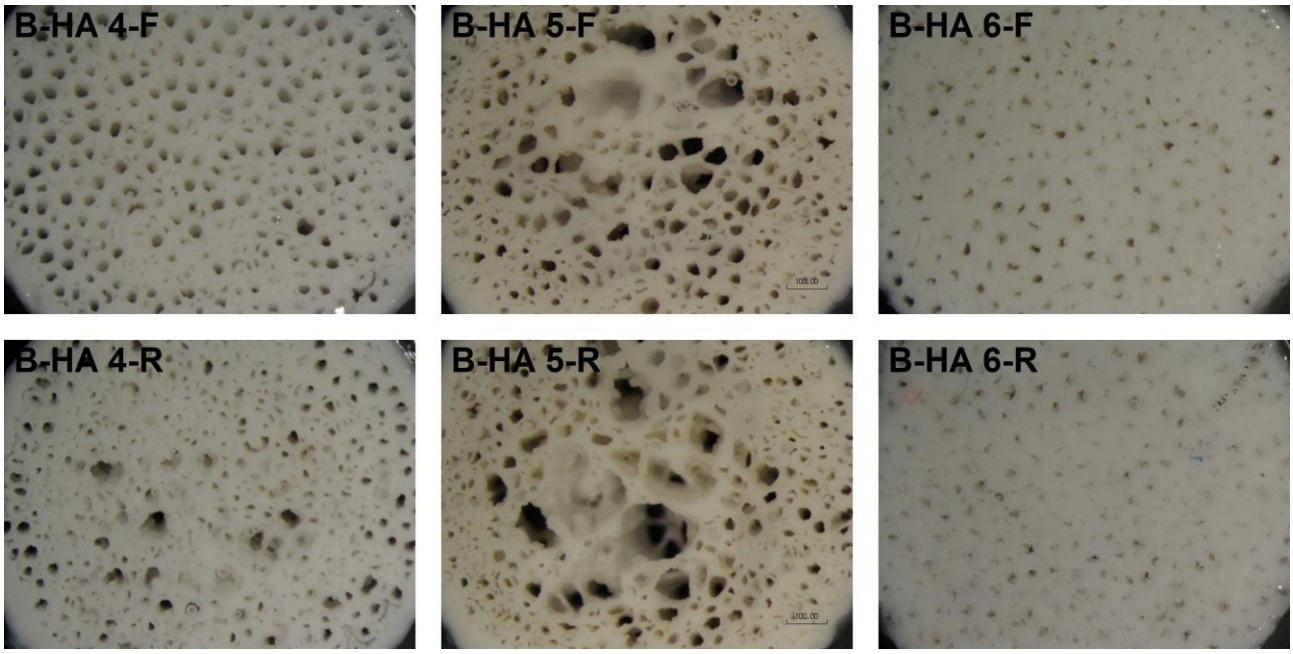

Fig. 4.7.1. *Flat faces of B-HA 4, 5, and 6 with the same magnification (by E. Salerno).*
Note: *(F) Front face. (R) Rear face.*

The dimensional and geometric differences of the scaffolds are due to the complex production process. The differences in the structure, size, and density of the pores instead are due to the natural and original morphology of the basic material, the rattan wood, which is never the same, even in the same plant.

4.7.3. Experimental characterization tests

The test procedure consisted of filling the upper reservoir of the test device above the first measurement step and filming the descent of the fluid level with a recording camera. The movie was viewed on the computer in frame-by-frame mode, recording the time of the instants of passage of the fluid level in each measurement step of the vertical ruler.

The first test was carried out with distilled water at a room temperature of 20°C on B-HA 1 and 2 scaffolds, repeating the procedure three times on each scaffold, hereinafter referred to as sub-test #1, #2, and #3. The test results are shown in Figure 4.7.2 and the screenshots of a sub-test procedure in Figure 4.7.3.

B-HA 1 + H2O @ 20°C					**#1**					**#2**				**#3**
H	h		t	$t_n - t_{n-1}$	**Rfsc**		t	$t_n - t_{n-1}$		**Rfsc**		t	$t_n - t_{n-1}$	**Rfsc**
mm	m	min.sec	s	s	Pa*s/m³	min.sec	s	s	min.sec	Pa*s/m³	min.sec	s	s	Pa*s/m³
10	0.097	0.20	20			0.23	23				0.22	22		
20	0.087	0.40	40	20	2.35E+08	0.44	44	21	2.47E+08		0.43	43	21	2.47E+08
30	0.077	1.01	61	21	2.25E+08	1.06	66	22	2.35E+08		1.06	66	23	2.46E+08
40	0.067	1.25	85	24	2.30E+08	1.31	91	25	2.40E+08		1.31	91	25	2.40E+08
50	0.057	1.51	111	26	2.19E+08	1.58	118	27	2.27E+08		1.59	119	28	2.36E+08
60	0.047	2.21	141	30	2.16E+08	2.28	148	30	2.16E+08		2.31	151	32	2.30E+08
70	0.037	2.57	177	36	2.13E+08	3.06	186	38	2.25E+08		3.09	189	38	2.25E+08
			$t_{70} - t_{10}$	**157**	2.21E+08		$t_{70} - t_{10}$	**163**	2.30E+08			$t_{70} - t_{10}$	**167**	2.35E+08
				Rfsc mean	2.29E+08	± 3%			**Rfsc mean/μ**	2.28E+11	m^{-3}			
B-HA 2 + H2O @ 20°C														
H	h	**#1**	t	$t_n - t_{n-1}$	**Rfsc**	**#2**	t	$t_n - t_{n-1}$	**Rfsc**		**#3**	t	$t_n - t_{n-1}$	**Rfsc**
mm	m	min.sec	s	s	Pa*s/m³	min.sec	s	s	Pa*s/m³		min.sec	s	s	Pa*s/m³
10	0.097	0.15	15			0.17	17				0.17	17		
20	0.087	0.28	28	13	1.53E+08	0.30	30	13	1.53E+08		0.31	31	14	1.65E+08
30	0.077	0.43	43	15	1.60E+08	0.45	45	15	1.60E+08		0.45	45	14	1.50E+08
40	0.067	0.58	58	15	1.44E+08	1.01	61	16	1.53E+08		1.01	61	16	1.53E+08
50	0.057	1.16	76	18	1.52E+08	1.19	79	18	1.52E+08		1.19	79	18	1.52E+08
60	0.047	1.35	95	19	1.37E+08	1.39	99	20	1.44E+08		1.40	100	21	1.51E+08
70	0.037	1.59	119	24	1.42E+08	2.04	124	25	1.48E+08		2.04	124	24	1.42E+08
			$t_{70} - t_{10}$	**104**	1.47E+08		$t_{70} - t_{10}$	**107**	1.51E+08			$t_{70} - t_{10}$	**107**	1.51E+08
				Rfsc mean	1.49E+08	± 1%			**Rfsc mean/μ**	1.49E+11	m^{-3}			

Fig. 4.7.2. *First test on B-HA 1 and 2 scaffolds with water at room temperature of 20°C.*
Note: *Red numbers are entered data, black numbers are calculated values.*

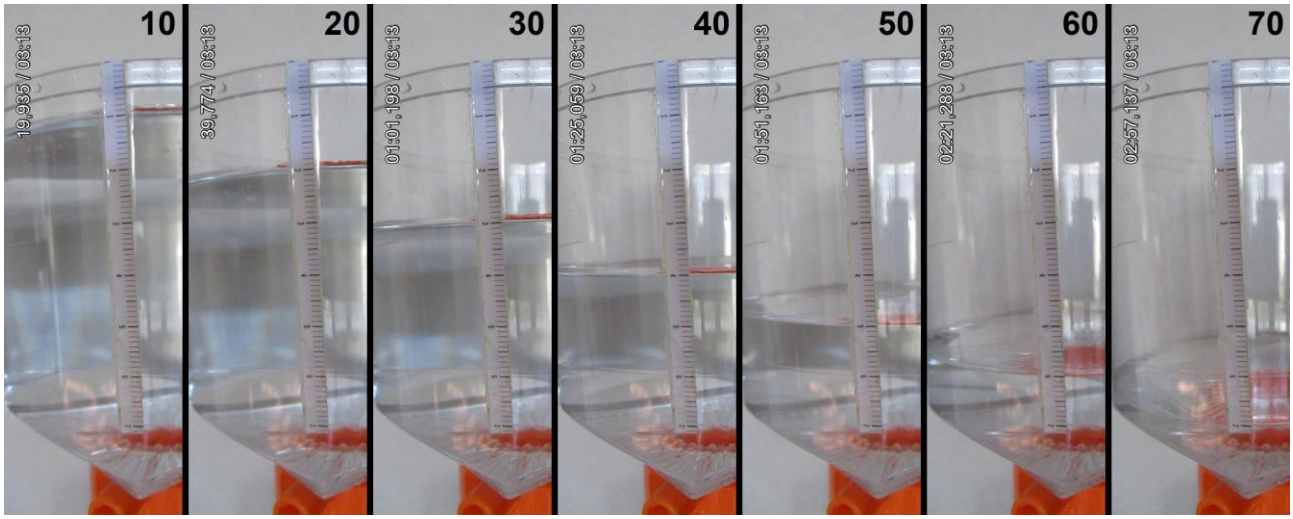

Fig. 4.7.3. *Screenshots of the fluid level at each measurement step for the sub-test #1 of the first test with water at room temperature of 20°C on B-HA 1 scaffold.*
Note: *The elapsed time at each step is shown in the upper left corner of its screenshot.*

As can be seen from Figure 4.7.2, in each sub-test the fluid dynamic resistance of the scaffold Rf_{SC} varies by a few percentage points and progressively from one measurement step to the next. These small but constant differences may be due to the simplification introduced in the physical model by the fully developed flow assumption in Section 4.7.1, but also to marginal physical phenomena such as the influence of the surface tension of the fluid droplets that form under the lower face of the scaffold.

It is important to note that, for each scaffold, the resistances calculated in each of the three sub-tests between the last 70 mm step and the first 10 mm step differ slightly, as can be seen from the little uncertainty range of the mean fluid dynamic resistance of the scaffold Rf_{SC} *mean*. This is despite the inevitable human errors in test execution, such as pinpointing exactly the position of the fluid level on the vertical ruler, or the possible small temperature variations between one sub-test and another. The test data and all these considerations suggest that the physical-mathematical model and the test procedure are correct and the results reliable.

The test data for the B-HA 1 scaffold differ not excessively but appreciably and proportionally from those for the B-HA 2 scaffold. This can only be explained by the dimensional and morphological differences between the two scaffolds, as already highlighted in Section 4.7.2, the relative influence of these physical differences in the fluid dynamic resistance of the scaffold Rf_{SC} is not altered by the nature of the fluid or by changes in the hydrostatic head on the scaffold, as can be deduced from Equation (2.3.27).

The second test was done with distilled water, the third test with 10-014 DMEM + 10% FBS (Corning, NY-USA), both in the oven at 37°C and on the same two scaffolds, B-HA 1 and 2. The sub-test procedure was repeated five times on each test. This choice was necessary for operational reasons, the operations took place inside the oven chamber and the device could not be filled to the maximum level, furthermore the limited spaces forced us to bring the camera very close to the device, reducing the view. This reduced the number of measurement points for each sub-test. To ensure an adequate number of total measurement points, it was decided to increase the number of sub-tests, from #1 to #5.

In the second and third tests it was decided to use a more temperature resistant but less performing camera with a shooting rate of one frame every two seconds. This led to a greater uncertainty in determining the exact time of passage of the fluid level on the measurement points. The measurement was improved by interpolating the times of the two frames, on the two sides of each measurement point, with their fluid levels.

The second test results are shown in Figure 4.7.4 and the screenshots of a sub-test procedure in Figure 4.7.5.

B-HA 1 + H2O@37°C				**#1**			**#2**			**#3**			**#4**			**#5**
H	h	t	$t_n - t_{n-1}$	**Rfsc**	t	$t_n - t_{n-1}$	**Rfsc**	t	$t_n - t_{n-1}$	**Rfsc**	t	$t_n - t_{n-1}$	**Rfsc**	t	$t_n - t_{n-1}$	**Rfsc**
mm	m	s	s	Pa*s/m³	s	s	Pa*s/m³	s	s	Pa*s/m³	s	s	Pa*s/m³	s	s	Pa*s/m³
20	0.087	0			0			0			0			0		
30	0.077	20	20	2.14E+08	21	21	2.25E+08	21	21	2.25E+08	22	22	2.35E+08	21	21	2.25E+08
40	0.067	42	22	2.11E+08	43	22	2.11E+08	44	23	2.20E+08	44	22	2.11E+08	43	22	2.11E+08
50	0.057	65	23	1.94E+08	69	26	2.19E+08	69	25	2.10E+08	70	26	2.19E+08	69	26	2.19E+08
60	0.047	96	31	2.23E+08	99	30	2.16E+08	98	29	2.09E+08	101	31	2.23E+08	100	31	2.23E+08
70	0.037	130	34	2.02E+08	134	35	2.08E+08	136	38	2.25E+08	137	36	2.13E+08	136	36	2.13E+08
	$t_{70} - t_{20}$	**130**	2.08E+08		**134**	2.15E+08		**136**	2.18E+08		**137**	2.19E+08		**136**	2.18E+08	
		Rfsc mean	2.16E+08	± 3%			**Rfsc mean/μ**	3.12E+11	m^{-3}							

B-HA 2 + H2O@37°C				**#1**			**#2**			**#3**			**#4**			**#5**
H	h	t	$t_n - t_{n-1}$	**Rfsc**	t	$t_n - t_{n-1}$	**Rfsc**	t	$t_n - t_{n-1}$	**Rfsc**	t	$t_n - t_{n-1}$	**Rfsc**	t	$t_n - t_{n-1}$	**Rfsc**
mm	m	s	s	Pa*s/m³	s	s	Pa*s/m³	s	s	Pa*s/m³	s	s	Pa*s/m³	s	s	Pa*s/m³
20	0.087	0			0			0			0			0		
30	0.077	13	13	1.39E+08	13	13	1.39E+08	13	13	1.39E+08	12	12	1.28E+08	14	14	1.50E+08
40	0.067	28	15	1.44E+08	27	14	1.34E+08	28	15	1.44E+08	27	15	1.44E+08	28	14	1.34E+08
50	0.057	43	15	1.26E+08	44	17	1.43E+08	44	16	1.35E+08	43	16	1.35E+08	45	17	1.43E+08
60	0.047	62	19	1.37E+08	63	19	1.37E+08	64	20	1.44E+08	63	20	1.44E+08	64	19	1.37E+08
70	0.037	84	22	1.30E+08	87	24	1.42E+08	88	24	1.42E+08	86	23	1.36E+08	87	23	1.36E+08
	$t_{70} - t_{20}$	**84**	1.35E+08		**87**	1.39E+08		**88**	1.41E+08		**86**	1.38E+08		**87**	1.39E+08	
		Rfsc mean	1.38E+08	± 2%			**Rfsc mean/μ**	2.00E+11	m^{-3}							

Fig. 4.7.4. *Second test on B-HA 1 and 2 scaffolds with water in the oven at 37°C.*

Note: *Red numbers are entered data, black numbers are calculated values*

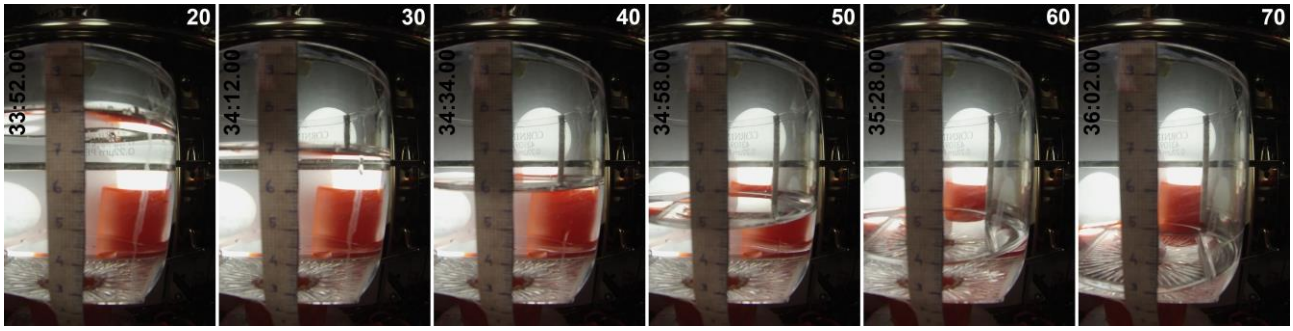

Fig. 4.7.5. *Screenshots of the fluid level at each measurement step for the sub-test #1 of the second test with water in the oven at 37°C on B-HA 1 scaffold (by E. Salerno).*

Note: *The elapsed time at each step is shown in the upper left corner of its screenshot.*

The third test results are shown in Figure 4.7.6 and the screenshots of a sub-test procedure in Figure 4.7.7.

B-HA 1 + DMEM@37°C				#1				#2				#3				#4			#5
H	h	t	$t_n - t_{n-1}$	Rfsc		t	$t_n - t_{n-1}$	Rfsc	t	$t_n - t_{n-1}$	Rfsc	t	$t_n - t_{n-1}$	Rfsc	t	$t_n - t_{n-1}$	Rfsc
mm	m	s	s	Pa*s/m³		s	s	Pa*s/m³	s	s	Pa*s/m³	s	s	Pa*s/m³	s	s	Pa*s/m³
20	0.087	0				0			0			0			0		
30	0.077	21	21	2.25E+08		19	19	2.03E+08	20	20	2.14E+08	22	22	2.35E+08	24	24	2.57E+08
40	0.067	40	19	1.82E+08		41	22	2.11E+08	42	22	2.11E+08	46	24	2.30E+08	48	24	2.30E+08
50	0.057	64	24	2.02E+08		64	23	1.94E+08	68	26	2.19E+08	72	26	2.19E+08	75	27	2.27E+08
60	0.047	93	29	2.09E+08		98	34	2.45E+08	98	30	2.16E+08	104	32	2.30E+08	110	35	2.52E+08
70	0.037	128	35	2.08E+08		137	39	2.31E+08	136	38	2.25E+08	140	36	2.13E+08	145	35	2.08E+08
		$t_{70} - t_{20}$	128	2.05E+08			137	2.19E+08		136	2.18E+08		140	2.24E+08		145	2.32E+08
		Rfsc mean		2.20E+08	± 6%				Rfsc mean/μ		3.18E+11	m^{-3}					
B-HA 2 + DMEM@37°C				#1				#2				#3				#4			#5
H	h	t	$t_n - t_{n-1}$	Rfsc		t	$t_n - t_{n-1}$	Rfsc	t	$t_n - t_{n-1}$	Rfsc	t	$t_n - t_{n-1}$	Rfsc	t	$t_n - t_{n-1}$	Rfsc
mm	m	s	s	Pa*s/m³		s	s	Pa*s/m³	s	s	Pa*s/m³	s	s	Pa*s/m³	s	s	Pa*s/m³
20	0.087	0				0			0			0			0		
30	0.077	13	13	1.39E+08		14	14	1.50E+08	13	13	1.39E+08	14	14	1.50E+08	15	15	1.60E+08
40	0.067	28	15	1.44E+08		29	15	1.44E+08	28	15	1.44E+08	28	14	1.34E+08	29	14	1.34E+08
50	0.057	42	14	1.18E+08		44	15	1.26E+08	43	15	1.26E+08	44	16	1.35E+08	45	16	1.35E+08
60	0.047	62	20	1.44E+08		64	20	1.44E+08	63	20	1.44E+08	64	20	1.44E+08	66	21	1.51E+08
70	0.037	87	25	1.48E+08		85	21	1.25E+08	90	27	1.60E+08	96	32	1.90E+08	97	31	1.84E+08
		$t_{70} - t_{20}$	87	1.39E+08			85	1.36E+08		90	1.44E+08		96	1.54E+08		97	1.55E+08
		Rfsc mean		1.46E+08	± 7%				Rfsc mean/μ		2.11E+11	m^{-3}					

Fig. 4.7.6. *Third test on B-HA 1 and 2 scaffolds with DMEM in the oven at 37°C.*

Note: *Red numbers are entered data, black numbers are calculated values.*

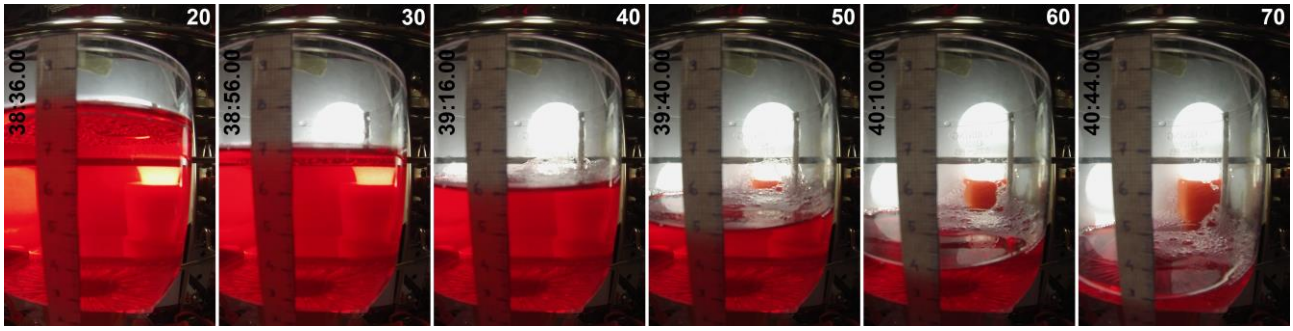

Fig. 4.7.7. *Screenshots of the fluid level at each measurement step for the sub-test #1 of the third test with DMEM in the oven at 37°C on B-HA 1 scaffold (by E. Salerno).*
Note: *The elapsed time at each step is shown in the upper left corner of its screenshot.*

In the second and third tests it is possible to notice a greater data dispersion than in the first test. This could be due to the blurry images of the movie, inconvenience caused by the short distance between the camera and the device, which made it difficult to pinpoint the exact location of the fluid level on the vertical ruler. In addition, the problem in the third test may have been amplified by DMEMS's tendency to foam on its surface. The decision to increase the total number of measurements allowed us to have a more reliable mean fluid dynamic resistance of the scaffold Rf_{SC} *mean*.

Another problem found in the tests is detected by the mean fluid dynamic resistance of the scaffold scaled by the dynamic viscosity of the fluid Rf_{SC} *mean*/μ, which does not exactly coincide in the three tests, especially between the first test and the other two, which are higher. From Equation 4.5.8, the scaled fluid dynamic resistance (SFDR) depends only on the characteristics of the scaffold and not on the temperature. A first cause may had been a short stabilization time of the fluid in the oven which did not allow the set temperature of the fluid to be reached, thus obtaining a real value of the dynamic viscosity μ higher than that assumed. This possible cause was subsequently eliminated in subsequent tests by preheating the fluid and increasing the stabilization time in the oven. A second cause may have been the increase in the mean constant fluid velocity u_{mean} in the channel-like pores due to the reduction in dynamic viscosity μ for the higher temperature of the tests. This velocity increase may had caused localized pressure drops, not foreseen by the fluidic model.

4.7.4. Experimental characterization summary

The tests were repeated on all scaffolds, carrying out two tests for each scaffold with distilled water, one at a room temperature of 20°C and one in the oven at 37°C, each test consisting of five identical sub-tests. The summary of the results of all tests are shown in Table 4.7.2, where the scaffolds SFDR *Rf/μ* were obtained from the mean of the tests of each scaffold.

Table 4.7.2. *Summary of fluid dynamic resistances of test scaffolds (by E. Salerno).*

	D_{SC}	H_{SC}	Rf/μ	$1\sigma_{Rf/\mu}$
B-HA	**mm**	**mm**	**10^{11} /m^3**	**10^{11} /m^3**
1	10.5	3.9	2.7	0.12
2	10.9	4.1	1.7	0.09
3	10.8	4.8	10.5	0.80
4	10.4	4.3	4.1	0.20
5	10.6	3.9	3.0	0.20
6	10.7	3.8	27.0	3.00
7	10.5	3.8	6.2	0.60
8	10.6	3.7	12.1	0.06
9	10.7	3.8	110.0	20.00
10	10.8	4.6	4.2	0.30
11	10.4	4.5	13.9	1.40
12	10.6	4.6	6.7	0.50
13	10.7	4.1	2.4	0.20
14	10.4	4.5	6.9	0.30
15	10.8	4.1	1.7	0.20
16	10.4	4.3	9.6	0.30
17	10.5	4.2	3.3	0.13

We can see in Table 4.7.3 the notable dispersion of the values mainly due, as previously mentioned, to the dimensional and morphological differences among the scaffolds.

In particular, for the B-HA 9 scaffold, its SFDR *Rf/μ* is more than an order of magnitude greater than average of the other scaffolds, indicating a distribution of the diameter of its pores that is significantly shifted towards minimum values, data confirmed by microscopic analysis, and in the scaffold averages its value was not counted.

4.8. Morphological and fluid dynamic characteristics of the scaffold

The notable dispersion of the values highlighted by the experimental characterization, Paragraph 4.7, prevent the use of a simple virtual sample for a correct FSS calculation, and the experimental determination of FSS in natural origin scaffolds is impossible [93].

A CFD model of a generic sample, to be characterized with a computational morphological analysis of the real sample, was validated by comparison with the fluid dynamic resistance data from experimental characterization.

This model avoids the complex testing procedure for experimental characterization and calculates the shear stress values within the sample as a function of pressure drop.

4.8.1. Morphological analysis

The stereo microscope images of both the sides of each scaffold, Section 7.2, were analyzed with the image processing software ImageJ (National Institutes of Health, MD-USA) to detect the surface profile of the pores. Figure 4.8.1 shows three scaffolds taken as an example.

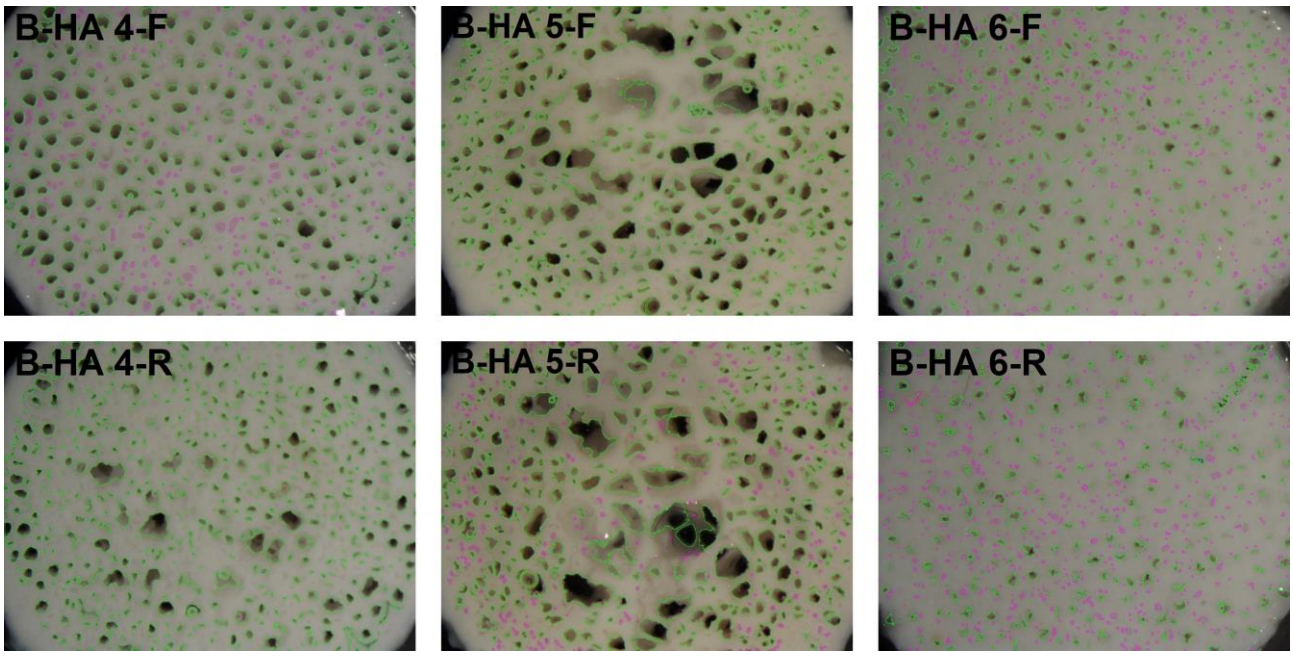

Fig. 4.8.1. *Processed images of flat faces of B-HA 4, 5, and 6 (by E. Salerno).*
Note: *(F) Front face. (R) Rear face.*

The image resolution was approximately 7 µm/pixel, and all pores with a surface profile area greater than 47 μm^2 were automatically measured and recorded by the software.

The equivalent diameter of the pore surface profiles was calculated from their area, approximating the profiles as circles.

Figure 4.8.2 shows the pore distribution, i.e. the counts of pores based on diameter classes, both on front and rear flat faces of the three scaffolds taken as an example.

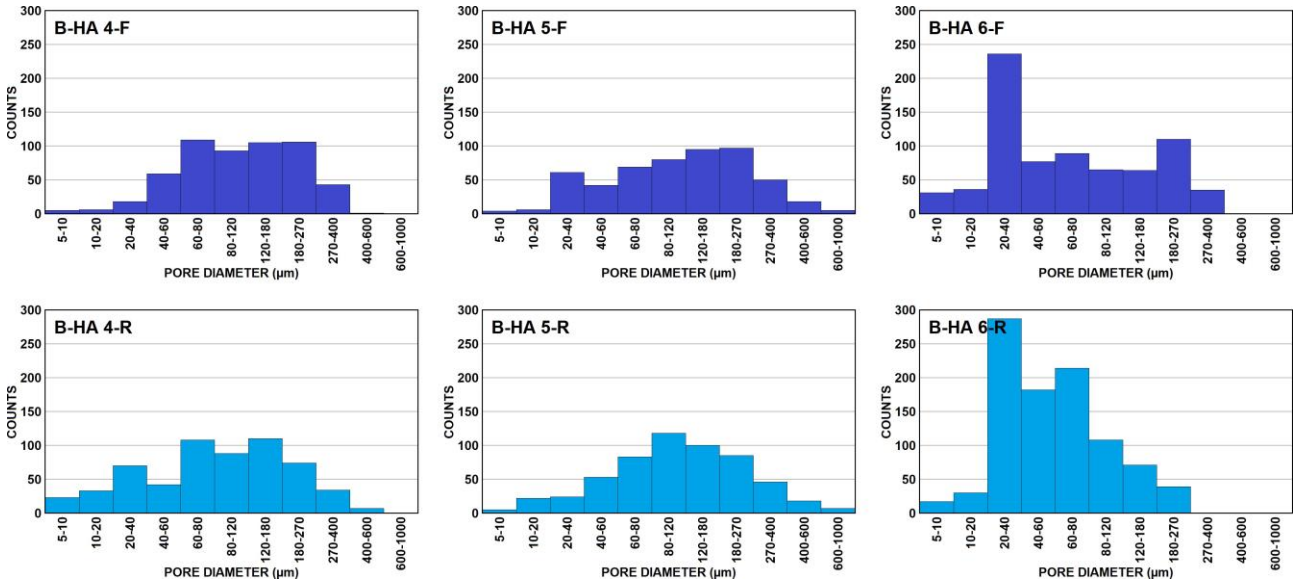

Fig. 4.8.2. *Pore distribution on flat faces of B-HA 4, 5, and 6 (redraw from E. Salerno).*
Note: *(F) Front face. (R) Rear face.*

The numerical data are reported in Table 4.8.1, where the average of the counts between the front and rear faces is also calculated.

Table 4.8.1. *Pore counts on the front and rear flat face of B-HA 4, 5, and 6 scaffolds.*

	Pore class	**1**	**2**	**3**	**4**	**5**	**6**	**7**	**8**	**9**	**10**	**11**
Diameter range	µm	**5**	**10**	**20**	**40**	**60**	**80**	**120**	**180**	**270**	**400**	**600**
	µm	**10**	**20**	**40**	**60**	**80**	**120**	**180**	**270**	**400**	**600**	**1000**
B-HA4	Front	5	6	18	59	109	93	105	106	43	1	0
	Rear	23	33	70	42	108	88	110	74	34	7	0
	Average	**14**	**20**	**44**	**51**	**109**	**91**	**108**	**90**	**39**	**4**	**0**
B-HA5	Front	4	6	61	42	69	80	95	97	50	18	5
	Rear	5	22	24	53	83	118	100	85	46	18	7
	Average	**5**	**14**	**43**	**48**	**76**	**99**	**98**	**91**	**48**	**18**	**6**
B-HA 6	Front	31	36	236	77	89	65	64	110	35	0	0
	Rear	17	30	287	182	214	108	71	39	0	0	0
	Average	**24**	**33**	**262**	**130**	**152**	**87**	**68**	**75**	**17**	**0**	**0**

4.8.2. Fluid dynamic analysis

The data of the pore diameter distribution from the morphological analysis of the three scaffolds taken as examples, B-HA 4, 5, E 6, were used to create three different models for the numerical analysis of their fluid dynamic characteristics (CFD) [94]. To reduce the computational time, preserving a good correspondence between the real scaffolds and the numerical models, only an equivalent 30° sector model was analyzed for each scaffold, with its real radius and height, rearranging the pore position but maintaining the same distribution.

Figure 4.8.3 shows the pore distribution of the 30° sectors compared with their full scaffolds.

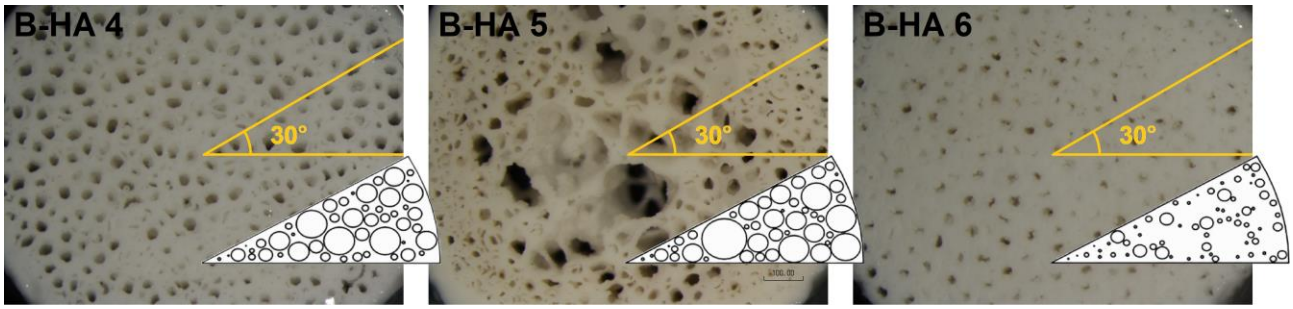

Fig. 4.8.3. *Sectors of 30° on B-HA 4, 5, and 6 scaffolds with their geometric models (redraw from* [94]*).*

Figure 4.8.4 compares the counts between full 360° scaffolds and 30° sector models. Each pore count diagram of the 30° sectors was scaled by its angle ratio with the full 360° scaffold. In the pore counts, each diameter class was represented by its central value and the counts of pores for each diameter class is the average between the counts of front and rear faces.

The figure shows that, for each scaffold, the 30° sector diagram is practically the same of the full 360° scaffold, confirming the correct pore diameter distribution of the 30° sector models for the CFD.

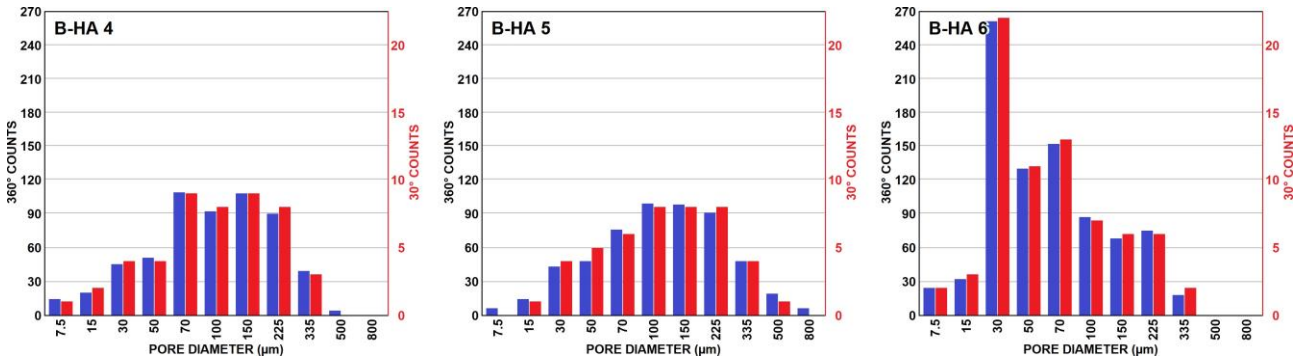

Fig. 4.8.4. *Comparison of pore counts between full 360° B-HA 4, 5, and 6 scaffolds, in blue bars, and their 30° geometric model, in red bars (redraw from* [94]*).*

The same assumptions as in Section 4.5.3 were adopted for the geometry of the pores.

The geometric models of the scaffolds were analyzed with the SIMCENTER STAR-CCM+ v2021.3 software (Siemens Digital Industries Software, CA-USA), to simulate the flow inside the pores and obtain their fluid dynamic characteristics. The analysis of each scaffold sector was performed by simulating the use of water at the two test temperatures, Low T of 21-22°C and High T of 35-37°C, according to the average fluid temperatures measured for each scaffold in the experimental characterization tests. Figure 4.8.5 shows the graphical result of the CFD simulation for the fluid flow velocity inside the pores of the B-HA 4 scaffold.

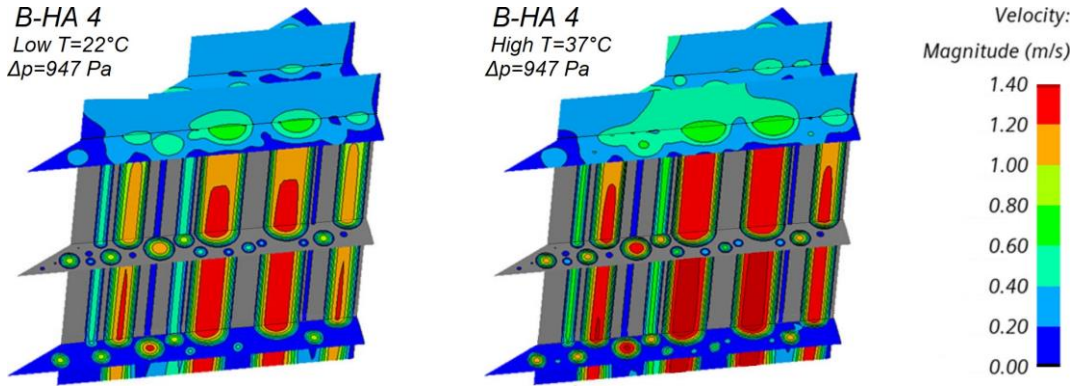

Fig. 4.8.5. *Velocity magnitude for B-HA 4 scaffold at Low and High T* [94].

From Figure 4.8.5 we can see an increase of the velocity magnitude of the fluid for the high temperature, compared to the low temperature, due to the reduction of the dynamic viscosity μ. However, this involves an increase in the pore entry region for the full development of the velocity profile, as highlighted in the vertical sectors above and below the pore inlets in the two representations.

4.8.2.1. Fluid dynamic resistance comparison

To evaluate whether the physical model of the CFD simulation was correct, the SFDR Rf/μ, obtained from the experimental characterization tests were compared with the results of the CFD analysis for B-HA 4, 5 and 6 scaffolds for the two test temperatures, Low T and High T, Figure 4.8.6.

From the experimental test data, we can see the large variation of the SFDR Rf/μ between the three scaffolds, well reproduced by the CFD simulation but with a generalized overestimation, equal to an average of 17%. This overestimation can be explained by a generalized underestimation of the ImageJ software in determining the area and number of pores of the scaffolds.

A subsequent analysis may lead to the determination of a correction coefficient, if supported by an adequate number of comparisons between experimental tests of fluid dynamic resistance and CFD simulations.

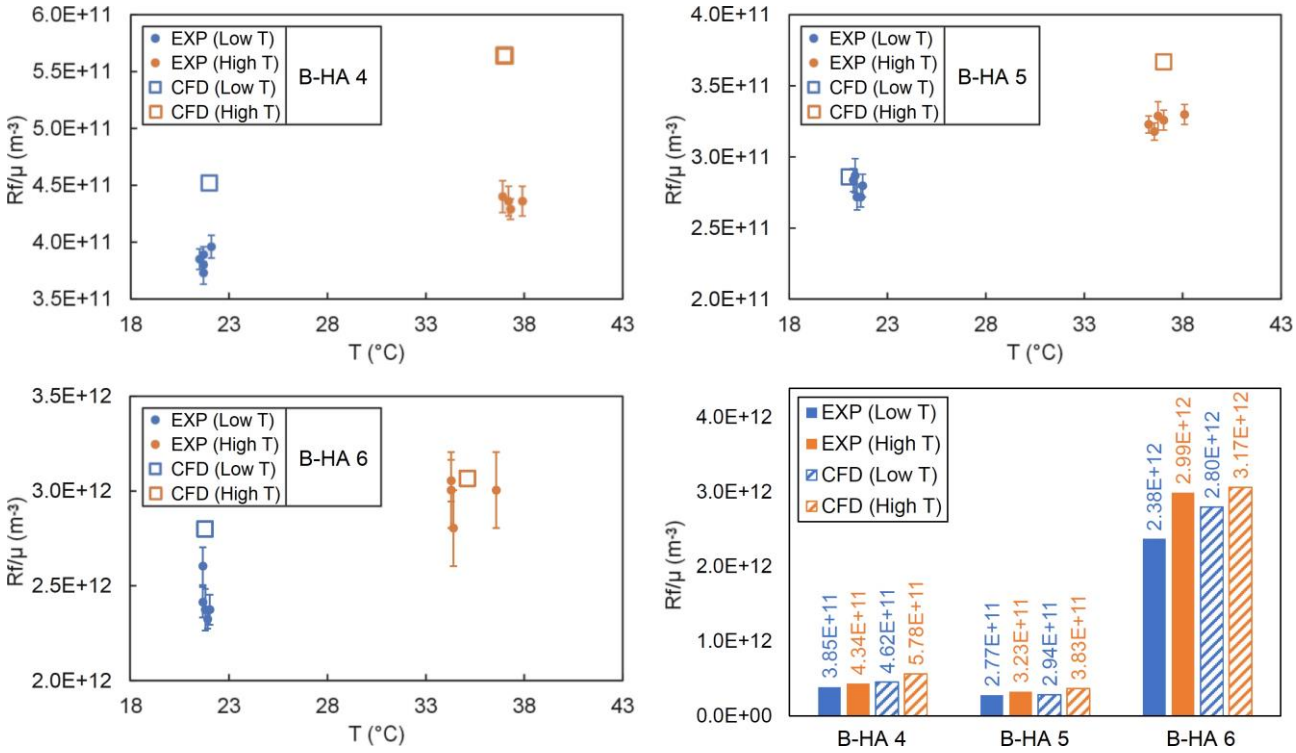

Fig. 4.8.6. SFDR *Rf/μ of experimental tests compared with CFD simulations for B-HA 4, 5 and 6 scaffolds with data summary* [94].

Furthermore, the CFD simulation also highlights, like the experimental tests, a generalized increase of the SFDR *Rf/μ* from low to high temperature[95], equal to an average of 21%, as seen in the Paragraph 4.7. A possible cause may be the increase in velocity magnitude inside the pores for the high temperature with an increase in the entry region, as in Figure 4.8.5, and the consequent reduction in validity of the fully developed flow assumption of Darcy's law, Equation (2.3.54), explaining the difference between experimental and theoretical data.

4.8.2.2. Fluid shear stress CFD simulation

After verifying that the geometric and physical model of the CFD simulation were sufficiently precise, it was possible to analyze the fluid shear stress on the wall of the pores. Figure 4.8.7 shows the graphical results of the CFD simulation for the fluid shear stress on the pore walls for the B-HA 4, 5, and 6 scaffolds for the two test temperatures, Low T and High T, with a pressure drop Δp of 947 Pa for the B-HA 4 and 5 scaffolds, and 458 Pa for B-HA 6 scaffold.

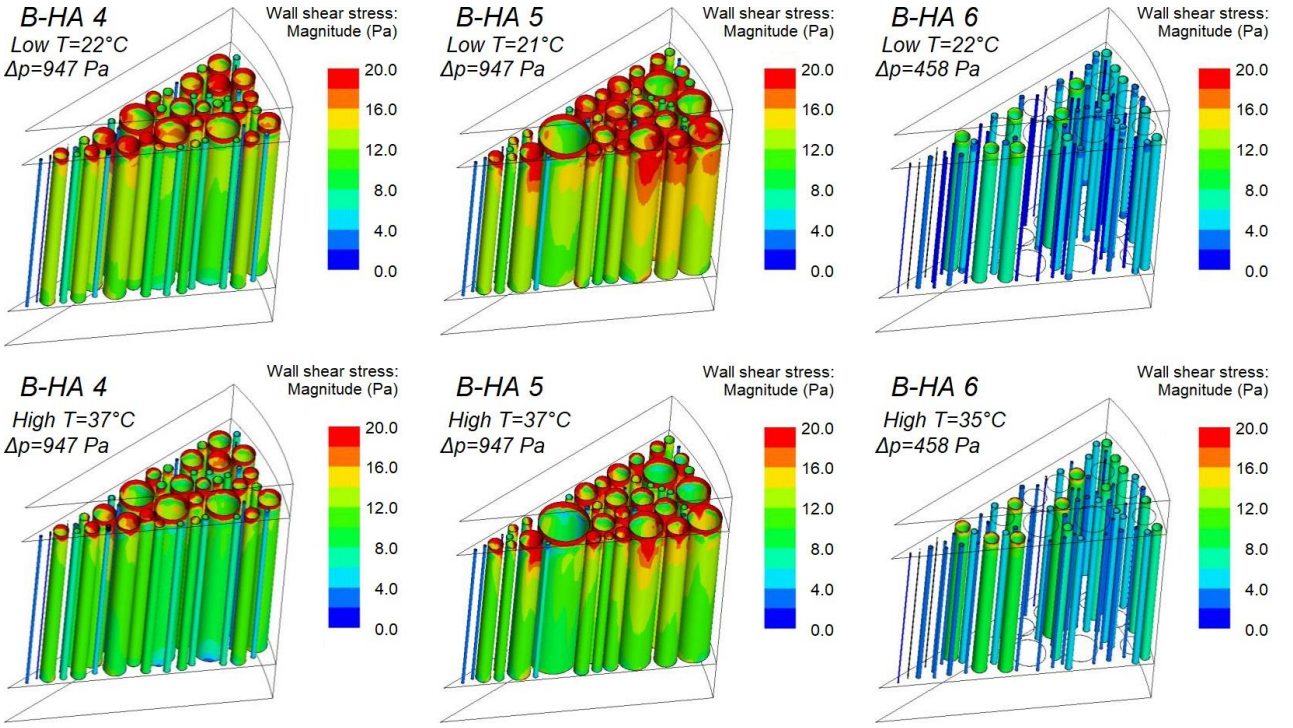

Fig. 4.8.7. *Fluid shear stress on pore walls with CFD simulation for B-HA 4, 5 and 6 scaffolds (redraw from* [94]*).*

From the numerical results of the CFD simulation, the discrete Probability Density Function (PDF) of the fluid shear stress on the pore walls of the B-HA 4, 5, and 6 scaffolds was calculated for the two test temperatures, Low T and High T, Figure 4.8.8. The shear stress range was divided in classes and for each class was calculated the fraction of the total pore area of the scaffold subject to the shear stress range of the class. The PDF for each class was the class area fraction divided by the width of the shear stress range of the class.

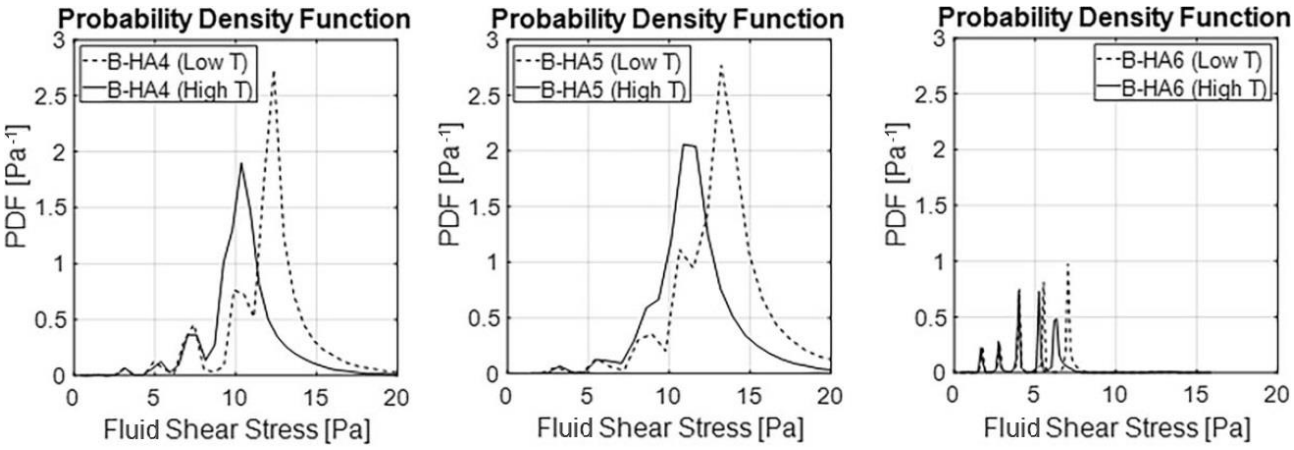

Fig. 4.8.8. *Probability Density Function of the fluid shear stress on the pore walls for B-HA 4, 5 and 6 scaffolds from CFD simulation data* [94]

Subsequently, the Cumulative Density Function (CDF), i.e. the sum of the probability from the first to a given class, was calculated by integrating the Probability Density Function from the lower limit of the shear stress range to the upper limit of the given class, Figure 4.8.9. The CDF ranges from the probability of the first class (i.e. its area fraction) to one (i.e. the 100% of the scaffold pore area, which is subjected to the full range of shear stresses).

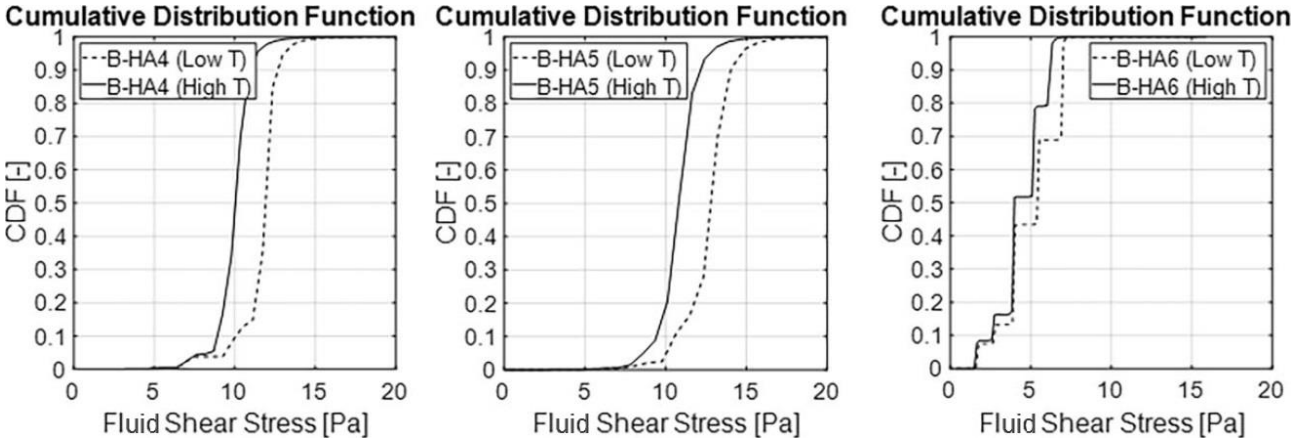

Fig. 4.8.9. *Cumulative Density Function of the fluid shear stress on the pore walls for B-HA 4, 5 and 6 scaffolds from CFD simulation data* [94].

It is possible to note that most of the shear stress contribution is concentrated around the value of 11.4 Pa for the B-HA 4 scaffold, 12.0 Pa for B-HA 5, and 5.1 Pa for B-HA 6. From Figure 4.8.7, these values can be associated with the central section of the pores, while the highest and lowest FSS values of the CPF curves can be associated respectively with the inlet and outlet section of the pores.

4.8.2.3. Theoretical calculation of the shear stress

It is possible to obtain the value of the fluid shear stress τ_i on the wall of the pores of the diameter class *i*, with mean diameter *Di*, from Equation (2.3.43):

$$\tau_i = -\frac{D_i \, \Delta p}{4 \, L_{PO}} \tag{4.8.1}$$

where Δp is the pressure drop between the two flat faces of the scaffold, and L_{PO} is the length of the pores, i.e. the scaffold height H_{SC}.

The influence of the shear stress τ_i on the average value of the whole scaffold τ_{SC} is proportional to the total surface area A_i of the pores in the diameter class i, and equal to:

$$A_i = \pi D_i L_{PO} c_i \tag{4.8.2}$$

where c_i is the pore count of the diameter class i

Then, the average value of the fluid shear stress on the pore wall of the scaffold τ_{SC} is the weighted average of the contribution of each shear stress τ_i with respect to the total pore area:

$$\tau_{SC} = -\frac{\sum_{i=1}^{n} \tau_i A_i}{\sum_{i=1}^{n} A_i} = -\frac{\sum_{i=1}^{n} \frac{D_i \Delta p}{4 L_{PO}} \pi D_i L_{PO} c_i}{\sum_{i=1}^{n} \pi D_i L_{PO} c_i} = -\frac{\Delta p}{4 L_{PO}} \frac{\sum_{i=1}^{n} {D_i}^2 c_i}{\sum_{i=1}^{n} D_i c_i} \tag{4.8.3}$$

With Equation (4.8.3) and the data of Table 4.8.1 it is possible to calculate the shear stress on the pore wall of the B-HA 4, 5, and 6 scaffolds subjected to the same pressure drop used in the CFD simulation, Figure 4.8.7.

Table 4.8.2. *Theoretical fluid shear stress on the pore walls of B-HA 4, 5, and 6 scaffolds.*

	D_{SC}	**H_{SC}**	**Δp**	**FSS**
B-HA	**mm**	**mm**	**Pa**	**Pa**
4	10.4	4.3	947	10.6
5	10.6	3.9	947	15.9
6	10.7	3.8	458	4.3

These values differ on average by 18% compared to the fluid shear stress values obtained from the CFD simulation, as shown in Figure 4.8.8 and Figure 4.8.9. Despite the simplicity of this theoretical model, for example the effect of the flow development is not considered, this result is to be considered sufficiently precise and the model useful for approximate calculations.

4.9. Device for experimental proliferation tests

After the experimental characterization of the scaffold, which confirmed the good approximation of the theoretical model, the next step of the research was to design a device that would allow the generation of a constant shear stress in the bone cells implanted in the scaffold and to perform the related tests.

From the project it emerged that, in this case too after a comparation of different systems, the simplest solution was to create a bioreactor by modifying the biological filter device of Section 4.6.2.

4.9.1. Shear stress systems for bone cell culture

In scientific literature, the two most used systems to generate constant shear stress in bone cell culture, considered with constant fluid dynamic resistance, are the syringe pump with constant flow rate [38], which generates constant shear stress as per Equation (2.3.47), and the recirculation system with a constant hydrostatic head [96], which generates a constant shear stress as per the Equation (2.3.44).

In the syringe pump, Figure 4.9.1-A, a brushless or stepper motor rotates a screw which, via a slider, pushes the piston of a commercial syringe, and it is possible to use different syringe sizes. Through the electronic control of the pump it is possible to set the advancement speed of the cursor and therefore the flow rate of the fluid exiting the syringe. A simplified diagram of a constant shear stress system with syringe pump is shown in Figure 4.9.1-B.

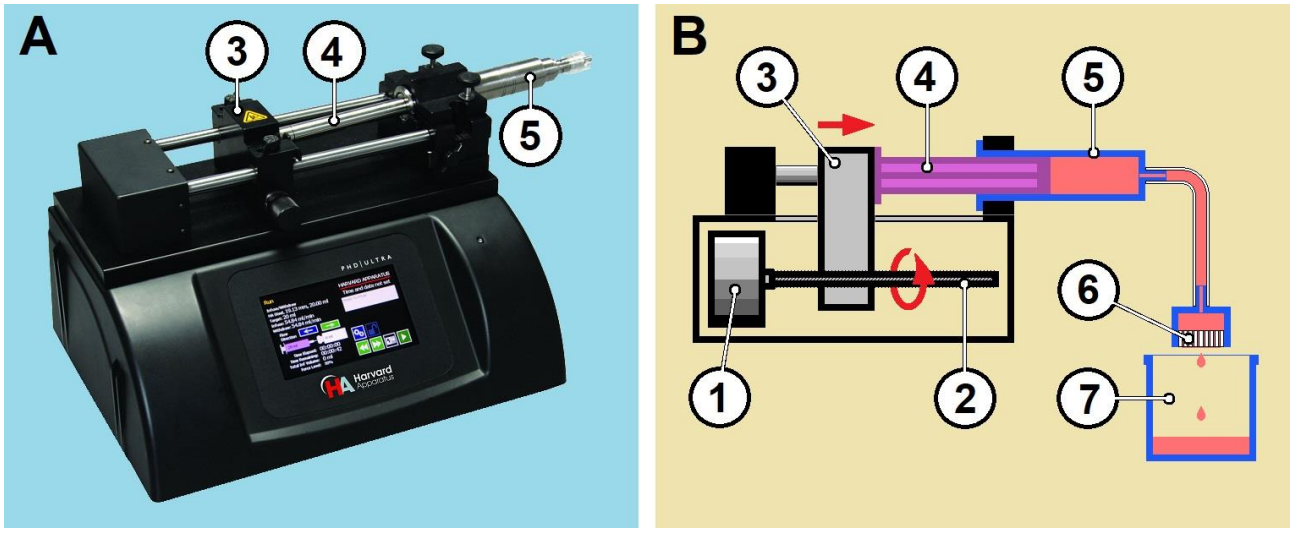

Fig. 4.9.1. *(A) Syringe pump* [97]. *(B) Syringe pump system for constant shear stress in bone cell culture. 1-Motor, 2-Screw, 3-Slider, 4-Piston, 5-Syringe, 6-Scaffold, 7-Drain.*

In the recirculating system, a peristaltic pump, Figure 4.9.2-A, draws fluid from a lower reservoir and delivers it to an upper reservoir. The scaffold is housed at the bottom of the upper reservoir, its outgoing fluid falls into the lower reservoir. The fluid flow rate of the peristaltic pump must be greater than the flow rate passing through the scaffold. The upper reservoir is equipped with an overflow drain which brings the excess fluid to the lower reservoir, keeping constant the fluid level in the upper reservoir and therefore constant the hydrostatic head on the scaffold. A simplified diagram of a recirculating system with constant hydrostatic head is shown in Figure 4.9.2-B.

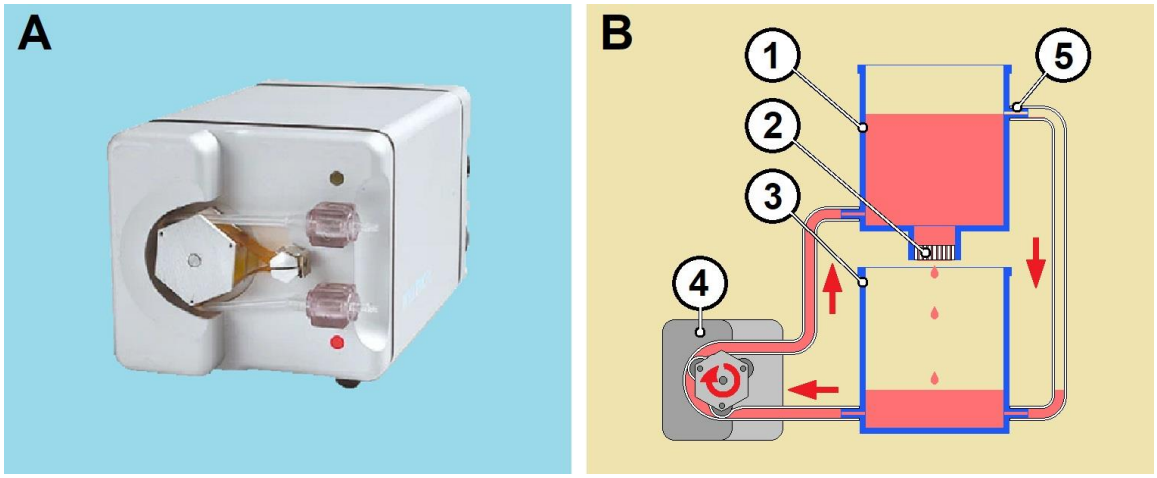

Fig. 4.9.2. *(A) Peristaltic pump* [98]. *(B) Recirculating system with constant hydrostatic head. 1-Upper Reservoir, 2-Scaffold, 3-Lower Reservoir, 4-Pump, 5-Overflow Drain.*

The syringe pump system is simple and precise, but its tests have an autonomy limited by the capacity of the syringe. The recirculation system is more complex and less precise, but its tests can have an unlimited autonomy, the only limitation is the hydrostatic head that if less than ten millimeters which would make the functioning of the overflow drain very imprecise.

Therefore the choice between the two systems is determined by the operating conditions of the tests. To evaluate them, we consider the theoretical characteristics of the scaffold, which were found to be compatible with the experimental tests, and the entire field of use of shear stress, as reported in Table 4.5.1 and Table 4.5.2, with DMEM + 10% FBS at 37°C as fluid.

In the case of the syringe pump system we consider using the plastic syringe with the maximum capacity compatible with a standard syringe pump, approximately corresponding to 140 mL [99], and a series of lower capacity syringes to analyze the low shear stress field. Figure 4.9.3 shows the maximum shear stress level obtainable with a syringe pump system, as a function of the test time and the syringe used.

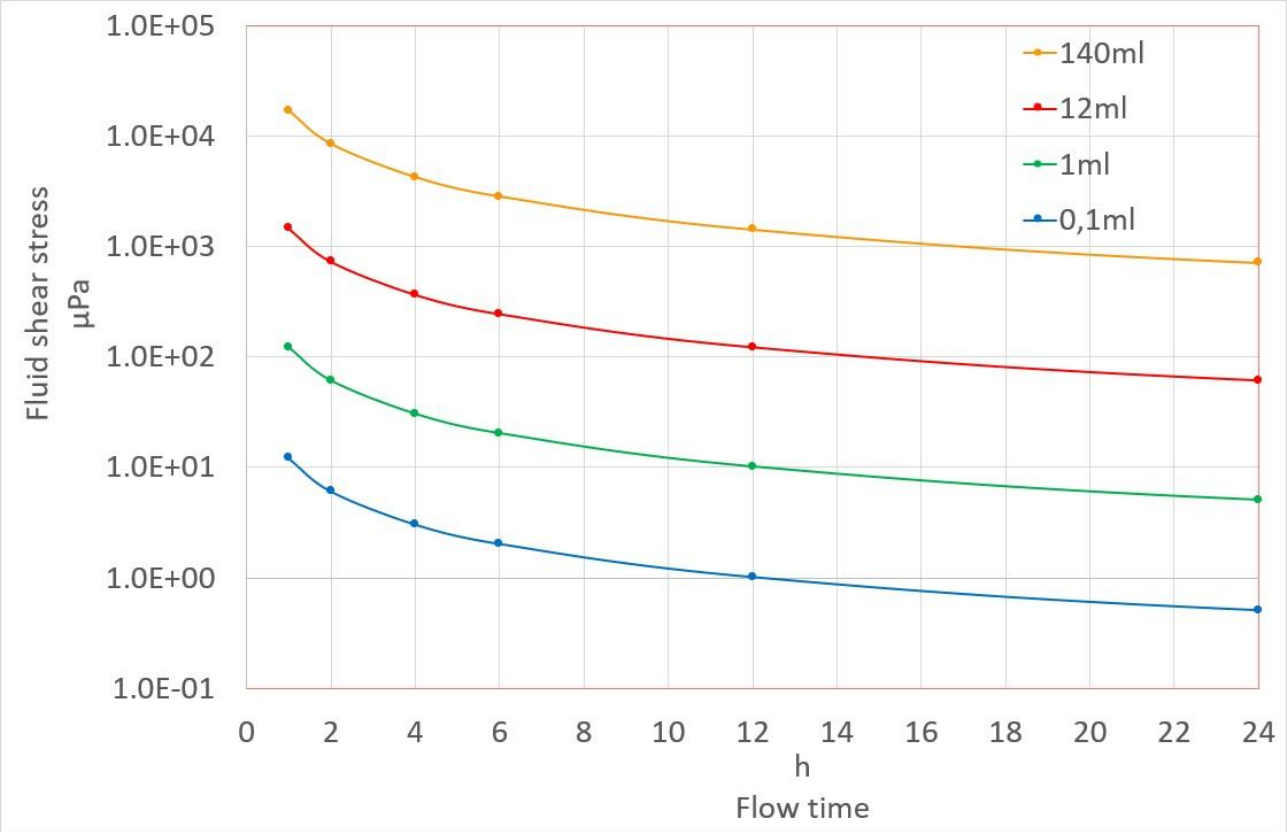

Fig. 4.9.3. *Fluid shear stress vs. syringe pump flow time.*

As we can see from Figure 4.9.3, even with the maximum capacity syringe, tests lasting more than two hours with the syringe pump system are not possible if a fluid shear stress higher than 10^{-2} Pa is required. However, tests in the lower range of low fluid shear stress are fully feasible with the syringe pump system.

In the case of the recirculation system, to have a hydrostatic head of adequate height at low fluid shear stress, i.e. low flow rate, one of three different fluid resistors, designed as perforated cylinders and reported in Table 4.9.1, is added in series after the scaffold.

Table 4.9.1. *Summary of the additional fluid resistor for the recirculation system.*

	D outer	D inner	Height	SFDR *Rf/µ* (theoretical)
	mm	µm	mm	Pa·s/m^3
Rf_{SC}	10	-	4	$1.5 \cdot 10^{11}$
Rf1r	10	700	8	$1.4 \cdot 10^{12}$
Rf2r	10	400	10	$1.4 \cdot 10^{13}$
Rf3r	10	200	6	$1.4 \cdot 10^{14}$

Figure 4.9.4 shows the theoretical maximum level of shear stress obtainable in a recirculation system with DMEM at 37°C, as a function of the hydraulic head and the additional fluid resistors. The hydraulic head is the sum of the fluid level above the scaffold plus the height of the scaffold, the additional fluid resistor, and their gap.

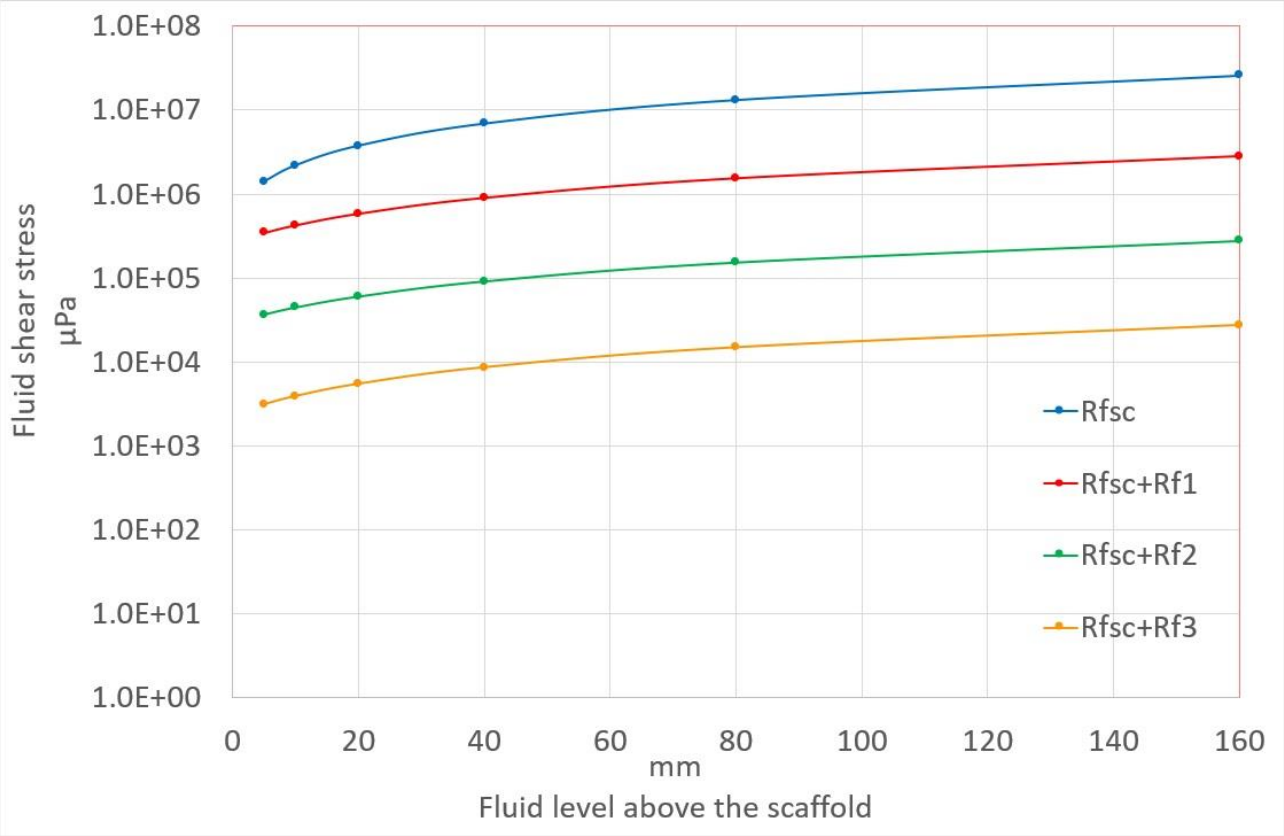

Fig. 4.9.4. *Fluid shear stress vs. hydraulic head in a recirculation system.*

As we can see from Figure 4.9.4, tests in the range of medium and high fluid shear stress are fully feasible with the recirculation system, but they are not possible if a fluid shear stress lower than 10^{-3} Pa is required.

4.9.2. Design of the proliferation device

The research main criteria, for deciding the test methodology and the choice of shear stress levels to be used in cell proliferation tests, were the duration of the tests and the number of tests.

It was decided to test two levels of shear stress on bone cells, a higher one of 3.0±1.0 Pa and a lower one of 0.5±0.1 Pa, for a duration of four hours. These two shear stress levels, according to the scientific literature, are in the range of the best proliferation ratio compared to proliferation without shear stress. The choice therefore fell on the recirculation system with two overflow levels and three different additional fluid resistors to obtain the two levels of shear stress and compensate for the differences in fluid dynamic resistance among the scaffolds.

If we look at Figure 4.9.2-B of the recirculation system, we can see that the bioreactor, the set of two reservoirs that contain the scaffold and the fluid, is very similar to Figure 4.6.2-B of the characterization device. This consideration made it clear that to create the bioreactor was sufficient to modify the characterization device by adding the necessary components, Figure 4.9.5.

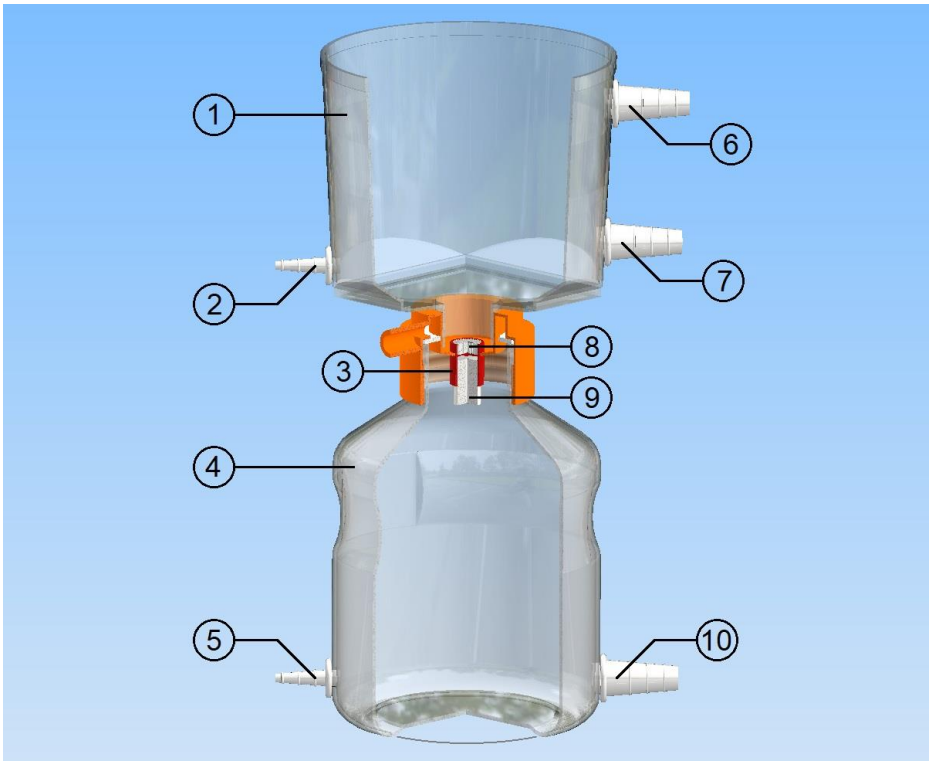

Fig. 4.9.5. *3D CAD drawing of the bioreactor. 1-Upper Reservoir, 2-Inlet from Pump, 3-Gasket, 4-Lower Reservoir, 5-Outlet to Pump, 6-Upper Overflow, 7-Lower Overflow, 8-Scaffold, 9-Fluid resistor, 10-Inlet from Overflows.*

The two overflow drains were positioned respectively 15 mm (upper overflow) and 65 mm (lower overflow) lower than the top of the upper reservoir, corresponding to a height of the fluid level over the scaffold bottom approximately of 92 mm and 42 mm. This means a hydrostatic head at the level of the lower face of the scaffold of 911 Pa and 416 Pa respectively with DMEM + 10% BSA at 37°C, without the additional fluid resistor.

The three additional fluid resistors for the proliferation device, Table 4.9.2, were made of PTFE and similar but dimensionally different from those for recirculation system, Table 4.9.1, because they do not have to optimize the field of application of the recirculation system but regulate the flow of the fluid passing through the scaffold to generate a shear stress in the design range.

Table 4.9.2. *Summary of the additional fluid resistors for the proliferation device.*

	D outer	D inner	Height	SFDR Rf/μ (theoretical)
	mm	µmm	mm	$Pa \cdot s/m^3$
Rf_{SC}	10		4	$1.5 \cdot 10^{11}$
Rf1p	10	1000	16	$6.5 \cdot 10^{11}$
Rf2p	10	600	9	$2.8 \cdot 10^{12}$
Rf3p	10	400	7	$1.1 \cdot 10^{13}$

4.9.3. Realization of the proliferation device

Based on the indications in Section 4.9.2, the proliferation device, Figure 4.9.6, was created using the following components:

- Bioreactor: 500 mL Vacuum Filter/Storage Bottle System (Corning® Inc., AZ-USA).
- Bioreactor connections: Polypropylene linear fittings for 4/5/6 mm and 10/11/12 mm hose internal diameter (Incofar S.r.l., Modena, Italy).
- Valves: Polypropylene (PP) and high density polyethylene (HDPE) shutoff valves with fittings for 10 mm hose internal diameter (Incofar S.r.l., Modena, Italy).
- Hoses: Do 6 mm/Di 4 mm and Do 14 mm/Di 10 mm silicone hoses (Incofar S.r.l., Modena, Italy).
- Pump: 500 mL/min 24V peristaltic pump (G928 Grothen, China).

The flow rate of the pump is adequate for the bioreactor because the request for such a flow rate with a hydrostatic head of 911 Pa involves a SFDR Rf/μ of $1.2 \cdot 10^{11}$ m^{-3}, lower than the minimum value of the additional fluid resistors, Table 4.9.2.

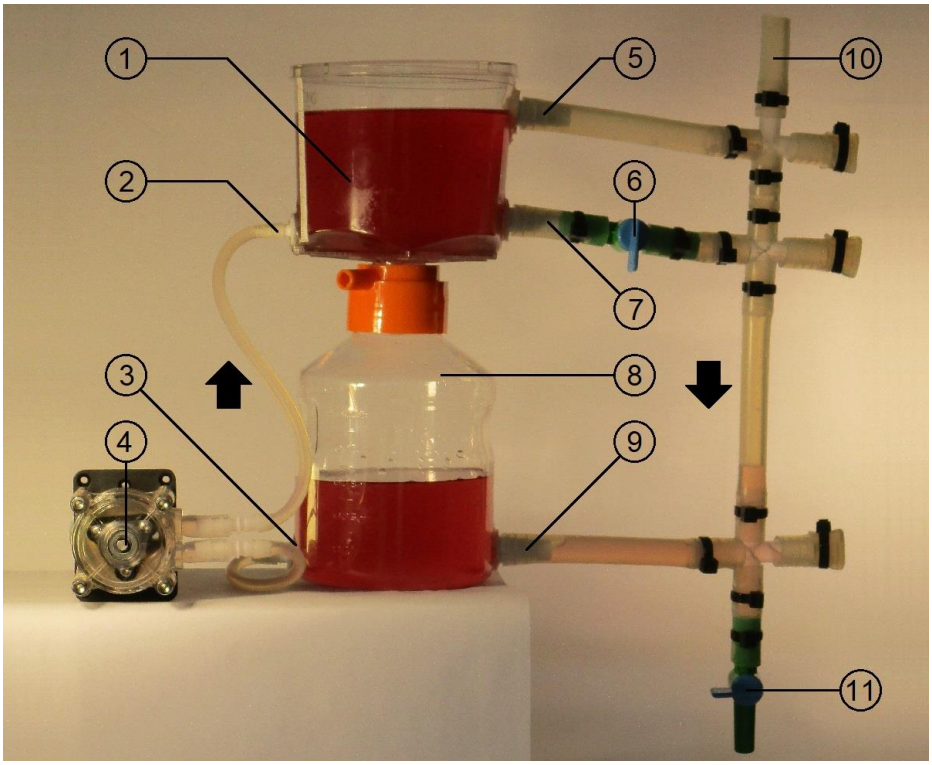

Fig. 4.9.6. *Proliferation device. 1-Upper reservoir, 2-Inlet from Pump, 3-Outlet to Pump, 4-Pump, 5-Upper Overflow, 6-Lower Overflow Valve, 7-Lower Overflow, 8-Lower Reservoir, 9-Inlet from Overflows, 10-Vent, 11-Drain Valve.*

To overcome the limitation of access to the laboratories, especially those for biological experiments, due to the Covid-19 emergency, an oven for the proliferation tests was built with a digital control of its temperature (XH W3001 Dolla Tek, China) and a digital thermometer for measuring the temperature of the fluid (T0388 WINGONEER, China), Figure 4.9.7.

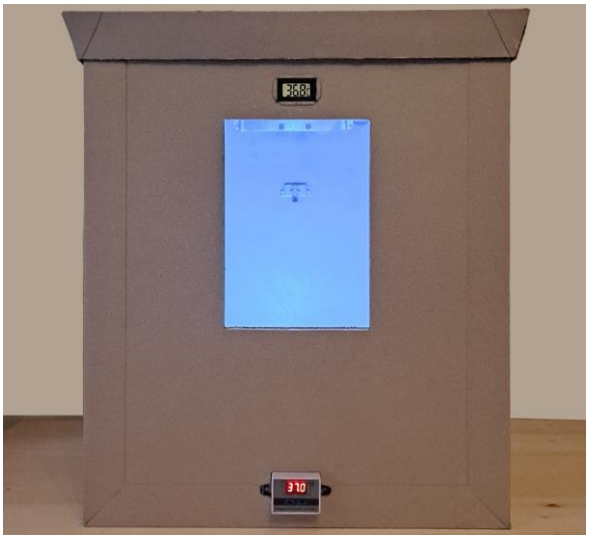

Fig. 4.9.7. *Oven for the proliferation tests.*

4.10. Experimental proliferation tests of bone cells on scaffold

After the creation of the device for the experimental proliferation tests, the experimental proliferation tests with shear stress were carried out.

The bone cells were implanted into the scaffolds and cultured in vitro, subsequently the cells of a part of the scaffolds were exposed to shear stress, finally all cell proliferations were measured and compared.

4.10.1. FSS proliferation scaffolds

For each test scaffold, Table 4.7.2, was calculated its theoretical fluid shear stress by Equation (4.8.3) in function of the two overflow levels and the three additional fluid resistors of Section 4.9.2.

From the results of the shear stress calculation, twelve scaffolds were selected for the FSS proliferation tests, Table 4.10.1, six scaffolds for the High FSS and six for the Low FSS level, as defined in Section 4.9.2.

Table 4.10.1. *FSS proliferation scaffolds, sorted by decreasing shear stress* [100].

Scaffold	D_{SC}	H_{SC}	FSS level	Resistor	Overflow	FSS
	mm	mm				Pa
B-HA 5	10.6	3.9	High	Rf1p	upper	3.50
B-HA 7	10.5	3.8	High	Rf1p	lower	3.20
B-HA 4	10.4	4.3	High	Rf1p	upper	3.10
B-HA 1	10.5	3.9	High	Rf1p	upper	2.50
B-HA 6	10.7	3.8	High	Rf2p	lower	2.50
B-HA 13	10.7	4.1	High	Rf1p	upper	2.20
B-HA 10	10.8	4.6	Low	Rf2p	lower	0.55
B-HA 15	10.8	4.1	Low	Rf2p	upper	0.53
B-HA 8	10.6	3.7	Low	Rf3p	lower	0.53
B-HA 12	10.6	4.6	Low	Rf3p	upper	0.48
B-HA 11	10.4	4.5	Low	Rf3p	lower	0.46
B-HA 14	10.4	4.5	Low	Rf3p	upper	0.43

As can be seen in Table 4.10.1, the fluid shear stress values, for each of the two levels, are in a narrower range than required, confirming the choice of overflow levels and the additional fluid resistors .

4.10.2. Cell culture, scaffold seeding, and FSS proliferation

Osteoblastic cell line MC3T3 (Subclone 14, Elabscience, TX-USA) was cultured in a complete medium composed of 15-012 AMEM (Corning, NY-USA) supplemented with 10% Fetal Bovine Serum (FBS), 1% L-glutamine, and 1% penicillin–streptomycin (100 U ml^{-1}/100 µg ml^{-1}) (Corning, NY-USA) at 37°C, under a humidified atmosphere of 5% CO_2.

The culture medium is very similar to characterization medium, DMEM + 10% FBS in Section 4.7.3, AMEM and DMEM are modifications of the original Minimal Essential Medium (MEM) and have few formulation differences [101] [102] but the same density and fluid dynamic viscosity [103] [104], the serum component is the same and equal to 10%, therefore the fluid dynamic characteristics of the two mediums can be considered equivalent.

The twelve FSS scaffolds, plus six reference scaffolds (CTR) not to be subjected to fluid shear stress, were placed in ethanol 70% v/v overnight and sterilized by UV radiation prior to use, were presoaked in culture medium for 72 h at 37°C. The scaffolds were seeded by carefully dropping 20 ml of MC3T3 cell suspension ($5.0 \cdot 10^5$ cells) onto the scaffold upper surface and were then placed in a cell incubator for 20 minutes to allow cell attachment, before the addition of 1 ml of growing cell culture medium. After 24 h of culture, the seeding procedure was repeated on the scaffold bottom side and the cellularized scaffold was maintained for 48 h in the cell incubator. For the FSS proliferation, the Low FSS and High FSS scaffolds were subjected to the respective shear stress level, Table 4.10.1, in the proliferation device for 4 h with the culture medium at 37°C, Figure 4.10.1.

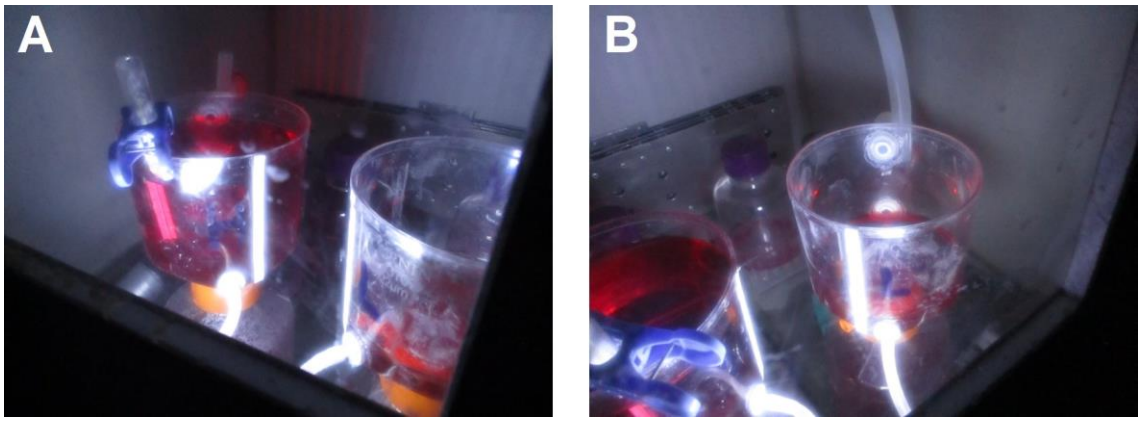

Fig. 4.10.1. *FSS proliferation with two devices simultaneously.*
(A) On the left, a High FSS test. (B) On the right, a Low FSS test.

Finally, all scaffolds were placed in 4% (w/v) paraformaldehyde for 15 min with pre- and post-washing with PBS, in order to fix their bone cells, and were ready for analysis [100].

4.10.3. Morphological cell analysis

For the morphological cell analysis, three scaffolds were used for each of the three groups, CTR, Low FSS, and High FSS.

Images of cells were acquired by using an Inverted Confocal Nikon Eclipse A1 fluorescence microscope (Nikon, NY-USA). For this purpose, the cells of one scaffold per group were stained with Cell Tracker Orange CMRA Dye (Thermo Fisher Scientific - Pierce Biotechnology, IL-USA) to highlight their cytoplasm, and the cells of one scaffold per group were stained with CellMask^{TM} Green Actin Tracking Stain (Thermo Fisher Scientific - Pierce Biotechnology, IL-USA) to highlight their F-actin.

More accurate images to detect the morphological modifications induced by the fluid shear stresses on the osteoblastic cells were further acquired by using a Field Emission Gun - Scanning Electron Microscope (FEG-SEM) on the remaining one scaffold per group [100].

4.10.4. Quantitative cell analysis

For the quantitative cell analysis, a batch of three scaffolds was used for each of the three groups, CTR, Low FSS, and High FSS, i.e. three replicates for each group experiment.

The influence of the FSS on the proliferation of osteoblastic cell was measured by a Quantitative Real-Time PCR analysis of the mRNA expression of three differentiation markers, alkaline phosphatase (ALPL), osteoblast stimulating factor 1 (PTN), and runt-related transcription factor 2 (RUNX2), the genes mainly expressed at early stage of osteogenesis in MC3T3 cell lines and proportional to the quantity of osteoblastic cells of each scaffold.

The relative gene quantification was performed using the comparative threshold (Ct) method ($\Delta\Delta$Ct), where relative gene expression level equals $2^{-\Delta\Delta Ct}$. The obtained fold changes in gene expression were normalized first to the internal control gene GAPDH and then to CTR values.

The real-time PCR data were processed by the statistical student t-test (one-tailed) and expressed as the means ± standard deviation from three independent experiments. The significance threshold α was set to 0.05 and there was statistical significance if $p < \alpha$ [100].

4.10.5. Morphological cell evaluation

In Figure 4.10.2-A are reported confocal fluorescence images of cells stained with Cell Tracker Orange CMRA Dye, and in Figure 4.10.2-B cells stained with CellMask^{TM} Green Actin Tracking Stain. Each figure is divided into three images, CTR, Low FSS, and High FSS cells. The cells adherent to the surface of the scaffolds are clearly visible (red and green spots).

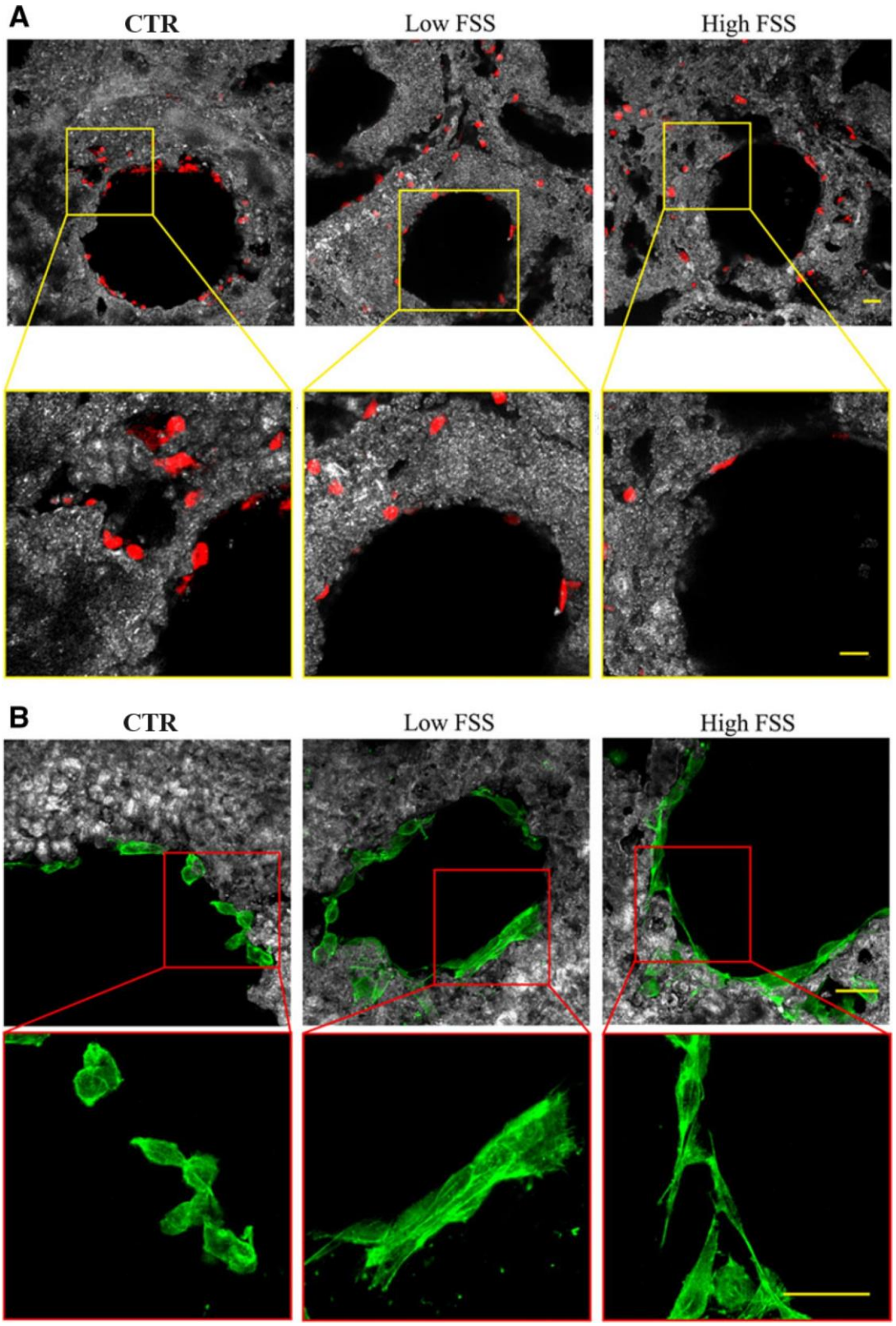

Fig. 4.10.2. *Confocal fluorescence images of three representative cellularized scaffolds divided in three groups (CTR, Low FSS, and High FSS)* [100]. *Osteoblasts were stained with (A) Cell tracker Orange CMRA Dye (20× magnification) and (B) CellMaskTM Green Actin Tracking Stain (40× magnification) markers. The yellow and red squares show a higher magnification of the images from top to bottom. Yellow scale bars: 50 μm.*

The images of Figure 4.10.2 suggest that cells on the FSS scaffolds tend to elongate in response to FSS conditions, compared to the cells on the CTR scaffolds. The enlargements of Figure 4.10.2-A show red fluorescence signals with a stretched elliptical shape returned by some cells localized near the pores edge of the FSS scaffolds, i.e. more exposed at FSS, in opposition to the circular signal generally obtained from the cells on the CTR sample.
In Figure 4.10.2-B, the modification of the green fluorescence signal is symptomatic of cell adaptation to FSS through displacement and deformation of the cytoskeletal filaments (actin filaments, microtubules and intermediate filaments), which get aligned with the direction of the flow [100].

In Figure 4.10.3 we can see the FEG-SEM images, which are divided in three columns, CTR, Low FSS, and High FSS scaffolds, and are also divided into three rows.

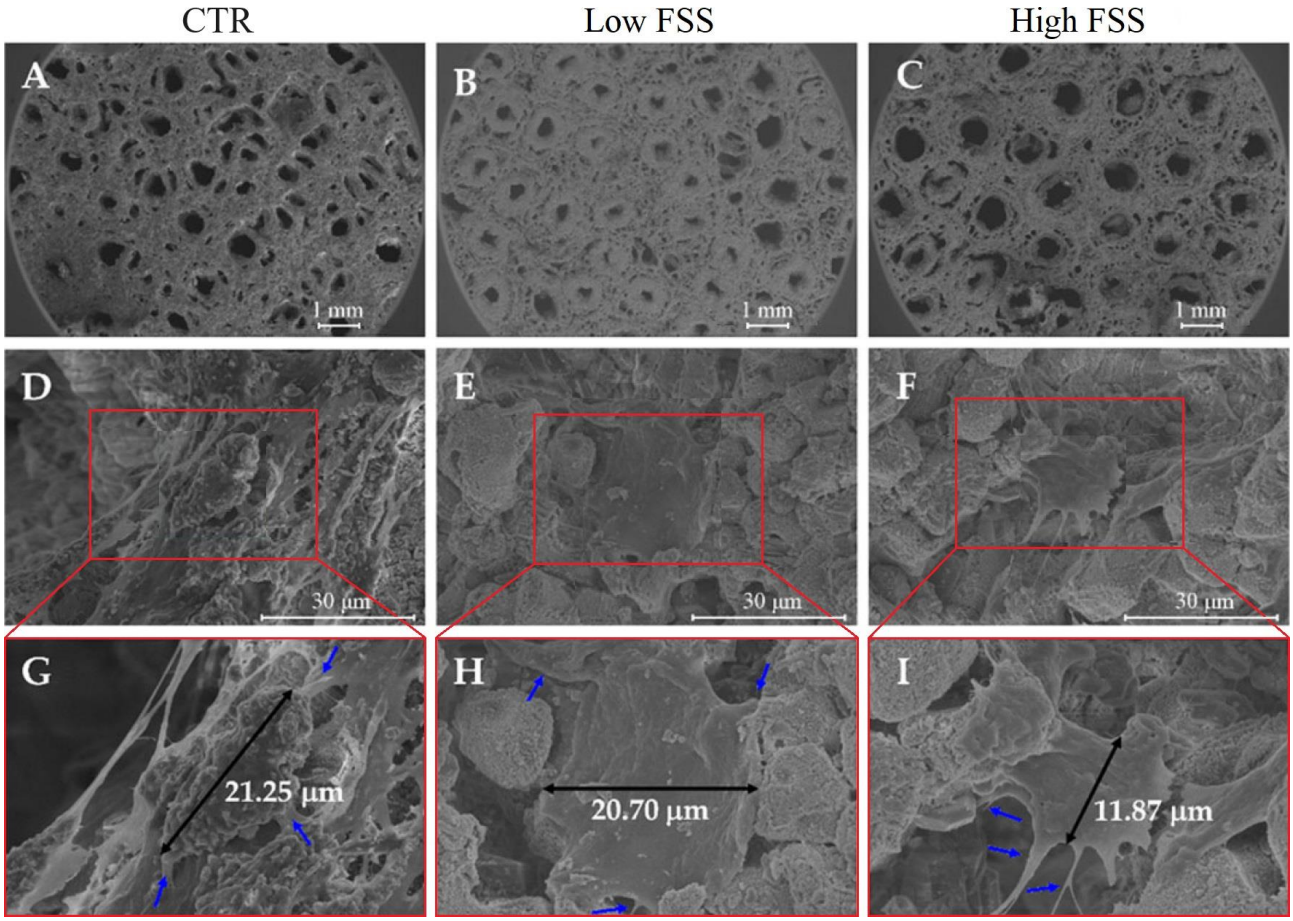

Fig. 4.10.3. *FEG-SEM images of three representative cellularized scaffolds divided in three columns, CTR, Low FSS, and High FSS (A-B-C, 40× magnification)* [100]. *The interconnected porosity of the scaffolds is clearly evident. (D-E-F, 5,000× magnification) Morphological structure of the cells. (G-H-I, 10,000× magnification) The same cells, enlargements of the red rectangles, with black and blue arrows indicating cell lengths and filopodia, respectively.*

In the images of the top row, Figure 4.10.3-A,B,C, shows the interconnected porous organization of scaffolds which mimics the hierarchical microstructure of the natural bone. In the images of the middle row, Figure 4.10.3-D,E,F, the greater magnification highlights the formation of cytoplasmic extensions from the osteoblasts, which are uniformly and abundantly distributed on the whole area of the scaffolds. In the images of the bottom row, enlargements of the red rectangles in the middle row, Figure 4.10.3-G,H,I, the cellular filopodia, indicated by blue arrows, are anchored to the surface of the scaffold. Cell lengths, indicated by black arrows, show that osteoblasts tended to elongate along the direction of flow. In particular, during high levels of FSS treatment, it can be observed that cells underwent a process of contraction and re-diffusion [100].

4.10.6. Quantitative cell results

The results of the Quantitative Real-Time PCR analysis on the mRNA expression of three differentiation markers (ALPL, PTN, and RUNX2) show higher marker values in scaffolds that were subjected to FSS compared to those that were not, with a statistically significant difference in High FSS scaffolds [100], Figure 4.10.4, results compatible with previous research.

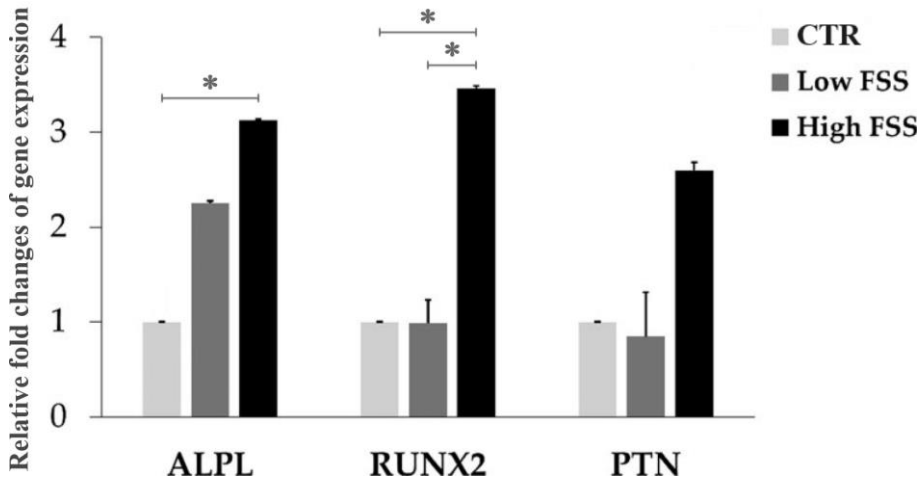

Fig. 4.10.4. *Relative quantification of ALPL, RUNX2, and PTN mRNA expression as markers of osteogenesis for osteoblast MC3T3 cell line* [100]. *(*) Student's t-test $p<0.05$.*

The values in Figure 4.10.4 are expressed in fold changes relative to the value of the control sample of each single test, normalized to one. If the ratio of the test value of a sample to the value of its control sample is *n*, the fold changes are $1+\log_2(n)$, e.g., if $n=1$ (the sample value is the same as the control value) the fold changes are 1, if 2 then 2, if 4 then 3, and so on.

Figure 4.10.5 shows the data from the most recent research on the influence of FSS culture time on bone cell proliferation, [105], [106], [107], [108], [109], comparing them with the data from the present research.

The FSS values are not shown because in the literature they are very different and a direct comparison between them is not possible. However, despite having a significant dispersion of data for this reason, the influence of time on cell proliferation is clear.

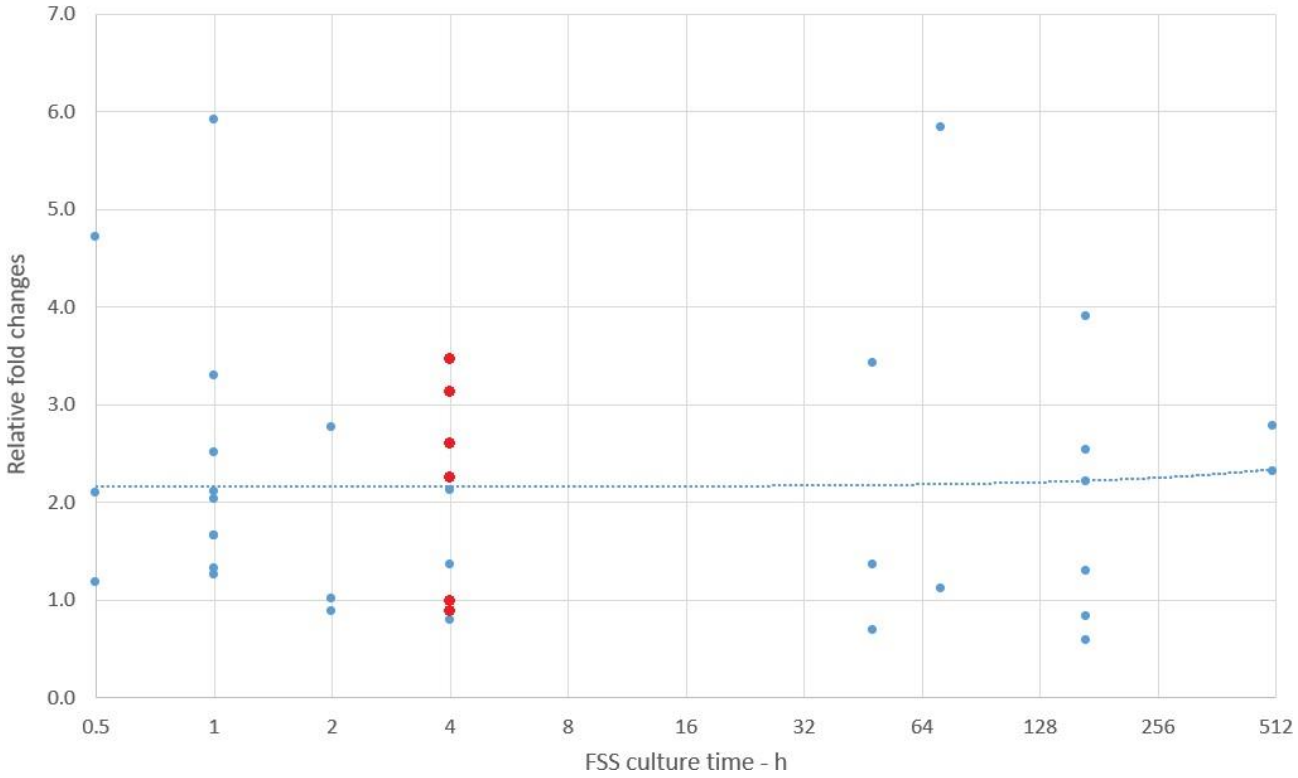

Fig. 4.10.5. *Comparison of the most recent research, blue dots, about the influence of FSS culture time on bone cell proliferation. Red dots represent the results of this research.*
Note: *Regression line does not appear straight due to the logarithmic scale of the axis.*

We can see that the data are well distributed along the regression line, which is almost horizontal, showing that the proliferation rate is constant over time, considering that the values of the samples are relative to the values of their control samples. The data from the present research, red dots, are also well distributed, highlighting a good correlation with the other research.

4.10.7. Proliferation test conclusion

The data of the tests indicate a significant positive influence of FSS in promoting proliferation in osteoblastic MC3T3 cells and the osteogenic potential of b.Bone™ scaffolds in guaranteeing bioactive support to cells equivalent to that of the human bone structure [100].

But it could be observed that the results of the present research are simply a confirmation of other research, the correlation between FSS and proliferation of bone cells has already been tested and demonstrated for a couple of decades and the *in vivo* applications of b.Bone™ scaffolds has been tested successfully for several years.

The novelty and importance of the present research do not lie in the correlation between FSS and cell proliferation or in the use of a 3D scaffold, but in the extensive study of the complexity of human bone with scaffolds obtained from natural structures for which traditional methodologies could not be used.

For this reason it was necessary to create a new theoretical model of these structures and an experimental methodology to adapt it to the different morphologies of the scaffolds, and to refine a procedure to calculate from this model the equivalent FSS on the bone cells as external conditions vary, for example, mimicking changes in pressure on human bones induced by pathological conditions or mechanical stress.

The significant number of samples and cross-tests of the present research allowed reliable results to be obtained, even in the face of the extreme variability of the samples. The fair correlation between previous research data and our data confirms the applied model and methodology.

4.11. PDMS microfluidic resistors for cell feeding

In the previous part of this chapter, was analyzed the range of fluid shear stress (FSS) which, according to the scientific literature, most influenced bone cell proliferation. This analysis led to the identification of FSSs in the range from 1 to 5 Pa and on these values was designed a feeding system for the bone cells supported by the same hydroxyapatite scaffold used in the previous Paragraph 4.4.

However, the analysis highlighted that there was a range of FSS in the order of micro Pascals, corresponding to those generated by the interstitial flow within the bone, which were equally interesting for scientific research. Given the very low value of FSS, the hydraulic head bioreactor previously designed for the higher range of FSS was no longer functional, as analyzed in Section 4.9.1.

As an alternative to using the standard syringe pump solution, was discussed the possibility of still using a hydraulic head device to generate the required flow but, to ensure measurable fluid heights, coupled in series with a precision microfluidic resistor to regulate the flow rate, and therefore the FSS.

The project was interesting and feasible because the microfluidic resistor could be made with PDMS technology, and the scaffold could be housed in a small plastic box made by 3D printing. Furthermore, the results and technologies of the project could be used for subsequent improvement by placing almost all functions into a single integrated microfluidic chip.

4.11.1. Design of the cell feeding system

The cell feeding system defined in the feasibility study can be summarized in Figure 4.11.1. In the diagram, the fluid contained in the reservoir flows proportionally to the hydrostatic head of the circuit ΔH, or Δp, and inversely to the fluidic resistance of the resistor Rf, Equation (2.3.56). After the resistor, the fluid enters the scaffold housing, passes through the scaffold from bottom to top, and falls laterally into the housing. The collected fluid is sucked by a peristaltic pump and sent back to the reservoir.

The figure is a simplified functional diagram, derived from Figure 4.9.2-B, where the bioreactor was separated into different devices. It is only representative of a possible system to feed the cells of the scaffold, e.g., the bubble separator is not shown.

The flow rate of the peristaltic pump must always be higher than the flow rate that passes through the scaffold to avoid variations in level in the reservoir.

This means that the flow rate exiting the scaffold is lower than the theoretical flow rate of the pump, which is therefore forced to suck in air which is introduced into the reservoir in the form of bubbles, requiring a separator to avoid the formation of foam.

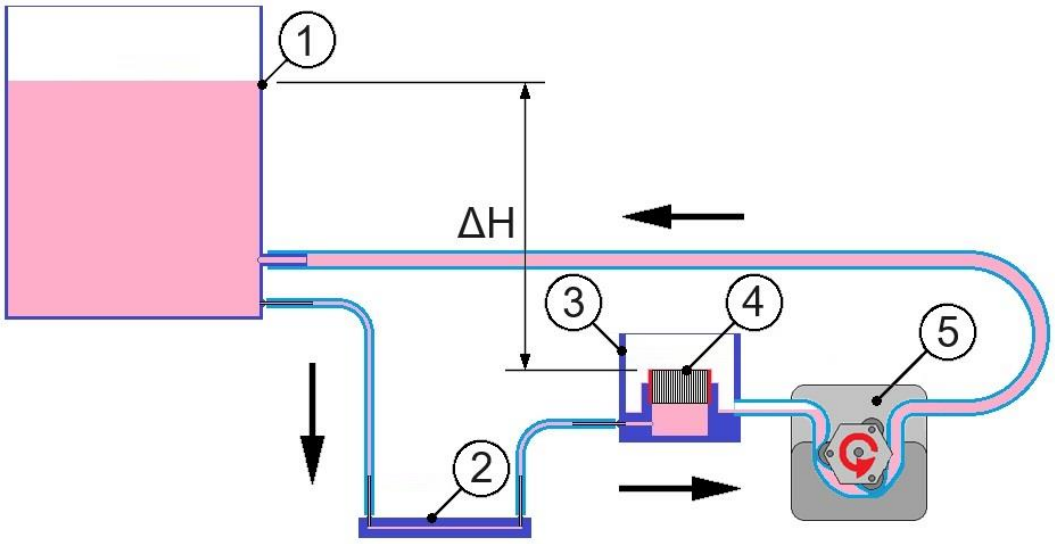

Fig. 4.11.1. *Cell feeding system (redraw from E. Salerno). (1) Reservoir. (2) Microfluidic resistor. (3) Scaffold housing. (4) Scaffold. (5) Peristaltic pump.*

The figure shows the direction of the fluid flow and the hydrostatic head ΔH that generates the flow. The flow is continuous, in a closed circuit, and without accumulation. Therefore the hydrostatic head ΔH always remains constant and can only be varied by changing the quantity of fluid in the reservoir or the height of the reservoir with respect to the scaffold.

4.11.2. Design of the scaffold housing

The scaffold housing had to have the following features:

- bio-compatible thermo-plastic material,
- 3D printing realization,
- house a scaffold with a diameter of 10 0/+1 mm and a height of 4 0/+0.6 mm,
- easy insertion and removal of the scaffold from the housing,
- strength and stiffness of its structure to insertion and removal operations,
- optimized structure without excess material,
- inlet connection with a 1.5 mm inner diameter hose,
- outlet connection with a 6 mm outer diameter hose.

A 2D CAD drawing of the scaffold housing is shown in Figure 4.11.2.

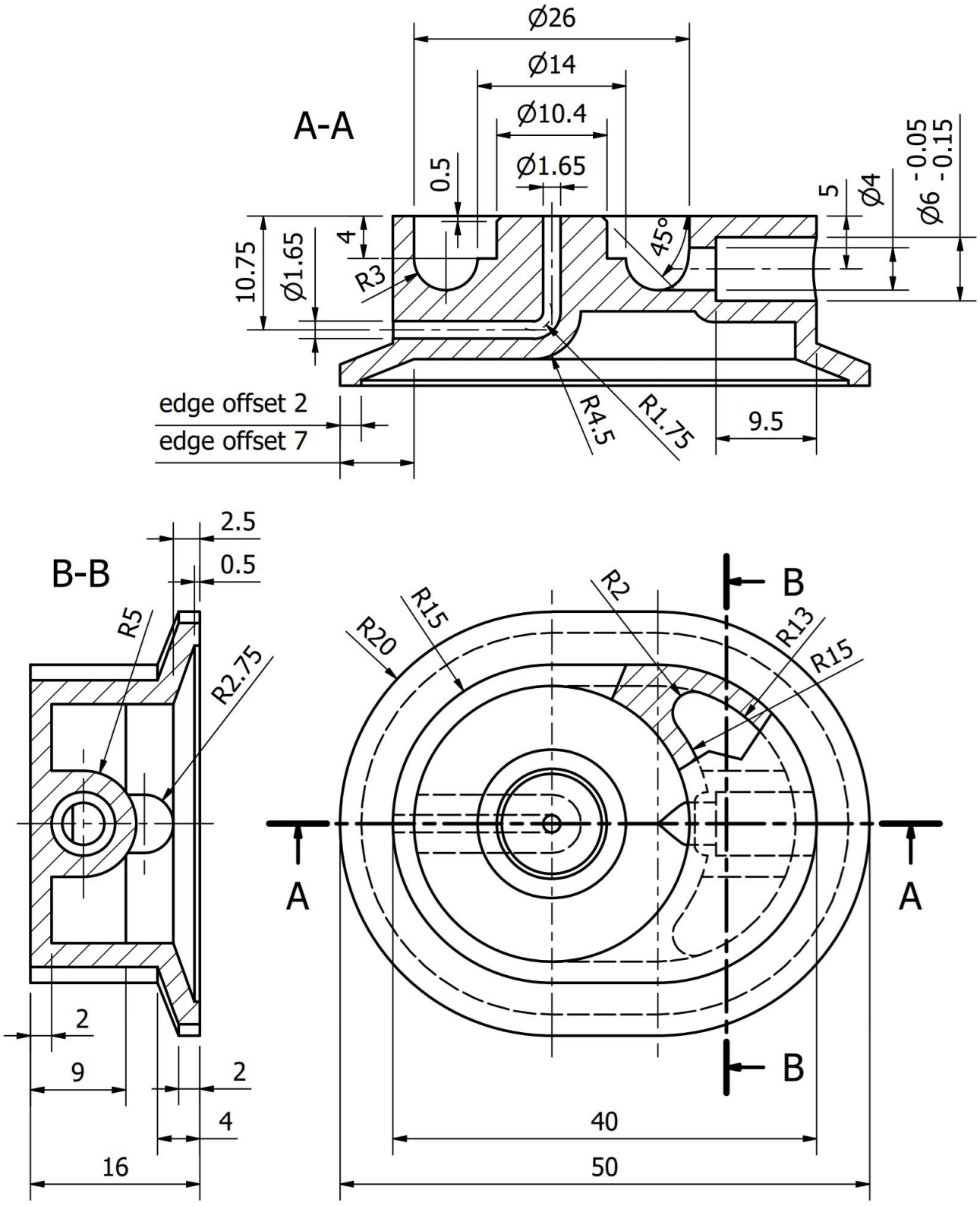

Fig. 4.11.2. *ISO technical drawing of the scaffold housing (dimensions in mm).*

A 3D CAD section of the housing with its accessories and scaffold is shown in Figure 4.11.3.

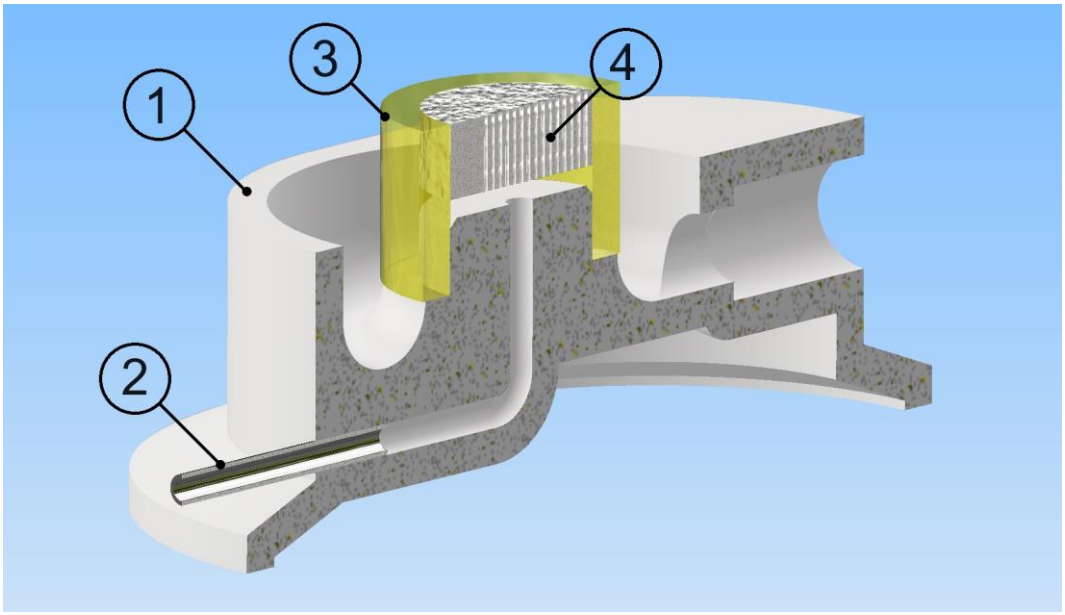

Fig. 4.11.3. *3D CAD drawing of the scaffold housing assembly.*
(1) Housing. (2) Coupler. (3) Gasket. (4) Scaffold.

As we can see from the figure, the fluid inlet is obtained via a 16G stainless steel straight coupler (Darwin Microfluidics, Paris, France), which can be coupled with a 1.6 mm ID x 3.2 mm OD Tygon tube. The scaffold is coupled to the housing using a gasket made by cutting a 15 mm length of Do 12 mm/Di 10 mm silicone hose (Incofar S.r.l., Modena, Italy), which allows to compensate for the differences in dimensions of the scaffolds. The diameter of the outlet hole allows the introduction and sealing of a Do 6 mm/Di 4 mm silicone hose.

4.11.3. Design of the PDMS microfluidic resistors

Considering the rectangular section for the resistor channel, the most used section with PDMS technology due to its simplicity, the design parameter that most affects its dimensions, width, length, and height was the FSS which was to be tested on bone cells and therefore the flow rate regulated by the resistor.

In the very low FSS range was chosen to test values of 10^2, 10^3, and 10^4 µPa which involved the design of three different types of microfluidic resistor.

The second important parameter was the hydrostatic head of the circuit ΔH which was set at around 100 mm, a variation of 1 mm was easily measurable and affected the FSS value relatively little.

Another assumption was that the other fluidic resistances of the circuit, distributed or concentrated, were negligible compared to that of the resistor.

The three resistors were designed based on these assumptions.

4.11.3.1. Microfluidic resistor calculations

For the calculation of the three resistors, based on Table 4.7.2 and Table 4.8.1, a reference scaffold was defined with average characteristics reported in Table 4.11.1, while for the fluid DMEM + 10% FBS at 37°C was considered with the characteristics reported in Table 4.5.1.

Table 4.11.1. *Average characteristics of the reference scaffold.*

	Diameter	Height	SFDR	Pore diameter	Pore number
	D_{SC}	H_{SC}	Rf/μ	D_{PO}	N_{PO}
	mm	mm	$1/m^3$	µm	-
H-BA Ref.	10.6	4.2	7.3E+11	260	200

Based on Equation 4.5.1 the mean constant fluid velocity u_{mean} in a channel-like pore was obtained as function of the fluid shear stress *FSS* on the cylindrical wall of the pore τ_{wall}, corresponding to the three test FSS values previously reported in this paragraph.

From the fluid velocity u_{mean}, thorough Equation 4.5.4, the total rate Q_{TOT} of the flow passing through the scaffold was obtained. The pressure drop Δp between the ends of the resistor channel is proportional to the hydrostatic head ΔH. From Q_{TOT} and Δp, thorough Equation 2.3.39, the relationship between the dimensions of the resistor channel was obtained.

Table 4.11.2 shows the dimensions of the microfluidic channel and the scaled fluid dynamic resistance (SFDR) Rf/μ of the three resistors corresponding to the three test FSS values.

Table 4.11.2. *Characteristics of the microfluidic resistors.*

	FSS	ΔH	h_R	w_R	l_R	Rf/μ
	µPa	mm	µm	µm	mm	$1/m^3$
FSS1 resistor	10^4	112	100	400	9.0	3.2E+14
FSS2 resistor	10^3	99	100	200	32.4	2.8E+15
FSS3 resistor	10^2	106	100	120	144.7	3.0E+16

As we can see, it was possible to keep the hydrostatic head ΔH around 100 mm for the three resistors, even if standard widths w_R were adopted for their channels. The value of the hydrostatic head is however theoretical, it is based on the characteristics of a reference scaffold and is subject to the imprecision of Equation 2.3.39. It will therefore have to be modified based on the actual morphological characteristics of the scaffolds under test.

An identical height h_R equal to 100 µm was used to obtain PDMS molds with the same relief height and therefore be able to use the same type of photoresist, as described in Section 3.2.2.

From Figure 4.11.1, Table 4.11.3 shows the SFDR of the circuit components [110].

Table 4.11.3. Circuit component SFDR.

	Number	Inner diameter Di_R	Length L_R	SFDR Rf/μ
		mm	mm	$1/m^3$
Reservoir-resistor hose	1	1.5	400*	3.2E+12
Resistor-scaffold hose	1	1.5	200*	1.6E+12
Coupler	4	1.2	15	3.0E+11
Scaffold housing	1	1.65	20	1.1E+11

Note: *(*) The length of the hoses is indicative, valid only for preliminary calculations.*

Comparing Table 4.11.1, 4.11.2, and 4.11.3, we can see that the SFDRs of microfluidic resistors are a few orders of magnitude higher than other SFDRs, confirming the assumption of considering only the resistance of the resistors for the calculation.

4.11.3.2. Design of the mask for the microfluidic resistors

Figure 4.11.4. shows the dimensions of the microfluidic resistors, according to Table 4.11.2.

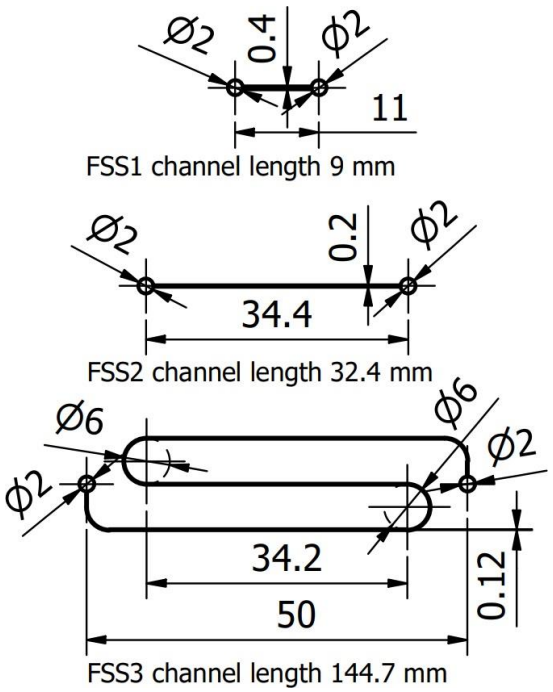

Fig. 4.11.4. *ISO technical drawing of the resistor (dimensions in mm).*

To standardize the overall dimensions of the three resistors, the longest channel, 144.7 mm long and corresponding to FSS3, was examined. With a simple "S" geometry it was possible to insert the channel inside a 60x17.5 mm rectangle, compatible with the 26x76 mm glass sealing slides, and with the possibility of inserting four molds on a single 4" diameter silicon wafer, as we can see in Figure 4.11.5 for the mask designed for the photolithography.

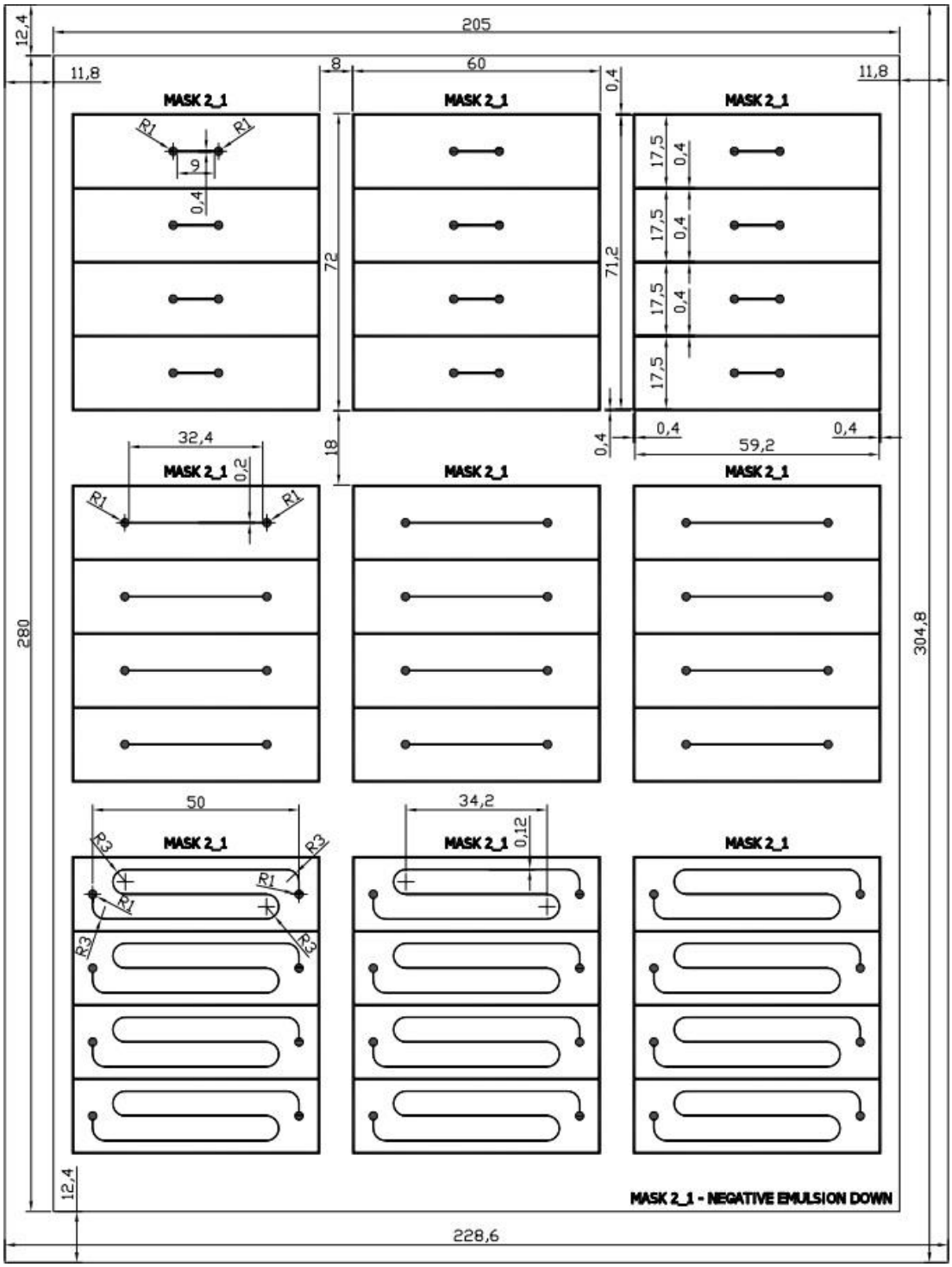

Fig. 4.11.5. *ISO technical drawing of the mask (dimensions in mm).*

4.11.4. Realization of the PDMS microfluidic resistors

The realization of the cell feeding system, and in particular of the microfluidic resistors, was carried out by Elisabetta Salerno and two graduate students, Alessandro Spila and Francesco Formentini. Below, in summary, are the main steps of realization.

The photomask, Figure 4.11.6, was made from chrome-coated glass (JD Photo Data, Hitchin, UK) at 1:1 scale from the 2D CAD drawing of Figure 4.11.5.

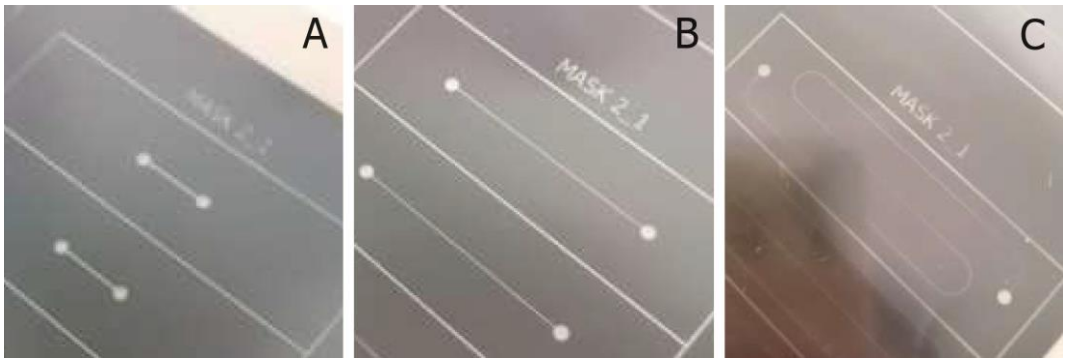

Fig. 4.11.6. *Details of the photomask (by E. Salerno).*
(A) FSS1 Resistor. (B) FSS2 Resistor. (C) FSS3 Resistor.

As explained in Section 3.2.2 and according to the manufacturer's instructions [52], a layer of SU-8 photoresist (Microchem - KAYAKU, MA-USA) top coated a 4" monocrystalline silicon wafer, then was selectively exposed to UV light through the photomask, and was developed by a solvent to remove unexposed parts of photoresist.

Liquid two-component Sylgard 184 PDMS (Dow Inc.-Dow Chemical Co., MI-USA) was poured onto the wafer with the SU-8 microfluidic circuits in relief, i.e., the negative mold, and polymerized according to the manufacturer's instructions [56], Figure 4.11.7.

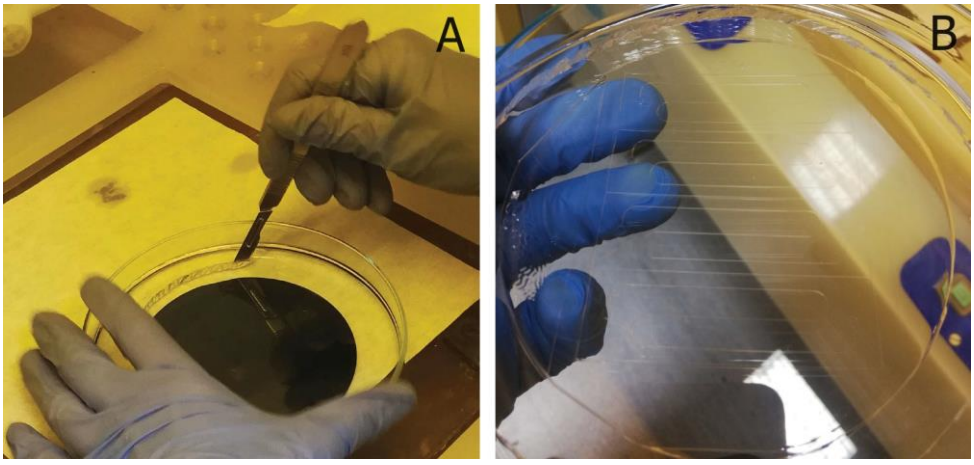

Fig. 4.11.7. *PDMS operations (by E. Salerno). (A) Cutting from the mold. (B) Raw resistors.*

The PDMS layer with etched microfluidic channels was cut into rectangles, according to Figure 4.11.5, to obtain the individual circuits, and the inlet/outlet pads of the PDMS circuits were pierced by a 0.5 mm biopsy puncher. Subsequently the PDMS rectangles were plasma bonded with 26x72 mm glass slides to seal the circuits, and tubing couplers were fixed in the inlet/outlet holes, obtaining the finished microfluidic resistors, Figure 4.11.8.

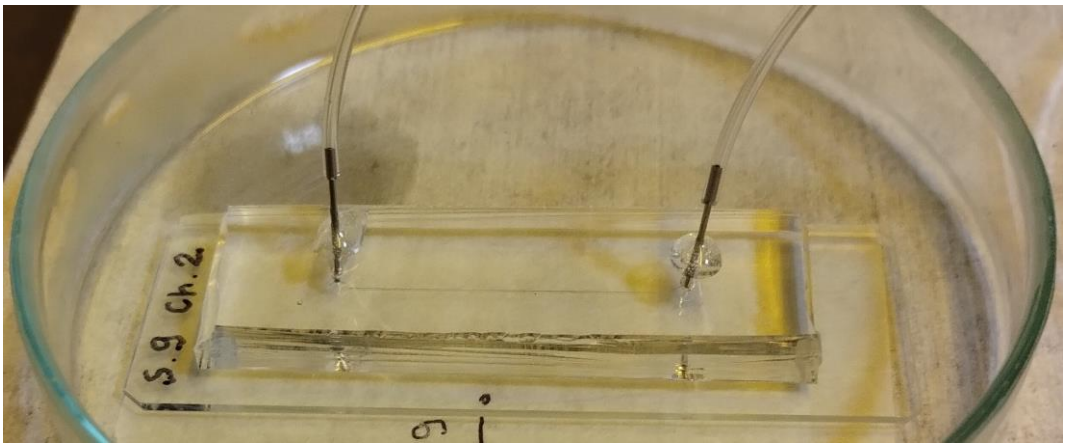

Fig. 4.11.8. *A finished microfluidic resistor with its tubing couplers (by E. Salerno).*

The main assembly of the cell feeding system was fluidic tested successfully, Figure 4.11.9. In the next phase the complete system will be tested with a reference scaffold, with known fluid dynamic characteristics, to verify the system parameters.

Biological tests will then begin.

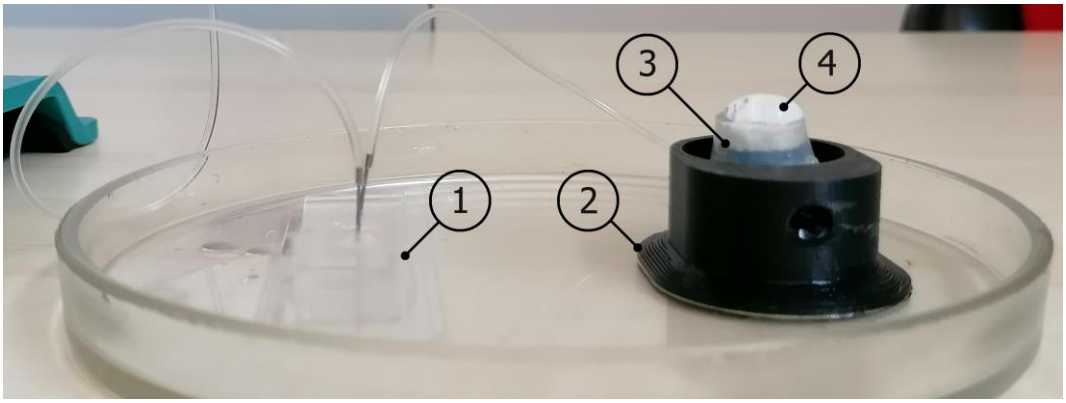

Fig. 4.11.9. *The main assembly of the cell feeding system (by E. Salerno).*
(1) Microfluidic resistor. (2) Scaffold housing. (3) Gasket. (4) Scaffold mockup.

4.11.5. Design of a microfluidic bioreactor-on-chip

The project to realize a PDMS microfluidic resistor was the first step to realize a more complex microfluidic bioreactor in which the functions of the resistors and the scaffold housing were packaged in a single, small-sized, reconfigurable chip.

Figure 4.11.10 shows the functional diagram of the chip. In it there are four inlets, two different resistors, and two outlets, as well as the scaffold housing. We can see that, by choosing different inlet points, one or the other of the two resistors can be selected.

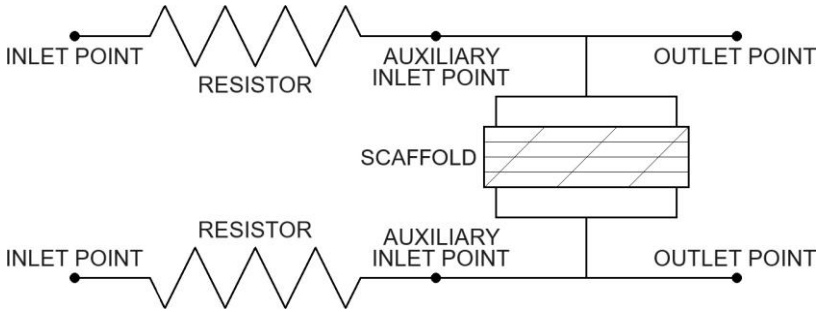

Fig. 4.11.10. *Fluidic diagram of the bioreactor-on-chip.*

Figure 4.11.12 shows a three-dimensional perspective drawing of the chip. The basis of the chip is a 26x72mm glass slide, the other layers are made of PDMS into which the microfluidic circuit and scaffold housing are made using the soft lithography technology of Paragraph 3.2.

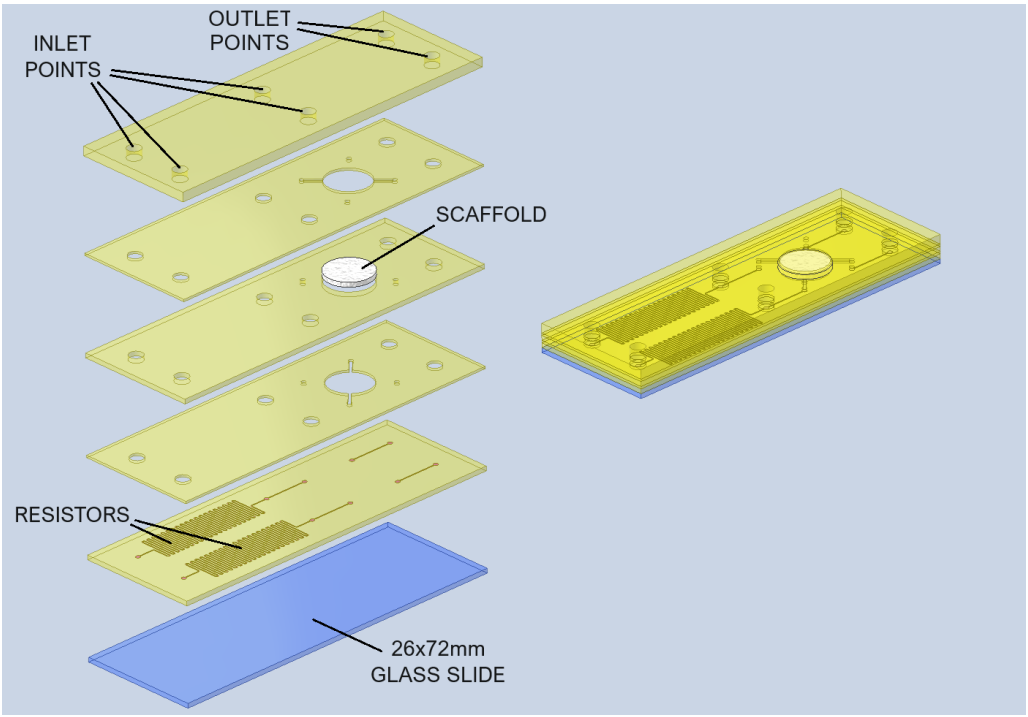

Fig. 4.11.12. *3D CAD drawing of the exploded and bonded bioreactor-on-chip.*

5. Microfluidic Chip Technology for Research

5.1. Introduction

The aim of this research was the production of microfluidic chips suited to the needs of scientific experiments which require quick and inexpensive device.

Indeed, in the research of Chapter 4, the chosen manufacturing solution for the microfluidic resistor was the classic PDMS technology. The choice was made for the advantages of this technology as reported in Paragraph 3.2, which were confirmed in the realization of the chip, as well as the disadvantages of numerous and critical processing steps, summarized in Figure 5.1.1, long production time and high costs.

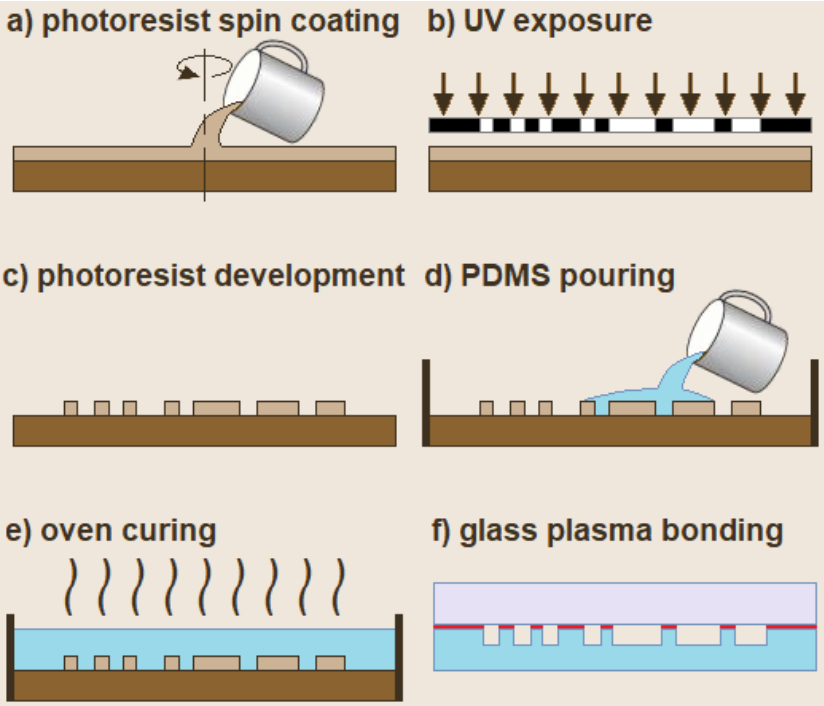

Fig. 5.1.1. *Manufacturing steps of PDMS technology (redraw from* [44]*).*

There are numerous types of commercial microfluidic chips, made with different technologies, to perform scientific experiments. But their biggest limitation, apart from their high price, is the impossibility of adapting their circuit to different research needs, limiting their use to simple applications.

This Appendix reports a project, developed as part of the doctoral course, of ablation with an ultra-short pulse laser on various materials such as cured silicone, as well as PDMS, in commercial sheets and glass for slides. Laser ablation was effective in engraving the material and cutting or drilling it to a depth of more than a millimeter without thermal deformations.

These experience suggested to design a new technology which involves the use of laser ablation on glass to create the circuit and subsequent plasma bonding with cured silicone in commercial sheets to seal the device, Figure 5.1.2.

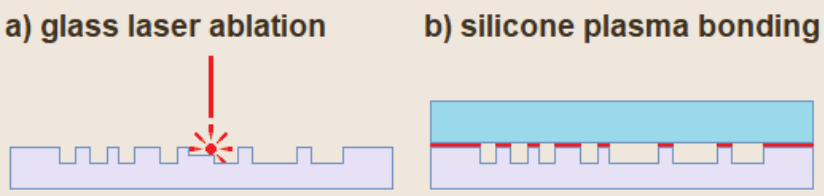

Fig. 5.1.2. *Manufacturing steps of the new technology.*

The simplicity and speed of laser ablation has been studied by several research [111], [112], [113], [114], but the sealing of the circuit was done solely by glass-to glass laser welding or gluing, solutions requiring a lot of precision and not indicated in biological tests due to the glass non-permeability to the gases necessary for the cell life, which is possible with silicone. There is no research available that validates or utilizes plasma bonding between glass and cured silicone in commercial sheets, including PDMS, despite the simplicity and cost-effectiveness of the solution.

The first step of the research was to compare the plasma bonding strength of some commercial silicones with laboratory cured PDMS, testing different process parameters. For this purpose a batch of simplified microfluidic devices was made and tested at increasing pressures.

The second step was to control the morphological characteristics of the microfluidic channels engraved by laser ablation. Accuracy in the realization of the microchannels, defects due to the shape of the laser beam and roughness of the ablated surfaces, may be different from that of the PDMS technology and affect the final result.

The third step was to compare the efficiency of devices realized with the new technology with those realized with the common technology, and highlight the points for improvement. This comparison has never been made in previous research on laser ablation. The type of device chosen for the comparison was a micromixer because it is simple and well-studied in many scientific researches. The methods used to measure the efficiency of the devices were experimental tests supported by CFD analysis.

5.2. Plasma bonding tests [115]

Polydimethylsiloxane (PDMS), Paragraph 3.2, is a silicone polymer that is easy to plasma bonding onto the glass, once the surfaces of the two materials have been activated, simply make them adhere to obtain the bonding, even without pressure. This is confirmed by the countless studies [51], [57], [116], and research that have used it [117], [38], [54], but only if the original components are used and the supplier's procedures are correctly followed [56].

Cured silicone in commercial sheets, including PDMS, are often not easy to plasma bond with glass. This problem, apart from the quality of the components, is due to the catalysts used for polymerization, such as tin, gold, palladium, and now platinum, useful for improving the stability of the polymer over time but which can reduce the activation of its surface with plasma treatment.

The aim of these tests was to select the best commercial products for plasma bonding and find the optimal parameters for their treatment. A selection was made through a qualitative test on the strength of the plasma bonding by simply trying to peel the silicones from their glass support. With some products, close control of the plasma treatment parameters was necessary to achieve effective bonding, with others bonding did not occur anyway. The chosen silicone was subsequently plasma bonded onto simplified glass microfluidic devices, realized by laser ablation, and subjected to a quantitative test by increasing pressure with a colored liquid. The pressure reached before the leaks occurred was a measure of the strength of the bond.

5.2.1. Plasma bonding

This technology consists of activating surfaces through treatment inside a cold plasma machine, i.e., a type of plasma in which the electrons are not in thermodynamic equilibrium with the other gaseous species present, as they are characterized by a much higher temperature than the heavier species (ions and neutral species). The gasses normally used in microfluidic devices are air and oxygen at an absolute pressure of some tenths of millibars. Collisional processes involving 'hot' electrons and 'cold' gas molecules can give rise to dissociation reactions and the formation of radical species. Considering our case of bonding between silicone and glass through surface activation, the silicone end groups can be replaced by silane groups (SiOH) making the surface more hydrophilic and increasing its wettability. After plasma activation, the silicone is immediately brought into contact with the glass surface, which is itself plasma-treated and therefore also rich in surface Si-OH groups, to form through a condensation reaction a Si-O-Si bond at the interface between the two materials [57].

The covalent Si-O bond, being a very strong bond, thus ensures irreversible and effective bonding between the two materials. So, to make this process happen, it is easy to understand that specific materials are needed so that these steps described above can take place.

In this research three different materials were used for glass bonding, two different types of PDMS and one FDA silicone, as well as other materials which proved to be unsuitable for plasma bonding. They are all part of the elastomeric silicone family, also known as silicone rubbers or silicones, i.e. synthetic polymers with repeating siloxane groups [Si(CH3)2O]n unit along the backbone.

The two different types of PDMS, the SSP-M823 (SSP Inc., NY-USA) is commercially available in sheets of different thickness and the liquid two-component Sylgard 184 kit (Dow Inc.-Dow Chemical Co., MI-USA) has to be cured in laboratory.

The last material is the L/SF silicone FDA (SATI Group S.p.A., Bologna, Italy), produced with components that are included in the list of suitable products according to U.S. Food & Drug Administration, Code of Federal Regulations Title 21, Chapter 1, Subchapter B, Paragraph 177.2600. Like SSP-M823, the silicone FDA is commercially available in sheets of different thicknesses, it has technical and physical properties like PDMS, but not its transparency. Furthermore, it is not as expensive as PDMS.

Bonding was carried out using the plasma cleaner Smart Plasma 2 (Plasma Technology GmbH, Herrenberg, Germany), Figure 5.2.1, with its data sheet reported in Table 5.2.1, which uses air as process gas.

Fig. 5.2.1. *Plasma cleaner Smart Plasma 2* [118].

Table 5.2.1. *Plasma cleaner Smart Plasma 2 – Data Sheet* [118].

	Description	Data
Inner dimension of vacuum chamber	W x H x D	110 x 110 x 200 mm
Chamber volume		11.5 liters
Material used	Vacuum chamber	Stainless steel
	Electrode	Aluminum
Plasma generator	Frequency	20 – 50 kHz
	Power	Max. 80W
Vacuum pump (recommended)	Flow rate	5 m^3/h
Operating pressure on the system		0.1 – 0.4 mbar
Pressure measurement		Pirani sensor
	Number of channels	1 (2 as option)
Process gas	Gas type	Air
	Primary pressure	Max, 0,5 bar
	Connections	6 mm hose connection

Before plasma treatment, glass and silicones were cleaned with an isopropanol (IPA) solution, then dried and heated with hot air.

Subsequently, the two materials were placed in the plasma machine chamber, together but separated, and processed for the set exposure time and power level. At the end of the process, they were extracted, joined and pressed together using a couple of spring clamps, and put back into the chamber for a second passage to stabilize the bonding.

7.2.2. Qualitative test

The qualitative test was performed using 26x76x1 mm glass slides (Waldemar Knittel GmbH, Bielefeld, Germany) and strips of identical size for the three types of silicone.

Glass and silicones were plasma bonded according to the procedures in Section 5.2.1, and based on the parameters present in the literature and after the first tests, it was set a chamber pressure at 0.3 mbar, three power levels of 40%, 60%, 100%, referring to a maximum power of 80 W, and three exposure times to plasma treatment of 30, 60, 120 seconds. In total, the plasma bonding of the three silicones was tested with nine different pairs of parameters, power and time, for a total of 27 samples.

The qualitative test was carried out immediately after the plasma bonding procedure, starting with a visual check of the amount of surface bonded between silicone and glass. Subsequently, by applying a tension to the edges of the silicone using tweezers was assessed the strength of the bond. The bonding was correct when bonding strength was equal to or greater than the material strength, i.e., the silicone was peeled off leaving a thin layer attached to the glass.

The qualitative assessment was assigned with figures ranging from 0 to 5, where 0 indicated no bonding and 5 a correct bonding on the whole surface. The middle values 1, 2, 3, and 4 were proportional to the bonding strength and bonding area.

The results obtained are shown in Figure 5.2.2, where in the three graphs, one for each type of silicone, the x-axis shows the exposure time, the y-axis the power, and the color map indicates the bonding assessment values.

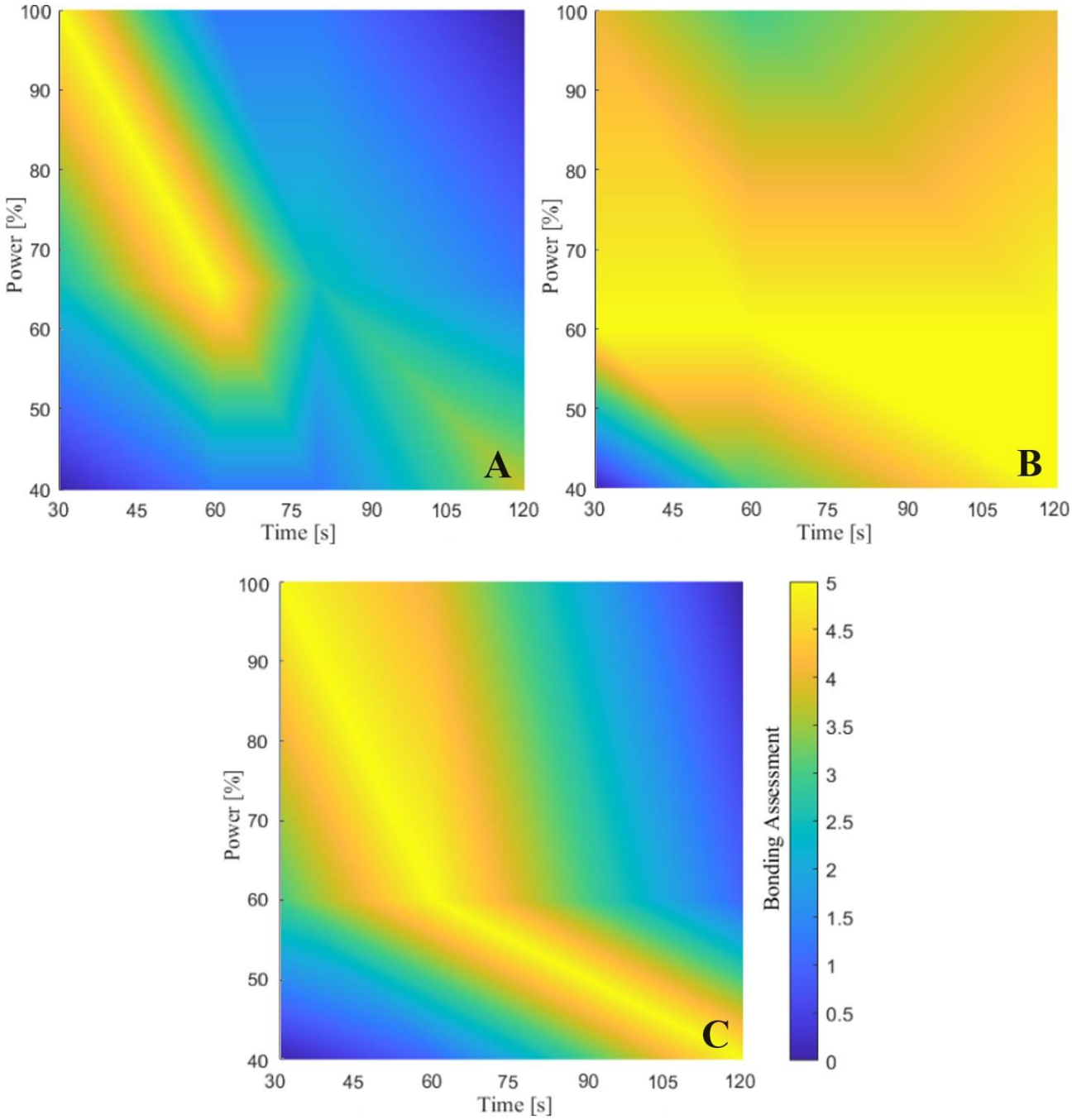

***Fig. 5.2.2**. Bonding assessment. (A) SSP-M823. (B) Sylgard 184. (C) L/SF silicone FDA.*

In all three graphs, the optimal parameters are positioned approximately on a diagonal. This suggests that the two parameters do not independently affect the bonding. However, to obtain the best bonding, the growth of one must correspond to the reduction of the other, and vice versa. PDMS SSP-M823 has a very narrow area of optimal parameters, PDMS Sylgard 184 has a large area, and L/SF silicone FDA has an intermediate area, which improves with high power levels.

5.2.3. Quantitative test

The result of the qualitative test highlighted that a narrow area of optimal parameters results in large deviations in bonding for small changes in parameters, so the SSP-M823 was discarded because it was not very reliable for plasma bonding. It was decided to utilize only the L/SF silicone FDA for the quantitative test because it has a sufficient area of optimal parameters, albeit smaller than Sylgard 184, is less expensive, has fewer work steps and a shorter lead time.

5.2.3.1. Test device

The test device, characterized by a simple geometry reported in Figure 5.2.3, was designed to test under pressure the bonding between glass and silicone layers. It was used the same 26x76x1 mm glass slides of Section 5.2.2, but three separated channels were engraved on the glass layer. The central one, the inlet channel, is sealed at one end and has a pocket at the other end. The two lateral channels are the drains, which are sealed at one end and open to the atmosphere at the other.

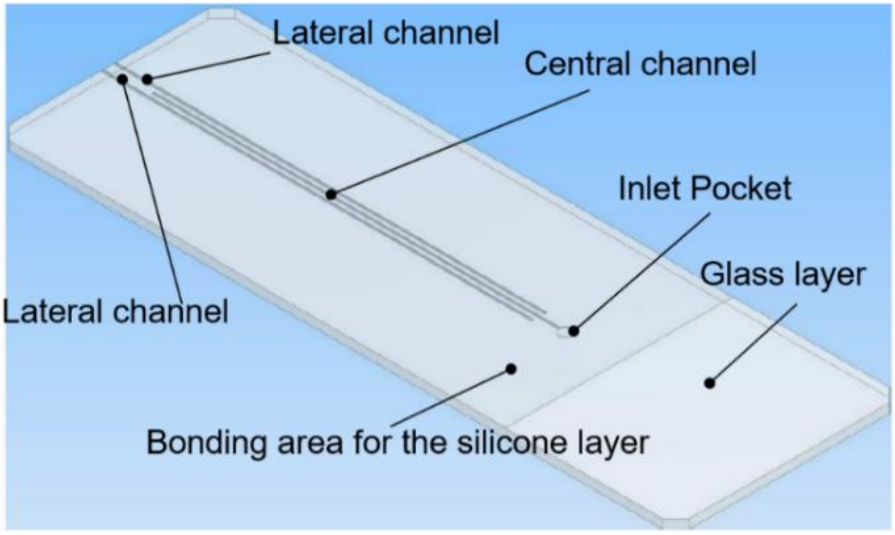

***Fig. 5.2.3**. Microfluidic device for the test under pressure.*

The geometry dimensions are reported in Figure 5.2.4. The area 0.8 mm wide and 33 mm long, between the central channel with pressurized colored liquid and the lateral channels open to the outside, is analyzed to validate the tightness of the plasma bonding. A leak in this area is detected by the liquid coming out from the lateral channels.

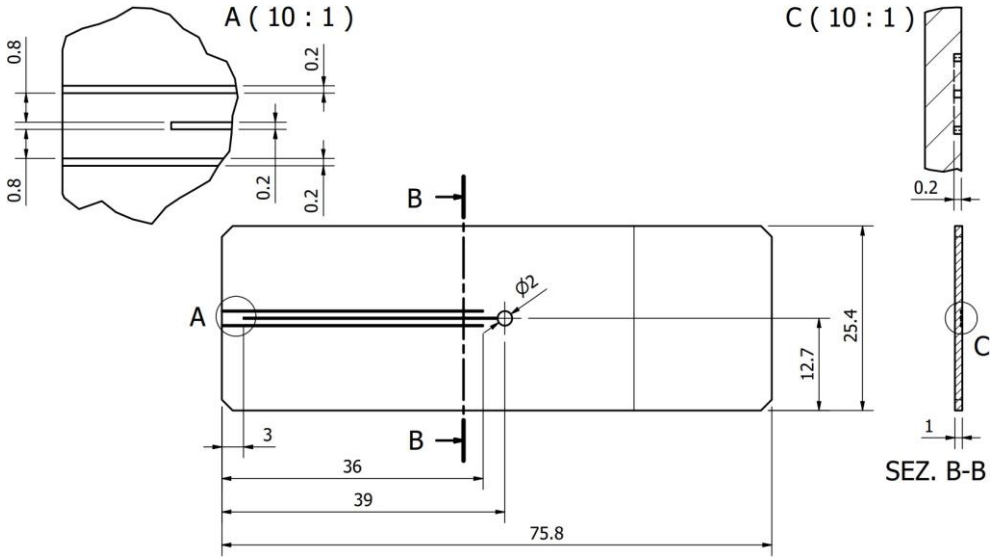

Fig. 5.2.4*. ISO technical drawing of the glass layer (dimensions in mm).*

5.2.3.2. Device laser ablation

The ultrashort laser systems opened new and unexpected possibilities in laser processing and micro-manufacturing such as laser processing in cold-ablation regime, with reduced heat affected zones and the processing of transparent materials such as glasses, ceramics, diamonds, polymers, and semiconductors thanks to multiphoton absorption [119]. It was decided to test this technology for the realization of the channels in our test device using the third harmonic beamline of an Atlantic 5 picosecond laser (EKSPLA, Vilnius, Lithuania). This source can produce pulses with a duration of about 10 ps with a repetition rate up to 1 MHz. In combination with a tight focus of about 10 μm it results in very high peak power, allowing sharp and fine engraving with limited glass heating and breaking, Figure 5.2.5.

The laser parameter, based on previous data collection on different test devices, were:

- 0,77 W measured power
- 355 nm wavelength
- 100 kHz repetition rate
- 300 mm/s scan speed
- 20-50-75-100 number of passes
- 3 μm fill spacing of the engraving lines

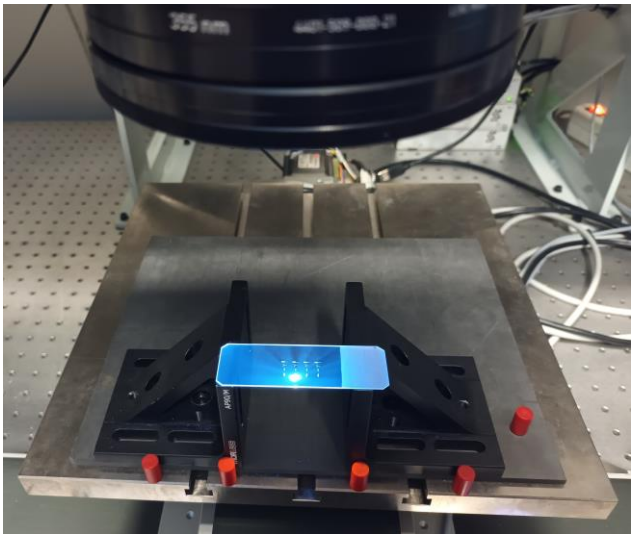

Fig. 5.2.5*. Ablation tests on a glass slide with the EKSPLA Atlantic 5 laser (by V. Siciliani).*

5.2.3.3. Ablation morphological analysis

The quality of the geometry obtained was analyzed measuring the dimensions of the channels and checking their shape by means of a confocal microscope Leica TCS SP8 (Leica Microsystems GmbH, Wetzlar, Germany). Scans were performed along the depth of the canal, with a step of 1μm for the 20 laser passes option, to reconstruct its shape, Figure 5.2.6.

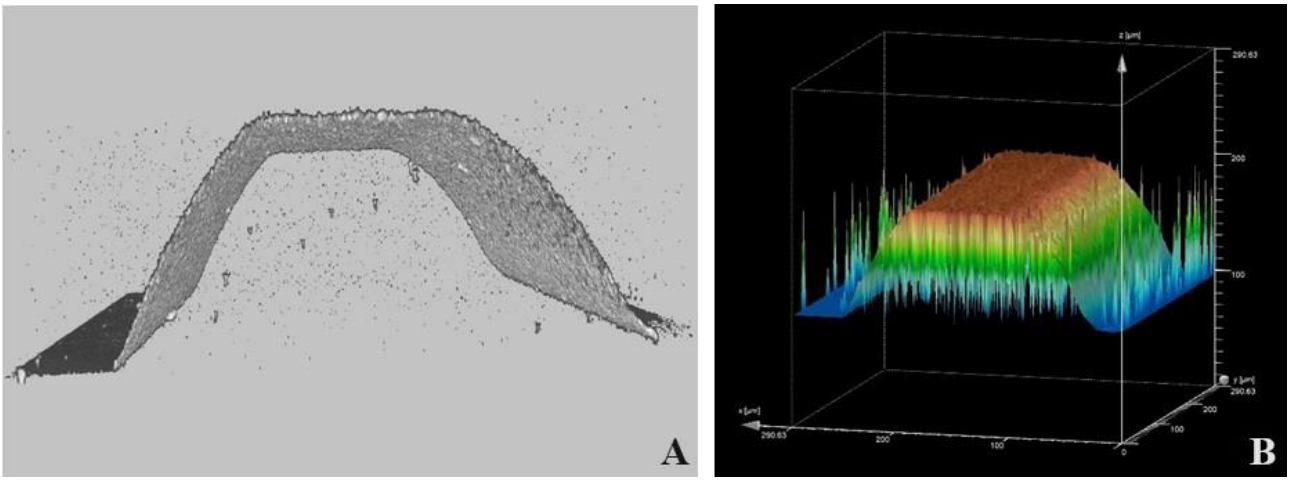

Fig. 5.2.6. *(A) Channel shape, 20 laser passes. (B) Channel dimensions, depth 100 μm.*

Factors such as depth/width ratio of the engraving, cone angle of the beam, and parallax errors inevitably lead to the U or V shape of the channel section [120].

The figure 5.2.7 shows the correlation found between the number of passes and the depth of the channel. The correlation is not linear beyond 50 passes, and the depth changes very little, probably for the same reasons that define the shape of the channel section.

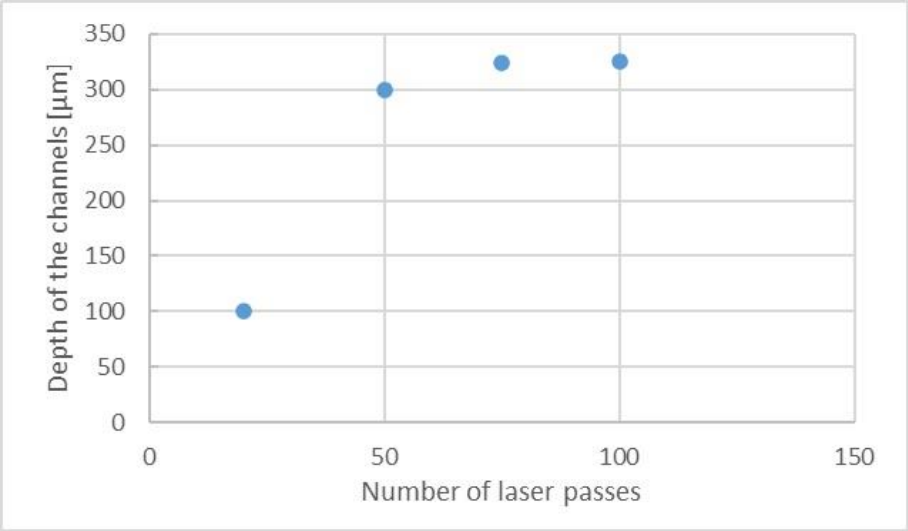

Fig. 5.2.7. *Correlation between the depth of the channels and the number of laser passes.*

It should be noted that while the shape and depth of the channels are very important for the correct functioning of microfluidic circuits, they are much less so for the devices used to test under pressure the bonding between glass layers and silicone layers. Furthermore, the depth of the channels of normal microfluidic circuits is much less than 0.1 mm and laser ablation is able to obtain channels with a very sharp section. All the samples used for pressure bonding tests were made with 20 laser passes, obtaining a channel depth of 0.1 mm.

5.2.3.4. Device plasma bonding

The plasma bonding was performed using the ablated glass slides and strips of identical size of L/SF silicone FDA but with a thickness of 3 mm.

Glass and silicone were plasma bonded according to the procedures in Section 5.2.1, and based on the qualitative test of Section 5.2.2, a chamber pressure at 0.3 mbar, three power levels of 40%, 60%, 100%, referring to a maximum power of 80 W, and three exposure times to plasma treatment of 40, 60, 90 seconds were set. Batches of three test devices were bonded with each pair of parameters, power and time, for a total of 27 samples.

5.2.3.5. First stage pressure test

The test procedures used to validate plasma bonding of glass and silicone using fluid pressure are not standardized and no common procedures exist, as far as is known. Therefore was decided, based on the experience, to create our own procedure that could simulate most of the needs of microfluidic circuits.

The first operation was to pierce the silicone of the test device above the inlet pocket with a 0.5 mm biopsy puncher (Darwin Microfluidics, Paris, France) in order to inject the pressurized fluid into the central channel of the device via a needle. The thickness of the silicone layer ensures a secure connection between the test device and the needle.

A hydraulic head pressure generator was created, Figure 5.2.8, with four different pressure of water levels, 200, 400, 800, and 1600 mm ($2.0 \cdot 10^3$, $3.9 \cdot 10^3$, $7.8 \cdot 10^3$, and $1.6 \cdot 10^4$ Pa). Liquid Flows Tygon Tubing Microfluidic Connection Kit (Darwin Microfluidics) was used for tubing and connections, 60 mL BD Biocoat Luer-Lock Disposable Syringe (Darwin Microfluidics) as water reservoir, graduated aluminum rod to support the reservoir, and water colored with Ponceau-S dye (Sigma-Aldrich - Merck KGaA, Darmstadt, Germany) as fluid.

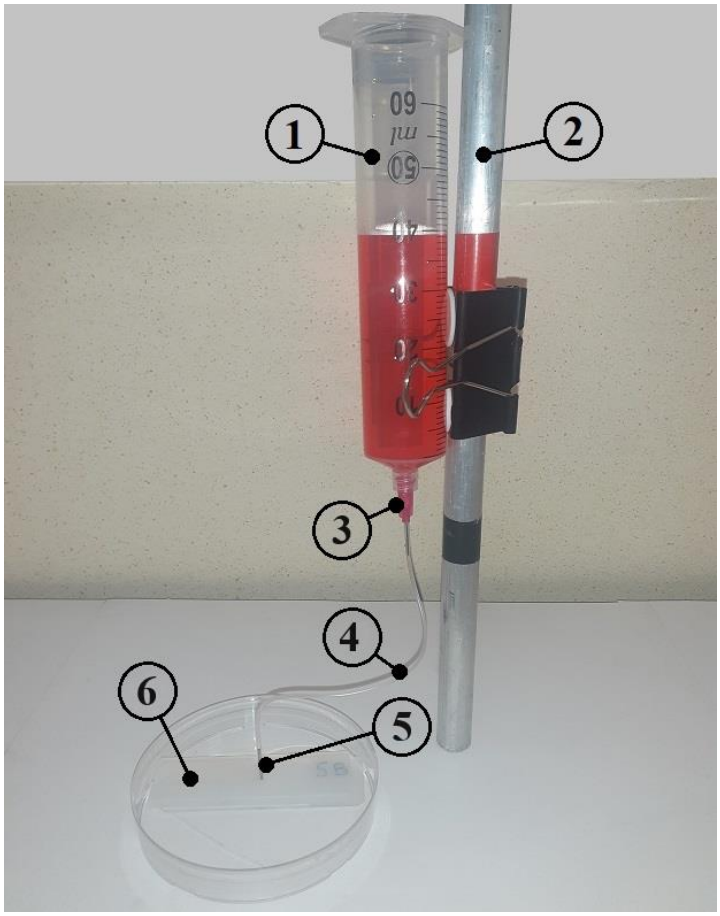

Fig. 5.2.8*. Hydraulic head pressure generator, 200 mm test. (1) Water reservoir. (2) Aluminum rod. (3) Syringe needle. (4) Micro tube. (4) Needle. (6) Test device.*

Each sample was tested at increasing pressure levels, raising the reservoir to the set levels, with a 60 seconds stand-by at each level. If a leak was detected during the 60 seconds stand-by, the test was terminated, and the sample was assigned the lower pressure level as exceeded.

5.2.3.6. Second stage pressure test

An air-water pressure generator was created, Figure 5.2.9, with three different pressure levels, $3.0 \cdot 10^4$, $6.0 \cdot 10^4$, and $1.0 \cdot 10^5$ Pa. It was used a manual mechanical pump to generate a maximum air pressure of 6 bar, a Do12 mm polyurethane air hose 5 m long as high-pressure air reservoir, a variable air restrictor with valve to reduce the pressure at the various output levels, a 0-1 bar pressure gauge, and a small reservoir as an air-water interface. All components were taken from the commercial market for industry, no manufacturer data.

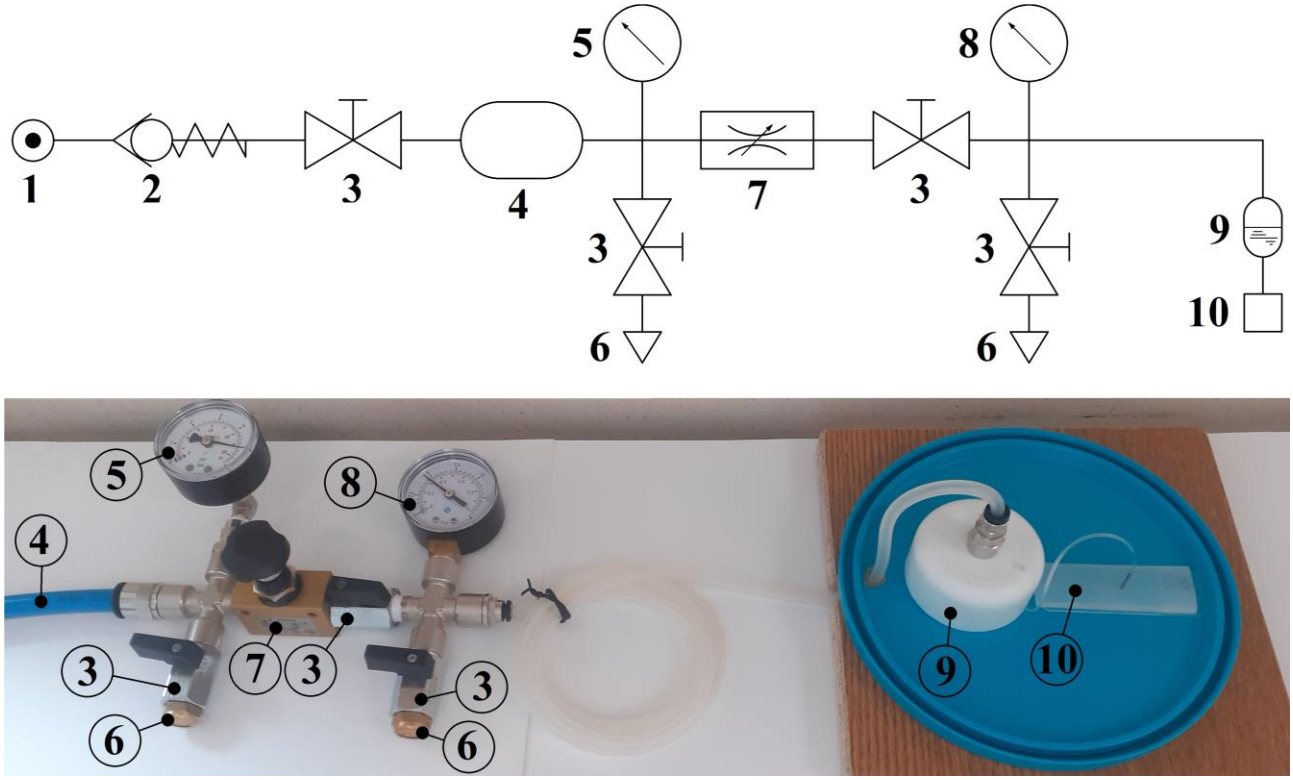

***Fig. 5.2.9**. Pressure generator. (1) Air inlet from the manual pump. (2) One-way valve. (3) Manual valve. (4) Air hose as high-pressure air reservoir. (5) 0-6 bar manometer. (6) Vent. (7) Air restrictor. (8) 0-1 bar manometer. (9) Air-water reservoir. (10) Test device.*

Each sample that passed the first step was tested at the new increasing pressure levels, opening the valve after the air restrictor and closing it again when the set pressure is reached, with a 60 seconds stand-by at each level. If a leak was detected during the 60 seconds stand-by, the test was terminated, and the sample was assigned the lower pressure level as exceeded.

5.2.3.7. Pressure test results

Figure 5.2.10 shows the pressure test values, average of the results of the three samples of each batch associated with its power level and time parameters in the plasma bonding process.

In Figure 5.2.11 the same values of the pressure tests are shown through a color chart, which more easily highlights the area of optimal parameters, centered on a power level of 80% and an exposure time of 60 seconds.

		Test pressure [Pa]		
Power [%]	100	Batch 3 8.7E+04	Batch 6 8.7E+04	Batch 9 7.2E+03
	60	Batch 2 6.7E+04	Batch 5 8.7E+04	Batch 8 6.7E+04
	40	Batch 1 6.5E+02	Batch 4 6.7E+04	Batch 7 6.7E+04
		40	60	90
		Time [s]		

Fig. 5.2.10. *Pressure test values*

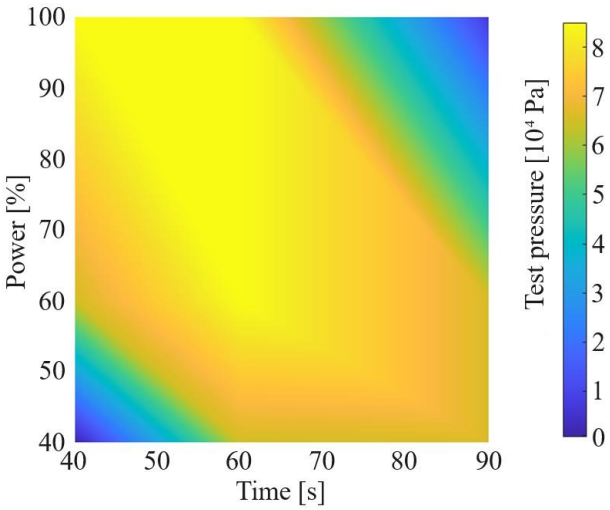

Fig. 5.2.11. *Pressure test chart*

5.2.4. Plasma bonding conclusions

The results of the pressure tests for the L/SF silicone FDA, shown in Figure 5.2.11, agree with the results of its qualitative tests, Figure 5.2.2-C. Again, the results confirm that the two parameters, power level and the exposure time, do not independently affect the bonding. However, to obtain the best bonding, the growth of one must correspond to the reduction of the other, and vice versa. The area of optimal parameters is large enough, allowing variations of the optimal parameters without compromising the quality of L/SF silicone bonding.
Furthermore, the pressure of $1.0 \cdot 10^5$ Pa (1 bar), withstood by the bonding of many samples in this area of optimal parameters, is very high and exceeds any need required by normal microfluidic circuits. It is conceivable that by restricting the area of optimal parameters, FDA silicone can withstand higher pressures in the case of special applications.

5.3. Efficiency tests

In Paragraph 5.2 it was demonstrated the reliability of this new, faster and simpler technology compared to PDMS technology which involves long processing times, specialized work and high costs. But accuracy in the realization of the microchannels, defects due to the shape of the laser beam and roughness of the ablated surfaces [121], may be different from that of the PDMS technology and affect the final result. The aim of these tests was to compare the efficiency of devices realized with the new technology with those realized with the common technology, and highlight the points for improvement. This comparison has never been made in previous research on laser ablation. The type of device chosen for the comparison was a micromixer because it is simple but with geometric characteristics that require precision and well-studied in many scientific research [122], [123], [124].

Based on the data in Section 5.2, microfluidic mixers were fabricated by laser ablation, the processing quality was checked by morphological analysis.

The methods used to measure the efficiency of the devices were experimental tests supported by CFD analysis. Experimental tests measured efficiency by analyzing and comparing the inlet and outlet fluids of the device. The tests were approximate by measuring the pH of the fluids and analytical by measuring the protein concentration of the fluids using the Bradford Protein Assay [125].

The simulation approach using CFD analysis [122], [126], [127], was investigated to verify whether it is a suitable tool for validating experimental tests for the case of the mixer device developed in this work. The proper setting of the mesh characteristics was carried out, highlighting the parameters chosen for model and mesh construction, and successively CFD analysis was applied to study the mixing efficiency of two fluids in the virtual device.

The results of the experimental tests and CFD were analyzed with each other and subsequently compared with those of devices obtained with common technologies. The discussion was able to judge the new technology and provide useful indications for its future improvement.

5.3.1. Mixing systems

The mixing system consisted of a syringe pump equipped with a pair of syringes that fed, through connections, the micromixing devices with different fluids but with the same flow rate. In the device the flows of the two fluids were united and then separated. The mixing efficiency was 100% when the compositions of the outlet fluids were equal to each other, 0% when the compositions of the outlet fluids were equal to those of the respective inlet fluids.

5.3.1.1 Mixing device

The mixing sector of the device was a microfluidic channel with herringbones. The herringbones were grooves with an asymmetrical V shape and were divided in mixing groups, each group was reversed in sequence, Figure 5.3.1 and Table 5.3.1. Each end of the mixing channel had two branches for the inlets or the outlets.

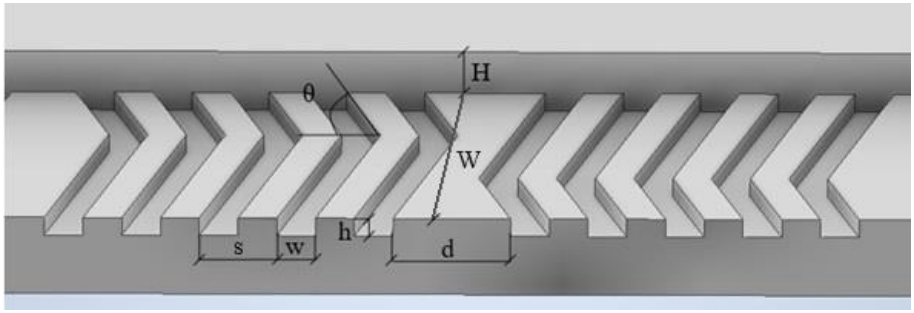

Fig. 5.3.1. *3D CAD mixing channel drawing.*

Table 5.3.1. Geometric parameters of the mixing channel.

Channel width	W	µm	200
Channel height	H	µm	70
Groove height	h	µm	30
Groove step	s	µm	90
Groove width	w	µm	45
Angle	θ	°	60
Distance	d	µm	140
N° of grooves per groups	-	-	5
N° of groups	-	-	60

Each end of the mixing channel had two branches for the inlets or the outlets, Figure 5.3.2.

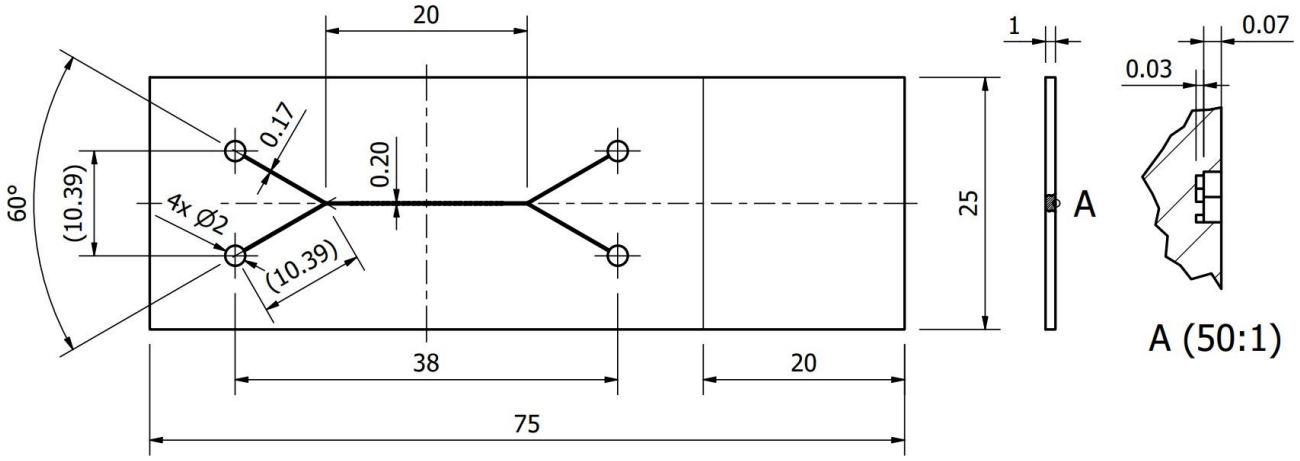

Fig. 5.3.2. *ISO technical drawing of the mixer device (dimensions in mm).*

The microfluidic circuit was engraved with an Atlantic 50 picosecond laser (EKSPLA, Vilnius, Lithuania) on a 26x76x1 mm glass slide (Waldemar Knittel GmbH, Bielefeld, Germany), at the end of each circuit branch a hole with a diameter of 2 mm was laser drilled through the slide.

The circuit was sealed by plasma bonding the glass slide with a 3 mm layer of L/SF Silicone FDA (SATI Group S.p.A., Bologna, Italy) with the same plasma cleaner Smart Plasma 2 (Plasma Technology GmbH, Herrenberg, Germany) of Section 5.2.1 which allowed us to use the same optimal parameters, power level of 80% and exposure time of 60 seconds.

Two strips of 3 mm silicone were plasma bonded on the free face of the glass slide, one for each pair of branch holes. The two silicone strips were pierced by a 1.5 biopsy puncher (Gima S.p.A, Milan, Italy) in correspondence with the holes, to allow fluids to enter and exit the microfluidic circuit, Figure 5.3.3.

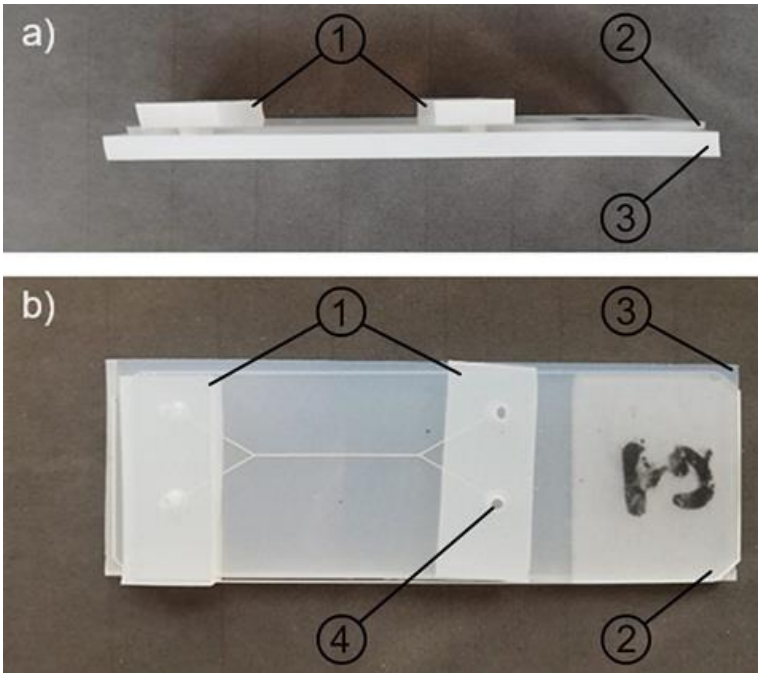

Fig. 5.3.3. *Microfluidic device side view(a) and top view (b).*
(1) Silicone strips. (2) Glass slide. (3) Silicone layer. (4) Inlet/outlet hole.

5.3.1.2 Syringe pump with connections

It was used a R462 Infusion/Withdraw syringe pump (RWD, Guangdong, China) to feed the inlets of the microfluidic device by two 50 ml plastic Luer Lock syringes (BD, NJ-USA) with 16G Blunt-end Luer Lock Syringe Needles, 1.6 mm ID x 3.2 mm OD Tygon tube, and 16G stainless steel straight couplers (Darwin Microfluidics, Paris, France), Figure 5.3.4.

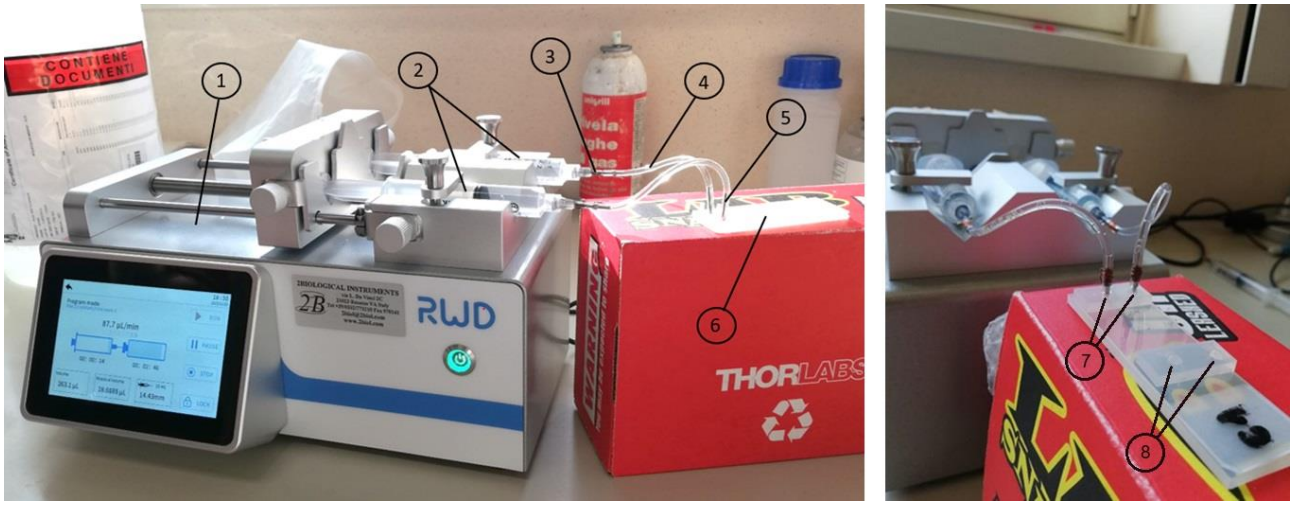

Fig. 5.3.4. *Mixing system. (1) Syringe pump. (2) Syringes. (3) Syringe needle. (4) Tygon tube. (5) Coupler. (6) Microfluidic device.(7) Inlets. (8) Outlets.*

5.3.2. Morphological analysis of the mixing device

The quality of laser engraving in the mixing device was checked using a confocal microscope Leica TCS SP8 (Leica Microsystems GmbH, Wetzlar, Germany), Figure 5.3.5, and a scanning electron microscope (SEM) ESEM Quanta-200 with ETD (Thermo Fisher Scientific - FEI , OR-USA), Figure 5.3.6 and Figure 5.3.7.

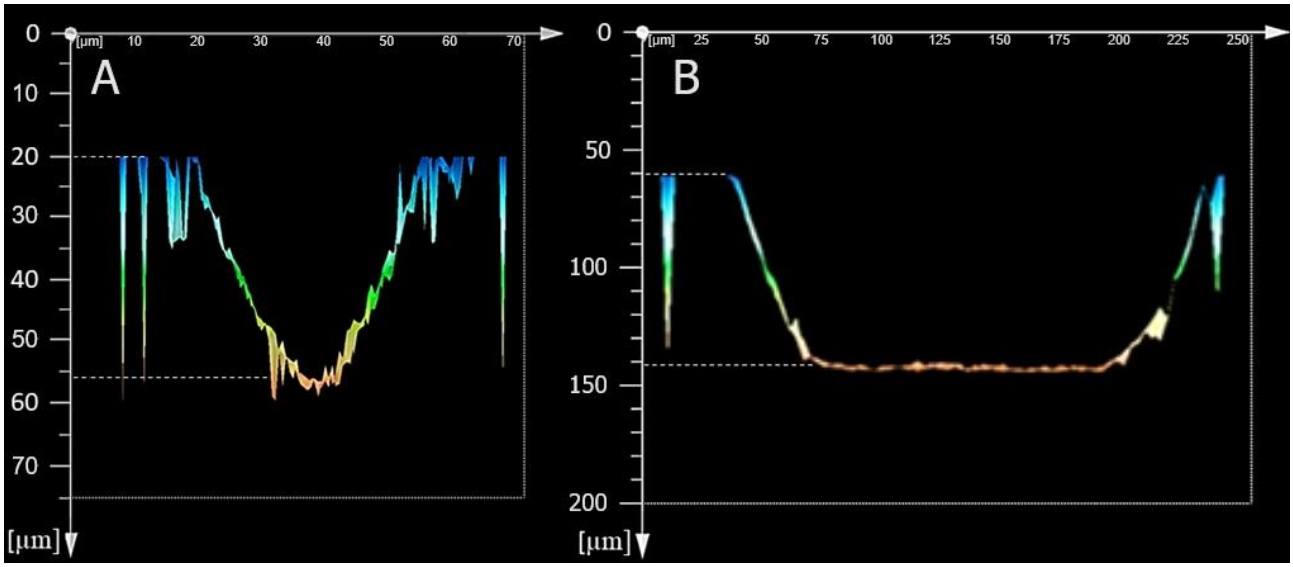

Fig. 5.3.5. *Cross-sectional profile reconstruction using confocal microscope of a single herringbone groove (A) and the main channel (B).*

The images obtained with the confocal microscope show that the cross-sectional profile of the herringbone groove (A) and the main channel (B) were not perfectly rectangular, with an inclination of the side walls of approximately 25° from the vertical, and their effective dimensions do not correspond exactly to the theoretical ones.

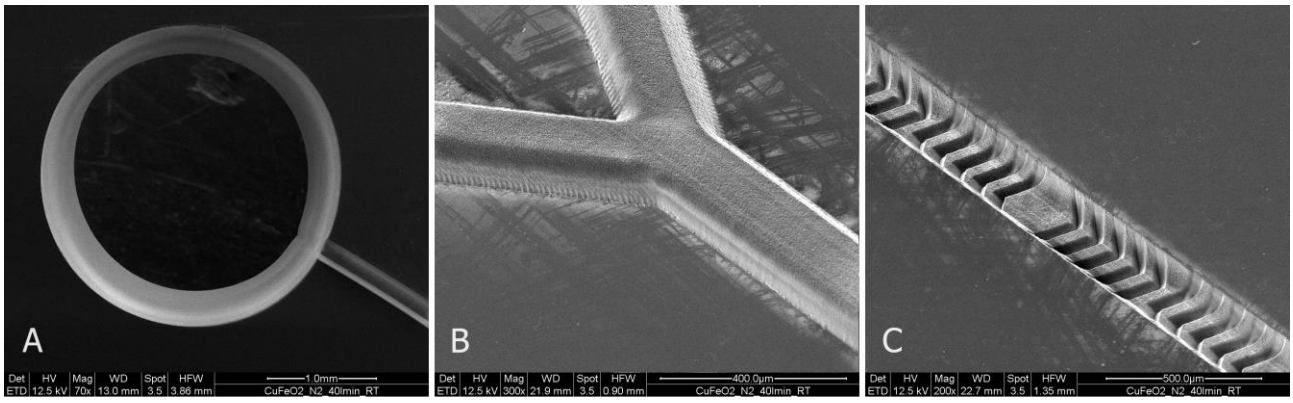

Fig. 5.3.6. *SEM microfluidic circuit details. (A) Laser-drilled hole and its branch. (B) Mixing channel and its branches. (C) Mixing channel with herringbones.*

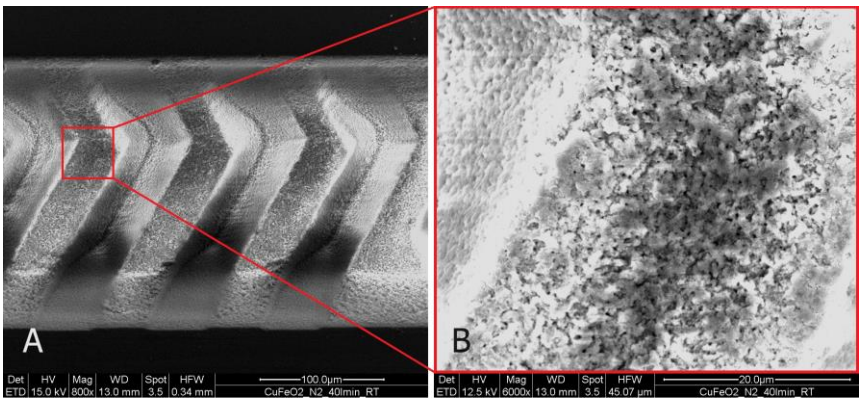

Fig. 5.3.7. *SEM herringbone magnification. (A) 800× and (B) 6,000× magnifications.*

The images obtained with the SEM show the roughness of the surface due to the ultrashort pulses of the laser. The peaks of the chaotic surface structure, Figure 5.3.7-B, are a few micrometers.

5.3.3. Test procedures

Three different flow rates were used for the mixing tests, with Reynolds numbers 0.5, 1.0, and 2.0, i.e. all in the range of perfect laminar flow. In this condition, two flows in a simple mixing channel do not interfere with each other, resulting in little or no mixing, Figure 2.2.1. Therefore, the correct design and execution of herringbones is essential for effective mixing.

To obtain the required volumetric flow rates *Q*, Table 5.3.2, the average velocity of the fluid u_{mean} in the mixing channel was calculated using the Reynolds number, Equation (2.4.24), for rectangular channel:

$$Q = u_{mean}\, A = \frac{\mu\, Re}{\rho\, D_H} A = \frac{\mu\, Re}{\rho}\, \frac{W + H}{2\, W \cdot H}\, W \cdot H = \frac{\mu\, Re\, (W + H)}{2\, \rho} \tag{5.3.1}$$

where *A* is the channel cross-section area, μ and ρ are respectively the average dynamic viscosity and density of the two fluids flowing in the mixing channel, D_H is the hydraulic diameter of the mixing channel calculated as Equation (2.4.22), *W* and *H* are the mixing channel width and height respectively. The presence of herringbones is not considered.

Table 5.3.2. Flow rates in the mixing channel at different Reynolds numbers and 20°C.

			Re	Velocity	Flow rate	Flow rate
Density average	1.00E+03	kg/m^3	-	m/s	m^3/s	µL/min
Dynamic viscosity average	1.01E-03	Pa·s	**0.5**	4.87E-03	6.82E-11	4.09
Channel hydraulic diameter	1.33E-04	m	**1.0**	9.74E-03	1.36E-10	8.18
Channel cross-section area	2.00E-08	m^2	**2.0**	1.95E-02	2.73E-10	16.36

Two different mixing devices were tested, one with herringbones (HMD) and the other without herringbones as a control (CTR).

Pairs of test samples were withdrawn at the same time from the devices, one sample for each outlet. The sampling time varied inversely with the flow rate to always have the same quantities of fluid for the samples. For each device, the different flow rates were performed sequentially with a stabilization time between them and varying the flow rate via the electronic control of the syringe pump.

5.3.4. Mixing test with pH measurement

The test was carried out feeding an inlet of the devices with distilled water (density 1.00 g/cm3, dynamic viscosity 1.00 mPa·s, pH 7.0, at 20°C), the other with acetic acid (density 1.05 g/cm3, dynamic viscosity 1.53 mPa·s, pH 2.5, at 20°C [8]) (ITW Reagents S.r.l., Monza, Italy).

One pair of test samples was withdrawn from the devices for each of the three flow rates.

A litmus paper kit was used to analyze the pH directly to the fluid samples. After wetting a litmus paper with a fluid sample, in a few seconds the change of the paper colors stabilized, in accordance with the pH of the sample, and it was possible to compare them with the color chart of the kit, determining the pH of the sample.

Figure 5.3.8 shows the pH of the sample inlets and outlets with a Re 1.0 flow rate; flow rates at the other Reynolds numbers showed no significant differences in pH compared to this figure.

The “0” strips show the pH of the inlets of all devices, the “1” and “2” strips show the pH of the outlets, HMD and CTR respectively. “A” strips show the pH of the inlet or outlet on the acetic acid side of a device, “B” strips show the pH on the water side.

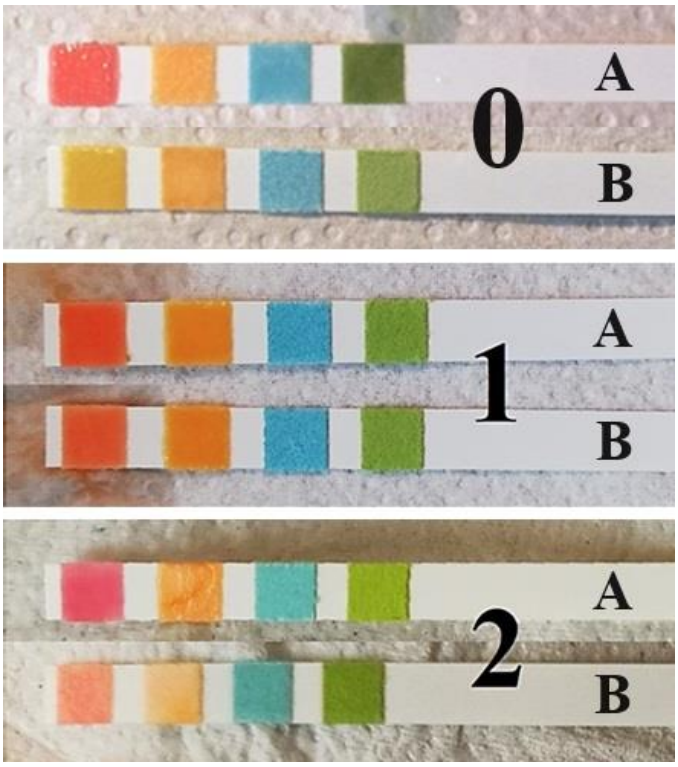

Fig. 5.3.8. *Litmus paper results. (0) Inlets of all devices. (1) CTR and (2) HMD outlets. (A) Inlets or outlets on the acetic acid side and (B) on the water side.*

The colors of HMD litmus papers (1) are not distinguishable from each other, the ends of the strips (A) and (B) both have an orange color corresponding to pH ≅ 4, showing good mixing of the device.

The colors of CTR litmus papers (2) are easily distinguishable from each other, the end of the strip (A) has a deep red color that is associated with a pH ≅ 3 and the end of the strip (B) has a light orange corresponding to a pH ≅ 5, showing poor mixing of the device.

5.3.5. Mixing test with Bradford Protein Assay

Bradford Protein Assay (BPA) is a colorimetric protocol utilized to determine the concentration of protein in a sample, the test was performed with the Pierce™ Bradford Protein Assay Kit (Thermo Fisher Scientific - Pierce Biotechnology, IL-USA) according to the manufacturer's instructions [128].

The first step was to freshly prepare a stock solution of 1 mg/mL Bovine Serum Albumin (BSA) (Sigma-Aldrich - Merck KGaA, Darmstadt, Germany) in distilled water.

The quantitative test was carried out feeding an inlet of the device with distilled water, the other with the 1 mg/mL BSA solution (density 1.00 g/cm3, dynamic viscosity 1.02 mPa·s, at 20°C [129]).

A batch of nine consecutive pairs of test samples was withdrawn from the devices for each of the three flow rates. Six standard samples were prepared only for the calibration curve with decreasing concentrations, via dilutions of the stock solution in distilled water, 1.0, 0.8, 0.6, 0.4, 0.2, and 0.0 (blank) mg/mL.

The assay was performed in three 96-well microplates (Fisher Scientific Italia, Segrate - Milan, Italy), one for each flow rate. For each microplate, 5 µL was pipetted into the wells from the standard samples, ten times, and from the test samples. Then, 250 µL of Coomassie reagent [128] was added to each well, Figure 5.3.9. The microplates were gently mixed with a plate shaker for 30 seconds, incubated for 5 min at room temperature, and mixed for another 30 seconds.

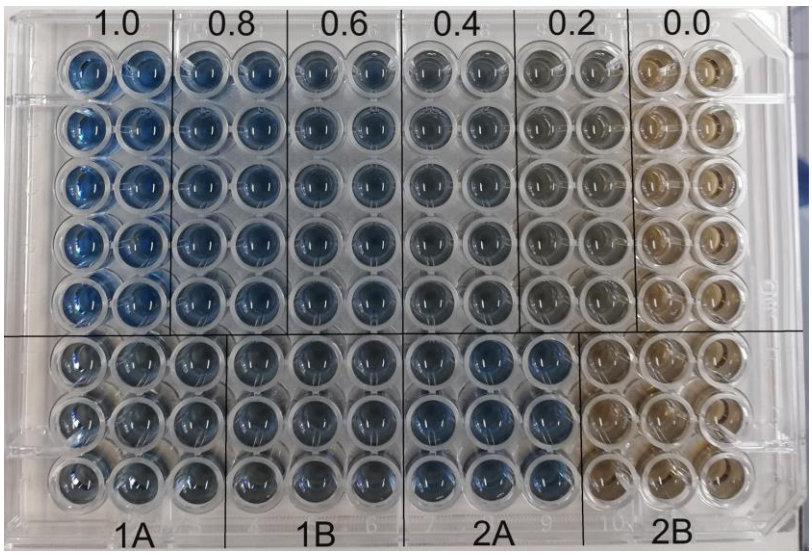

Fig. 5.3.9. *A microplate with Coomassie reagent. Above, wells with fluids from the standard samples, BSA concentration in mg/mL. Below, wells with fluid from test samples, (1) HMD samples, (2) CTR samples, (A) BSA side samples, (B) water side samples.*

Due to the reagent, the well colors change from blue, maximum concentration of BSA, to light gray, zero concentration of BSA, as in the standard sample wells. Wells of the two outlets of the same device with equal colors indicate equal concentration, i.e. good mixing, as in wells 1A and 1B. Different colors, conversely, indicate different concentration, i.e. poor mixing, as in wells 2A and 2B.

The absorbance of the wells was measured at 595 nm using a Multiskan FC Microplate Photometer (Thermo Fisher Scientific - Thermo Scientific, MA-USA). For a given flow rate, the calibration curve was made up of straight lines joining consecutive points, each point being equal to the average of the absorbances of the ten withdrawals from the standard sample of the corresponding concentration. The concentration of a test sample was obtained by interpolating its absorbance with the calibration curve [130], Figure 5.3.10.

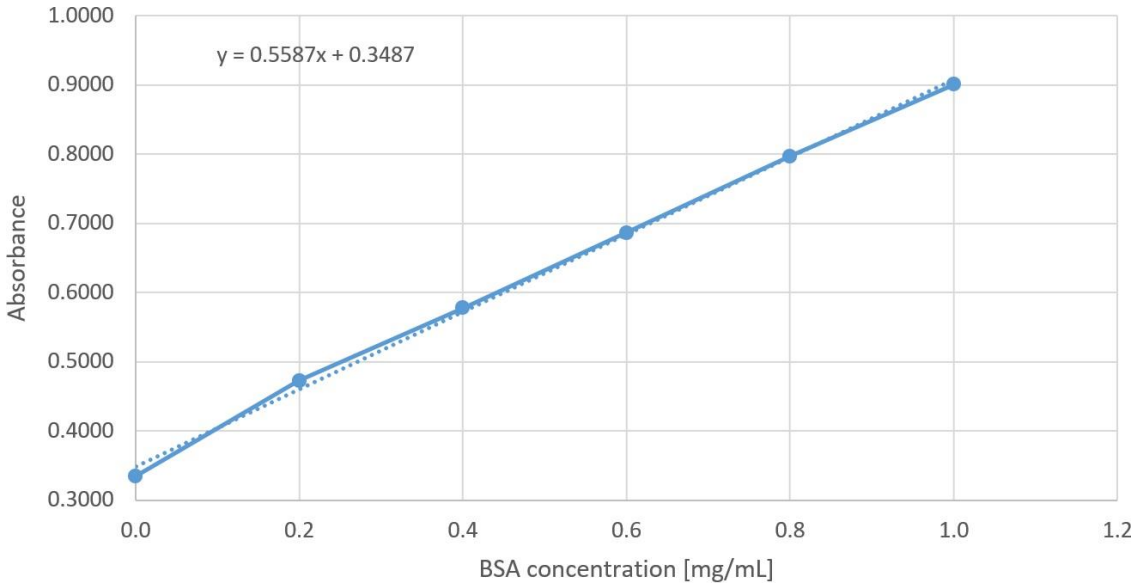

Fig. 5.3.10. *Calibration curve with regression line for the Re 1.0 microplate.*

The mixing efficiency *ME* for a given pairs of test samples was calculated with [131]:

$$ME = 1 - \frac{c_i - \bar{c}}{\bar{c}} \tag{5.3.2}$$

where $\bar{c}$ is the average of the concentrations of the samples, c is the concentration of the sample withdrawn on the BSA side of the device.

The mixing efficiency of a device, for a given flow rate, was expressed as the average of the mixing efficiencies of the nine pairs of test samples from a batch.

Statistical analysis using Student's t-test was performed with Excel Analysis ToolPak (Microsoft, WA-USA) to test the significance of difference in mixing efficiency between HMD and CTR, i.e., whether the null hypothesis H_0 of equality between the efficiencies was rejected by the test. The number of efficiency values n was equal to 3, the HMD and CTR values were paired for flow rate, the alternative hypothesis H_a was that the efficiency of HDM was always greater than CTR, one-tailed distribution, and the significance threshold α was set to 0.01, i.e., the difference probability p was considered statistically significant if $p<0.01$.

Figure 5.3.11 shows mixing efficiency of HMD, blue bars, compared with the mixing efficiency of CTR, orange bars, for each flow rate. Bars of the same color show their standard deviation (with Bessel's correction) at the top.

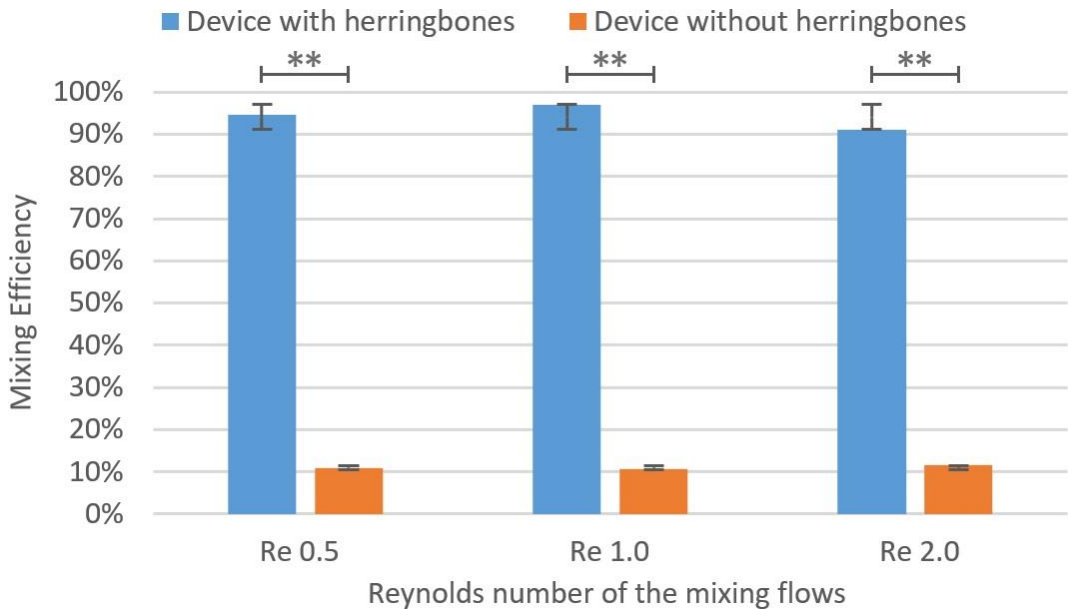

Fig. 5.3.11. *Blue bars represent the mixing efficiency of HMD at the different flow rates indicated by their Reynold numbers, orange bars represent the mixing efficiency of CTR. The line on the bar tops indicates the standard deviation. (**) Student's t-test $p < 0.01$.*

For all flow rates, the mixing efficiency of HMD, average of 94.1%, is much higher than that of CTR, average of 11.0%, a trend confirmed by the significant statistical differences reported by the Student's t-test analysis. This mixing efficiency is very close to that of devices obtained with current technologies which, with similar characteristics of the mixing channel, show values close to 100% [132], [133], [127], [124].

The results of the two devices show a reduced standard deviation, 1.7% for HDM and 0.3% for CTR, confirming their statistical reliability but also a non-significant influence of the flow rate on the mixing efficiency for the studied range of Reynolds numbers.

5.3.6. CFD mixing simulation

A CFD analysis was conducted on HMD with Fluent software (ANSYS Inc., PA - USA) to support the experimental tests and optimize the device. Furthermore, the comparison between test results and simulations will allow to improve the CFD approach in studying microfluidic flows and therefore will be useful for future research in this field.

5.3.6.1 Model and mesh

The system was modeled without the two inlet and outlet branches to simplify the geometry and reduce the computational cost. Therefore, only the mixing channel was modeled, with the two flows separated only at its beginning and end. Since the herringbones started at an appropriate distance from the branches, the flows were considered fully developed before mixing. The model, shown in Figure 5.3.12, represents the volume of fluid to be simulated.

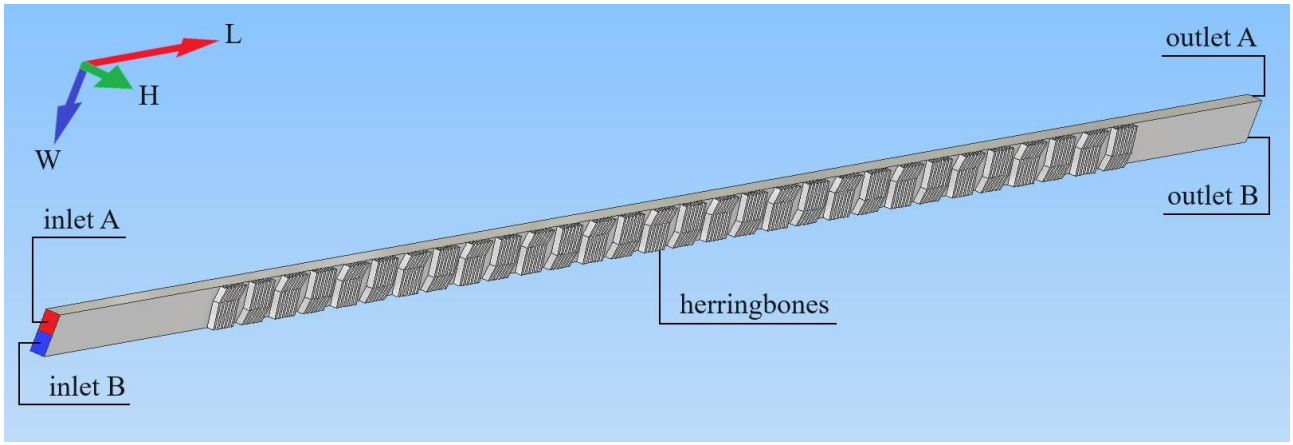

Fig. 5.3.12. *CFD geometry model.*

The Watertight Geometry interface of ANSYS Fluent has been used for the realization of the mesh. It started by generating a 2D mesh, Figure 5.3.13, by setting the ‘maximum size’ and ‘minimum size’.

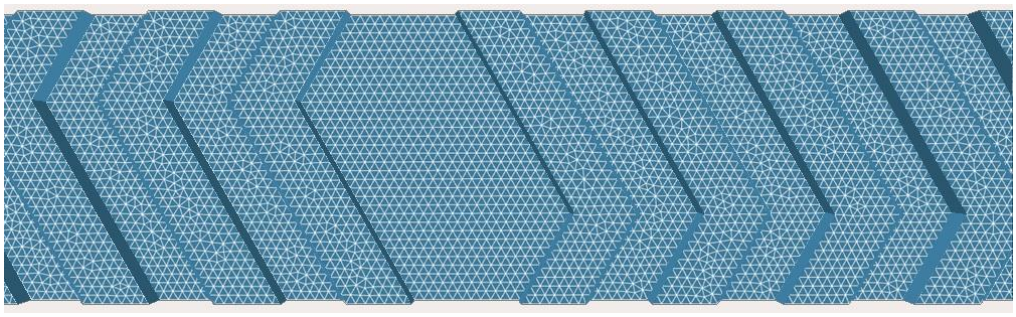

Fig. 5.3.13. *CFD 2D mesh.*

The ‘maximum size’ is normally set as 10% of the characteristic size of the inlet. In our case, starting from a height of 70 μm, a size of 7 μm was obtained. There was no need for 'local sizing' as the herringbones are extended over the entire length of the channel and the flow is of equal interest over the entire geometry. The resulting mesh is quite dense and has elements with a skewness of less than 0.7 and is therefore acceptable. It was then proceeded with the creation of the 3D mesh where ‘boundary layers’ were added on the walls with the ‘smooth transition’ offset method for the first three layers with a growth rate of 1.2. The elements were set up as ‘poly-hexcore’ to reduce computational weight resulting in a mesh of approximately 2,200,000 elements.

5.3.6.2. Simulation set up

ANSYS Fluent was used for simulation, switching to the interface for setting up and processing the results. To simplify the simulation set up It was considered the 1.0 mg/mL BSA solution as if it were water, given that their physical properties, density and dynamic viscosity, at 20°C are practically the same. With this assumption, a static simulation ran with water as the fluid for both inlets, then a patch was applied with an assigned tracer to one of the two inlets. In this way, by simulating with transient time, it is possible to quantify the mixing by comparing the tracer concentration values at the outlets.

The two inlets were set up as ‘velocity-inlets’ in which the velocity was calculated from the geometric parameters and by setting different Reynolds numbers, considered constant without transients with regard to Section 5.3.3. As with the experimental tests, the three flow rates at Re = 0.5, 1.0, and 2.0, which correspond to the velocities $v = 4.87 \cdot 10^{-3}$, $9.74 \cdot 10^{-3}$, and $1.95 \cdot 10^{-2}$ m/s, were investigated. A no-slip condition was set for the walls and the outlets were set as ‘pressure-outlets’ with atmospheric pressure. A laminar model was used for the simulation without considering heat exchange.

5.3.6.3. Mesh independence analysis

It is assumed that a coarse mesh, i.e. with relatively few elements, does not have the possibility of correctly representing the degree of mixing and that therefore the calculated efficiency is lower than the real efficiency. Therefore by increasing the number of elements, the calculated efficiency tends to increase asymptotically up to the real efficiency.

A mesh analysis was carried out to assess whether the parameters chosen to construct it were appropriate. Four meshes were chosen, two coarser than the reference mesh and two more precise, Table 5.3.3, to compare their mixing efficiency with that of the reference mesh.

Table 5.3.3. Mesh element numbers for the mesh independence analysis.

Mesh	1	2	3 - Ref.	4	5
Min-Max scaling factor	1/2	1/1.5	1	1.5	2
Element number	497,218	926,077	2,198,588	4,222,970	6,157,934

The mixing efficiency *ME* and the derived mixing efficiency D_{ME} were used to compare the correctness of the results of the different meshes. The mixing efficiency deviation σ_{ME}, modified from [127], [131], [133], can be defined as:

$$D_{ME} = 1 - \frac{1}{N}\sum_{i=1}^{N} \frac{c_i - \bar{c}}{\bar{c}} \tag{5.3.3}$$

where $\bar{c}$ is the average of the concentrations of the fluids and c_i is the concentration on the half-channel of the tracer side, calculated in *N=20* steps of 1 mm over the entire length of the mixing channel.

The derived mixing efficiency D_{ME}, unlike the mixing efficiency *ME*, does not evaluate the final efficiency but how soon the final efficiency is reached in the mixing channel.

The concentrations in the steps and outlets were calculated in the CFD simulation by integrating the local concentration values in the corresponding half-cross sections along the mixing channel. To obtain the values of the mixing efficiency *ME*, Equation 5.3.2, and the derived mixing efficiency D_{ME}, Equation 5.3.3, their formulas were entered into the simulation using the Equations Tool of ANSYS Fluent.

As we can see from Figure 5.3.14, with its values calculated for the Re 1.0 flow rate, the mixing efficiency *ME* remains the same for the five meshes, with values close to 100% indicating that the tracer has completely mixed throughout the entire flow, because *ME* is calculated only at the outlet of the mixing channel and is barely affected by the mesh, while the mixing efficiency deviation σ_{ME} is more affected by the mesh, because it is calculated over the entire length of the mixing channel.

The reference mesh, with approximately 2,200,000 elements, has an efficiency deviation σ_{ME} very close to that of meshes with a much higher number of elements, so it is acceptable to use it for the simulation to avoid a computational cost higher and longer times with a small improvement in terms of mixing resolution.

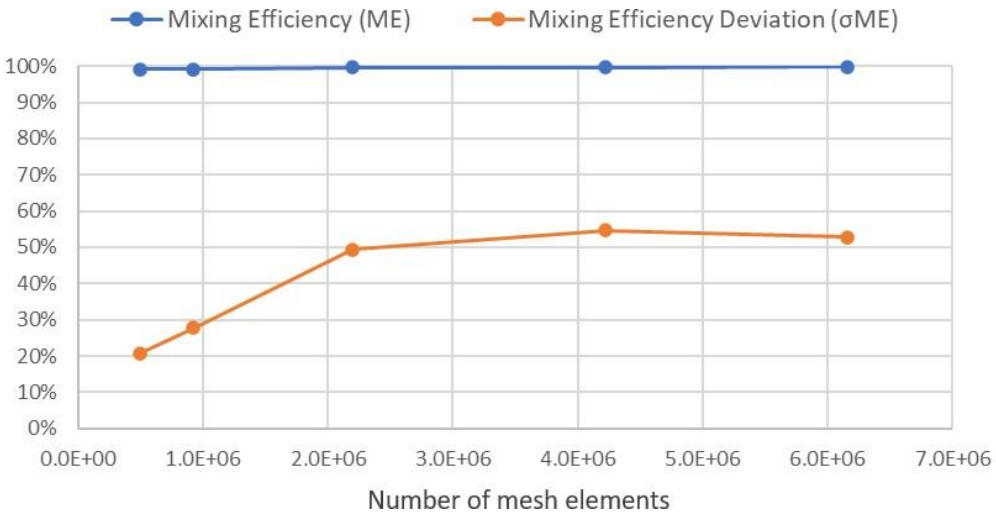

Fig. 5.3.14. *Mesh sensitivity analysis graph.*

5.3.6.4. CFD results and comparisons

Student's t-test was performed to test the significance of equality in mixing efficiency calculated with experimental BPA test and CFD simulation, i.e., whether the null hypothesis H_0 of equality between the efficiencies was not rejected by the test. The number of efficiency values n was equal to 3, experimental and CFD values were paired for flow rate, the alternative hypothesis H_a was that the efficiency of HDM was different from CFD, two-tailed distribution, and the significance threshold α was set to 0.05, i.e., the null hypothesis H_0 was not rejected if the difference probability $p \geq 0.05$.

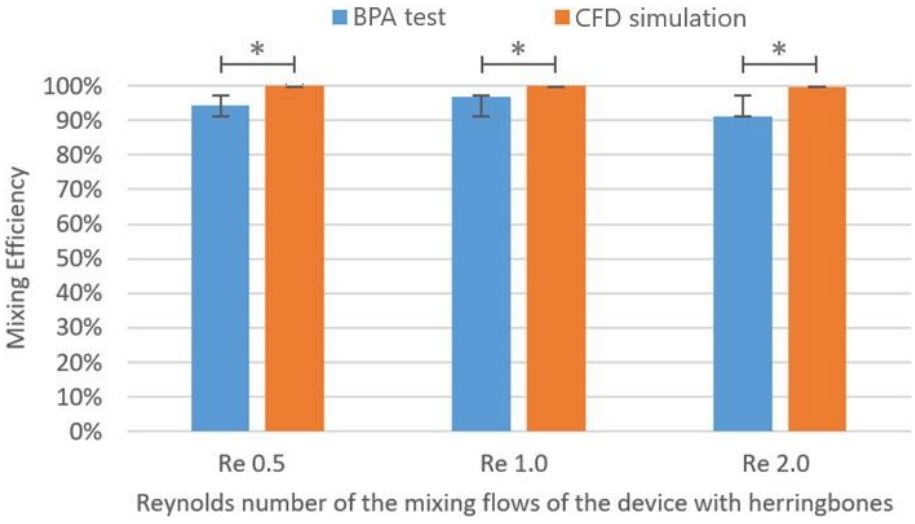

Fig. 5.3.15. *Mixing efficiency of HMD at the different flow rates indicated by their Reynold numbers. Blue bars represent the result of the BPA test, orange bars represent the CFD simulation. The line on the bar tops indicates the standard deviation. (*) Student's t-test* $p \geq 0.05$.

Figure 5.3.15 shows mixing efficiency results obtained from the CFD simulation on the HDM, orange bars, compared with those obtained from the experimental BPA test, blue bars, for the flow rates defined by the three different Reynolds numbers. Bars of the same color show their standard deviation (with Bessel's correction) at the top.

Flow and contour plots were taken to show the flow behavior and how and after how many cycles mixing takes place. As we can see from the Figure 5.3.16, as we expected, increasing the flow rate requires more cycles to achieve complete mixing. In addition, it can be seen that the tracer is deflected when the directions of the herringbones are changed, and it is this phenomenon that induces its mixing with water.

Flow and contour graphs were obtained from the CFD simulation to show the flow behavior and after how many cycles complete mixing occurs. As we can see from Figure 5.3.16, as expected, increasing the flow rate requires more cycles to achieve complete mixing. Furthermore, it can be seen that the tracer is deflected when the herringbone direction changes, and it is this behavior that increases its mixing with water.

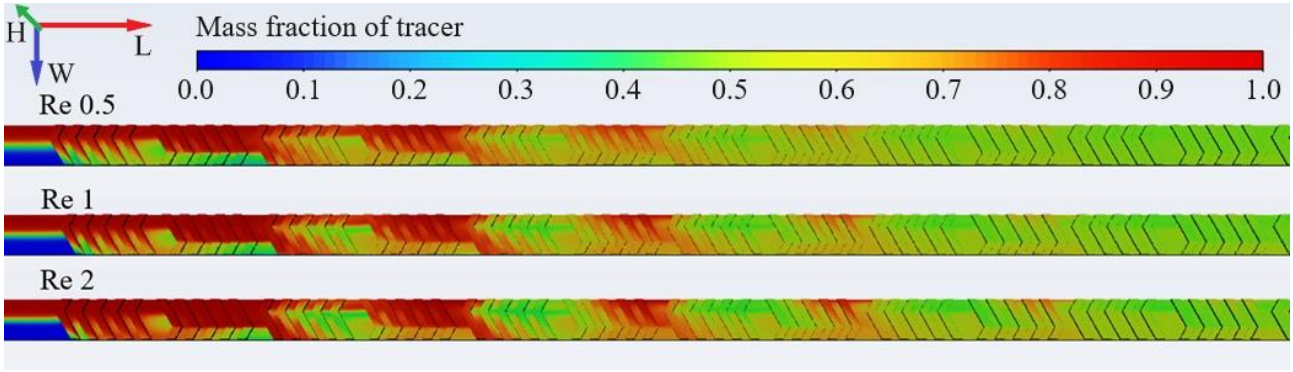

Fig. 5.3.16. *Flow mixings at different Reynolds numbers. The red flows represent tracer, while the blue flows represent water without tracer.*

To better understand the dilution of the tracer in the mixing channel, its concentration was measured along two axes, from the center of each of the two inlets to the respective center of the two outlets, and represented on a two-dimensional graph, Figure 5.3.17. Indeed, the contour diagram of the volume of the mixing channel, Figure 5.3.16, allows us to visualize only what happens on the walls, not the mass exchanges that take place inside the two flows. As we can see in Figure 5.3.17, for the two lines to both stabilize at the concentration value corresponding to complete mixing, almost all herringbone groups are needed. Furthermore, the concentration variation of the two lines is not monotonic but their values oscillate in counter-phase around opposite average values which tend to match.

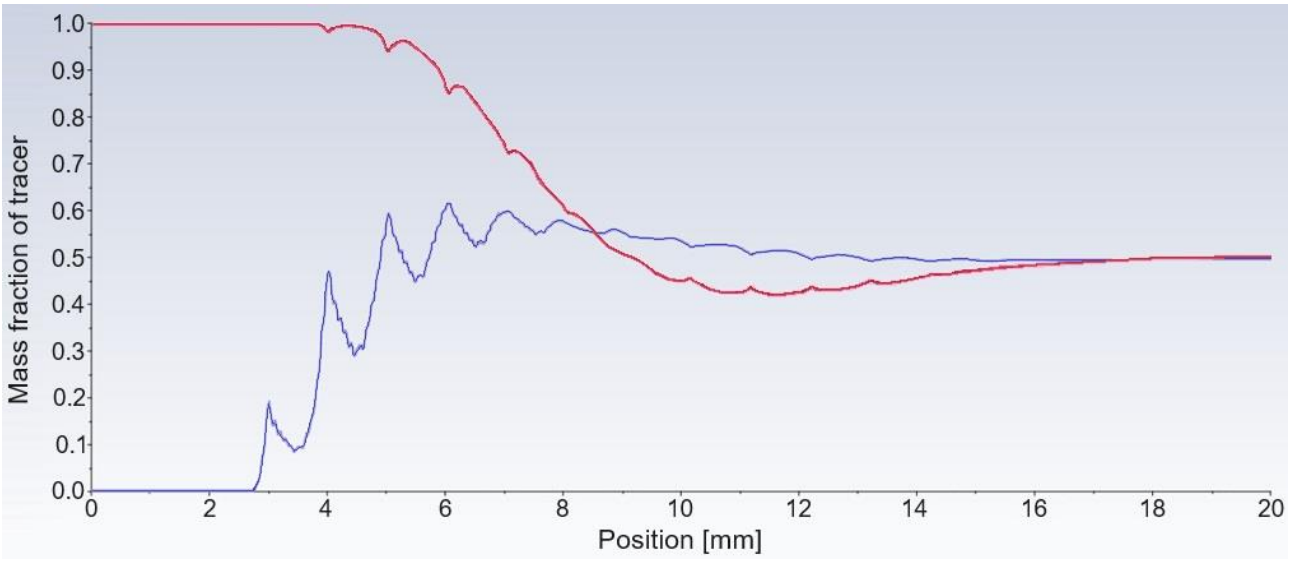

Fig. 5.3.17. *Tracer concentrations along the mixing channel. Red line represents the concentration along the tracer side of the device, blue line the water side.*

This, as before, can be explained by the particular arrangement of the herringbones which, by varying their direction between one series and another, move the flows of the two fluids from one part of the mixing channel to the other.

Indeed, after the first mixing cycle, this deflection causes the tracer flow to disrupt the water flow, creating a central vortex, the zone where complete mixing first occurs, Figure 5.3.18.

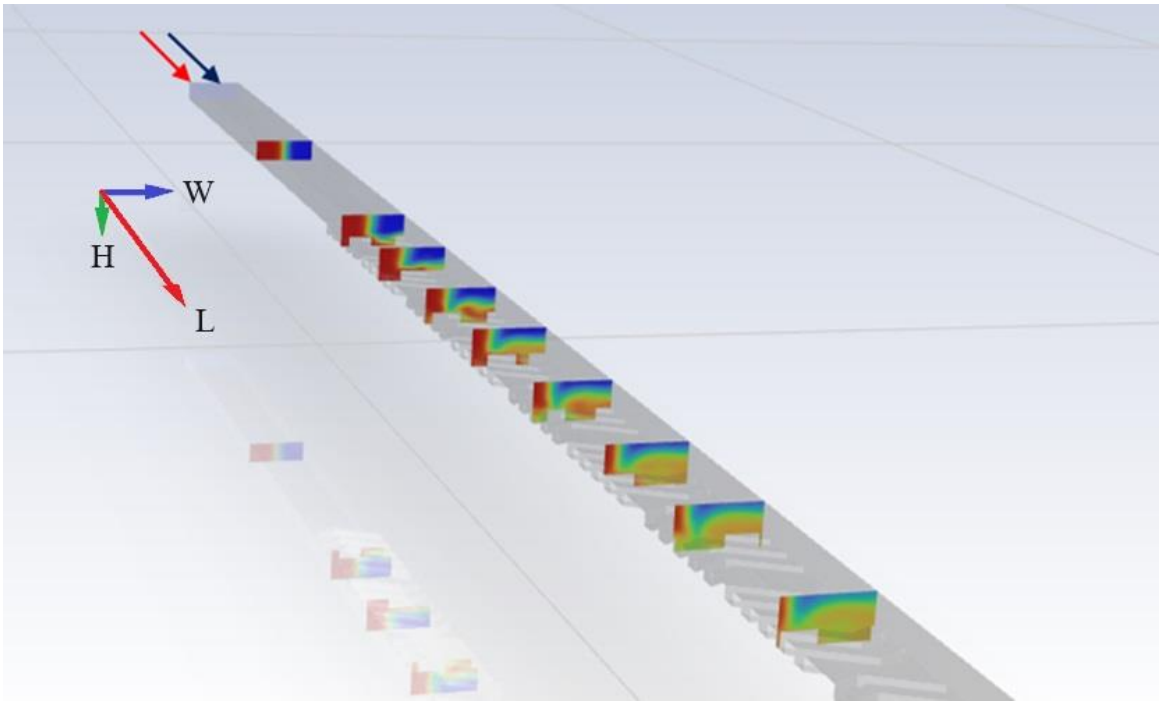

Fig. 5.3.18. *Step cross sections along the mixing channel representing the evolution of mixing between the tracer flow and the water flow.*

5.4. Conclusions on microfluidic chip technology

The current technologies for the manufacturing of microfluidic circuits are expensive and slow, this research was aimed to test a new technology, with reduced times and costs, consisting in the realization of microfluidic devices with a layer of glass sealed with a layer of silicone. The device channels were produced on the glass layer by laser ablation using an ultrashort laser source. A commercial silicone layer was joined to the glass layer using the plasma bonding process.

Although these two technologies are not new in the scientific literature, their use for the production of the microfluidic devices has only been explored to some extent. It is very challenging to find clear indications for the laser ablation manufacturing of the channels on the glass layer, in particular regarding the setting of the laser parameters and number of passes with respect to the channel geometry, the surface finish and also the control of the shape of the channels section.

The plasma bonding of the glass and silicone layer was thoroughly investigated, using several silicone layers, testing different plasma machines, polishing and pre-heating the surfaces and setting different parameters. These data are not readily available in literature and have been reported in this article to describe the work done, the criticality of the process and to guide other researchers who need to go through the same process and test other materials. Finally, two different tests were described for the validation of the bonding and the assessment of its quality, showing then the results obtained and the effectiveness of the process.

Two mixing devices, one with herringbones and another without, were realized with this new technology to compare their mixing efficiency. At low Reynolds numbers mixing is poor without herringbones, and the quality of the herringbones is important for good mixing. The mixer efficiency of the two devices were quantitatively tested by measuring the outlet concentrations in protein of two different fluids. The results of the experimental tests demonstrated a high mixing efficiency of the device with herringbones, only slightly lower than that of devices realized with the commonly used technology. The results of the CFD simulation also demonstrated a high mixing efficiency, but higher than that of the experimental tests, and equal to that of commonly used technology.

This lower value of the experimental tests, apart from random errors, can be explained by the incorrect execution of the laser engraving geometry. Considering that the laser beam is focused by a galvanometric head, the deviation from the theoretical profile probably depends on conicity of the beam, parallax errors, oblique reflections of the beam on the walls of the engraving, and plasma formation in the cavity.

Another cause may be the influence of surface roughness created by the pulse laser processing, and the successive passes of the laser beam to obtain the requested engraving depth.

These observations suggest two directions for future research, modify the laser processing parameters to obtain an engraving geometry that better matches the theoretical geometry and test the effectiveness of final smoothing passes to reduce surface roughness, modify the geometry of the CFD model to better match the effective geometry of the engraving and verify whether the mixing efficiency of this new CFD simulation is closer to the results of the experimental tests.

In conclusion, the test results show that this new technology is reliable, and that the quality of its achievements is almost comparable with that of current technologies and also susceptible to further improvements. These qualities make it ideal for microfluidic research projects where reduced costs and manufacturing times are important to quickly obtain information from preliminary tests to be refined with subsequent modifications.

6. Conclusions and Publications

6.1. Conclusions

At the end of this PhD course, the aim of acquiring a basic knowledge of microfluidics can be said to have been achieved. Of course, the whole field of this topic has not been explored, such as droplet generators that try to imitate cellular structures, disposable paper device technology for sensors and swabs, implantable devices, and many other aspects even in non-biological fields, such as physics or engineering. However, an overall vision, albeit imperfect, has been given which will help new researchers to orient themselves and progress in unexplored fields of this topic.

Microfluidics is a very powerful tool that allows researchers to carry out processes, which would normally require expensive and bulky equipment, with small, inexpensive chips, in relatively little time, and easily replicable. Where the amount of mass is not mandatory, with due care, any process involving fluids can be replicated with microfluidics, especially analysis ones.

This research is not a simple collection of information from scientific articles or books on the subject, but on the one hand it has tried to provide a logical link between the theoretical bases and applications, on the other it has brought original and experimental scientific experiences, with results supported by computational calculation.

Indeed, the research produced interesting results. On the one hand, research on the relationship between shear stress and cell proliferation produced a better understanding of the phenomenon, being able to reproduce *in vitro* a 3D environment more similar to that *in vivo* compared to that of simple 2D devices. On the other hand, research into the production of microfluidic chips better suited to the needs of scientific experiments produced a technology that has proven to be more competitive with that of the more traditional PDMS, in terms of simplicity and number of steps. All this was possible thanks to the collaboration with other researchers and other laboratories, which led to a better general understanding of microfluidics, its possible technologies and materials, and the creation of a network of skills.

Below is a list of publications resulting from these experiences.

6.2. Published articles

- E. Salerno *et al.*, “Liquid flow in scaffold derived from natural source: experimental observations and biological outcome,” *Regen Biomater*, vol. 9, Apr. 2022, doi: 10.1093/rb/rbac034.

- A. d’Adamo *et al.*, “Experimental measurements and CFD modelling of hydroxyapatite scaffolds in perfusion bioreactors for bone regeneration,” *Regen Biomater*, vol. 10, Jan. 2023, doi: 10.1093/rb/rbad002.

6.3. Published conference papers

- C. Ongaro *et al.*, “An Alternative Solution for Microfluidic Chip Fabrication,” *J Phys Conf Ser*, vol. 2385, no. 1, p. 012029, Dec. 2022, doi: 10.1088/1742-6596/2385/1/012029.

- V. Siciliani, A. Betti, C. Ongaro, L. Orazi, B. Zardin, and B. Reggiani, “UV picosecond laser processing for microfluidic applications,” in *Materials Research Proceedings*, Oct. 2023, pp. 334–341. doi: 10.21741/9781644902714-40.

- D. Goldoni, C. Ongaro, L. Orazi, L. Rovati, and L. Selmi, “Estimation of Analyte’s Vertical Positions above the Surface of Nanocapacitor Array Biosensors,” in *2023 IEEE SENSORS, IEEE*, Oct. 2023, pp. 1–4. doi: 10.1109/SENSORS56945.2023.10325169.

- E. Salerno et al., “Fluid dynamic parameters of naturally derived hydroxyapatite scaffolds for in vitro studies of bone cells,” J Phys Conf Ser, vol. 2685, no. 1, p. 012058, Jan. 2024, doi: 10.1088/1742-6596/2685/1/012058.

7. Appendix

7.1. PDMS Microfluidic Gasket for Impedance Spectroscope

This project involved a high-frequency impedance spectroscope for the detection of analytes flowing in a microfluidic circuit [134], Figure 7.1.1.

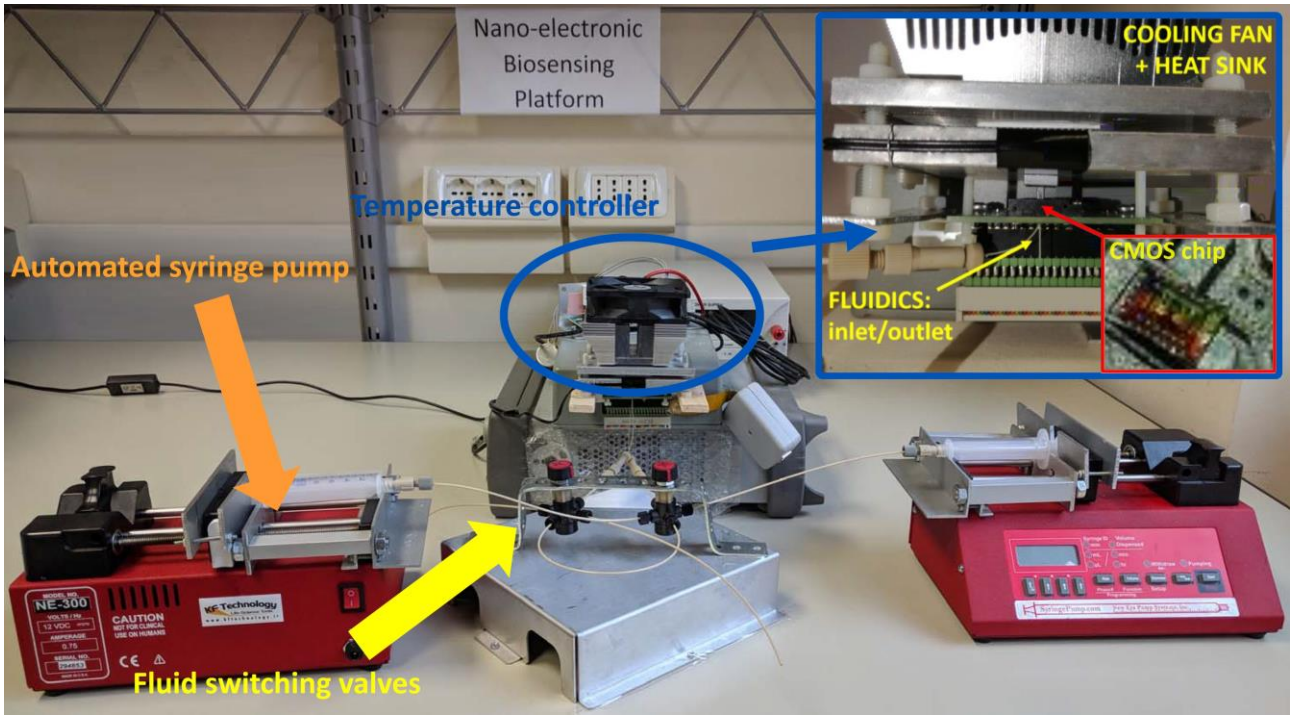

Fig. 7.1.1. *The high-frequency impedance spectroscope with its microfluidic circuit (redraw from* [134]*).*

The two syringe pumps work in push-pull mode, when one pump infuses the medium with the analytes into the microfluidic circuit, the other withdraws it. When the first syringe reaches the end of its stroke, the motion of the two pumps and the operation of the two switching valves is reversed, guaranteeing a continuous flow in the same direction to the spectroscope.

The spectroscope biosensor faces the microfluidic circuit via a planar gasket which, in addition to the seal, channels the fluid under the biosensor. This gasket was obtained from a 250 µm thick PDMS sheet SSP-M823 (SSP Inc., NY-USA) by cutting with a CO_2 laser.

This gasket was not satisfactory because, due to the high heat produced by the laser, it resulted in a very distorted shape and with chipped edges, so the aim of this project was to find another less invasive and more precise cutting technology.

These features would have allowed a better positioning of the gasket under the biosensor, ensure regular walls for laminar flow, optimize the shape of the microfluidic channel under the biosensor to improve its detection performance.

For precision machining, a valid alternative to the CO2 laser is the pulsed picosecond laser in which the energy of the light beam is concentrated in very short pulses, removing micrometric portions of any material by ablation with reduced heat generation, obtaining any shape on the sample surface by moving the laser beam via a galvanometric head.

After first positive laser cutting tests of PDMS sheet samples, the new gasket for the spectroscope was designed, based on this technology.

7.1.1. Impedance Spectroscopy

Since 1886, when electrical impedance spectroscopy (EIS) was originally conceptualized by Oliver Heaviside, it has evolved into a powerful and widely used experimental technique.

The EIS analyzes the electric properties of a medium, measuring the electrical current passing through it at various frequencies of the excitation voltage.

As a label-free, non-optical, non-destructive, and easy to implement technique, EIS has become a promising experimental approach in biological and medical applications, such as biosensing technologies, and diagnosis of diseases, including cancer and virus detection [135]. In these applications, the current flowing from the metal electrode of the device in the electrolyte (physiological medium) generates an electric field inside it. The biological matter (cells, tissues, macromolecules), which is inside the medium, alters the electric field and therefore the time- or frequency-domain impedance measured by the device.

To have a sufficiently large detection area, but capable of detecting more details of the analytes, the most advanced EIS devices are equipped with an array made up of numerous electrodes of sub-micrometer dimensions. If this array faces into the wall of a microfluidic channel, it is possible to analyze in real time the flow of biological matter passing through the channel.

EIS has remarkably high sensitivity within the electrical double layer (EDL) of the electrode/electrolyte interface, but sensitivity to analytes beyond the EDL is very poor due to the Debye screening effect which, at physiological salt concentrations of 150 mM and with frequency sweeps up to 1 MHz, limit the probing distance to only approximately 0.8 nm [136], whereas analytes often extend well beyond this limit.

To overcome these limitations, high-frequency impedance spectroscopy (HFIS) biosensors based on CMOS nano-electrode arrays (NEA), Figure 7.1.2, were realized with measurement frequencies up to 300 MHz [134] and above [136], which demonstrated the capability to overcome the Debye screening limit, thus enabling label-free detection and imaging of analytes far above the sensor surface, Figure 7.1.3.

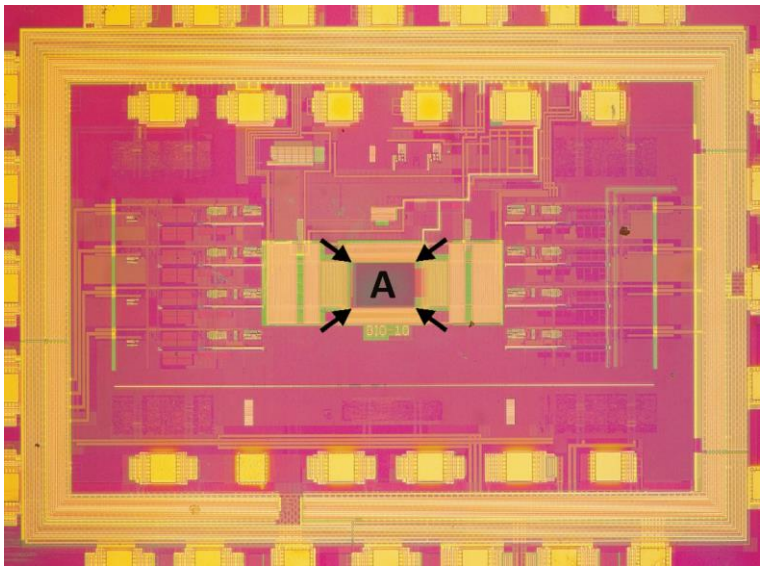

Fig. 7.1.2. *A CMOS impedance spectrometry microchip showing its array of 256 x 256 nanoelectrodes (A)* [137]*. The overall size of the microchip is 3.2 x 2.1 mm and that of the array is 228 x 153 µm.*

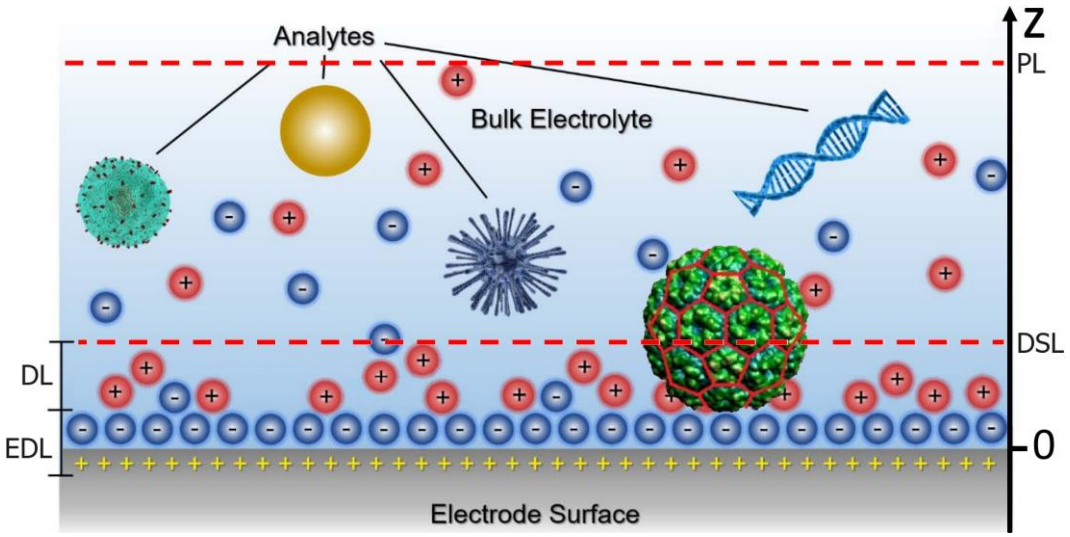

Fig. 7.1.3. *Probing field of high-frequency impedance spectroscopy (HFIS) (redraw from A. Cossettini). (EDL) Electric double layer. (DL) Diffuse layer. (DSL) Debye screening length. (PL) Probing length.*

7.1.2. Design of the PDMS gasket

Figure 9.1.4-A shows the biosensor chip, on its outside there are the metallic pads for the electrical contacts with the external electronic circuit controlling the process and managing the detection signals. In the center of the chip, between the two green areas corresponding to the two signal reading circuits, there is the nano electrode array. Around the array is positioned the old gasket whose geometry is not very precise due to the thermal deformations of CO_2 laser cutting.

Figure 7.1.4-C shows the chip, held by tweezers, about to be inserted into its housing, called interposer, on the printed circuit board (PCB) connected to the external electronic circuit.

In the enlargement of the interposer, Figure 7.1.4-B, we can see the edges for positioning the chip, the spring pins for the electrical contacts between the chip and the PCB, and the two inlet/outlet holes for the fluid that flows in contact with the array of the chip.

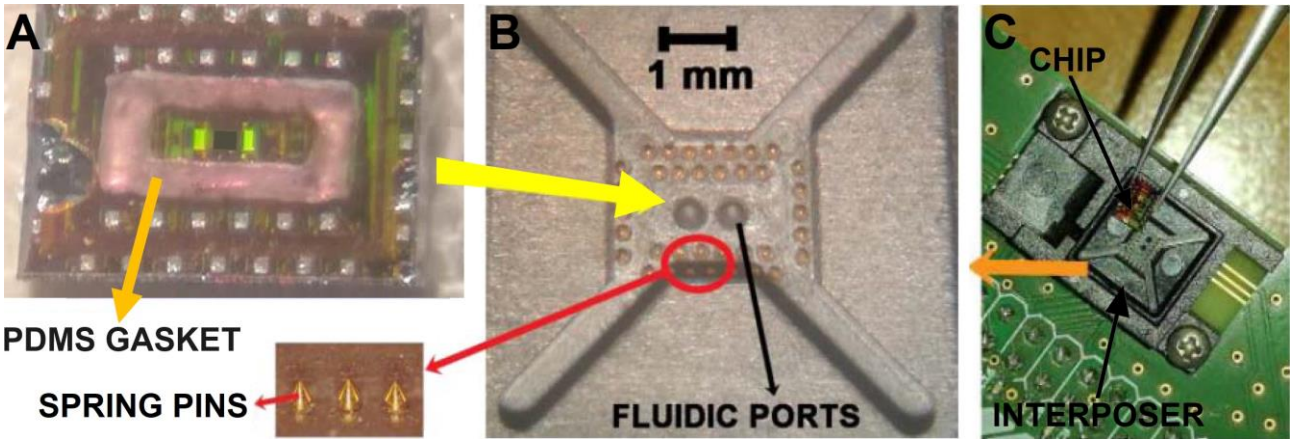

Fig. 7.1.4. *The gasket, the biosensor chip (A), and its interposer (B, C) (redraw from* [134]*).*

The features, that the new gasket had to have, were:

- increased size of the gasket to allow its positioning against the same edges of the interposer used by the chip,
- be able to allow the passage of the spring pins through the gasket, repeating the same matrix of holes as the interposer,
- convey the fluid flow into contact with the nano electrode array, but avoiding overlapping with the gasket.

Due to the small dimensions of the chip, Figure 7.1.5, careful design of the coupling gaps and precise laser cutting were necessary. In Figure 71.6 and Figure 7.1.7 the new gasket drawings, the upper left corner was cut off for reference because the chip shape is slightly asymmetrical.

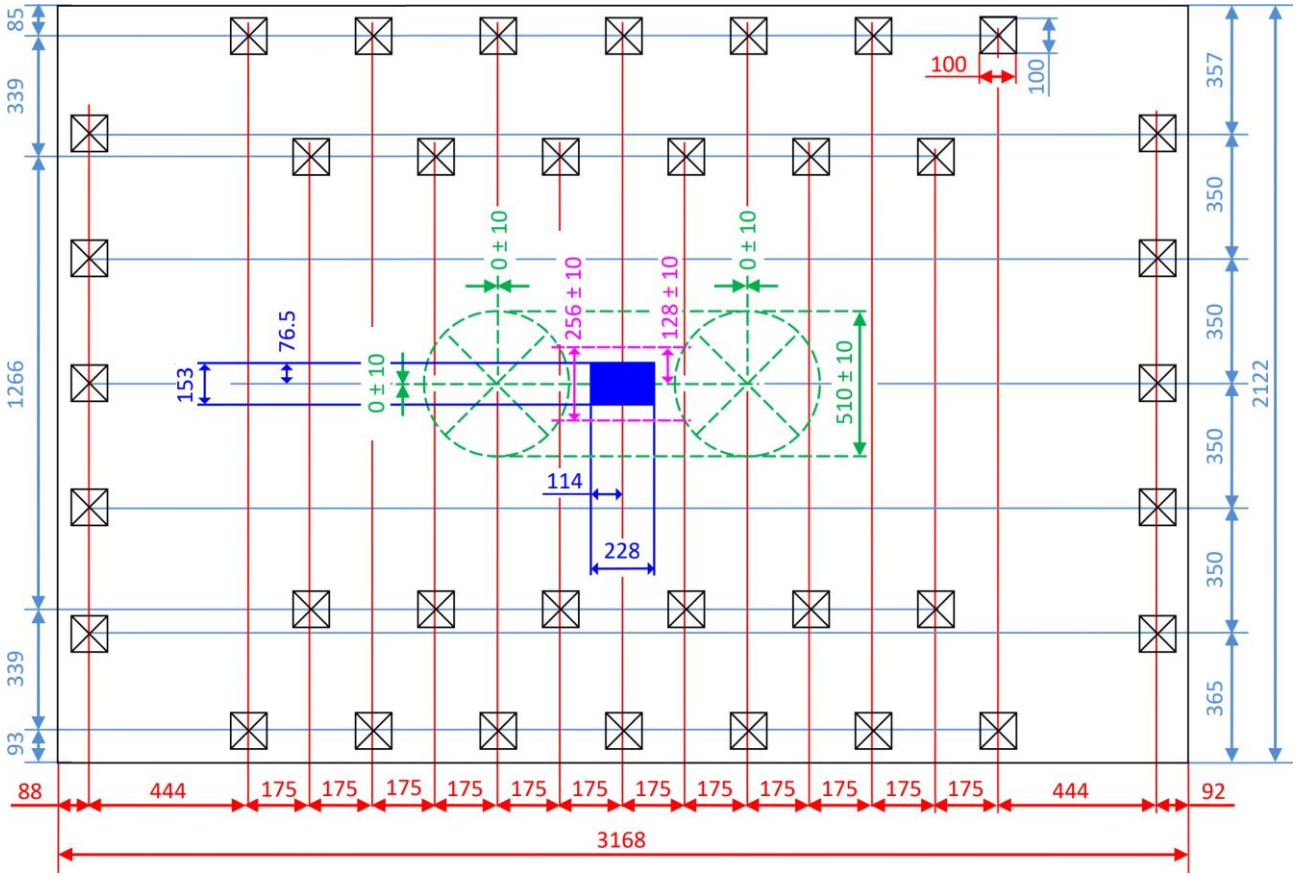

Fig. 7.1.5. *Drawing of the biosensor chip (dimensions in µm).*

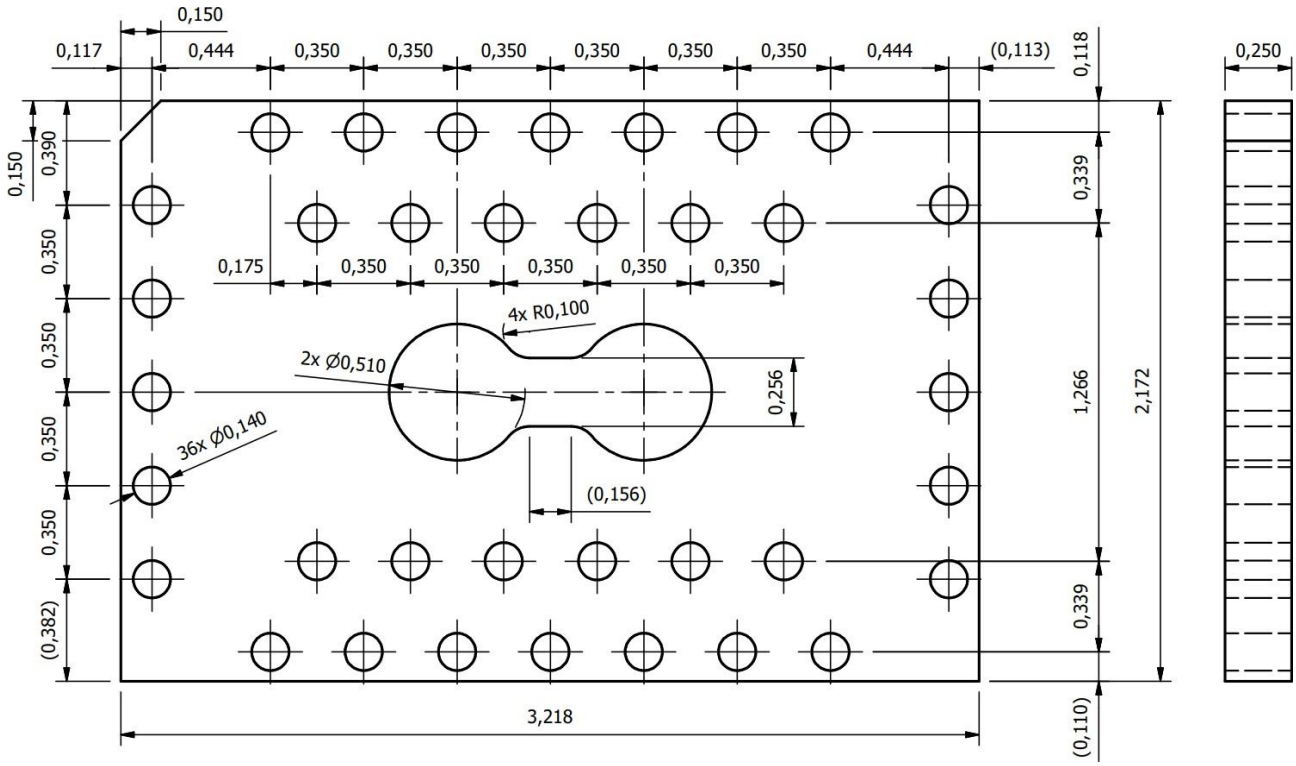

Fig. 7.1.6. *ISO technical drawing of the new gasket (dimensions in mm).*

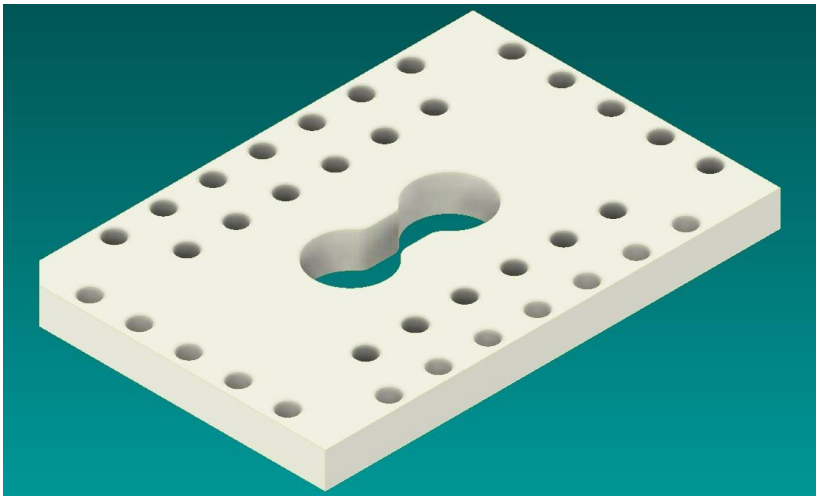

Fig. 7.1.7. *3D CAD drawing of the new gasket.*

7.1.3. Realization of the PDMS gasket

After some cutting tests on samples of the 250 µm thick SSP-M823 PDMS sheet using an Atlantic 5 picosecond laser (EKSPLA, Vilnius, Lithuania) with a galvanometric head, the CAD drawing of the new gasket was loaded into the laser computer and its profile was cut. In Figure 7.1.8 a view of the gasket on a coin for comparison.

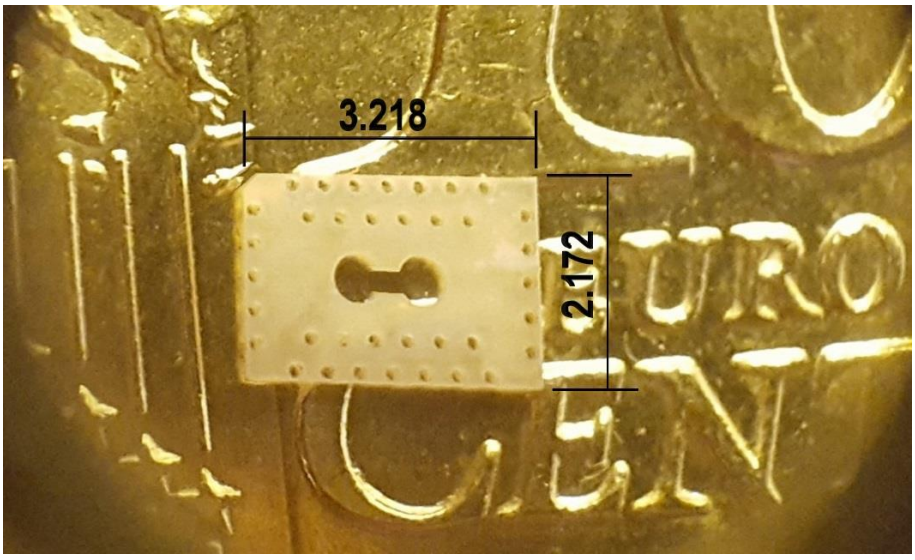

Fig. 7.1.8. *Comparison between the new gasket and a coin (dimensions in mm).*

The compatibility of the new seal with the biosensor chip was checked via optical microscope. It was found a general precision in the execution of the gasket and its good coupling with the chip and the interposer, Figure 7.1.9.

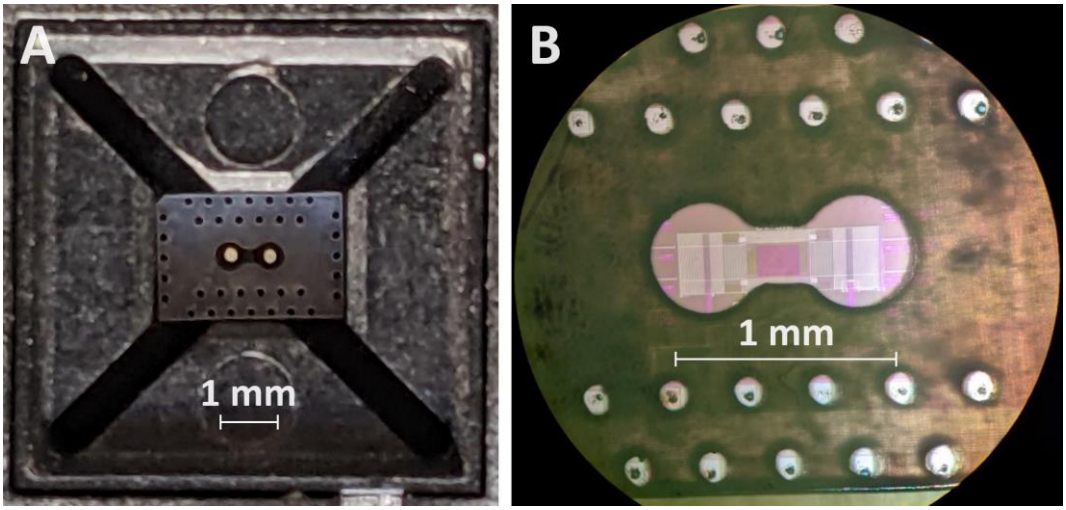

Fig. 7.1.9. *(A) Coupling between the gasket and the interposer, and (B) between the gasket and the chip (redraw from D. Brandalise).*

In Figure 7.1.9-A we can see the correct concentricity between the internal holes of the inlet/outlet microfluidic tubes, white dots, and the circular ends of the central slot of the gasket which is held in position by the edges of the interposer.

In Figure 7.1.9-B we can see the correct positioning of the central part of the gasket slot with the array of nano electrodes of the chip, and similarly of its holes for the spring pins with the metallic pads of the chip. The black dots in the metallic pads are the marks left by the pressure of the spring pins.

The only significant observation was the drilling of spring pin holes in the gasket, which in the rows near the edges were denting the edges themselves, Figure 7.1.10. This was probably due to the laser beam, which due to its focus, is slightly conical like the holes, affecting the thin layer of the edges.

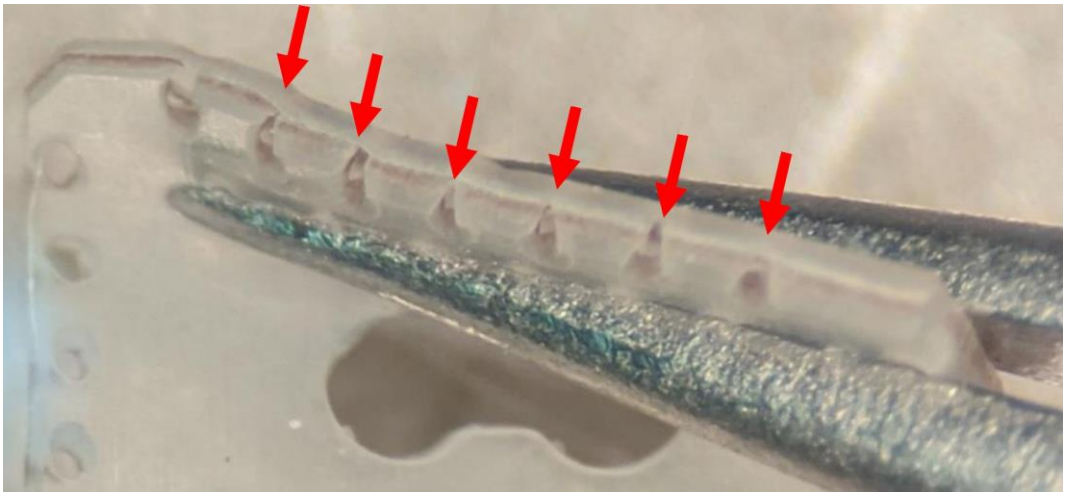

Fig. 7.1.10. *Geometry deformation of the spring pin holes (by D. Brandalise).*

A dimensional check, Figure 7.1.11-A, was done with a confocal microscope ConfoSurf CLV150 (Confovis GmbH, Jena, Germany), Figure 7.1.11-B, on two batches of new gaskets, one batch cleaned with IPA and the other without cleaning, to check if there was any swelling of the PDMS gasket due to the solvent. The measurement values were within a tolerance range of ±30 µm and did not show any significant swelling.

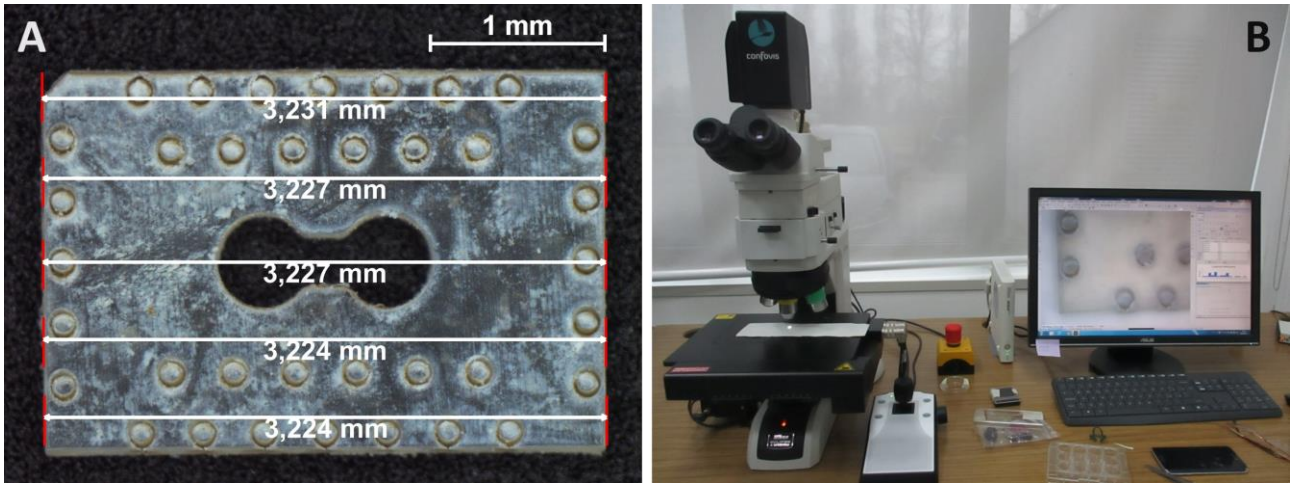

Fig. 7.1.11. *Gasket measures (A). Measurement with the confocal microscope (B).*

Tests on the sealing of the gasket and the functioning of the system were carried out by Brandalise with positive results. The new gasket is currently used in the spectroscope [138].

7.1.4. Design of an improved flow PDMS gasket

For the most laminar possible flow of the fluid in contact with the nano electrode array, i.e. with reduced or gentle variations in section or direction, a three-dimensional gasket was designed to be obtained through differentiated laser ablation.

The features, that the design of the improved flow PDMS gasket had to have, were:

- use of the same 250 µm thick SSP-M823 PDMS sheet,
- material to be ablated without undercuts, with processing from one side only,
- width of the channel equal to that of the internal diameter of the inlet/outlet tubes,
- best join the vertical flow of the fluid in the input/output tubes with the horizontal flow in contact with the nano electrode array.

Figure 7.1.12 shows the 3D CAD drawing of the improved flow PDMS gasket assembly.

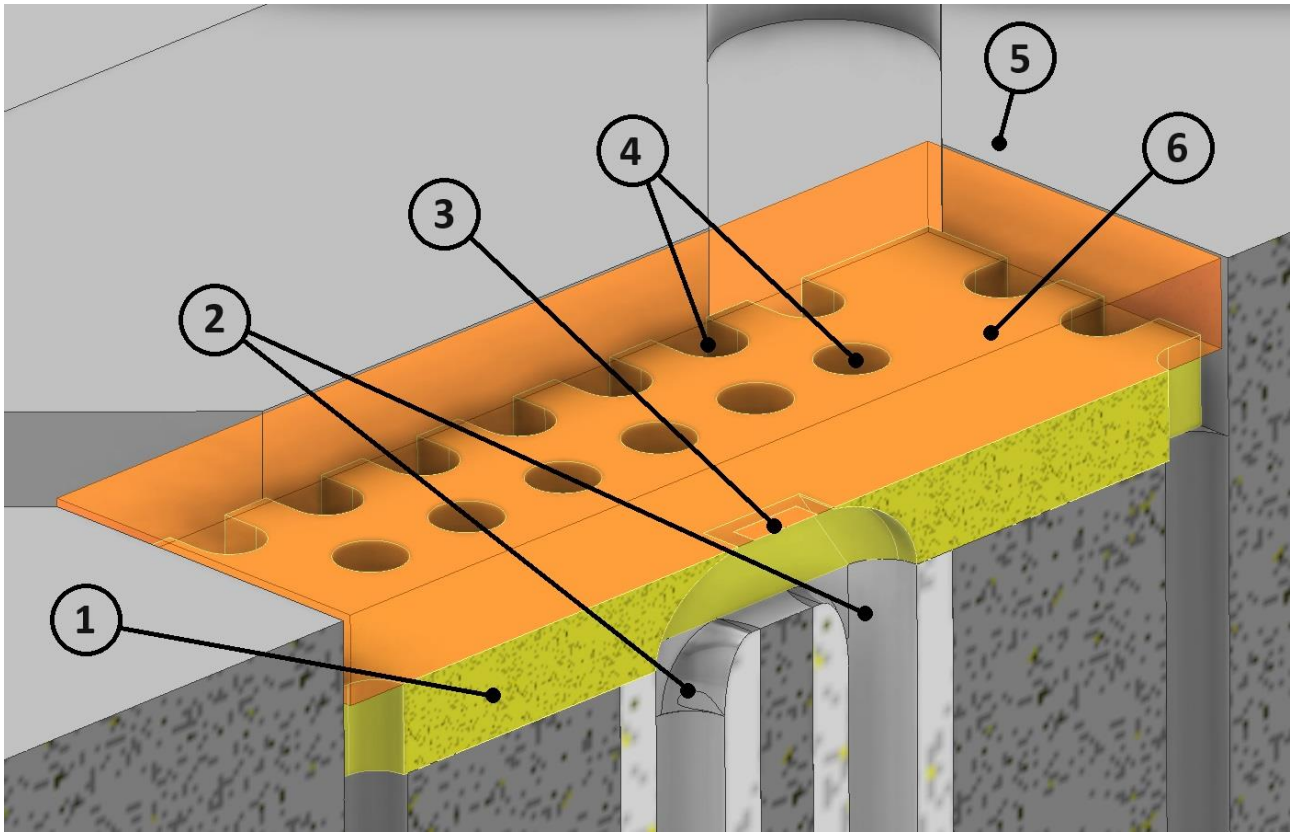

Fig. 7.1.12. *Biosensor chip assembly. (1) Gasket. (2) Inlet/outlet tubes. (3) Chip nano electrode array. (4) Spring pin holes. (5) Interposer. (6) Biosensor chip.*

As we can see, in addition to complying with the project specifications, the drawing shows the modification to the external holes for the passage of the spring pins, widening their diameter to 200 µm, and eliminating the thin layer of material that separated them from the edges of the gasket.

The project is waiting to be implemented.

8. References

[1] “Wärtsilä-Sulzer RTA96-C,” Wikipedia. Accessed: Jan. 11, 2023. [Online]. Available: https://en.wikipedia.org/wiki/W%C3%A4rtsil%C3%A4-Sulzer_RTA96-C

[2] “Three Gorges Dam,” Wikipedia. Accessed: Jan. 11, 2023. [Online]. Available: https://en.wikipedia.org/wiki/Three_Gorges_Dam

[3] “Microfluidics,” *Segen’s Medical Dictionary*. Farlex, Inc., 2011. Accessed: Jan. 11, 2023. [Online]. Available: https://medical-dictionary.thefreedictionary.com/microfluidics

[4] “Litre,” Wikipedia. Accessed: Jan. 11, 2023. [Online]. Available: https://en.wikipedia.org/wiki/Litre

[5] N. Convery and N. Gadegaard, “30 years of microfluidics,” *Micro and Nano Engineering*, vol. 2, pp. 76–91, Mar. 2019, doi: 10.1016/j.mne.2019.01.003.

[6] T. M. Squires and S. R. Quake, “Microfluidics: Fluid physics at the nanoliter scale,” *Rev Mod Phys*, vol. 77, no. 3, pp. 977–1026, Oct. 2005, doi: 10.1103/RevModPhys.77.977.

[7] P. Abgrall and A.-M. Gué, “Lab-on-chip technologies: making a microfluidic network and coupling it into a complete microsystem—a review,” *Journal of Micromechanics and Microengineering*, vol. 17, no. 5, pp. R15–R49, May 2007, doi: 10.1088/0960-1317/17/5/R01.

[8] S. C. Terry, J. H. Jerman, and J. B. Angell, “A gas chromatographic air analyzer fabricated on a silicon wafer,” *IEEE Trans Electron Devices*, vol. 26, no. 12, pp. 1880–1886, Dec. 1979, doi: 10.1109/T-ED.1979.19791.

[9] G. M. Whitesides, “The origins and the future of microfluidics,” *Nature*, vol. 442, no. 7101, pp. 368–373, Jul. 2006, doi: 10.1038/nature05058.

[10] R. Mukhopadhyay, “When PDMS isn’t the best,” *Anal Chem*, vol. 79, no. 9, pp. 3248–3253, May 2007, doi: 10.1021/ac071903e.

[11] “Microfluidics Market,” Emergen Research. Accessed: Jan. 27, 2023. [Online]. Available: https://www.emergenresearch.com/industry-report/microfluidics-market

[12] F. K. Balagaddé, L. You, C. L. Hansen, F. H. Arnold, and S. R. Quake, “Long-Term Monitoring of Bacteria Undergoing Programmed Population Control in a Microchemostat,” *Science (1979)*, vol. 309, no. 5731, pp. 137–140, Jul. 2005, doi: 10.1126/science.1109173.

[13] P. Marguet, F. Balagadde, C. Tan, and L. You, “Biology by design: reduction and synthesis of cellular components and behaviour,” *J R Soc Interface*, vol. 4, no. 15, pp. 607–623, Aug. 2007, doi: 10.1098/rsif.2006.0206.

[14] A. Francesko, V. F. Cardoso, and S. Lanceros-Méndez, “Lab-on-a-chip technology and microfluidics,” in *Microfluidics for Pharmaceutical Applications*, Elsevier, 2019, pp. 3–36. doi: 10.1016/B978-0-12-812659-2.00001-6.

[15] “Microfluidics,” Scopus. Accessed: Jan. 28, 2023. [Online]. Available: https://www.scopus.com/results/results.uri?sort=plf-f&src=s&st1=microfluidics&sid=130cbdd154851b0a2cea17363cb91021&sot=b&sdt=b&sl=18&s=ALL%28microfluidics%29&origin=searchbasic&editSaveSearch=&yearFrom=Before+1960&yearTo=Present

[16] D. Huh, G. A. Hamilton, and D. E. Ingber, “From 3D cell culture to organs-on-chips,” *Trends Cell Biol*, vol. 21, no. 12, pp. 745–754, Dec. 2011, doi: 10.1016/j.tcb.2011.09.005.

[17] R. Z. Jafri *et al.*, “A Three-Way Accuracy Comparison of the Dexcom G5, Abbott Freestyle Libre Pro, and Senseonics Eversense Continuous Glucose Monitoring Devices in a Home-Use Study of Subjects with Type 1 Diabetes,” *Diabetes Technol Ther*, vol. 22, no. 11, pp. 846–852, Nov. 2020, doi: 10.1089/dia.2019.0449.

[18] “Long-term Implantable Continuous Glucose Monitoring (GCM) System,” Senseonics. Accessed: Jan. 28, 2023. [Online]. Available: https://www.senseonics.com/

[19] Ki-Hun Jeong, G. L. Liu, N. Chronis, and L. P. Lee, “Tunable microdoublet lens array,” in *17th IEEE International Conference on Micro Electro Mechanical Systems. Maastricht MEMS 2004 Technical Digest*, IEEE, pp. 37–40. doi: 10.1109/MEMS.2004.1290516.

[20] J. Wu and M. Gu, “Microfluidic sensing: state of the art fabrication and detection techniques,” *J Biomed Opt*, vol. 16, no. 8, p. 080901, 2011, doi: 10.1117/1.3607430.

[21] F. Simoni, P. Spegni, S. Bonfadini, D. E. Lucchetta, S. Lo Turco, and L. Criante, “Optofluidic Microlasers based on Femtosecond Micromachining Technology,” *Optofluidics, Microfluidics and Nanofluidics*, vol. 4, no. 1, Aug. 2017, doi: 10.1515/optof-2017-0002.

[22] E. Bassous, H. H. Taub, and L. Kuhn, “Ink jet printing nozzle arrays etched in silicon,” *Appl Phys Lett*, vol. 31, no. 2, pp. 135–137, Jul. 1977, doi: 10.1063/1.89587.

[23] H. Shi *et al.*, “Inductive-Capacitive Coulter Counting: Detection and Differentiation of Multi-Contaminants in Hydraulic Oil Using a Microfluidic Sensor,” *IEEE Sens J*, vol. 21, no. 2, pp. 2067–2076, Jan. 2021, doi: 10.1109/JSEN.2020.3016000.

[24] C. Bai, H. Zhang, L. Zeng, X. Zhao, and Z. Yu, “High-Throughput Sensor to Detect Hydraulic Oil Contamination Based on Microfluidics,” *IEEE Sens J*, vol. 19, no. 19, pp. 8590–8596, Oct. 2019, doi: 10.1109/JSEN.2019.2922319.

[25] L. Souza and A. Al-Tabbaa, “Microfluidic fabrication of microcapsules tailored for self-healing in cementitious materials,” *Constr Build Mater*, vol. 184, pp. 713–722, Sep. 2018, doi: 10.1016/j.conbuildmat.2018.07.005.

[26] S. Cheng and Z. Wu, “Microfluidic electronics,” *Lab Chip*, vol. 12, no. 16, p. 2782, 2012, doi: 10.1039/c2lc21176a.

[27] S. He, N. Joseph, S. Feng, M. Jellicoe, and C. L. Raston, “Application of microfluidic technology in food processing,” *Food Funct*, vol. 11, no. 7, pp. 5726–5737, 2020, doi: 10.1039/D0FO01278E.

[28] S. Hosseini, M. A. Espinosa-Hernandez, R. Garcia-Ramirez, A. S. Cerda-Kipper, S. Reveles-Huizar, and L. Acosta-Soto, *BioMEMS*. Singapore: Springer Singapore, 2021. doi: 10.1007/978-981-15-6382-9.

[29] S. Argentiere, G. Gigli, M. M. Irini Gerges, and L. Blasi, “Smart Microfluidics: The Role of Stimuli- Responsive Polymers in Microfluidic Devices,” in *Advances in Microfluidics*, InTech, 2012. doi: 10.5772/38072.

[30] “Status of the Microfluidics Industry 2020,” Yole Développement. Accessed: Jan. 28, 2023. [Online]. Available: https://s3.i-micronews.com/uploads/2020/09/YDR20117-Status-of-Microfluidics-Industry-Sample.pdf

[31] F. Malloggi, *Soft Matter at Aqueous Interfaces*, vol. 917. Cham: Springer International Publishing, 2016. doi: 10.1007/978-3-319-24502-7.

[32] Y. Song, X. Zhao, Q. Tian, and H. Liang, “Fundamental Concepts and Physics in Microfluidics,” in *Microfluidics: Fundamental, Devices and Applications*, Weinheim, Germany: Wiley-VCH Verlag GmbH & Co. KGaA, 2018, pp. 19–111. doi: 10.1002/9783527800643.ch2.

[33] V. Italia *et al.*, “Laser-Inscribed Glass Microfluidic Device for Non-Mixing Flow of Miscible Solvents,” *Micromachines (Basel)*, vol. 10, no. 1, p. 23, Dec. 2018, doi: 10.3390/mi10010023.

[34] Seth Darling, “Sizing Up a Molecule.” Accessed: Feb. 13, 2023. [Online]. Available: https://nnci.net/sites/default/files/inline-files/nanooze_edition_11-1ljz4uy.pdf

[35] R. Pethig and S. Smith, *Introductory Bioelectronics*. Wiley, 2012. doi: 10.1002/9781118443293.

[36] F. M. White, *Viscous Fluid Flow*, Second Edition. McGraw-Hill Science/Engineering/Math, 1991.

[37] H. Schlichting and K. Gersten, *Boundary-Layer Theory*. Berlin, Heidelberg: Springer Berlin Heidelberg, 2017. doi: 10.1007/978-3-662-52919-5.

[38] W. Yu *et al.*, “A Microfluidic-Based Multi-Shear Device for Investigating the Effects of Low Fluid-Induced Stresses on Osteoblasts,” *PLoS One*, vol. 9, no. 2, p. e89966, Feb. 2014, doi: 10.1371/journal.pone.0089966.

[39] M. Muskat, *The Flow of Homogeneous Fluids Through Porous Media*. J. W. EDWARDS, Inc., 1946. doi: 978-0934634168.

[40] T. M. Squires, R. J. Messinger, and S. R. Manalis, “Making it stick: convection, reaction and diffusion in surface-based biosensors,” *Nat Biotechnol*, vol. 26, no. 4, pp. 417–426, Apr. 2008, doi: 10.1038/nbt1388.

[41] M. Koch, D. Chatelain, A. G. R. Evans, and A. Brunnschweiler, “Two simple micromixers based on silicon,” *Journal of Micromechanics and Microengineering*, vol. 8, no. 2, pp. 123–126, Jun. 1998, doi: 10.1088/0960-1317/8/2/020.

[42] M. J. Mescher *et al.*, “Fabrication Methods and Performance of Low-Permeability Microfluidic Components for a Miniaturized Wearable Drug Delivery System,” *Journal of Microelectromechanical Systems*, vol. 18, no. 3, pp. 501–510, Jun. 2009, doi: 10.1109/JMEMS.2009.2015484.

[43] Z. Zhou, D. Chen, X. Wang, and J. Jiang, “Milling Positive Master for Polydimethylsiloxane Microfluidic Devices: The Microfabrication and Roughness Issues,” *Micromachines (Basel)*, vol. 8, no. 10, p. 287, Sep. 2017, doi: 10.3390/mi8100287.

[44] C. H. Ahn and J.-W. Choi, *Springer Handbook of Nanotechnology*. Berlin, Heidelberg: Springer Berlin Heidelberg, 2010. doi: 10.1007/978-3-642-02525-9.

[45] Y. Xia and G. M. Whitesides, “Soft Lithography,” *Angewandte Chemie International Edition*, vol. 37, no. 5, pp. 550–575, Mar. 1998, doi: 10.1002/(SICI)1521-3773(19980316)37:5<550::AID-ANIE550>3.0.CO;2-G.

[46] V. N. Goral, Y.-C. Hsieh, O. N. Petzold, R. A. Faris, and P. K. Yuen, “Hot embossing of plastic microfluidic devices using poly(dimethylsiloxane) molds,” *Journal of Micromechanics and Microengineering*, vol. 21, no. 1, p. 017002, Jan. 2011, doi: 10.1088/0960-1317/21/1/017002.

[47] X. Tong, L. Ga, R. Zhao, and J. Ai, “Research progress on the applications of paper chips,” *RSC Adv*, vol. 11, no. 15, pp. 8793–8820, 2021, doi: 10.1039/D0RA10470A.

[48] K. Raj M and S. Chakraborty, “PDMS microfluidics: A mini review,” *J Appl Polym Sci*, vol. 137, no. 27, p. 48958, Jul. 2020, doi: 10.1002/app.48958.

[49] G. Robbins, “Photomask Making,” The University of Texas at Dallas. Accessed: May 22, 2023. [Online]. Available: https://cleanroom.utdallas.edu/manuals/photomask-making/

[50] “Designing Your Mask,” Photo Data. Accessed: May 23, 2023. [Online]. Available: https://www.calameo.com/read/000127425169ab7facf84

[51] N.-T. Nguyen, S. T. Wereley, and S. A. M. Shaegh, *Fundamentals and applications of microfluidics*. 2019.

[52] “SU-8 Permanent Negative Epoxy Photoresist,” KAYAKU Advanced Materials. Accessed: Dec. 20, 2023. [Online]. Available: https://kayakuam.com/wp-content/uploads/2020/09/KAM-SU-8-50-100-Datasheet-9.3.20-Final.pdf

[53] S. M. Langelier, E. Livak-Dahl, A. J. Manzo, B. N. Johnson, N. G. Walter, and M. A. Burns, “Flexible casting of modular self-aligning microfluidic assembly blocks,” *Lab Chip*, vol. 11, no. 9, p. 1679, 2011, doi: 10.1039/c0lc00517g.

[54] S. Razavi Bazaz *et al.*, “Rapid Softlithography Using 3D-Printed Molds,” *Adv Mater Technol*, vol. 4, no. 10, p. 1900425, Oct. 2019, doi: 10.1002/admt.201900425.

[55] K. Raj M and S. Chakraborty, “PDMS microfluidics: A mini review,” *J Appl Polym Sci*, vol. 137, no. 27, p. 48958, Jul. 2020, doi: 10.1002/app.48958.

[56] “SYLGARD™ 184 Silicone Elastomer Kit,” Dow Inc. Accessed: May 24, 2023. [Online]. Available: https://www.dow.com/en-us/pdp.sylgard-184-silicone-elastomer-kit.01064291z.html?productCatalogFlag=1#tech-content

[57] A. Borók, K. Laboda, and A. Bonyár, “PDMS Bonding Technologies for Microfluidic Applications: A Review,” *Biosensors (Basel)*, vol. 11, no. 8, p. 292, Aug. 2021, doi: 10.3390/bios11080292.

[58] C.-H. Cho, W. Cho, Y. Ahn, and S.-Y. Hwang, “PDMS–glass serpentine microchannel chip for time domain PCR with bubble suppression in sample injection,” *Journal of Micromechanics and Microengineering*, vol. 17, no. 9, pp. 1810–1817, Sep. 2007, doi: 10.1088/0960-1317/17/9/009.

[59] T. C. Merkel, V. I. Bondar, K. Nagai, B. D. Freeman, and I. Pinnau, “Gas Sorption, Diffusion, and Permeation in Poly(dimethylsiloxane),” *J Polym Sci B: Polym Phys*, vol. 38, pp. 415–434, 2000, doi: 10.1002/(SICI)1099-0488(20000201)38:3%3C415::AID-POLB8%3E3.0.CO;2-Z.

[60] J. N. Lee, C. Park, and G. M. Whitesides, “Solvent Compatibility of Poly(dimethylsiloxane)-Based Microfluidic Devices,” *Anal Chem*, vol. 75, no. 23, pp. 6544–6554, Dec. 2003, doi: 10.1021/ac0346712.

[61] S. Bhattacharya, A. Datta, J. M. Berg, and S. Gangopadhyay, “Studies on surface wettability of poly(dimethyl) siloxane (PDMS) and glass under oxygen-plasma treatment and correlation with bond strength,” *Journal of Microelectromechanical Systems*, vol. 14, no. 3, pp. 590–597, Jun. 2005, doi: 10.1109/JMEMS.2005.844746.

[62] I. D. Johnston, D. K. McCluskey, C. K. L. Tan, and M. C. Tracey, “Mechanical characterization of bulk Sylgard 184 for microfluidics and microengineering,” *Journal of Micromechanics and Microengineering*, vol. 24, no. 3, p. 035017, Mar. 2014, doi: 10.1088/0960-1317/24/3/035017.

[63] S. Samal, B. Svomova, M. Spasovová, O. Tyc, D. Vokoun, and I. Stachiv, “Physical, Thermal, and Mechanical Characterization of PMMA Foils Fabricated by Solution Casting,” *Applied Sciences*, vol. 13, no. 2, p. 1016, Jan. 2023, doi: 10.3390/app13021016.

[64] H. Becker, “Polymer microfluidic devices,” *Talanta*, vol. 56, no. 2, pp. 267–287, Feb. 2002, doi: 10.1016/S0039-9140(01)00594-X.

[65] Y. Chen, L. Zhang, and G. Chen, “Fabrication, modification, and application of poly(methyl methacrylate) microfluidic chips,” *Electrophoresis*, vol. 29, no. 9, pp. 1801–1814, May 2008, doi: 10.1002/elps.200700552.

[66] B. Jing, J. Zhao, Y. Wang, X. Yi, and H. Duan, “Water-Swelling-Induced Morphological Instability of a Supported Polymethyl Methacrylate Thin Film,” *Langmuir*, vol. 26, no. 11, pp. 7651–7655, Jun. 2010, doi: 10.1021/la1004566.

[67] J. S. Papanu, D. W. Hess, D. S. Soane (Soong), and A. T. Bell, “Swelling of poly(methyl methacrylate) thin films in low molecular weight alcohols,” *J Appl Polym Sci*, vol. 39, no. 4, pp. 803–823, Feb. 1990, doi: 10.1002/app.1990.070390404.

[68] E. T. da Costa, M. F. Mora, P. A. Willis, C. L. do Lago, H. Jiao, and C. D. Garcia, “Getting started with open-hardware: Development and control of microfluidic devices,” *Electrophoresis*, vol. 35, no. 16, pp. 2370–2377, Aug. 2014, doi: 10.1002/elps.201400128.

[69] L. Orazi, V. Siciliani, R. Pelaccia, K. Oubellaouch, and B. Reggiani, “Ultrafast laser micromanufacturing of microfluidic devices,” *Procedia CIRP*, vol. 110, pp. 122–127, 2022, doi: 10.1016/j.procir.2022.06.023.

[70] R. Osellame, H. J. W. M. Hoekstra, G. Cerullo, and M. Pollnau, “Femtosecond laser microstructuring: an enabling tool for optofluidic lab-on-chips,” *Laser Photon Rev*, vol. 5, no. 3, pp. 442–463, May 2011, doi: 10.1002/lpor.201000031.

[71] B. Clarke, “Normal Bone Anatomy and Physiology,” *Clinical Journal of the American Society of Nephrology*, vol. 3, no. Supplement_3, pp. S131–S139, Nov. 2008, doi: 10.2215/CJN.04151206.

[72] S. C. Cowin and L. Cardoso, “Blood and interstitial flow in the hierarchical pore space architecture of bone tissue,” *J Biomech*, vol. 48, no. 5, pp. 842–854, Mar. 2015, doi: 10.1016/j.jbiomech.2014.12.013.

[73] C. Wittkowske, G. C. Reilly, D. Lacroix, and C. M. Perrault, “In Vitro Bone Cell Models: Impact of Fluid Shear Stress on Bone Formation,” *Front Bioeng Biotechnol*, vol. 4, Nov. 2016, doi: 10.3389/fbioe.2016.00087.

[74] N. Udagawa *et al.*, “Osteoclast differentiation by RANKL and OPG signaling pathways,” *J Bone Miner Metab*, vol. 39, no. 1, pp. 19–26, Jan. 2021, doi: 10.1007/s00774-020-01162-6.

[75] L. F. Bonewald, “The amazing osteocyte,” *Journal of Bone and Mineral Research*, vol. 26, no. 2, pp. 229–238, Feb. 2011, doi: 10.1002/jbmr.320.

[76] F. D. Allen, C. T. Hung, S. R. Pollack, and C. T. Brighton, “Serum modulates the intracellular calcium response of primary cultured bone cells to shear flow,” *J Biomech*, vol. 33, no. 12, pp. 1585–1591, Dec. 2000, doi: 10.1016/S0021-9290(00)00144-5.

[77] R. C. Riddle and H. J. Donahue, “From streaming-potentials to shear stress: 25 years of bone cell mechanotransduction,” *Journal of Orthopaedic Research*, vol. 27, no. 2, pp. 143–149, Feb. 2009, doi: 10.1002/jor.20723.

[78] D. J. Papachristou, K. K. Papachroni, E. K. Basdra, and A. G. Papavassiliou, “Signaling networks and transcription factors regulating mechanotransduction in bone,” *BioEssays*, vol. 31, no. 7, pp. 794–804, Jul. 2009, doi: 10.1002/bies.200800223.

[79] S. Kou *et al.*, “A multishear microfluidic device for quantitative analysis of calcium dynamics in osteoblasts,” *Biochem Biophys Res Commun*, vol. 408, no. 2, pp. 350–355, May 2011, doi: 10.1016/j.bbrc.2011.04.044.

[80] W. L. Grayson *et al.*, “Engineering anatomically shaped human bone grafts,” *Proceedings of the National Academy of Sciences*, vol. 107, no. 8, pp. 3299–3304, Feb. 2010, doi: 10.1073/pnas.0905439106.

[81] A. R. Pereira *et al.*, “Modeling of the Human Bone Environment: Mechanical Stimuli Guide Mesenchymal Stem Cell–Extracellular Matrix Interactions,” *Materials*, vol. 14, no. 16, p. 4431, Aug. 2021, doi: 10.3390/ma14164431.

[82] J. W. Lee, K. S. Kang, S. H. Lee, J.-Y. Kim, B.-K. Lee, and D.-W. Cho, “Bone regeneration using a microstereolithography-produced customized poly(propylene fumarate)/diethyl fumarate photopolymer 3D scaffold incorporating BMP-2 loaded PLGA microspheres,” *Biomaterials*, vol. 32, no. 3, pp. 744–752, Jan. 2011, doi: 10.1016/j.biomaterials.2010.09.035.

[83] S. Lopa *et al.*, “Translational Application of Microfluidics and Bioprinting for Stem Cell-Based Cartilage Repair,” *Stem Cells Int*, vol. 2018, pp. 1–14, 2018, doi: 10.1155/2018/6594841.

[84] C. F. Buchanan, E. E. Voigt, C. S. Szot, J. W. Freeman, P. P. Vlachos, and M. N. Rylander, “Three-Dimensional Microfluidic Collagen Hydrogels for Investigating Flow-Mediated Tumor-Endothelial Signaling and Vascular Organization,” *Tissue Eng Part C Methods*, vol. 20, no. 1, pp. 64–75, Jan. 2014, doi: 10.1089/ten.tec.2012.0731.

[85] “b.Bone™,” GreenBone Ortho S.p.A. – Faenza, Italy. Accessed: Jul. 21, 2023. [Online]. Available: https://greenbone.it/b-bone

[86] A. Ruffini, M. Sandri, M. Dapporto, E. Campodoni, A. Tampieri, and S. Sprio, “Nature-Inspired Unconventional Approaches to Develop 3D Bioceramic Scaffolds with Enhanced Regenerative Ability,” *Biomedicines*, vol. 9, no. 8, p. 916, Jul. 2021, doi: 10.3390/biomedicines9080916.

[87] A. Tampieri, S. Sprio, A. Ruffini, G. Celotti, I. G. Lesci, and N. Roveri, “From wood to bone: multi-step process to convert wood hierarchical structures into biomimetic hydroxyapatite scaffolds for bone tissue engineering,” *J Mater Chem*, vol. 19, no. 28, p. 4973, 2009, doi: 10.1039/b900333a.

[88] A. Ruffini, S. Sprio, and A. Tampieri, “Study of the hydrothermal transformation of wood-derived calcium carbonate into 3D hierarchically organized hydroxyapatite,” *Chemical Engineering Journal*, vol. 217, pp. 150–158, Feb. 2013, doi: 10.1016/j.cej.2012.11.107.

[89] “Patent WO2017021894 - Large 3d Porous Scaffolds Made of Active Hydroxyapatite Obtained by Biomorphic Transformation of Natural Structures and Process for Obtaining Them,” World Intellectual Property Organization (WIPO). Accessed: Jul. 23, 2023. [Online]. Available: https://patentscope.wipo.int/search/en/detail.jsf?docId=WO2017021894

[90] E. Kon *et al.*, “Bone Regeneration in Load-Bearing Segmental Defects, Guided by Biomorphic, Hierarchically Structured Apatitic Scaffold,” *Front Bioeng Biotechnol*, vol. 9, Sep. 2021, doi: 10.3389/fbioe.2021.734486.

[91] C. Poon, “Measuring the density and viscosity of culture media for optimized computational fluid dynamics analysis of in vitro devices,” *J Mech Behav Biomed Mater*, vol. 126, p. 105024, Feb. 2022, doi: 10.1016/j.jmbbm.2021.105024.

[92] “500 mL Vacuum Filter/Storage Bottle System,” Corning®. Accessed: Aug. 12, 2023. [Online]. Available: https://ecatalog.corning.com/life-sciences/b2c/US/en/Cell-Culture/Filtration/Vacuum-Filters/Vacuum-Filtration-Systems/p/430758

[93] F. Maes, T. Claessens, M. Moesen, H. Van Oosterwyck, P. Van Ransbeeck, and P. Verdonck, “Computational models for wall shear stress estimation in scaffolds: A comparative study of two complete geometries,” *J Biomech*, vol. 45, no. 9, pp. 1586–1592, Jun. 2012, doi: 10.1016/j.jbiomech.2012.04.015.

[94] A. d’Adamo *et al.*, “Experimental measurements and CFD modelling of hydroxyapatite scaffolds in perfusion bioreactors for bone regeneration,” *Regen Biomater*, vol. 10, Jan. 2023, doi: 10.1093/rb/rbad002.

[95] E. Salerno *et al.*, “Fluid dynamic parameters of naturally derived hydroxyapatite scaffolds for in vitro studies of bone cells,” *J Phys Conf Ser*, vol. 2685, no. 1, p. 012058, Jan. 2024, doi: 10.1088/1742-6596/2685/1/012058.

[96] A. K. Wong, P. LLanos, N. Boroda, S. R. Rosenberg, and S. Y. Rabbany, “A Parallel-Plate Flow Chamber for Mechanical Characterization of Endothelial Cells Exposed to Laminar Shear Stress,” *Cell Mol Bioeng*, vol. 9, no. 1, pp. 127–138, Mar. 2016, doi: 10.1007/s12195-015-0424-5.

[97] “Standard Infuse/Withdraw PHD ULTRA™ 4400 Programmable Syringe Pump,” Harvard Apparatus. Accessed: Sep. 21, 2023. [Online]. Available: https://www.harvardapparatus.com/standard-infuse-withdraw-phd-ultra-153-4400-programmable-syringe-pump.html

[98] “P720 Peristaltic Pumps,” Instech Laboratories, Inc. Accessed: Sep. 21, 2023. [Online]. Available: https://www.instechlabs.com/products/pumps/peristaltic/p720

[99] “Syringe Selection Guide,” Harvard Apparatus. Accessed: Sep. 22, 2023. [Online]. Available: https://www.harvardapparatus.com/media/harvard/pdf/Syringe%20Selection%20Guide.pdf

[100] E. Salerno *et al.*, “Liquid flow in scaffold derived from natural source: experimental observations and biological outcome,” *Regen Biomater*, vol. 9, Apr. 2022, doi: 10.1093/rb/rbac034.

[101] “15-012 AMEM (Alpha Modification of Eagle’s Medium) Formulation,” Corning Incorporated. Accessed: Nov. 03, 2023. [Online]. Available: https://www.corning.com/catalog/cls/documents/formulations/CLS-CG-FM-001.pdf

[102] “10-014 DMEM (Dulbecco’s Modified Eagle’s Medium) Formulation,” Corning Incorporated. Accessed: Nov. 03, 2023. [Online]. Available: https://www.corning.com/catalog/cls/documents/formulations/CLS-CG-BR-001-DMEM-Formulations.pdf

[103] “MEM-A SDS,” Biological Industries. Accessed: Oct. 25, 2023. [Online]. Available: https://www.bioind.com/media/wysiwyg/documents/msds/01-043-1__US_.pdf

[104] “DMEM SDS,” Biological Industries. Accessed: Oct. 25, 2023. [Online]. Available: https://www.bioind.com/worldwide/media/wysiwyg/documents/msds/01-055-1__US_.pdf

[105] T. Pei *et al.*, “Fluid Shear Stress Regulates Osteogenic Differentiation via AnnexinA6-Mediated Autophagy in MC3T3-E1 Cells,” *Int J Mol Sci*, vol. 23, no. 24, p. 15702, Dec. 2022, doi: 10.3390/ijms232415702.

[106] M. Schröder, J. E. Reseland, and H. J. Haugen, “Osteoblasts in a Perfusion Flow Bioreactor—Tissue Engineered Constructs of TiO2 Scaffolds and Cells for Improved Clinical Performance,” *Cells*, vol. 11, no. 13, p. 1995, Jun. 2022, doi: 10.3390/cells11131995.

[107] K. Sampson *et al.*, “Cultivation of hierarchical 3D scaffolds inside a perfusion bioreactor: scaffold design and finite-element analysis of fluid flow,” *SN Appl Sci*, vol. 3, no. 12, p. 884, Dec. 2021, doi: 10.1007/s42452-021-04871-3.

[108] J. Han *et al.*, “Development of a Scaffold-on-a-Chip Platform to Evaluate Cell Infiltration and Osteogenesis on the 3D-Printed Scaffold for Bone Regeneration,” *ACS Biomater Sci Eng*, vol. 9, no. 2, pp. 968–977, Feb. 2023, doi: 10.1021/acsbiomaterials.2c01367.

[109] P. F. Wood *et al.*, “The Action of Angiocrine Molecules Sourced from Mechanotransduction-Related Endothelial Cell Partially Explain the Successful of Titanium in Osseointegration,” *J Funct Biomater*, vol. 14, no. 8, p. 415, Aug. 2023, doi: 10.3390/jfb14080415.

[110] H. E. , Merritt, *Hydraulic Control Systems*. John Wiley & Sons, Inc., 1967.

[111] K. Wlodarczyk *et al.*, “Rapid Laser Manufacturing of Microfluidic Devices from Glass Substrates,” *Micromachines (Basel)*, vol. 9, no. 8, p. 409, Aug. 2018, doi: 10.3390/mi9080409.

[112] A. Fornell, P. Söderbäck, Z. Liu, M. De Albuquerque Moreira, and M. Tenje, “Fabrication of Silicon Microfluidic Chips for Acoustic Particle Focusing Using Direct Laser Writing,” *Micromachines (Basel)*, vol. 11, no. 2, p. 113, Jan. 2020, doi: 10.3390/mi11020113.

[113] P. R. Konari, Y.-D. Clayton, M. B. Vaughan, M. Khandaker, and M. R. Hossan, “Experimental Analysis of Laser Micromachining of Microchannels in Common Microfluidic Substrates,” *Micromachines (Basel)*, vol. 12, no. 2, p. 138, Jan. 2021, doi: 10.3390/mi12020138.

[114] Chen Cong *et al.*, “Rapid Picosecond Laser Seal Welding of Glass Using a Two-Step Scanning Strategy,” *Chinese Journal of Lasers*, vol. 50, no. 20, p. 2002101, 2023, doi: 10.3788/CJL230602.

[115] C. Ongaro *et al.*, “An Alternative Solution for Microfluidic Chip Fabrication,” *J Phys Conf Ser*, vol. 2385, no. 1, p. 012029, Dec. 2022, doi: 10.1088/1742-6596/2385/1/012029.

[116] S. Scott and Z. Ali, “Fabrication Methods for Microfluidic Devices: An Overview,” *Micromachines (Basel)*, vol. 12, no. 3, p. 319, Mar. 2021, doi: 10.3390/mi12030319.

[117] M. A. Eddings, M. A. Johnson, and B. K. Gale, “Determining the optimal PDMS–PDMS bonding technique for microfluidic devices,” *Journal of Micromechanics and Microengineering*, vol. 18, no. 6, p. 067001, Jun. 2008, doi: 10.1088/0960-1317/18/6/067001.

[118] “SMART PLASMA 2,” Plasma Technology GmbH. Accessed: Dec. 20, 2023. [Online]. Available: https://plasmatechnology.de/smartplasma-2.html

[119] L. Orazi, L. Romoli, M. Schmidt, and L. Li, “Ultrafast laser manufacturing: from physics to industrial applications,” *CIRP Annals*, vol. 70, no. 2, pp. 543–566, 2021, doi: 10.1016/j.cirp.2021.05.007.

[120] A. Al-Halhouli, W. Al-Faqheri, B. Alhamarneh, L. Hecht, and A. Dietzel, “Spiral Microchannels with Trapezoidal Cross Section Fabricated by Femtosecond Laser Ablation in Glass for the Inertial Separation of Microparticles,” *Micromachines (Basel)*, vol. 9, no. 4, p. 171, Apr. 2018, doi: 10.3390/mi9040171.

[121] V. Siciliani, A. Betti, C. Ongaro, L. Orazi, B. Zardin, and B. Reggiani, “UV picosecond laser processing for microfluidic applications,” in *Materials Research Proceedings*, Oct. 2023, pp. 334–341. doi: 10.21741/9781644902714-40.

[122] Y. Du, Z. Zhang, C. Yim, M. Lin, and X. Cao, “A simplified design of the staggered herringbone micromixer for practical applications,” *Biomicrofluidics*, vol. 4, no. 2, Jun. 2010, doi: 10.1063/1.3427240.

[123] T. P. Forbes and J. G. Kralj, “Engineering and analysis of surface interactions in a microfluidic herringbone micromixer,” *Lab Chip*, vol. 12, no. 15, p. 2634, 2012, doi: 10.1039/c2lc40356k.

[124] A. G. Hadjigeorgiou, A. G. Boudouvis, and G. Kokkoris, “Thorough computational analysis of the staggered herringbone micromixer reveals transport mechanisms and enables mixing efficiency-based improved design,” *Chemical Engineering Journal*, vol. 414, p. 128775, Jun. 2021, doi: 10.1016/j.cej.2021.128775.

[125] M. M. Bradford, “A rapid and sensitive method for the quantitation of microgram quantities of protein utilizing the principle of protein-dye binding,” *Anal Biochem*, vol. 72, no. 1–2, pp. 248–254, May 1976, doi: 10.1016/0003-2697(76)90527-3.

[126] B. Hama, G. Mahajan, P. S. Fodor, M. Kaufman, and C. R. Kothapalli, “Evolution of mixing in a microfluidic reverse-staggered herringbone micromixer,” *Microfluid Nanofluidics*, vol. 22, no. 5, p. 54, May 2018, doi: 10.1007/s10404-018-2074-0.

[127] I. Sabotin *et al.*, “Preliminary Study on Staggered Herringbone Micromixer Design Suitable for Micro EDM Milling,” 2019, pp. 229–236. doi: 10.1007/978-3-319-99353-9_25.

[128] “Pierce™ Bradford Protein Assay Kit - USER GUIDE,” Thermo Fisher Scientific - Pierce Biotechnology. Accessed: Nov. 27, 2023. [Online]. Available: https://www.thermofisher.com/document-connect/document-connect.html?url=https://assets.thermofisher.com/TFS-Assets%2FLSG%2Fmanuals%2FMAN0011181_Coomassie_Bradford_Protein_Asy_UG.pdf

[129] M. Wagner, K. Reiche, A. Blume, and P. Garidel, “Viscosity measurements of antibody solutions by photon correlation spectroscopy: an indirect approach – limitations and applicability for high-concentration liquid protein solutions,” *Pharm Dev Technol*, vol. 18, no. 4, pp. 963–970, Aug. 2013, doi: 10.3109/10837450.2011.649851.

[130] “How to use a protein assay standard curve,” Thermo Fisher Scientific - Pierce Biotechnology. Accessed: Nov. 27, 2023. [Online]. Available: https://www.thermofisher.com/document-connect/document-connect.html?url=https://assets.thermofisher.com/TFS-Assets%2FLSG%2FApplication-Notes%2FTR0057-Read-std-curves.pdf

[131] A. W. Etchells and C. F. Meyer, “Mixing in Pipelines,” in *Handbook of Industrial Mixing*, Wiley, 2003, pp. 391–477. doi: 10.1002/0471451452.ch7.

[132] M. Jain, A. Rao, and K. Nandakumar, “Numerical study on shape optimization of groove micromixers,” *Microfluid Nanofluidics*, vol. 15, no. 5, pp. 689–699, Nov. 2013, doi: 10.1007/s10404-013-1169-x.

[133] K. Karthikeyan and L. Sujatha, “Study of Permissible Flow Rate and Mixing Efficiency of the Micromixer Devices,” *International Journal of Chemical Reactor Engineering*, vol. 17, no. 1, Jan. 2019, doi: 10.1515/ijcre-2018-0047.

[134] F. Widdershoven *et al.*, “A CMOS Pixelated Nanocapacitor Biosensor Platform for High-Frequency Impedance Spectroscopy and Imaging,” *IEEE Trans Biomed Circuits Syst*, vol. 12, no. 6, pp. 1369–1382, Dec. 2018, doi: 10.1109/TBCAS.2018.2861558.

[135] D. D. Stupin *et al.*, “Bioimpedance Spectroscopy: Basics and Applications,” *ACS Biomater Sci Eng*, vol. 7, no. 6, pp. 1962–1986, Jun. 2021, doi: 10.1021/acsbiomaterials.0c01570.

[136] A. Cossettini *et al.*, “Ultra-High Frequency (500 MHz) Capacitance Spectroscopy for Nanobiosensing,” in *2020 IEEE SENSORS*, IEEE, Oct. 2020, pp. 1–4. doi: 10.1109/SENSORS47125.2020.9278583.

[137] C. Laborde *et al.*, “Real-time imaging of microparticles and living cells with CMOS nanocapacitor arrays,” *Nat Nanotechnol*, vol. 10, no. 9, pp. 791–795, Sep. 2015, doi: 10.1038/nnano.2015.163.

[138] D. Goldoni, C. Ongaro, L. Orazi, L. Rovati, and L. Selmi, “Estimation of Analyte’s Vertical Positions above the Surface of Nanocapacitor Array Biosensors,” in *2023 IEEE SENSORS*, IEEE, Oct. 2023, pp. 1–4. doi: 10.1109/SENSORS56945.2023.10325169.